

An Investigation of Entorhinal Spatial Representations in  
Self-Localisation Behaviours

Harry Clark



Doctoral Thesis in Precision Medicine  
Biomedical Sciences  
School of Medicine and Veterinary Medicine  
University of Edinburgh  
2022

## Abstract

Spatial-modulated cells of the medial entorhinal cortex (MEC) and neighbouring cortices are thought to provide the neural substrate for self-localisation behaviours. These cells include grid cells of the MEC which are thought to compute path integration operations to update self-location estimates. In order to read this grid code, downstream cells are thought to reconstruct a positional estimate as a simple rate-coded representation of space.

Here, I show the coding scheme of grid cell and putative readout cells recorded from mice performing a virtual reality (VR) linear location task which engaged mice in both beaconing and path integration behaviours. I found grid cells can encode two unique coding schemes on the linear track, namely a position code which reflects periodic grid fields anchored to salient features of the track and a distance code which reflects periodic grid fields without this anchoring. Grid cells were found to switch between these coding schemes within sessions. When grid cells were encoding position, mice performed better at trials that required path integration but not on trials that required beaconing. This result provides the first mechanistic evidence linking grid cell activity to path integration-dependent behaviour.

Putative readout cells were found in the form of ramp cells which fire proportionally as a function of location in defined regions of the linear track. This ramping activity was found to be primarily explained by track position rather than other kinematic variables like speed and acceleration. These representations were found to be maintained across both trial types and outcomes indicating they likely result from recall of the track structure.

Together, these results support the functional importance of grid and ramp cells for self-localisation behaviours. Future investigations will look into the coherence between these two neural populations, which may together form a complete neural system for coding and decoding self-location in the brain.

## Lay Summary

Navigating to food, away from danger and in search of mates, forms the basis of movement for all life in the animal kingdom. The brain's solution to planning the routes we take comes in the form of a "cognitive map" found in the hippocampus and medial entorhinal cortex (MEC) in the form of neurons that fire electrical signals at rates proportional to specific locations, heading direction and running speed. Neurons called grid cells fire at multiple locations that resemble a triangular grid in an environment. These cells are thought to play a role in calculating how mammals update the estimate of where they are within an environment. A further group of cells termed readout cells are likely needed to read the grid code. One possible type of readout cell termed a ramp cell fires proportionally to the distance to a specific location and resembles a ramping firing profile.

In this thesis, I recorded from grid and ramp cells in the MEC and neighbouring brain areas of mice trained to navigate along a virtual reality (VR) linear track and stop at a specific location to receive a reward. This location was either marked with a visual cue or not. I found grid cells fired at similar locations across trials when mice were successful on trials in which the visual cue was absent, suggesting grid cell firing is associated with navigation without the need of visual cues. The firing of ramp cells were not affected by the success of mice navigating to the reward nor the type of navigation required of the mice. This suggested ramp cells form a memory of the linear track which can be used to guide the stopping behaviour of the mouse.

The results in this thesis show that these two types of cell are important for navigation of mice and most likely humans. Understanding how these two cell types work together to guide navigation will be the next step to uncovering how mammals navigate in the real world.

## Acknowledgements

I would like to thank those who have helped me deliver a body of work that I believe can and will progress the neuroscience of spatial navigation. I would first like to thank Matthew Nolan, his supervision and insight has forged me from a novice scientist to something entirely different and unexpected from when I first began my PhD. How I think about the world and how to address questions scientific or otherwise has changed me forever and for the better. I would like to thank members of my PhD committee, Thanasis Tsanas, Ram Ramamoothry and Emma Wood, whose feedback helped me deliver a clear research question.

Thank you to all members of the Matthew Nolan and Gulsen Sürmeli lab who helped me to deliver many different types of neuroscience methods and data collection. Thank you to Ian Hawes and Teris Tam for their help and assistance with data analysis and programming questions. Thank you to Junji Hua and Wannan Yang for collecting data from several mice. Thank you to Sau Tsoi for assisting me with brain preparations for cresyl violet staining and imaging. Thank you to Robert Wallace, Holly Stevens and Steph Collishaw for their help and assistance with the MicroCT imaging of the mice brains. Thank you to Sarah Tennant and Klara Gerlei who took much time to train and help me with behavioural, data analysis and wet lab procedures. You have been my rocks both inside and outside of the lab.

While I cannot thank them, I would like to remember the lives of the mice which provided the neurological and behavioural data upon which this thesis stands. I can only hope this body of work will not be in vain. The lives in which we sacrifice in the name of science cannot be forgotten however small, even if (selfishly or not) as a society we have deemed it necessary for the betterment of human life. During the course of my work with these small critters, they provided me with so much joy and can only hope I served them as well as I could.

Finally, I would like to thank those that gave their time to make me feel comfortable and loved during my time in Edinburgh, and survived living with me, providing countless memories, Michael Cutter, Brooke Myers, Sau Tsoi, Lazaros Mitskopoulos and Klara Gerlei. I would also like to thank my partner and friend Cerys Hughes who has provided me with the happiness and spirit to complete my thesis while also travelling the world. And finally I would like to thank my loving parents Adrian and Kim Clark who moulded me into a caring and mindful individual, with an inquisitive mind that kept me going throughout.

# Declaration

This thesis was composed by Harry Clark. The work detailed in this thesis was carried out by Harry Clark. Data collection, experimental setups and analysis detailed in this thesis was largely a collaborative effort between members of the Matthew Nolan research group. Work carried out by researchers other than Harry Clark are clearly detailed where appropriate. Key contributors are listed below. This work has not been submitted for any other degree or professional qualification. Detailed below are all contributions to this body of work.

## Chapter 2

- Sarah Tennant and Lukas Fischer designed and created the virtual reality system.
- Sarah Tennant and Klara Gerlei designed and created the open field system.
- Sarah Tennant and Klara Gerlei established the electrophysiology and behavioural analysis pipeline.
- Sarah Tennant established the virtual reality linear location estimation task and behavioural protocol.
- Sarah Tennant and Holly Stevens assisted with the preparation of brain tissue for MicroCT imaging.
- Robert Wallace and Steph Collishaw carried out the MicroCT imaging.
- Ian Hawes assisted with the high throughput computing with the Eddie remote computer cluster

## Chapter 4

- Sarah Tennant established the analysis of spatial modulated cells with ramp-like positional coding.
- Sarah Tennant, Junji Hua, Wannan Yang contributed collectively to the data collection of 5/11 mice presented.
- Ian Hawes and Wing Kin Tam contributed additional analysis briefly discussed in this thesis.

# Contents

<b><u>1 Introduction</u></b>	<b>10</b>
1.1 Spatial navigation as a model for studying the brain	12
1.2 Spatial navigation strategies	14
1.2.1 Beaconing	14
1.2.2 Path integration	16
1.3 The cognitive map	17
1.3.1 Building blocks of a cognitive map	17
1.3.2 The cognitive map and navigation	18
1.3.3 Connectivity of the cognitive map	21
1.3.4 Towards a generalised cognitive map	23
1.4 Grid cells and path integration	25
1.4.1 Properties of the grid cell system	25
1.4.2 Emergence of grid patterns	28
1.4.3 Spatial content of grid cells	32
1.4.4 Reading a grid code	34
1.4.5 Possible behaviour roles of grid cells	38
1.5 Thesis aims	41
<b><u>2 Materials and methods</u></b>	<b>42</b>
2.1 Ethical statement	42
2.2 Research animals	42
2.3 Tetrode microdrives	42
2.3.1 Overview	42
2.3.2 Microdrive assembly	43
2.3.3 Implantation	47
2.4 Experimental setups	50
2.4.1 Overview	50
2.4.2 Virtual reality	50
2.4.3 Open field	61
2.5 In vivo behavioural tasks	70
2.5.1 Overview	70
2.5.2 Virtual reality	71
2.5.2.1 Task design	71
2.5.2.2 Linear track	73
2.5.2.3 Reward	75
2.5.2.4 Animal housing	75
2.5.2.5 Animal handling	75
2.5.2.6 Animal habituation	76
2.5.2.7 Food deprivation protocol	76
2.5.2.8 Behavioural training	81

2.5.3 Open field	83
2.5.3.1 Task design	83
2.6 Tissue Imaging	84
2.6.1 Overview	84
2.6.2 Perfusion fixation	84
2.6.3 Micro-CT	85
2.6.3.1 Tissue processing	85
2.6.3.2 Imaging	86
2.6.4 Cresyl violet staining	88
2.7 Data Processing and Analysis	89
2.7.1 Overview	89
2.7.2 Pre-processing	89
2.7.3 Spike sorting	91
2.7.4 Curation	91
2.7.5 Post-processing	92
2.7.6 Remote computing services	92
2.8 Identifying spatial cells in open field and virtual reality environments	93
2.8.1 Concatenated spike sorting	93
2.8.2 Classification of cell types in the open arena	95

---

<b>3 Self-localisation behaviours in a VR linear location task</b>	<b>97</b>
3.1 Introduction	97
3.2 Methods	98
3.2.1 Subjects	98
3.2.2 Data analysis	99
3.2.3 Quantification of spatial behaviours	99
3.2.4 Classification of trial outcome	103
3.3 Results	106
3.3.1 Mice learn to solve a linear location estimation task	106
3.3.1.1 Performance summary	106
3.3.1.2 Mice optimise a stopping strategy over learning	111
3.3.2 Task improvements: Improving non-beaconed task engagement	116
3.3.2.1 Motivation	116
3.3.2.2 The effect of expected reward allocation on task performance	119
3.4 Discussion	122
3.4.1 Technical challenges	122
3.4.2 Do animals path integrate in a VR linear location estimation task?	122

---

<b>4 How do grid representations relate to task performance?</b>	<b>124</b>
4.1 Introduction	124
4.2 Methods	125
4.2.1 Subjects	125

4.2.2 Data analysis	125
4.2.3 Calculating spatial periodicity	125
4.2.3.1 Possible coding schemes	125
4.2.3.2 Quantification of spatial periodicity	128
4.2.3.3 Classifying spatial periodicity using a field shuffle method	132
4.2.3.4 Classifying spatial periodicity across a single session	136
4.3 Results	138
4.3.1 Grid cells encode position and distance on a linear track	138
4.3.2 Grid cells are not locked to a single coding scheme	142
4.3.3 Pairs of grid cells switch between periodic coding schemes coherently	145
4.3.4 Grid coding is associated with path integration-dependent behaviours	147
4.4 Discussion	152
4.4.1 Technical challenges	153
4.4.2 Behavioural and computational roles	154
4.5 Appendix	155
4.5.1 Tetrode localisation	155

---

<b>5 Spatial representation by ramping activity of neurons</b>	<b>158</b>
5.1 Introduction	158
5.2 Methods	159
5.2.1 Subjects	159
5.2.2 Data analysis	159
5.2.3 Measuring ramp-like spatial codes	159
5.2.3.1 Possible coding schemes	159
5.2.3.2 Classifying spatial ramp-like neural activity	162
5.2.4 Generalised linear mixed effect model for position, speed and acceleration	164
5.2.5 Measuring theta index and local field potentials	164
5.3 Results	166
5.3.1 Encoding of location by ramping activity	166
5.3.2 Interruption of ramp-like firing profiles encode rewarded locations	170
5.3.3 Differential influence of position, speed and acceleration	171
5.3.4 Ramp codes across trial outcomes	174
5.3.5 Ramp codes across trial types	177
5.3.6 Ramp cells in the open field	180
5.3.7 Ramp cells are found within the retrohippocampus	184
5.3.8 Ramping activity is similar across retrohippocampal regions	190
5.3.9 Theta modulation of ramp cells	191
5.4 Discussion	192
5.4.1 Technical challenges	192
5.4.2 Relationship to neural activity in other brain areas	193
5.4.3 Behavioural and computational roles	194

<b><u>6 Discussion</u></b>	<b>195</b>
6.1 What role do grid cells play in self localisation?	197
6.2 What role do ramp cells play in self localisation?	200
6.3 Joint grid-ramp system for self-localisation?	202
6.4 Wider applications of the research findings	203
6.4.1 Models for self-localisation and beyond	203
6.4.2 Diagnosis of Alzheimer's disease	205
<b><u>7 Conclusions</u></b>	<b>207</b>
<b><u>8 Bibliography</u></b>	<b>208</b>

# Introduction

The goal of modern neuroscience is to understand the organic computer that is the brain, so that we might cure illness, learn from its algorithmic solutions to information processing and uncover what makes life so *je ne sais quoi*. In Chapter 1.2 of Vision (Marr 1982), David Marr describes the three levels at which an information processing machine must be understood, these are (1) the goal of the computation being carried out, (2) the algorithmic solution to the computation and (3) the physical implementation of the algorithm. Studying spatial navigation in rodents is one of the leading paradigms in modern neuroscience because it offers a complete reconciliation of these three levels. First, it offers a clear behavioural readout in the form of trackable spatial variables, providing an objective measure of the performance of the computation. Secondly, in combination with electrophysiological recording, the algorithmic solutions can be unearthed by resolving these spatial variables with neural activity. And finally, the implementations of these algorithms might be deduced with precision manipulations, to reconstruct the network blueprints underlying the spatial behaviour.

In this thesis, I will address the neural computation of self localisation, a process in which self-location is estimated within an environment. Estimates of one's location can be calculated through landmark-driven beaconing and path integration, a spatial navigation strategy used in invertebrates (Wehner and Wehner 1986) and mammals (Mittelstaedt and Mittelstaedt 1980) to update their estimate of self-location through integrating self-motion signals. How mammals implement path integration operations in the brain is an outstanding question. The principal candidates for this computation are grid cells of the medial entorhinal cortex, a spatial modulated cell type that fires periodically such that their firing fields appear at the vertices of a hexagonal lattice and tile the environment (Hafting et al. 2005). I will argue that key features of their firing activity correlates with the behaviour of mice performing path integration. I will then argue a new spatial modulated cell type is linked to the effective readout of a spatial estimate of self-location. To establish the premise of this research, In Chapter 1, I will review the literature highlighting the research of self-localisation and path integration, grid cell firing and the lack of viable evidence for reconciling the causal relationships of the two. In Chapter 2, I will describe the technical specifications for reproduction of work discussed in this thesis. In Chapter 3, I will present a spatial navigation task which can only be solved by performing path integration-based navigation. I will then detail improvements I have made to the task to reproduce reliable path integration behaviours. In Chapter 4, I will address what grid cells encode while performing the self-localisation task and investigate whether the coding is linked to accurate

self-localisation. In Chapter 5, I will present work in which I was joint co-first author concerning a newly discovered spatial-modulated cell type we called positional “ramp cells”. These novel cells found for the first time in in-vivo electrophysiological recordings have long been hypothesised as a functional component to the readout of a path integration neural network. And finally in Chapter 6, I will discuss the implications of the findings of this thesis and will contextualise future research directions and predictions spawned from this work.

## 1.1 Spatial navigation as a model for studying the brain

Spatial navigation encompasses the ability to plan, guide and execute routes to target locations in physical space. Unsurprisingly, it is an essential skill for survival in all locomotive animals. Its origins however can be seen in the earliest examples of life on earth. Single-celled life has long been expected to have begun around hydrothermal vents in the deep oceans approximately 4.5 billion years ago (Betts et al. 2018). Here, early lifeforms would have collected nutrients by navigating chemical gradients similar to microbes alive today, in a process called chemotaxis (Porter, Wadhams, and Armitage 2011). This was the first example of an organism using its sensation of its local environment to inform its future actions. Being able to move to advantageous locations for nourishment and away from danger fuelled the evolution of complex life as we know it. Moreover, it was the first evidence of an organism implementing a navigational strategy consistent with having a spatial model of a physical environment. This can be seen in [Figure 1](#), where a single-celled agent detects nutrients and uses the relative abundances of the nutrients on its cell surface to inform its future direction. In this case the agent moves north, and over time will move closer to the highly enriching region of the environment. If the single-celled agent's movement was not informed by the nutrients it accumulates, its movement would resemble random chaotic motion. The important implication is that the agent is no longer naive to the distribution of nutrients and can use this newly acquired knowledge to make informed navigational choices, and can thus minimise the energy expended to locate more nutrients. These organisms could then outcompete their naive relatives. Fast-forward to the present day, organisms have developed a host of sensory systems to inform their local position in their environment such as visual, tactile, auditory and chemical perception. A mouse in addition to following chemical gradients via its olfactory system uses vision to find food. It thus follows that the study of spatial navigation is not just the study of how animals guide their locomotion, but can also be a study of how a model of physical space emerged in the brain to guide locomotion.

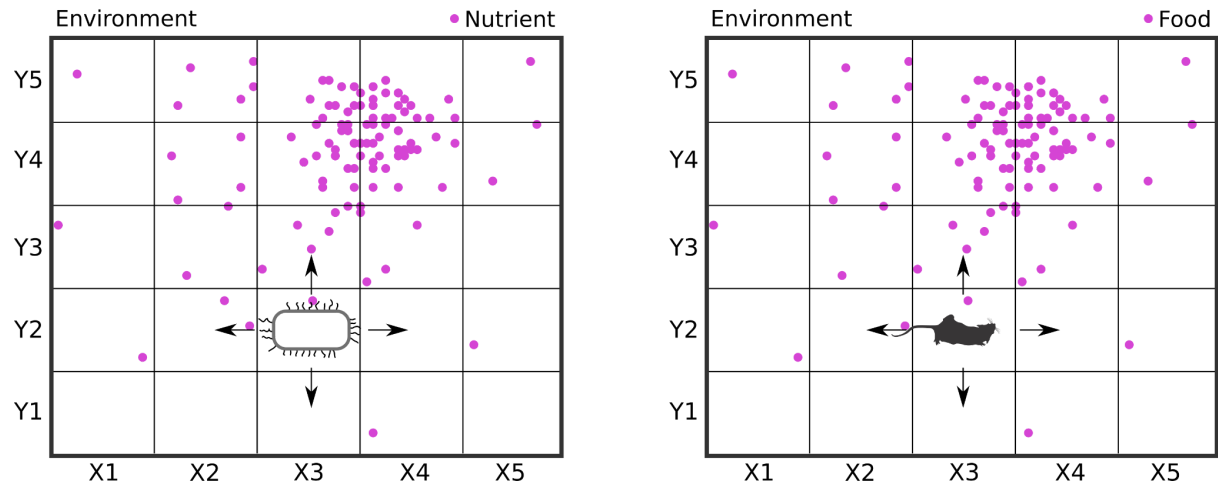
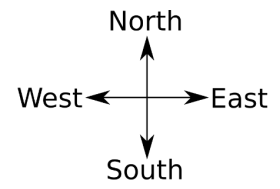


**Figure 1. Relationship between single cell and multicellular spatial navigation.** Agents navigating through a 2D environment explore for nutrition. Left: A single-celled organism uses chemotaxis to move toward regions of an environment with high concentrations of nutrients. Right: A mouse exploring for food primarily uses its vision and olfaction to detect regions of an environment with high concentrations of food.

## 1.2 Spatial navigation strategies

Mammals inhabit a vast range of environments including ground, underground, water and sky. These environments demand different navigational strategies as they vary in physical structure and the sensory cues available. Some mammals can be found in multiple of these environments and thus require a brain with a capacity to execute and switch between a host of strategies. It is important to note that navigational strategies can be subdivided on a number of different levels of abstraction. These include categorization based on the type of sensory information utilised, the frames of reference used, the types of spatial memory implicated or the utility of an internal spatial model, with a large degree of overlap between these subdivisions. In this section, navigation strategies will be reviewed with a focus on the types of sensory information utilised, as this will be central to the questions addressed in this thesis with regards to the functional role of spatially-modulated cells.

Sensory information available to animals comes in two classes of sensory cues namely allothetic and idiothetic information. Allothetic information is provided by the environment and is picked up mainly through sensory signals external to the body including visual, auditory and olfactory sensation. Conversely, idiothetic information is provided internally and is created through the process of motion. These self-generated motion cues come in the form of proprioception (the body's ability to sense the location of body parts relative to itself), motor-efferent copies (movement-generating signals produced by the motor system), and sensory flow (relative motion of sensory stimuli caused by the movement of an observer in an environment). Navigation directly towards allothetic cues is called beaconing whereas navigation with idiothetic cues is called path integration (Geva-Sagiv et al. 2015).

### 1.2.1 Beaconing

Navigation using beaconing involves the use of external sensory cues (or "beacons") to inform the trajectory taken towards a target location. In its simplest form, a beacon is a static navigational landmark which serves as the target location. Beacons can also serve as way-points along a trajectory or a proximal landmark to a target location in the cases of route-following and piloting strategies respectively. All such examples have been shown in bats. Visual beaconing in bats was observed in Trinidad where the central mountain range was used as a beacon (Williams, Williams, and Griffin 1966). Auditory piloting was observed in which the sounds of chorusing swamp frogs were used as a proximal beacon to possibly hunt for insects co-localising with the frogs (Buchler and Childs 1981). Route-following was also observed in which forest paths (Jones and Holderied 2007) and passageways of

underground caves (Blatchley 1896) were used as beaconed routes. A simple example of beaconing via route following is shown in [Figure 2A](#) in the case of animal homing.

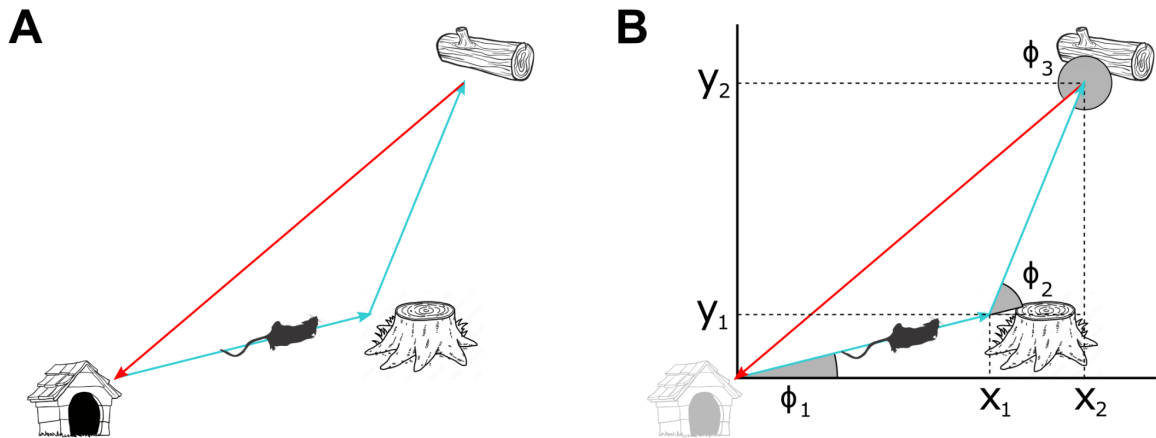


**Figure 2. Homing behaviour by visual beaconing and path integration.** (A) A mouse ventures out of its house and moves towards a tree stump followed by a log, before returning home. The tree stump, log and house all serve as visual sensory cues to guide its trajectory. (B) The mouse makes the same outbound journey to the tree stump and log but this time, navigates back to its house without using the house as a sensory cue (as if the house wasn't visible due to fog). Here, the mouse can theoretically calculate a homing vector by keeping track of the distance that it traversed and its change in heading direction on its outbound legs of its journey. Part B is adapted from Mcnaughton et al. (2006).

### 1.2.2 Path integration

Idiothetic cues provide the self-motion information necessary to calculate the displacement (or velocity vector) between two locations. When this information is integrated over time, a displacement from the starting point can be calculated by summing all velocity vectors together. These calculations afford the observer to estimate their relative location from some starting point without the need for beaconing cues. This form of navigation was particularly useful for oceanfaring navigators as beaconing cues were sparingly available. Navigators estimated their speed by casting a weighted string into the water and counted how many knots in the string passed through their fingers in 30 seconds. This idiothetic information was used to calculate the distance they travelled over time and logged their expected location on a map. This was termed “dead reckoning” as one could only do as well to ‘reckon’ where they were. The process naturally accumulated positional errors over time and thus required correction when beaconing cues were available. Static beacons were used for this correction as they provided a measure of the ground truth position to compare their best estimates with. These came in the form of stars at night whose position in the sky provided vital angular reorientation and other static landmarks such as a recognisable island for which self-location estimates could be corrected in both location and heading direction.

To effectively use path integration navigation, self-location must be tracked over time. Without a log book of its own, an animal must store a representation of its location internally. Early rodent experiments demonstrated rats could learn about their environment without explicit rewards (Blodgett, 1929). When rewards became available in a maze, rats quickly exploited shortcuts. This demonstrated rats could learn about their environment latently and suggested the formation of a “cognitive map” of the environment within the rats’ brain (Tolman, 1948). The first experimental evidence for mammals tracking their linear and angular motion came from Mittelstaedt and Mittelstaedt (1980). Female gerbils journeyed out of their nests onto a circular arena in complete darkness to search for and bring back their pups which had been displaced into cups. If the arena was quickly rotated while the mother was inside a cup, they could return directly back to their nest. This showed angular information had been actively tracked, possibly through vestibular input. If the cup was moved without rotation however, the gerbil missed the nest by the same amount as the cup was moved. This showed the positional displacement had been tracked during the outbound journey, and was being used to construct the return trajectory. This experiment also highlights that different types of idiothetic cues are required to accurately update linear and angular motion. Vestibular input was the only idiothetic information available to the mother while in the cup and was sufficient to account for rotations but not translations. Consider the

mouse in [Figure 2](#), when it arrives at the log, in order to compute a homing vector it must integrate the distance travelled with the changes in angular velocity to accurately compute the return direction and distance. This neatly demonstrates that navigation by path integration can be subdivided into two components, angular and linear path integration but must be reconciled to accurately navigate in real-world environments.

### 1.3 The cognitive map

#### 1.3.1 Building blocks of a cognitive map

How are these navigational strategies set to action in the brain? Substantiating Tolman's cognitive map hypothesis, O'Keefe and Dostrovsky (1971) discovered "place cells" in the hippocampus that fired only when a rat was at a particular location in its environment. This has since been followed up by the discovery of numerous spatially-modulated cell types including border cells in the entorhinal cortex (Solstad et al. 2008), boundary vector cells in the subiculum (Lever et al. 2009), head direction cells in the postsubiculum (J. Taube, Muller, and Ranck 1990), speed cells in the medial entorhinal cortex (MEC; Kropff et al. 2015), grid cells in the MEC (Hafting et al. 2005) and cells with mixed or heterogeneous spatial firing properties (Sargolini et al. 2006; Hardcastle et al. 2017). Furthermore, the theta oscillation (4–12 Hz) in local field potentials in the hippocampal formation is closely associated with spatial functions. Individual neurons show phase precession in place and grid cells (Hafting et al. 2008; John O'Keefe and Recce 1993). Border cells fire exclusively at borders or boundaries in an environment. Boundary vector cells fire exclusively at set distances from borders or boundaries . Head direction cells fire preferentially to a single heading direction within an environment. Speed cells fire proportionally to the current speed of the animal. Grid cells fire periodically such that their firing fields appear at the vertices of a hexagonal lattice and tile the environment. Conjunctive representations also exist between these cell types with large overlaps. Several examples are shown in [Figure 3](#). The presence of this array of cells within the hippocampus and neighbouring retrohippocampal regions shows the brain holds representations of both allocentric space and egocentric spatial variables, which are the key ingredients for beaconing and path integration-based navigation respectively.

What do these cells add to the navigation system? Place cells as a population can encode an animal's current position within an environment. Robinson et al. (2020) showed activation of place cells with firing fields associated with a reward zone could drive behaviours associated with a mouse being in the reward zone. This showed direct evidence for a causal role of place cells in spatial navigation. Placing task demands on an animal has been shown to dramatically remap locations of place fields (Griffin, Eichenbaum, and Hasselmo 2007;

Geva-Sagiv et al. 2015). These findings are consistent with place cells reflecting a code of distinct spatial memories within the same environment and not a general purpose spatial map. Head direction cells provide a population metric for quantifying the relative heading direction of the animal in relation to the environment. This could be considered as the compass upon the navigator's map. Border cells are thought to provide an anchoring signal to other spatial cell types like place and grid cells (Solstad et al. 2008). This is supported by evidence that border representations are found before place and grid cells in developing rats (Bjerknes, Moser, and Moser 2014). Moreover, border representations were predicted from early emergent models of place cells (Hartley et al. 2000). Grid cells are thought to play a role in path integration (Hafting et al. 2005; McNaughton et al. 2006) as they are ideally localised to brain regions which receive both head direction and speed inputs that are required to compute changes in positional updates. Moreover, many computation models have demonstrated how populations of grid cells might be employed to encode position (McNaughton et al. 2006; Bush et al. 2015; Fiete, Burak, and Brookings 2008). Speed cells are thought to provide a speed input to grid cells to support their path integration computations. Non-specific spatial cells can encode a conjunctive representation of spatial variables and may contribute to the firing properties of specific spatial cell types or are recruited when task demands are placed on the animal.

### 1.3.2 The cognitive map and navigation

Does this cognitive map play an active role in navigation? To test the role of the hippocampus, Packard and McGaugh (1996) trained rats to solve a T-maze task in which the animal must choose between an East or West turn to reach a food reward (in this case, the west goal of the maze). The navigational strategy employed by the rat could be probed by rotating the T-maze 180°. If the animal took the path East, a response strategy was employed as the navigational actions were maintained (e.g. go forward and turn left). If the animal took the path West, a place strategy was employed as the navigation actions were altered in response to the changes in the spatial relationships between environment cues. After 8 days of training, rats favoured the place strategy consistent with the employment of a cognitive map that embedded cues and their spatial relations into a common framework. Inactivation of the hippocampus with lidocaine removed this preference for a place strategy. This task was extended to require rats to continuously alter their choices on consecutive trials (Ainge et al. 2007). Hippocampal lesions did not affect performance but did when a delay was introduced between trials. This is consistent with the hippocampus playing a role in the recall of the spatial memories from the preceding trial. In the Morris water maze task, animals learn to swim to invisible water-submerged platforms from a number of different

starting positions (Morris et al. 1982). When trained only from a single starting location, rats with hippocampal lesions successfully navigate to the platform, however they fail when trained from multiple starting locations and are required to take novel routes (Eichenbaum, Stewart, and Morris 1990). This points to the hippocampus supporting a cognitive map in which novel navigation can be generalised from previous experiences.

In the neighbouring entorhinal cortex, lesions caused impaired sensory integration and spatial learning in rats (Davis, Gimenez, and Therrien 2001). Path integration behaviour is also impaired when glutamate receptors AMPA and NMDA are experimentally ablated in retrohippocampal regions with a noted change in grid cell spatial firing properties (Allen et al. 2014; Gil et al. 2018). Tennant et al. (2018) targeted layer II MEC stellate cells and found inactivation reduced spatial learning in a spatial memory task for both beaconing and path integration behaviours. These findings in rodents are backed up by evidence by Kunz et al. (2018) that showed spatial behaviours in a virtual reality path integration task to differ in humans that carried the Alzheimer's genetic risk factor APOE-e4 with a significant reduction of blood-oxygen-level-dependent (BOLD) signal in the temporal lobe associated with grid cell representations.

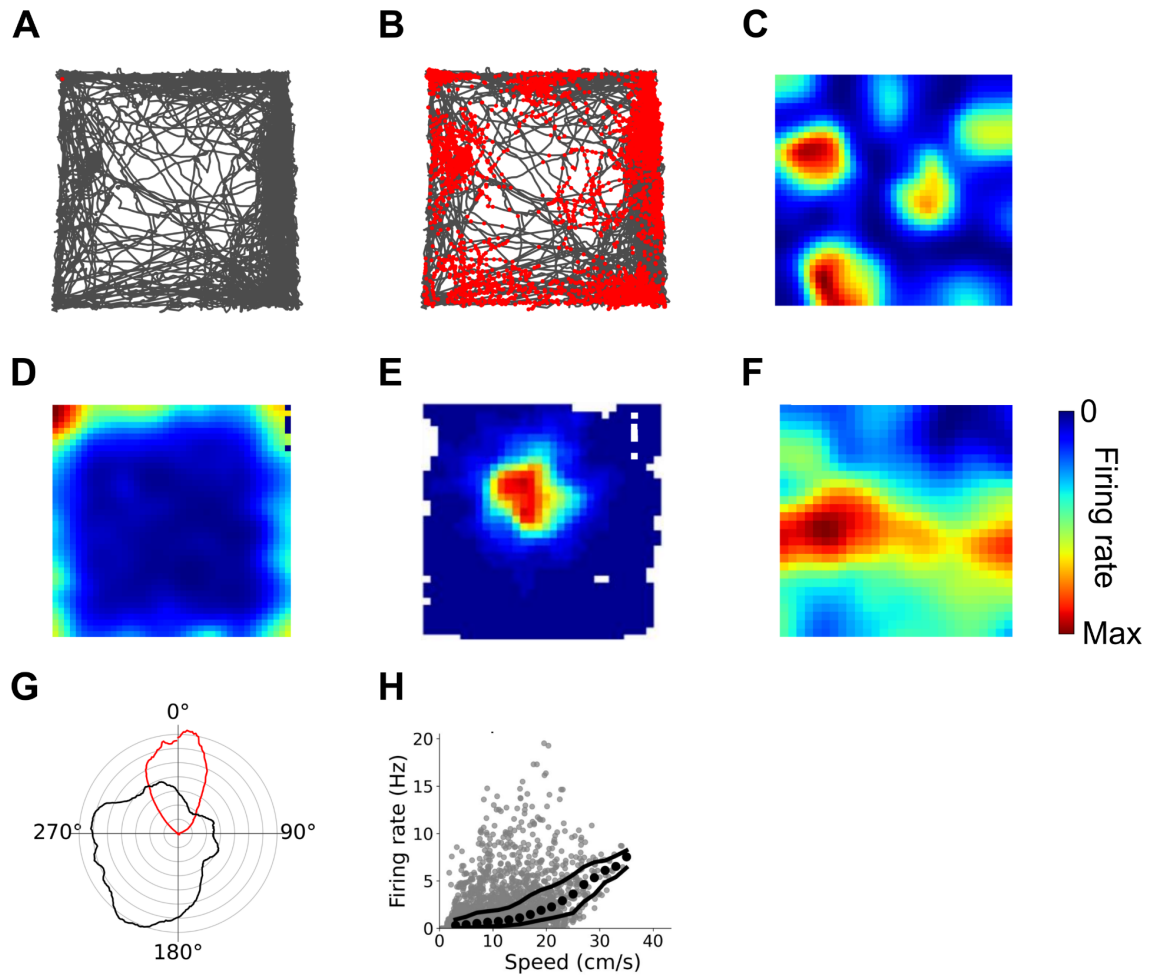


**Figure 3: Examples of spatial modulated cell types found when a mouse freely explores an open field arena.** A mouse explores a square arena, tracing a trajectory over time and sampling all parts of the environment (A). Recorded spikes (B) are binned in space (as in C-F) or binned by heading direction (as in G) and firing rates calculated as the number of spikes within a bin divided by the total time spent in the bin across the session to create firing rate maps over space (C-F) or direction (G). Example spatial cells include a (C) grid cell, (D) border cell, (E) place cell, (F) non-specific spatial cell, (G) head direction cell and (H) speed cell. White portions of the rate map are locations not sampled by the mouse. The polar plot in E shows the firing rate preference in red and relative proportions of directional sampling in black. Scatter plot in F shows the instantaneous firing rate vs the instantaneous speed. The black dots indicate the mean firing rate as a function of speed, and black line indicates standard error of the mean.

### 1.3.3 Connectivity of the cognitive map

How do these cells work together to inform navigational decisions and form the cognitive map? [Figure 4](#) shows a high level schematic of the connectivity and strength of cortical input to the hippocampal formation. The vast majority of input to the hippocampus proper is delivered through the entorhinal areas. These areas receive input from many sensory areas such as visual, auditory, and somatosensory cortices, which provides the pathways to deliver information that can be used to build spatial representations. The proximity of the various spatially-modulated cell types within the hippocampal formation suggests a collaborative function for the navigating animal. [Figure 5](#) outlines the information flow between regions in the hippocampal formation. Place cells are found in the dentate gyrus and hippocampus proper. Head direction signals are conveyed to the hippocampus via the parasubiculum, presubiculum and MEC (J. S. Taube 2007). Positional input to the hippocampus may come in the form of border representations from the subiculum (Barry et al. 2006; Colin Lever et al. 2009; Stewart et al. 2014), MEC (Savelli, Yoganarasimha, and Knierim 2008; Solstad et al. 2008), presubiculum and parasubiculum (Boccara et al. 2010) or from grid cells in layer II/III of the MEC (Hafting et al. 2005). Border and head direction cells emerge early in rat development (Langston et al. 2010; Wills et al. 2010; Bjerknes, Moser, and Moser 2014) so might form the spatial substrates for positional coding, while place cells and then grid cells emerge at later developmental stages (Langston et al. 2010; Wills et al. 2010). While place cells can exist in the absence of grid cells, lesioning layer III of the MEC, which removes the MEC-CA1 and MEC-subiculum projection, was shown to disrupt place coding in CA1 but not CA3, presumably because grid cells in layer II provide sufficient positional input to support place codes (Brun et al. 2008). On the other hand, inactivation of the hippocampus has been shown to disrupt grid cell periodicity (Bonnevie et al. 2013) suggesting the stability of spatial coding in the entorhinal-hippocampal circuit is dependent at least to some extent on one another.

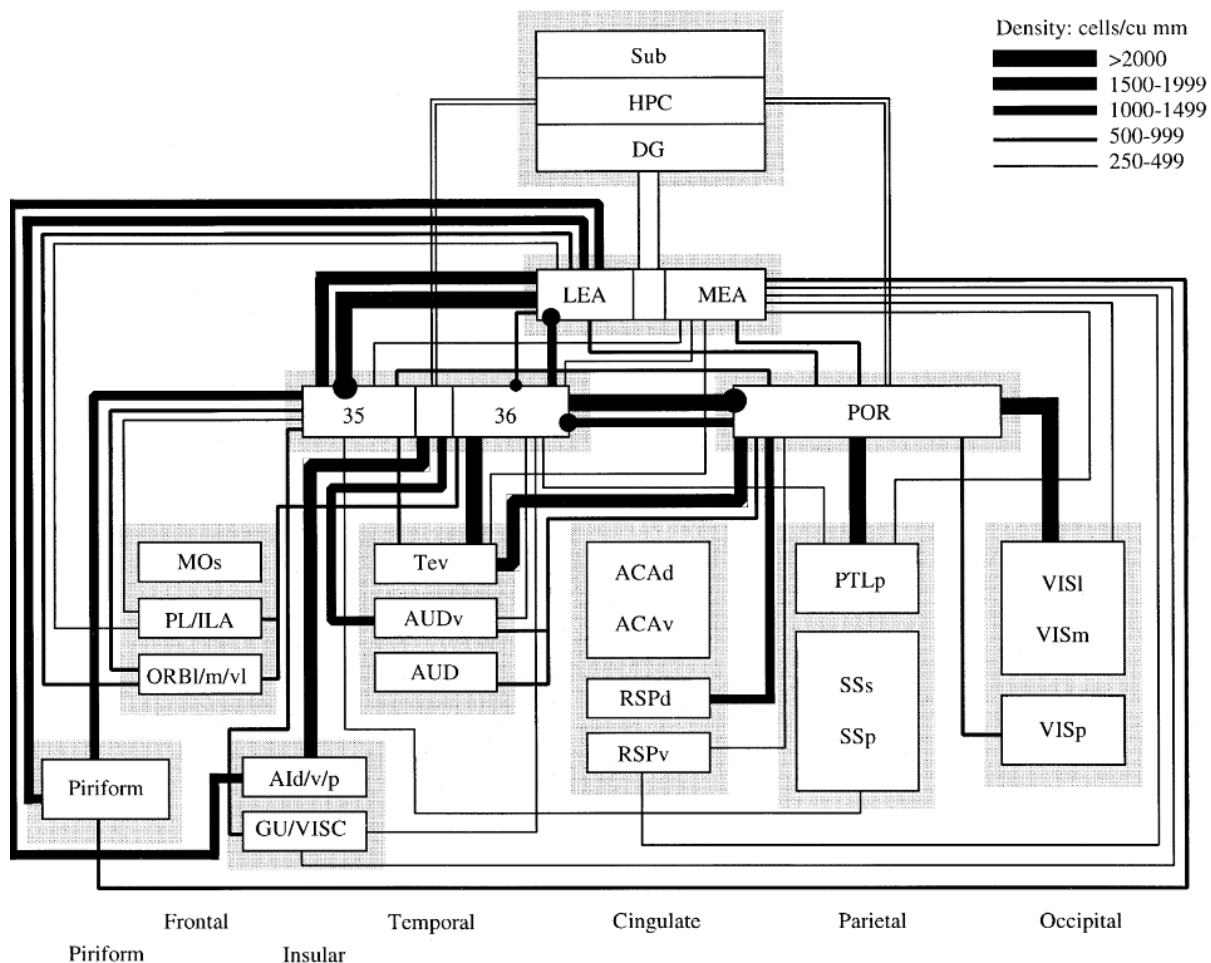


**Figure 4: Connectivity strength between cortical and hippocampal regions.** Strength of the connections are indicated by the thickness of the lines. Open lines indicate connections that are known but were quantified in the study. Regions are abbreviated as follows, subiculum (Sub), hippocampus proper (HPC), dentate gyrus (DG), lateral entorhinal area (LEA), medial entorhinal area (MEA), perirhinal cortex (PR, areas 35 and 36), postrhinal cortex (POR), motor areas (MOs), prelimbic and infralimbic areas (PL/ILA), orbital areas (ORB), temporal areas (Tev), auditory areas (AUD), anterior cingulate areas (ACA), retrosplenial areas (RSP), posterior parietal areas (PTL), somatosensory areas (SS), visual areas (VIS), agranular insular areas (AI) and gustatory areas (GU). Figure taken from Burwell (2006).

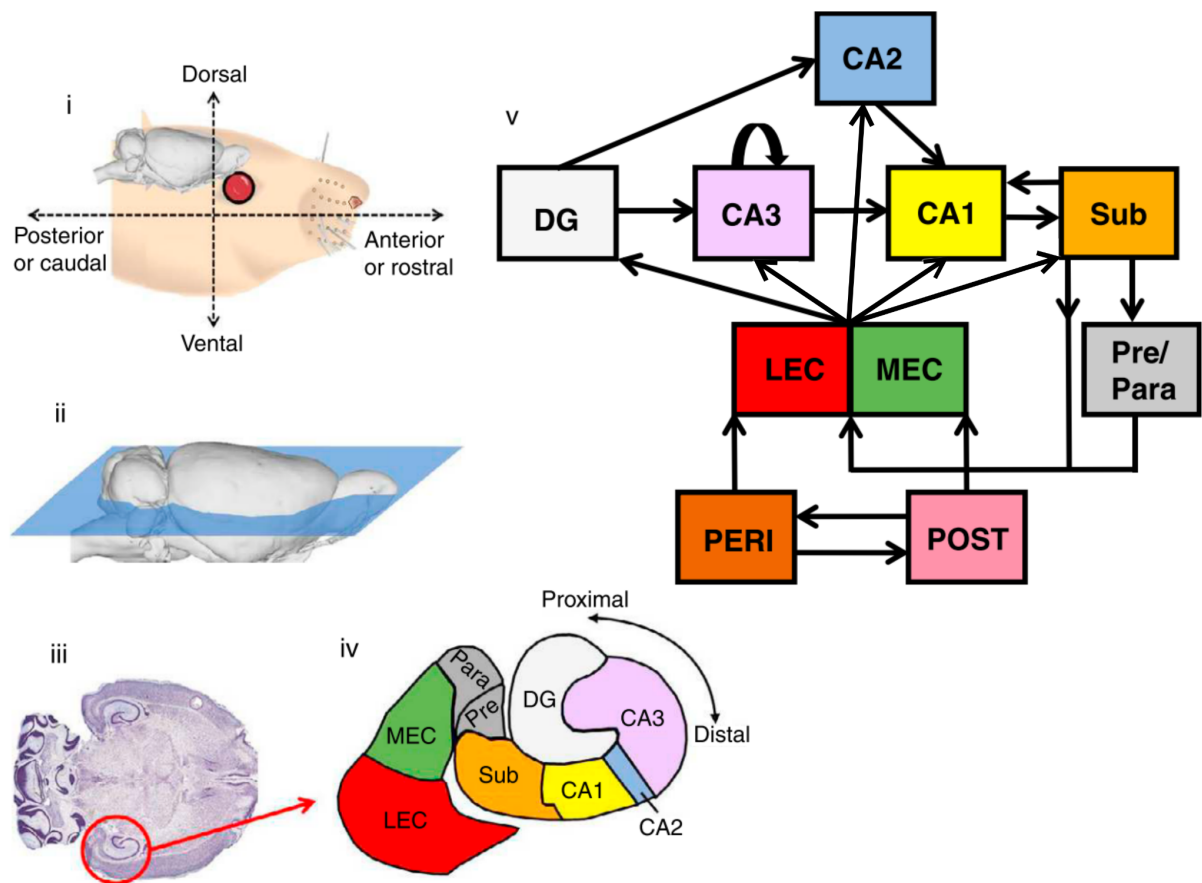


**Figure 5: Hippocampal and retrohippocampal connectivity.** (I) Cartoon of a rat brain within the head. (II) A horizontal plane through the brain reveals a (III) histology cross section with the hippocampal formation circled in red. This region can be subdivided (IV) into the lateral entorhinal cortex (LEC), medial entorhinal cortex (MEC), parasubiculum (Para), presubiculum (Pre), subiculum (Sub), CA1, CA2, CA3 and dentate gyrus (DG). (V) Graphical connectivity map between these regions showing the directionality of inputs and outputs. Figure adapted from Poulter, Hartley and Lever (2018).

#### 1.3.4 Towards a generalised cognitive map

While the cognitive map hypothesis was first devised as a means of explaining how animals could forge an internal model of their external environment, new evidence has emerged supporting the idea of a generalised cognitive map that extends beyond the domain of spatial navigation. The discovery of location-specific firing in the hippocampus was particularly surprising given the hippocampus was thought to play a role in declarative memory since the clinical studies of hippocampal lesions in the case of H.M. (Squire 1992). To reconcile space and memory functions, a common framework was devised that combined the brain functions. Evidence emerged showing hippocampal neurons responding to nonspatial features of an environment such as odours (Eichenbaum et al. 1987), tactile inputs (Wood et al. 2000), time (Hampson, Heyser, and Deadwyler 1993) and sound (Aronov, Nevers, and Tank 2017). These same cells produced spatial firing fields suggesting a more nuanced hippocampal function. In the example of sound, Aronov et al. (2017) trained rats to control the frequency of a sound with a joystick and to stop at a specific frequency to receive a reward. Place cells were shown to exhibit firing fields within the frequency space ([Figure 6](#)) supporting the idea that the hippocampus and neighbouring cortices play a more general role in mapping continuous variables (Buzsáki and Moser 2013; Schiller et al. 2015). Following this conceptual framework, Constantinescu et al. (2016) showed humans navigating in abstract feature spaces had increasing BOLD signals in their temporal lobe indicative of grid cell firing. These signals were first demonstrated by Doeller, Barry, and Burgess, 2010 while humans navigated virtual environments with a joystick, and were later observed while humans participated in navigation of imagined environments (Horner et al. 2016). Taken together, these findings indicate that the hippocampus and entorhinal cortex operate a generalised cognitive map for navigating continuous feature spaces, whether it be physical space, time, sound frequency domains, chemical gradients or more abstract feature spaces. Understanding how the brain is able to navigate feature maps either in physically real or abstract domains is a critical aspect to reconciling practical implementations of model-based learning, a key feature of intelligent life.

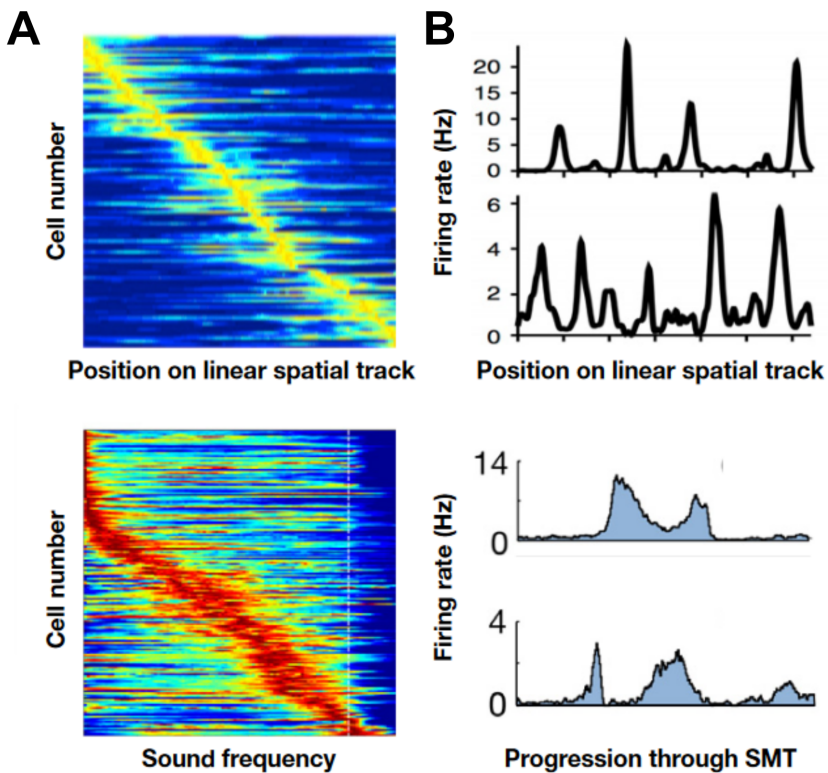


**Figure 6. Non-spatial coding in hippocampal place cells and MEC grid cells.** Rats were trained in a sound manipulation task (SMT) to manipulate a joystick to control the frequency of a sound and stop at a specific frequency to receive a reward within the target zone. (A) A population of recorded cells from CA1 map the full range of locations visited during a linear track task (top), similarly, CA1 cells map the full range of sound frequencies observed during the sound manipulation task. Example neuron plots are taken and adapted from Yoon et al. (2016) and Aronov, Nevers, and Tank (2017). (B) MEC grid cells exhibit periodic firing fields during a linear track task (top), similarly, MEC grid cells exhibit periodic firing fields during the frequency task. Example neuron plots are taken and adapted from Miao et al. (2015) and Aronov, Nevers, and Tank (2017). The examples were originally compiled in Behrens et al. (2018).

## 1.4 Grid cells and path integration

Grid cells are widely believed to play a key role in path integration (McNaughton et al. 2006). Within the context of a cognitive map, path integration can be used as the mechanism to update a positional estimate across the map (Etienne and Jeffery 2004). Even though pure path integration is not a wise navigation strategy for any animal to adopt when sensory cues are available as it is prone to accumulating errors, it may serve as a temporary solution when sensory cues are unavailable or in combination with beacons navigation between landmarks. Grid cells are well suited as a candidate for a path integration system, not only by their connectivity within the hippocampal formation but also because they provide a context-independent metric of distance travelled. In this section, the properties of the grid cell system will be discussed before evaluating the current theories of path integration with grid cells.

### 1.4.1 Properties of the grid cell system

Grid cells were first observed in the dorsal MEC of rats exploring a sufficiently large arena to record the spatial regularity of the grid-like firing pattern (Hafting et al. 2005). Recording from a wealth of grid cells at different locations within the MEC revealed grid cells have at least three dimensions of variation, namely the phase, orientation and scale of the grid fields. In terms of geometric transformations, these variations reflect translations, rotations and scaling of the grid fields respectively ([Figure 7](#)).

Grid cells were found to be organised topographically along the dorsoventral axis of the MEC in discrete modules, whereby grid scales and orientations are fixed within individual modules but individual cells may be translated with respect to one another (H. Stensola et al. 2012). Distortions of the grid fields from a perfect hexagonal structure and the specific frequency of theta-modulated firing were also shown to be maintained within grid modules (Barry et al. 2007). To test whether grid modules coherently remap, a test environment was compressed to induce grid rescaling and grid modules were found to remap independently of other modules. Taken together, individual modules might be considered as functionally independent from one another (H. Stensola et al. 2012).

Grid orientations of grid cells recorded from square arenas were found to be very similar across different animals suggesting a common function. The cardinal axes of the square arenas used to measure grid activity actually determined the orientation of the grids (T. Stensola et al. 2014; Krupic et al. 2015). Grid cells did not perfectly align with the arena walls

but rather orientations peaked at  $\pm 7.5^\circ$ . This particular alignment in square arenas corresponded to a maximal asymmetry with the environment suggesting a common mechanism was at play to help disambiguate geometrically similar regions of a square arena. Orientations at  $60^\circ$  multiples of the cardinally aligned grid axes differed from the  $7.5^\circ$  offset measured at the cardinal axes, suggesting the grid was not perfectly hexagonal but rather had undergone ellipification. Stensola et al. (2014) suggested this ellipification was a result of a shearing transformation from the borders of the environment. When the offset was compared between familiar and novel environments, it was shown novel environments lacked the grid offset that maximised grid asymmetry. This suggests the grid cell system evolves over spatial learning to inherit information into its code containing spatial context. Krupic et al. (2015) found similar ellipification of the grid pattern in highly polarised environments like trapezoid arenas. Further distortions from the a perfect hexagonal structure was shown when a reward was introduced to the open field, grid fields were more frequently located proximally to rewarded locations (Butler, Hardcastle, and Giocomo 2019), possibly reflecting an increased spatial precision around reward locations.

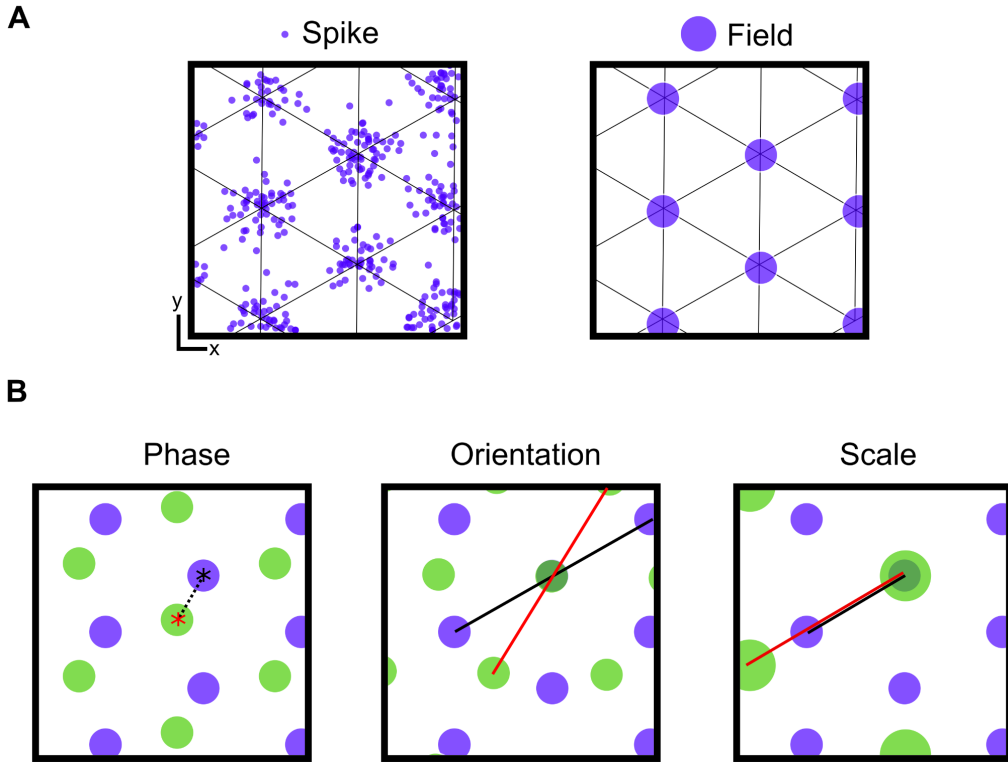


**Figure 7. Spatial firing properties of the grid cell system.** (A) A grid cell fires preferentially within firing fields that resemble a triangular grid (overlaid). (B) Variations in grid cells can take the form of geometric transformations include a phase shift; translation of grid fields across the plane, a change in field orientation; a rotation of the grid fields about a reference point, and scaling of the distances between adjacent fields; uniform scaling of the grid fields. Red indicates the necessary geometric transformation to alter the grid code from some reference (black) grid phase, orientation and scale. Figure inspired from Moser (2014).

#### 1.4.2 Emergence of grid patterns

The striking regularity of the grid structures produced by grid cells has compelled much computational effort to seek out solutions to the emergence of grid-like spatial firing patterns. The proximity of grid cells to speed and head direction input, as well as the strong connectivity between the MEC and hippocampus lead to a working consensus that grid cells provide a computational solution to path integration (Hafting et al. 2005; McNaughton et al. 2006; Fuhs and Touretzky 2006).

This led to two main algorithmic models being proposed based on the integration of velocity signals into positional updates in the allocentric reference frame. First, grid cell firing might result from continuous attractor dynamics. Here, localised firing may be generated by excitation of grid cells with similar grid phases and inhibition of grid cells with more distant phase relationships. This difference of Gaussians model resembles a ‘Mexican hat’ excitatory/inhibitory relationship between grid cells in a neural sheet arranged according to their grid phase. Activity in this sheet can be translated in accordance with the animals movement with inputs from speed and head direction cells (Fuhs and Touretzky 2006; Burak and Fiete 2009). As grid phase is a cyclic variable, in some models this neural sheet can be wrapped around onto itself to form a torus (McNaughton et al. 2006) or twisted torus topology (Guanella, Kiper, and Verschure 2007). Points on this torus can therefore be mapped to multiple locations of an animal in an environment, and inversely the numerous firing fields of a grid cell are mapped to a single position on the torus ([Figure 9](#)). The hexagonal structure can then be explained by self-organisation between competing excitation bumps in this neural manifold, where distances between bumps are maximised similar to maximise the spatial coding capacity (McNaughton et al. 2006; [Figure 8](#)).

Second, grid cell firing might result from the interference pattern between two or more velocity-controlled oscillators (VCOs; Burgess, Barry, and O’Keefe 2007). If the frequency of the oscillator is determined by velocity, the phase difference between oscillators is proportional to the displacement of the animal. While there is some evidence to support theta-frequency modulation as a function of running speed (Geisler et al. 2007) and heading direction (Welday et al. 2011), evidence for continuous attractor dynamic-based grid firing on the other hand has proliferated both in terms of physiological evidence for continuous attractor dynamics. K. Yoon et al. (2013) showed the population activity of concurrently recorded grid cells on the same tetrode could be explained to reside on a 2D manifold in support of continuous attractor dynamics. Recent evidence from high density grid cell recordings has provided further evidence for grid cell networks exhibiting continuous

attractor dynamics. Gardner et al. (2022) demonstrated that the activity of a large population of grid cells within a single grid module does indeed reside on a toroidal manifold as expected from a 2D attractor network ([Figure 9](#)).

While most grid cell models were designed with the computational operation of path integration in mind, an alternative approach might be to train an artificial neural network agent to solve spatial tasks and to ask whether any network units contain grid-like representations of space. Banino et al. (2018) showed units within a reinforcement learning (RL) agent that adopted a recurrent neural network architecture exhibited grid-like representations. Competing RL agents using some of the most state-of-the-art RL algorithms consistently performed worse than the grid-cell agent. Furthermore, this grid cell agent executed the shortest possible path to goal locations, even when not exposed to these shorter paths during training epochs. This work suggested the grid cell system is a general solution to navigation because it is an emergent feature of a high performance navigating agent, just like mammals. However, Schaeffer, Khona, and Fiete (2022) advise caution when concluding emergent grid cells result as a natural solution to path integration. They found the vast majority of networks trained to perform path integration did not form grid cell representations and only a small percentage of the swept hyperparameter space yielded grid cells. This suggests the grid cell solution to path integration may only be a single solution of many and thus attempts to infer grid cells as a natural consequence of path integration may have been inadvertently baked into the trained networks by tuning hyperparameters in search of that small hyperparameter subset that can yield grid cell representations.

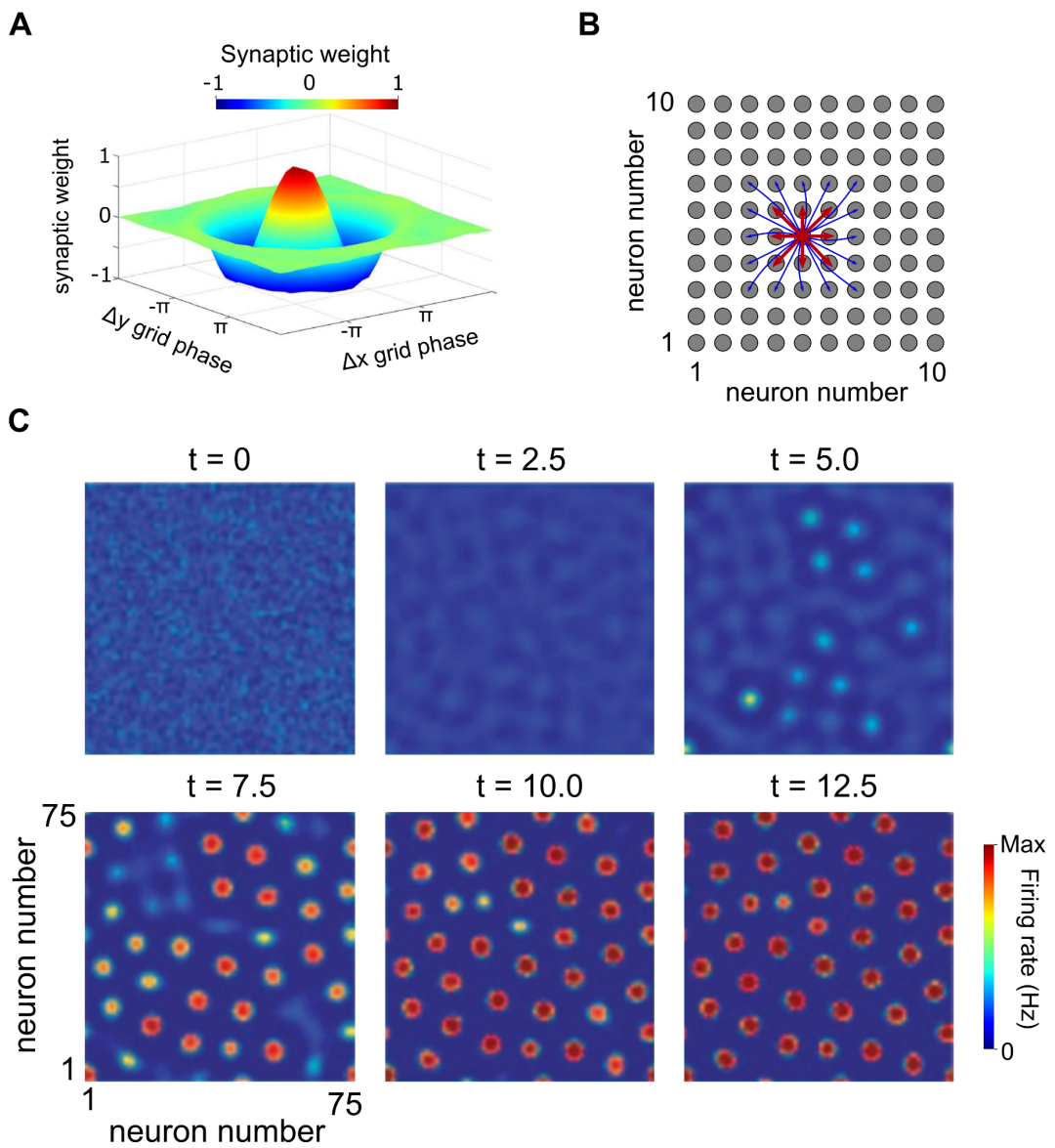


**Figure 8. Emergence of hexagonal grid firing.** (A) A difference of Guassian (or “Mexican hat”) connectivity profile used for grid emergence. A grid cell within a module is connected to another grid cell with a synaptic weight according to the phase relationship between the cells where 1 is a strong excitatory synapse and -1 is a strong inhibitory synapse. (B) Neurons arranged in a neural sheet according to their grid phase. Using the Mexican hat connectivity, neighbouring cells excite each other whereas distant cells inhibit each other. (C) Network simulation of grid emergence. Neurons are arranged in a 75-by-75 array, representing 5625 unique neurons. Starting from initially random conditions and iterating the Mexican hat connectivity over time, neurons begin to resemble and then stabilise as a hexagonal grid. Figure adapted from McNaughton et al. (2006).

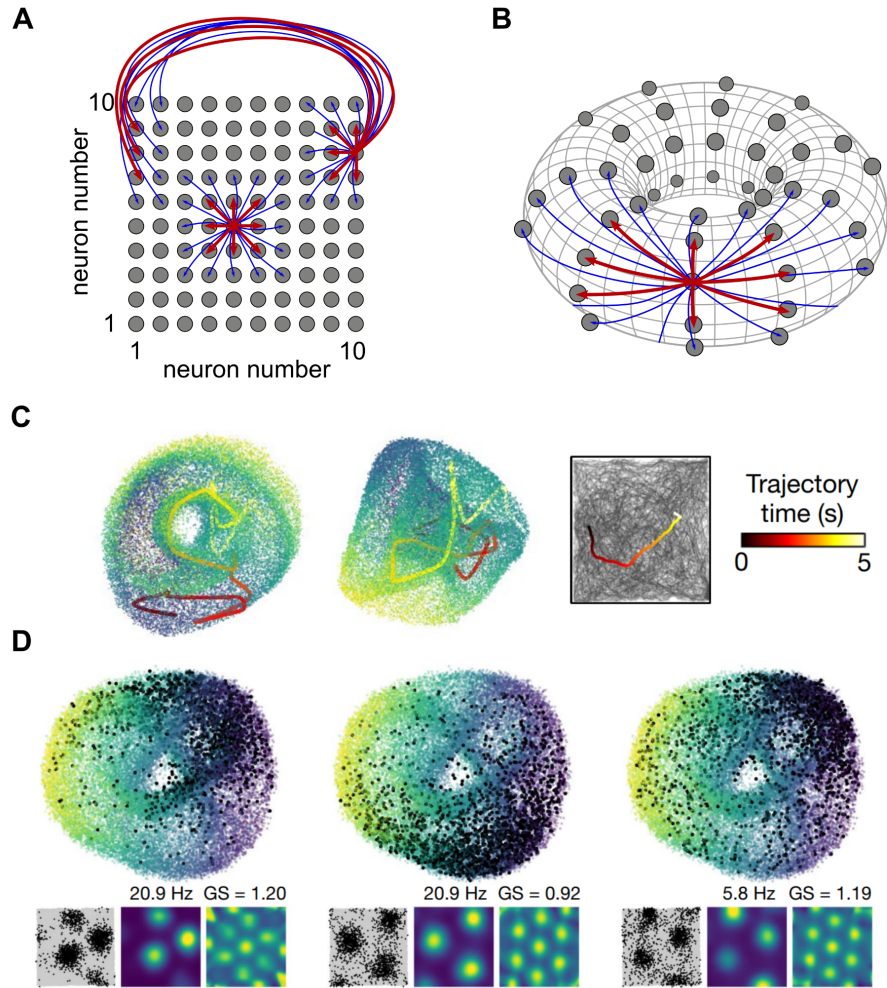


**Figure 9. Toroidal topology of a grid module.** (A) On the boundaries of a neural sheet as in Figure 8B, connectivity can be wrapped along each axis to create a (B) continuous toroidal surface in which the neural sheet has no boundaries. (C) Gardner et al. (2022) recorded from 149 simultaneous grid cells within a single module and performed dimensionality reduction on the population activity which revealed a toroidal architecture predicted of grid cells with underlying continuous attractor dynamics. Each dot represents the population activity at a single time point and colours indicate the first principal component. Two different views of the torus are shown. An example 5 second trajectory of the rat is overlaid, showing adjacent positions on the torus correspond to a smooth translation of location in physical space. (D) Individual spikes (black dots) from three example grid cells map to singular field locations on the toroidal manifold. Spike plots, rate maps and spatial autocorrelograms are shown below. Peak firing rates for the rate maps and grid scores (GS) are labelled above their respective plots.

### 1.4.3 Spatial content of grid cells

The exact role grid cells play in spatial coding is still far from clear. With a population of grid cells that span different orientations and scales, two different types of spatial information can be theoretically derived, position within an environment and distance to or from a reference point (Fiete, Burak, and Brookings 2008). The positional-dependent firing of these cells suggest they play a role in encoding a position estimate. On the other hand, the multiple firing fields of grid cells affords only an ambiguous representation of position when derived directly from single cells. With the addition of multiple grid modules, position can be encoded in the grid code by a combination of the activity bumps across different modules as a phase vector (Fiete, Burak, and Brookings 2008; Stemmler, Mathis, and Herz 2015) with a range of locations that far exceeds the largest grid module spacing (Fiete, Burak, and Brookings 2008), which is comparable to observed foraging ranges (Russell et al. 2005). Distance can be calculated as the difference between two phase vectors representing two locations (Burak and Fiete 2009; Stemmler, Mathis, and Herz 2015; Bush et al. 2015).

The grid phase vector represents the points on the neural sheet from each available grid module creating an n-dimensional representation of space where n is the number of grid modules. Phase from single grid modules has been proposed to be represented by a modular arithmetic scheme, a.k.a. modulo code (Fiete, Burak, and Brookings 2008) or a maximum likelihood approach (Stemmler, Mathis, and Herz 2015). The modulo code calculates a phase estimate from the remainder following integer division of the internal positional estimate. As the modulo code operates using the residual number system (RNS), the phase code can be straightforwardly updated as a result of the animal's displacement due to the carry-free property of the RNS. This affords no carry-over operations between grid modules and is consistent with the functional independence of grid modules. The maximum likelihood code calculates a phase estimate from the joint probability distribution of grid firing within an individual grid module. Again, each phase representation is independent across grid modules and affords no carry over operations between grid modules. Combining the probability distributions across grid modules produces a maximum likelihood estimate of position with smaller-period modules providing the finer spatial resolution. As individual grid cell firing is known to be highly variable (Nagele, Herz, and Stemmler 2020), error-correction is required to avoid catastrophic errors in the positional estimate. In the maximum likelihood scheme, error-correction of the grid phase is achieved inherently at the level of the grid module through the maximum likelihood operation whereas error-correction in the modulo scheme would be required during the phase readout as some phase vectors are impossible with any given set of grid module periods. The correction would thus require the phase

vector readout to map to the closest valid phase combination. Deviations from a perfect hexagonal grid such as adding contextual information from learning an environment (T. Stensola et al. 2014), a reward location (Butler, Hardcastle, and Giocomo 2019) or ellipification (T. Stensola et al. 2014; Krupic et al. 2015) as previously discussed can be easily incorporated into the phase code and is compatible with the modulo and maximum-likelihood approaches provided grid distortions are consistent within modules, which is exactly what has been experimentally observed (H. Stensola et al. 2012).

Accurate positional coding with a grid phase vector requires grid cells to become anchored to features of an environment, that is, the firing fields must not drift over time otherwise the phase vector would encode a different location compared to before the firing field drift. If firing fields are not anchored to fixed positions in an environment, distance travelled from a reference point can still be decoded from phase changes across the neural sheet. Jacob et al. (2019) showed using a circular track that some grid cells in rats do not anchor to features of a track but rather encode the integrated distance travelled. To test whether the periodic firing of grid cells breaks down when there are no allothetic cues to anchor to, all traces of allothetic cues must be removed. Open field arenas even in darkness are very difficult to remove allothetic cues from, such as odour or sound cues. As such, recording a grid cell without the influence of sensory cues can be achieved using the modern virtual or augmented reality set ups, for examples, see (Domnisoru, Kinkhabwala, and Tank 2013; Tennant et al. 2018; Jayakumar et al. 2019). Recent evidence from (Campbell et al. 2021) showed a subset of MEC neurons encoded distance on a treadmill in complete darkness, however did not identify the 2D spatial properties of these cells.

Position and distance coding need not be mutually exclusive coding functions. Indeed, grid cells clearly encode position information as over repeated trajectories or trials of an environment, grid fields remain in the same location, while also firing periodically at equidistant intervals consistent with distance coding. Landmarks may provide the reference points from which the distance codes are generated through path integration. Hardcastle et al. (2015) showed the positional estimate encoded by grid cells tended to drift in more open regions of an environment, supporting the idea the grid cell system is reset following the accumulating errors during path integration. Furthermore, directional-dependence within the error correction suggested border cells serve as the neural substrate for error correction.

#### 1.4.4 Reading a grid code

How are these spatial representations readout by downstream systems? The hypothesised combinatorial code of modular phases is a diffuse population code that spans the entire length of the MEC, this undoubtedly raises questions about how the brain makes sense of this code to guide navigational decisions. Two broad classes of potential readout mechanisms, which are not necessarily mutually exclusive schemes are place-label readouts and metric readouts.

Place-labels may be as simple as a position represented by place cells in the hippocampus that can be formed through the summation of grid cell inputs across different grid modules (Solstad, Moser, and Einevoll 2006). Using the phase vector representation, place-labels can be generated as unique codewords as if defined in a codebook or look-up table. Consider a translation across a 1D track from locations 10 - 50 cm using a phase vector from three distinct grid modules of periods  $L = \{10 \text{ cm}, 30 \text{ cm}, 60 \text{ cm}\}$ . A potential readout may treat the absolute phase vector at locations 10 and 50 cm as a unique neural label  $P = \{1/2\pi \text{ rad}, 3/2\pi \text{ rad}, 5/4\pi \text{ rad}\}$  without using the metric information of the integrated 40 cm distance over the journey (Fiete, Burak, and Brookings 2008). Alternatively, the phase vector could be decoded into displacements throughout the journey so that downstream neurons reflect the metric information of physical distances (in this case a 40 cm displacement) rather than abstract vectors in modular phase space (Fiete, Burak, and Brookings 2008; Stemmler, Mathis, and Herz 2015; Bush et al. 2015). Such metrics information is useful for animals computing homing trajectories for example, whereby a distance and direction is readout from the difference between the phase vector code for current location and home. This vector-navigation permits animals to execute novel routes home even after taking circuitous routes away from home. However, metric information like distance and head direction is difficult to extract from the grid code without the addition of dedicated neural networks (Burak and Fiete 2009).

Computational work has proposed candidates for these readout networks, each with predictions of novel spatial-tuned cells from which metric readouts can be made (Fiete, Burak, and Brookings 2008; Bush et al. 2015; Stemmler, Mathis, and Herz 2015). In the metric readout model proposed by Fiete et al. (2008) and inspired by a single layer recurrent neural network conceived by Sun and Yao (1994), grid phases represented as modulo residues are inputs to the network and the network outputs to a neuron with a firing rate proportional to the displacement of the animal. This network utilises residue-to-decimal conversion using a non-symmetrical Hopfield neural network which boasts biological

plausibility. In the distance cell model proposed by Huhn et al. (2009) and Bush et al. (2015), grid cells within the same module project to distance cells that encode distance travelled as the summated activity of grid cells results in a periodic signal equal to the grid spacing of the module. Competing distance cells from different innerating grid modules then project with winner-take-all dynamics to a readout neuron that exhibits a firing rate proportional to the distance travelled along a particular cardinal axis. In the rate-coded vector cell model proposed by Bush et al. (2015), pairs of grid cells within single modules that encode current and goal locations project to vector cells that encode the displacement between the current and goal location as the phase difference between the grid cells through multiplicative synapses onto vector cells. The phase difference across modules corresponds to the displacement between current and goal locations. When pairs of grid cells encoding current and goal location fire simultaneously across modules, a single vector cell is activated corresponding to the consistent displacement and winner-take-all dynamics eliminate activity in other vector cells. This model requires less additional neurons than the distance cell model but lacks biological plausibility as synapses don't support multiplicative operations. To overcome this constraint, the phase difference may be inferred from the theta firing phase (termed the phase-coded vector cell model; Bush et al. 2015) as many grid cells exhibit theta phase precession, that is, firing spikes appear progressively earlier relative to the theta local field potential as the animal moves through the grid field and results in an approximate linear relationship between theta phase and distance travelled through the field. This model however requires the theta phase precession to align along cardinal axes.

An alternative neural implementation utilises a linear look-ahead function in which simulations of movement signals search out the place-label correspondence between the current location and the target location in the modular phase code (Erdem and Hasselmo 2012; 2014; Kubie and Fenton 2012). Under this scheme, the integrated distance travelled from a starting point is encoded by the duration of the look ahead event. Readout models are understandably speculative at best however the testable predictions that spawn from them provide tangible lines of enquiry for in vivo electrophysiologists.

These theorised readout mechanisms form a starting point for analysis of in-vivo electrophysiological experiments which can probe for the predicted cell-types. Across the discussed readout theories, predicted cell-types include distance, vector and readout cells. In the broadest terms, readout theories indicate that additional spatially tuned neurons are required downstream of the grid cell system. A common predicted cell type is a rate-coded cell with firing rate proportional to distance travelled from a reference point up to some salient point like a rewarded location, corresponding to a linear ramp (Fiete, Burak, and

Brookings 2008; Bush et al. 2015; Stemmler, Mathis, and Herz 2015). If these representations do indeed exist, the behavioural task utilised within this thesis is well suited to identify these neurons.

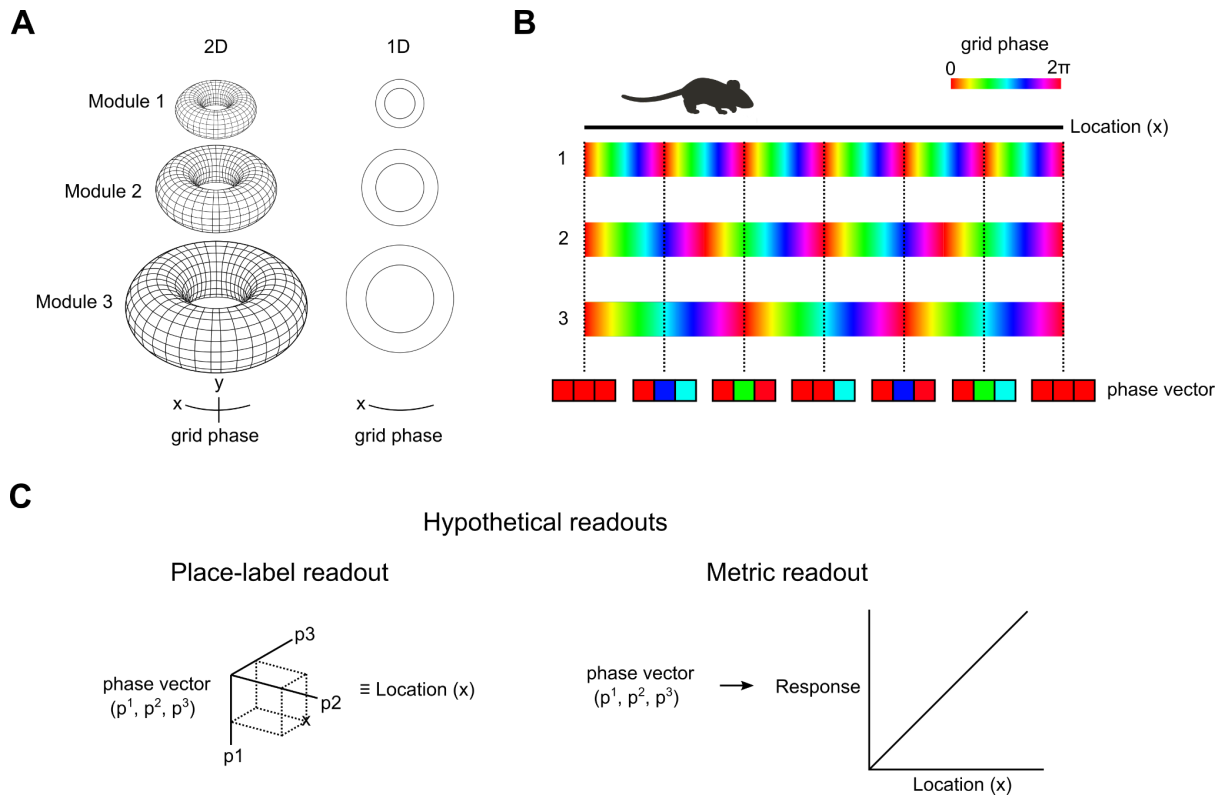


**Figure 10. Grid cell readout.** (A) The grid cell system is arranged into modules of grid cells which share a common grid scale within modules but increase in size along the dorsal ventral axis of the medial entorhinal cortex. A population code of allocentric position can be decoded across these modules as a vector of grid phases on a toroidal (shown) or flat neural sheet in the 2D case or a ring in the 1D case. (B) Using the 1D case for simplicity, these grid phases can uniquely encode locations along a linear path up to the point the phase vector is repeated. (C) The phase vector may be read directly as a place label, discarding the metric information of the displacements or the metric information recalculated from the phase vector into readout response neurons.

#### 1.4.5 Possible behaviour roles of grid cells

What evidence is there for a behavioural role of grid cells? Discussions up to this point have been focused on the theoretical potential of the grid cell system. Whether the above schemes are physically realised remains to be seen. To add credence to the behavioural claims of grid cell function, grid cells must be recorded while a behavioural task is taking place. To date, few studies corroborate the claims made upon discovery that grid cells are utilised for navigation. To investigate beaconing and path integration behaviours and the roles played by grid cells, appropriate experimental designs are required beyond the standard open field settings used to record the spatial firing properties of grid cells. For example, recording grid cells during an open field task cannot be used to link path integration and grid cell activity as whether the animal is actively path integrating during the task remains ambiguous while beaconing cues are available. Errors naturally accumulate during path integration so when navigation via beaconing is possible, it stands to reason the animal will utilise beaconed-based approaches to navigate to target locations to avoid positional uncertainty that comes with pure path integration. To overcome this, a navigation task is required that eliminates beaconing as a viable strategy. Simply turning out the lights or cleaning an open field arena thoroughly cannot guarantee the removal of these visual or olfactory beaconing cues respectively. Virtual environments on the other hand can be controlled such that beaconing cues can be omitted or limited in their utility in a beaconing strategy. For example, a visual beacon can be removed on some trials to probe the interaction between grid cell activity and trial behaviour. Other potential beaconing cues originating from outside of the virtual environment but still within perception of the animal could not usefully inform positional information if these cues do not consistently align with cues on the track, for example if the circumference of a treadmill matched the distance of the linear track, discernible features on the treadmill like odours and visual imperfection could be used as track beacons by proxy. When this possibility is removed, the beaconing cues available to the animal is entirely controlled by the experimenter.

Allen et al. (2014) developed a L-maze task in which mice were trained to navigate via an L-shaped corridor to a hidden platform submerged in an opaque liquid in complete darkness. On test trials, the corridor was removed to test the shortest route taken by the mouse. As no allocentric cues were available to guide navigation, path integration was the only viable strategy to self-locate in the arena. A beaconing version of this task was introduced by Gil et al. (2018) where lights were turned on and a flag signalled the submerged platform. To assess the impact of grid cell firing on beaconing and path integration behaviours, glutamate receptors AMPA and NMDA were experimentally ablated in retrohippocampal regions and

were shown to disrupt grid cell firing. Mice with this disrupted grid firing performed significantly worse than controls on the path integration but not beaconing versions of the task. While this offers some of the first evidence linking grid cell firing with navigational operations specific to path integration, the specific grid activity that causes the navigational impairment remains elusive.

An alternative approach to real world environments is to utilise virtual navigation. Sensory cues in a virtual environment can be controlled completely by the researcher, as established by Domnisoru, Kinkhabwala, and Tank (2013). Tennant et al. (2018) developed a task in which mice were trained to stop at a specific rewarded location on a virtual reality linear track. The reward zone was either marked by a visual cue or left unmarked. The rest of the track consisted of visual cues not specific to any single location of the track. Trials in which the reward zone was marked by a visual cue could be completed with a beaconing strategy, whereas when the reward zone was unmarked, only a path integration strategy was viable. This task offers the benefit of assessing both beaconing and path integration behaviours while also concurrently recording the activity of grid cells. As mentioned in [1.3.2](#), Tennant et al. (2018) targeted layer II MEC stellate cells and found inactivation reduced spatial learning in both beaconing and path integration behaviours. As the task operates on a linear track rather than a 2D arena, it offers the potential of recording the periodic firing of grid cells without the need for a mouse to sample all locations like is necessary in open field recordings. Consequently, trial-by-trial analysis is possible and offers the finest temporal resolution of grid cell recording to address the variable dynamics throughout a recording session. Whether grid cell coding remains stable over the course of a virtual navigation task is not clear. Within an open field exploration task and a virtual linear track task, (Nagele, Herz, and Stemmler 2020) showed grid cells do not always fire as the mouse crosses through a grid field or are significantly shifted away from the grid field. This spiking variability might reflect behavioural states or may simply be a feature of a noisy population code. Pettit, Yuan, and Harvey (2022) showed water-deprived mice disengaged from a virtual linear track task over the course of a recording session and this was coupled with a decreased decoding accuracy of a population of simultaneously recorded place cells. Should this extend to the grid cell system, the variability of grid cell firing may reflect changes in task engagement. If grid codes are gated by task engagement, we might expect codes to be behaviourally gated during path integration behaviours but not when beaconing is available.

In humans, Doeller, Barry, and Burgess (2010) showed a BOLD signal associated with grid cell firing correlated with the performance in a virtual spatial memory task. Further, Kunz et al. (2018) showed spatial behaviours in a virtual reality path integration task to differ in

humans that carried the Alzheimer's genetic risk factor APOE-e4 with a significant reduction of BOLD signal in the temporal lobe associated with grid cell representations. To extract this signal used to quantify the grid representation in humans, the navigational task must be completed in a 2D arena to assess the 60° rotational symmetry associated with grid cell firing. While this task benefits from concurrent electrophysiological and behaviour recording, the requirement of a 2D arena does not afford the temporal resolution of periodic grid firing possible from the linear location task established by Tennant et al. (2018).

## 1.5 Thesis aims

The overall aims of the thesis are to identify the coding scheme of grid and cells that might carry out readout operations. I will look to answer to what extent spatial coding can be explained in terms of beaconing and path integration-based behaviours exhibited.

In Chapter 2, I will describe the means of building and implementing an open field exploration task and linear location task. I will then detail how these tasks were combined with electrophysiology apparatus to record single unit activity while mice perform these tasks and how the spatial firing properties of individual neurons were calculated to detect classically defined spatially-modulated cell types.

In Chapter 3, I will show that mice can be trained on a virtual reality navigation task following a training protocol developed by Sarah Tennant (Tennant 2017; Tennant et al. 2018) and improved over the course of this work. This task recruits both beaconing and path integration-based navigation and will be used to delineate roles of grid and readout cells in Chapters 4 and 5.

In Chapter 4, I will ask how grid cells of the MEC spatially code during the linear location task and address whether this coding is (1) stable and (2) dependent on the trial outcome during either beaconed or path integration behaviours.

In Chapter 5, I will ask whether cells in the retrohippocampus that exhibit ramp-like firing profiles reflect a new positional code for space and address whether this coding is (1) stable and (2) dependent on the trial outcome during either beaconed or path integration behaviours.

In Chapter 6, I will look to reconcile my findings with the wider literature.

# Materials and methods

## 2.1 Ethical statement

All research was conducted in accordance with the The University of Edinburgh Animal Welfare committee and performed under the UK Home Office project license (no. PC198F2A0). All procedures complied with the Animals (Scientific Procedures) Act, 1986 and the European Directive 86/609/EEC on the protection of animals used for experimental purposes. All procedures were approved by the Named Veterinary Surgeon.

## 2.2 Research animals

Wild type male C57BL/6NCrl mice were obtained (Charles River) and housed in a secure animal facility. Mice of 10-15 weeks old were used for experiments. Male mice were preferred due to their increased size. This afforded a larger space on the skull to attach the headpost. (It should be stated for anyone reading this thesis, that selecting male mice for their increased size is not a valid justification for not including female mice in an experiment and upon reflection, mice should have been size and weight matched instead).

## 2.3 Tetrode microdrives

### 2.3.1 Overview

Electrophysiological measurements via tetrodes offer a continuous recording of the extracellular potential difference in the brain. Four electrodes bundled together simultaneously record spatial disparate voltage traces, which when combined can be used to reconstruct single unit activity. As the aim of this thesis focuses on reconciling single unit activity with spatial behaviours, it was necessary to implement and refine a reproducible tetrode microdrive design that was compatible with these aims. In particular, the microdrive needed to have the stability to remain in place for chronic recordings across weeks (up to 3 months in some cases) and needed to accommodate a headpost to head-fix the mouse during virtual reality experiments. In this section, the microdrive assembly and implantation are described and briefly discussed.

### 2.3.2 Microdrive assembly

*Board assembly.* A 16-channel Omnetics board (Neuralynx, EIB-16) was mounted to a Omnetics to Mill-Max adapter (Axona, HSADPT-NN1) held off the surface of a work bench with a helping hand. A cannula was cut to size (Stainless Tube and Needle Co, 17 gauge/7 mm), sanded and cleaned inside. The inner cannula was glued to the corner of the board with epoxy resin. Two 3cm ground wires (thin insulated wire) were cut and 1cm insulation removed from each end. These were then pinned into the ground slots on the board.

*Tetrodes.* To create a tetrode bundle, 30cm of platinum-iridium wire (Axona, EW-17PI) was cut and taped at both ends to a single small 1 cm patch of electrical tape such that the wire ends were parallel on the tape. The wire was cut at the midpoint to make two wires of the same length. These wires were lined up flush with the tip of a finger slightly wetted with saline. The ends of the wires not attached to the tape were folded over onto the tape to line up 4 parallel wires on the tape connected by two loops below the tape. The tape was grasped tightly with a hemostat and suspended from a horizontal pole and spun gently to twist the 4 wires into a bundle. Once the bundle is longer than 4 cm, a heat gun set to 250 degrees celsius was wafted over the bundle for 6 seconds to adhere the bundle together.

*Wiring.* Four tetrode bundles were created per board and individually loaded into the inner cannula and wired under a microscope to each pin. To load a tetrode, the tetrode was bathed in ethanol in a weighing boat and picked up by the loop with fine tweezers before being slotted down the inner cannula. The top loop was cut, producing four wire-ends that could be fed through the board pinholes bottom to top. All wire-ends from a single tetrode were wired to a single side of the square Omnetics board. Once a wire was fed through a pinhole, a gold pin was punched into the top hole, this severed the top of the wire and in the process removed sufficient electrical insulation to connect the board pin to the wire.

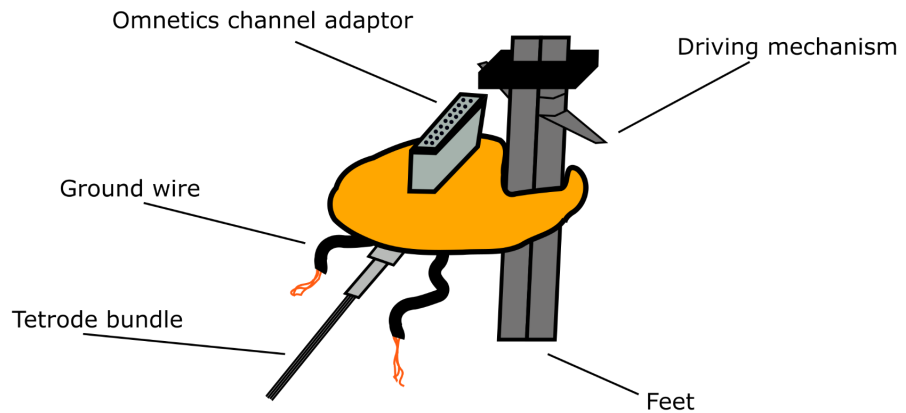
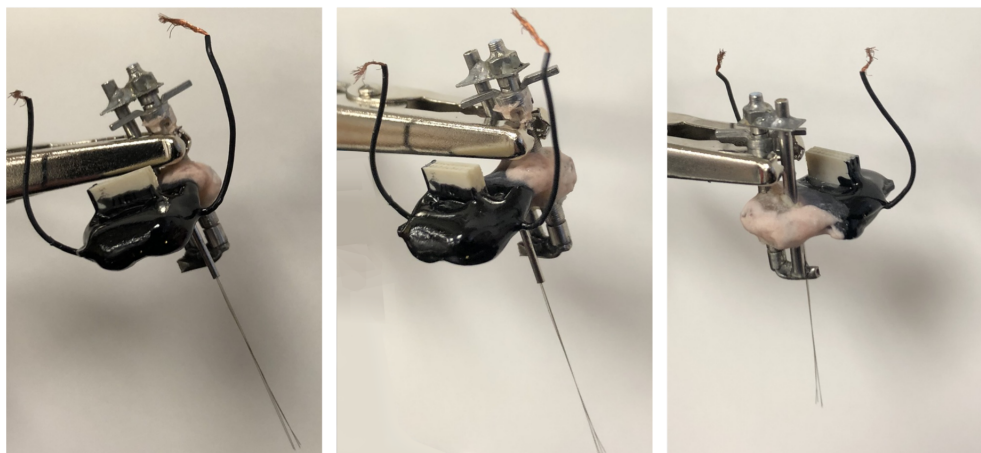
With all wires connected, connections were tested using a “bubble test” circuit. A small well was filled with saline and the tetrode ends suspended such that they were making contact with the saline. The saline well was connected to the positive terminal of a 9V battery and a pin adapter compatible with a single pin of the Omnetics to Mill-Max adapter connected to the negative terminal. Connecting this pin adaptor to a single pin created bubbles in the saline if the connection was true. The connection was satisfactory if it could be verified no pin connection created bubbles from multiple tetrodes, and bubbles created from the same tetrode consistent with the channel map did indeed come from the same tetrode end. If the connections could not be verified by bubble testing the wiring stage was repeated in full.

Once wiring was complete and verified, the connections were covered with layers of epoxy resin to ensure the connections stayed true throughout the experiment. This took place over days to allow adequate time for the epoxy to cure between layers. Both sides of the board were covered where tetrode connections existed, as illustrated by [Figure 11A](#). The minimum of epoxy resin was used to maintain a low total weight of the microdrive.

*Drive mechanism.* In order to move the tetrodes down while in the brain to record from multiple sites, a drive mechanism was installed adjacent to the Omnetics board. A bare microdrive frame (Axona, MDR-01) was suspected next to the board with bluetac and adhered to the board using dental cement (Kemdent, ACR807 and ACR924). The remainder of the exposed epoxy was covered with the dental cement to create a strong connection between frame and board. The position of the frame relative to the board was decided based on the target location of the craniotomy. All experiments described in this thesis targeted the MEC of the right hemisphere, thus illustrations in [Figure 11](#) and [12](#) are compatible with this design.

*Outer cannula.* A thicker outer cannula was cut, sanded and cleaned inside (Stainless Tube and Needle Co, 21 gauge). A single end was sanded to angle the cannula slightly so it might fit the curvature of the skull when lowered during implantation. The other end was shortened such that there was just enough space to move the microdrive down throughout the experiment and also to cover the exposed tetrode wires lowered into the brain region of interest. Once cut to size and shape, the microdrive was positioned upside down with the tetrodes pointing upwards and the lumen of the cannula passed through the tetrode bundle. If the tetrodes were not sufficiently close, they were wetted with ethanol with fine forceps. To temporarily secure the outer cannula before it could be lowered during implantation, vaseline was deposited between the cannula and the microdrive board.

*Gold plating.* In final preparation for the microdrive implantation, the tips of the electrodes were individually gold plated in order to create a similar conductance across electrodes in each tetrode bundle. This was done within 24 hours of the implantation surgery. Tetrodes were lowered into a non-cyanide gold solution (Neuralynx) connected to an open source gold plater circuit (Matsumoto 2019). The circuit enabled a readout of the impedance from each electrode from an oscilloscope (1 kHz sine wave). This could be reduced to an ideal target range of 150-200 K $\Omega$  for later spike sorting by pressing the switch and passing a 2.5  $\mu$ A current for gold plating. The microdrive was fastened to the lip of a storage jar (Fisher Scientific, 30 mL wide-mouth screw cap jar) with blue tac and stored in a dry area ready for implantation.

**A****B**

**Figure 11. Tetrode microdrive design.** (A) Schematic of custom built tetrode microdrive and (B) photographs from several different angles. Note that the microdrives were photographed before the final cut of the tetrodes took place.

### 2.3.3 Implantation

*Pre-op.* To prepare for surgery, surfaces were wiped down with 95 % ethanol then autoclaved surgical tools and drapes were laid adjacent to the surgical area. The mouse was collected from its holding room and brought to the surgical room. A pre-surgery weight was recorded to gauge the post-operative health of the mouse. It was transferred to an anaesthetic chamber supplied with 5 % isoflurane (Abbott Laboratories IL) to induce anaesthesia. Once anaesthetised (confirmed by showing no locomotive movement, sharp deep breaths and the absence of a pedal pinch reflex), the hair on the surface of the skull was clipped and the mouse was placed on a stereotaxic frame, with a continuous supply of 2 % isoflurane to maintain anaesthesia throughout surgery. Heart rate was monitored throughout surgery and isoflurane levels adjusted accordingly. 30 µL analgesic (Vetergesic 1:10 sterile water) was injected subcutaneously behind the neck. The mouse's eyes were covered with Ocry-gel to avoid them drying out during the surgery and the top of the head was cleaned with 10 % Betadine (povidone-iodine) to sterilise the incision site. Finally, the mouse's body was draped to keep it warm.

*Initial incision.* Ear and nose bars were tightened to fix the head in place. This was checked and maintained throughout. An incision was made between the ears and sufficient skin removed to expose the skull in order to accommodate space for the headpost. Neck muscles were disconnected with a spatula to expose sufficient skull area. Connective tissue was scraped off the surface of the skull and cleaned away to create a dry contact for headpost fixing. The skull was scored with a scalpel to increase contact points. A craniotomy location was chosen and roughly marked with a fine permanent marker pen.

*Headpost.* The headpost (Osborne and Dudman 2014) (Attenborough Labs) was superglued to the base of the skull, providing adequate room for the cannula of the microdrive to sit within the headpost appropriately above the craniotomy site. Ultraviolet-activated dental cement (Dental Sky, RelyX Unicem 2 Automix A3, 123-0006) was used to create strong contact points between the skull and headpost. Vetbond was then used to seal any loose skin around the headpost. The final headpost position is illustrated in [Figure 12](#).

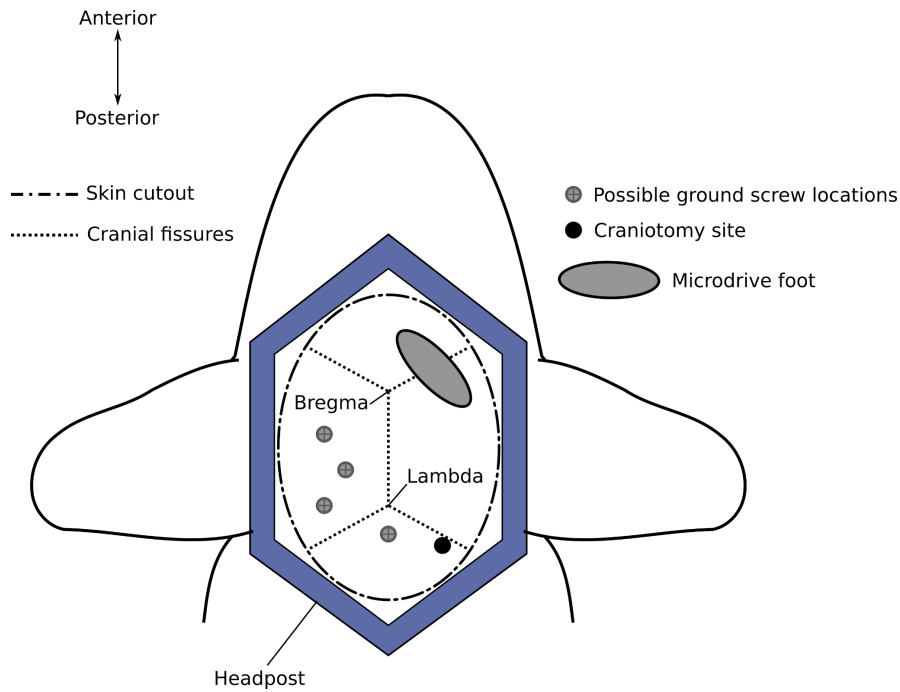


**Figure 12. Headpost position and possible ground screw locations on the skull.**

**Ground screws.** Two ground screw locations were marked with a permanent marker on the skull. Locations varied depending on skull size and headpost position. Figure 12 shows possible locations for ground screws. Most ground screw locations were contralateral of the craniotomy site. Screw sites were drilled several millimetres into the skull, not going all the way through. The drill bits used did not exceed the width of the screw. Ground screws were screwed into the drill sites until fastened. Superglue was added to the base of the screw to create stronger contact between screw and skull.

**Craniotomy.** The craniotomy location was drilled to expose the surface of the brain. Surfacing blood was soaked up with sterile tissues and cleaned with saline until it stopped. An injection pipette was lowered no more than 1 mm into the tip of the craniotomy (typically 500  $\mu\text{m}$  less than the tetrode implantation depth) to assess whether the tetrodes would be obstructed while being moved down into position within the brain. If the injection pipette was obstructed, the craniotomy was expanded and reassessed.

**Tetrode implantation.** The microdrive was mounted to an Omnetics adaptor above the headpost and adjusted to the correct angle of entry and implantation coordinates. Tetrodes were cleaned with 95 % ethanol and then saline. The tetrodes were lowered to the surface of the craniotomy and then lowered slowly (roughly one minute) to the correct location. Vaseline was placed around the surface of the craniotomy to prevent cement from entering.

The outer cannula was lowered and RelyX Unicem 2 resin cement (3M) dental cement added to the base of the outer cannula and feet of the microdrive. Ground wires were wrapped around ground screws and fixed in place with silver paint (RS components 101-5621). Dental cement was pipetted into the headpost to fill all remaining gaps and create further contact points between the microdrive feet, headpost and outer cannula. Once all cement had dried, the microdrive was unmounted.

*Post-operative care.* The mouse was removed from the stereotaxic frame and weighed. The weight differential between pre and post op was used to estimate the weight of the microdrive. The mouse was injected subcutaneously with 300 µL saline for rehydration purposes before being placed in a warm box until it showed signs of waking up. It was then transferred back to a fresh home cage atop a heated pad and monitored until moving around its cage. It was provided with water, water-covered food pellets, edible analgesic jelly and bedding. No enriching objects were placed in the cage for two days to avoid the chance of haemorrhages due to the mouse knocking into objects in the cage. The mouse was monitored daily by animal technicians and the surgeon until showing full signs of health.

## 2.4 Experimental setups

### 2.4.1 Overview

Mice were head-restrained and trained to run on a treadmill while a projection of a virtual corridor was visualised and updated in accordance with their movement on the treadmill. Mice were then placed in a square open arena to freely explore. In both behavioural tasks, the electrical activity within the brain was recorded. To successfully record the electrical activity within the brain, all erroneous sources that are electrically ‘louder’ than this activity must be removed. This was done both by electrically grounding the experimental hardware used during the behaviours and pre-processing the raw voltage traces through the OpenEphys software. In this section, the construction of the hardware and the data collection procedures will be discussed for the two spatial navigation tasks central to this thesis.

### 2.4.2 Virtual reality

A mouse is head-restrained using a 3D printed headpost (Attenborough Labs) on a cylindrical polystyrene treadmill (Graham Sweet Studios). A projector (InFocus, IN3118HD) beams an image of a virtual linear track onto the inside of a torus shaped screen (Talbot Designs Limited) with the mouse at the centre of the torus. A rotary encoder (Pewatron, E6-2500-472-IE) translates the rotation of the circular treadmill into inputs to the image rendering software (Blender3D). These inputs update the image in real-time (30 Hz frame-rate) to complete a closed loop system between the movement of the mouse and the image displayed. This creates an immersive virtual reality experience of traversing a virtual linear track with the locomotion of the mouse. The mounted position of the mouse and its point of view (POV) is illustrated in [Figure 13](#).

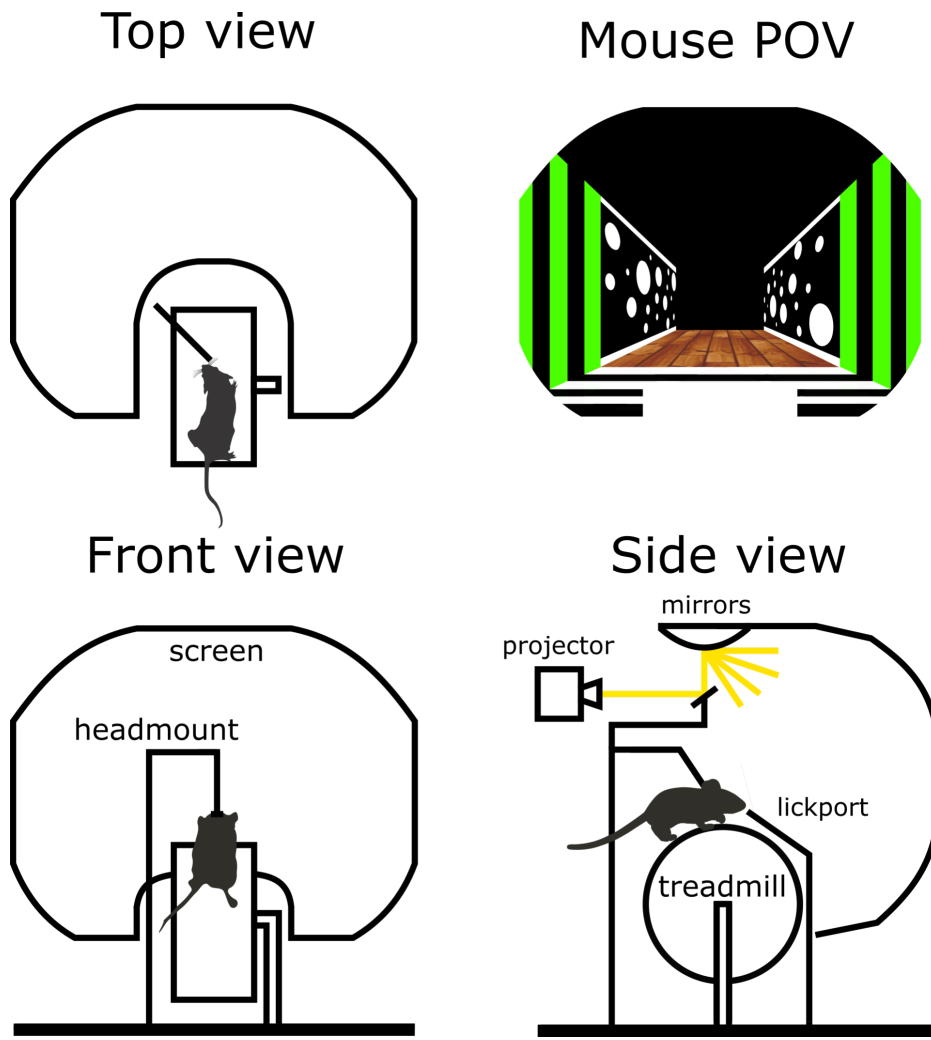


**Figure 13. Schematic of mouse head-restrained in the virtual reality rig.**

Two different virtual reality rigs were used for experiments discussed in this thesis, both built for the same purpose and not functionally different. They differed only in their outer casing used to shield them from electrical noise from the computers and experimenters. The rigs were constructed atop an aluminium breadboard (Thor Labs) inside a custom designed frame (CSI products). The concave screen, mirrors and the treadmill were fixed to the breadboard with M6 connectors and screws (Thor Labs) as in [Figure 15](#).

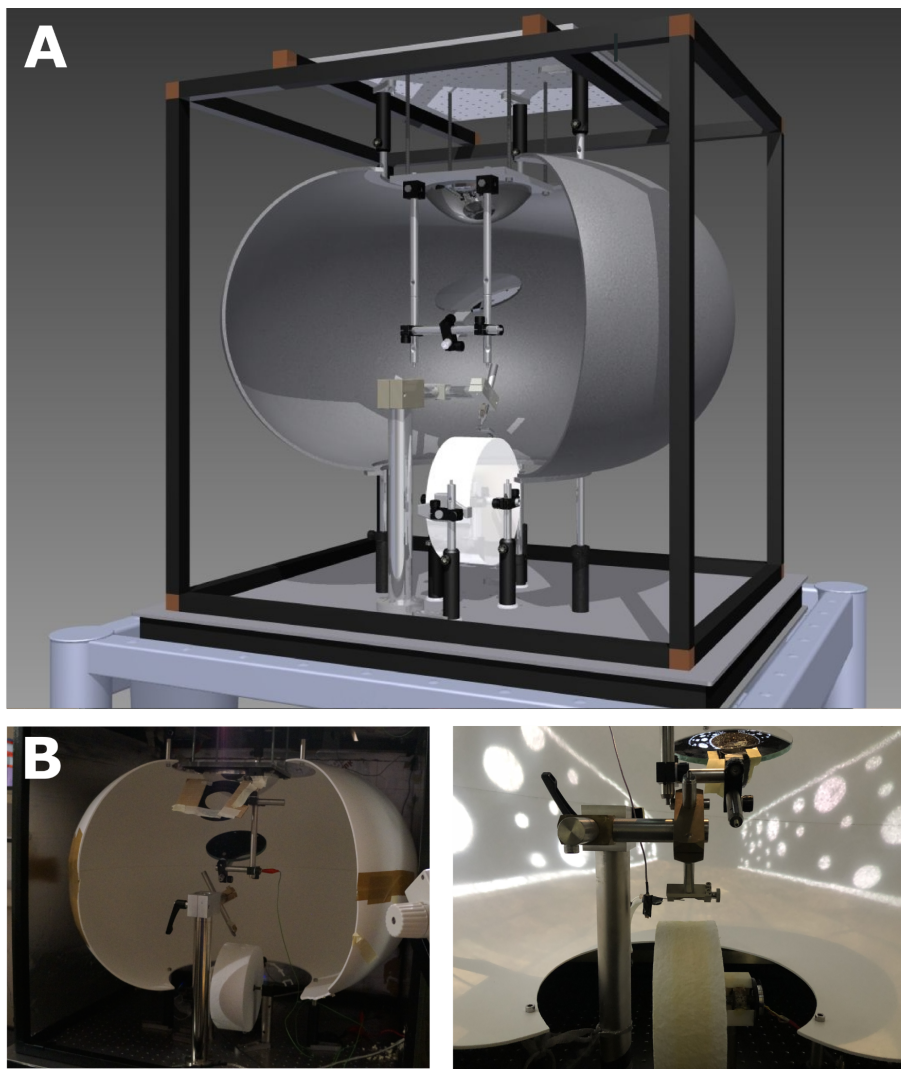


**Figure 14. Virtual reality setup.** (A) Graphic rendering of the virtual reality rig. (B) Photographs of the rig (left) and while projecting the track (right).

Electrical shielding of the two rigs was achieved by surrounding the frame with metal to create a faraday cage. For the first rig, a single layer of chicken wire was used. For the second rig, the faraday cage consisted of a custom-built metal box with stainless steel panels (Frame parts from Kanya UK, C01-1, C20-10, A33-12, B49-75, B48-75, A39-31, ALU3). Further electrical shielding was carried out and maintained throughout experiments by assuring strong electrical contacts between all metal components in the rig. A combination of crocodile clips and M6 screws were used to conduct adjacent metal parts together. This was repeated until voltage traces (roughly on the scale of 10-100 mV) on the magnitude of neuron spike events could be discerned from the baseline electrical noise.

*Track rendering.* Track designs were created in Blender3D. Dimensions and textures used for the track are described in [2.5.2.2](#) A camera object was positioned at the start of the virtual track, directed down the corridor, just as though a mouse was staring down a corridor. During runtime of the Blender3D program, the projected image was geometrically transformed such that the resulting image passing through the mirrors and onto the screen appeared as a linear track. This image was projected onto a flat mirror (Knight Optical Limited, 140 mm diameter aluminium front coated mirror), followed by an angular amplification mirror (AAM; Protolabs) onto the toroidal screen. This is schematised in [Figure 14](#) and mirror components shown in [Figure 15](#).

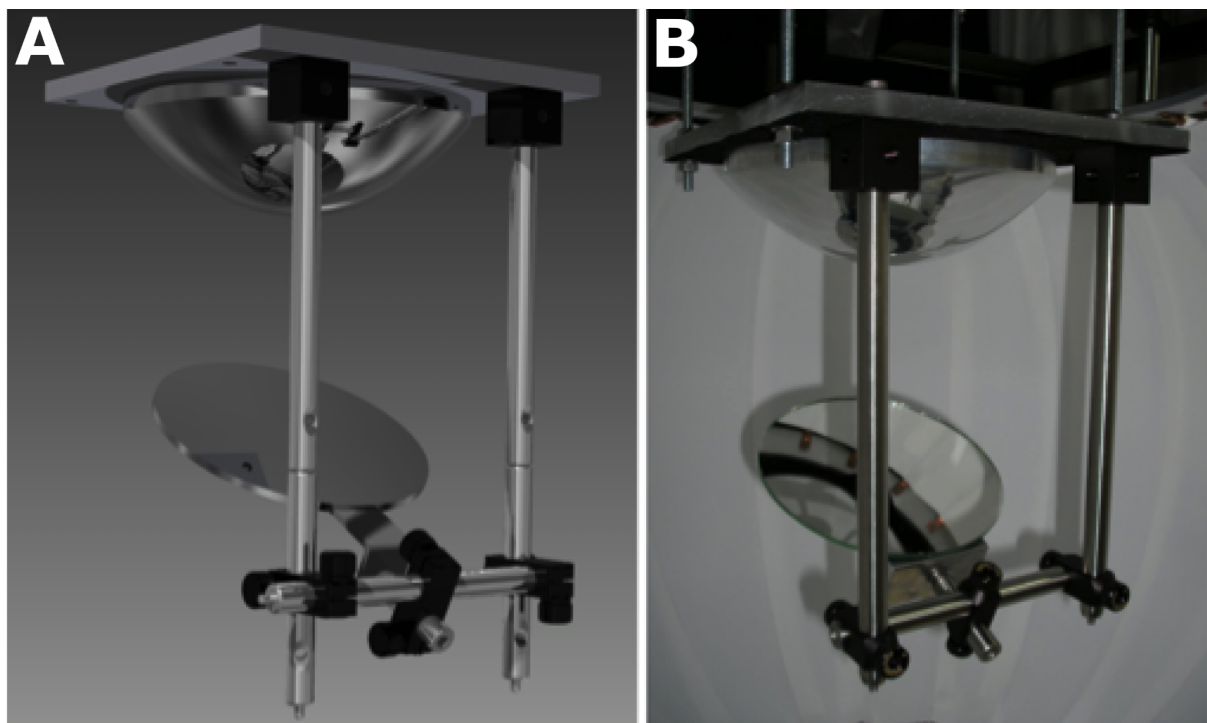


**Figure 15. Mirror components of the virtual reality rig.** (A) 3D-rendering of the mirror assembly (B) Photograph of the mirror assembly.

*Motion tracking.* To update the projected image, input from a rotary encoder coupled to the treadmill ([Figure 16](#)) is sent to the Blender3D program during runtime. This effectively translates physical movement into virtual movement within the virtual track. The rotary encoder consisted of two optical sensors directed at the circumference of an evenly grated disk. As the treadmill spins on its axis, the optical sensors either detect a light or dark portion of the grating. There were 5000 of these pulses per rotation (PPR). The number of dark portions passed per unit time is proportional to the velocity of the treadmill. To update the location of the camera object (and thus the projected image), Blender3D received the number of pulses passed at a rate of 60 Hz, this was then used to calculate the displacement since the last updated location, given by

$$(1) \text{ displacement (cm)} = \frac{N \text{ pulses}}{\text{PPR}} \times 2\pi \times \text{treadmill radius (cm)}$$

and

$$(2) \text{ displacement (virtual units)} = \frac{\text{displacement (cm)}}{\text{centimetres per virtual unit (cm)}}$$

Where the radius of the treadmill was 10 cm, PPR was 5000 and centimetres per virtual unit was set to 10 cm. The location of the camera object was then updated accordingly.

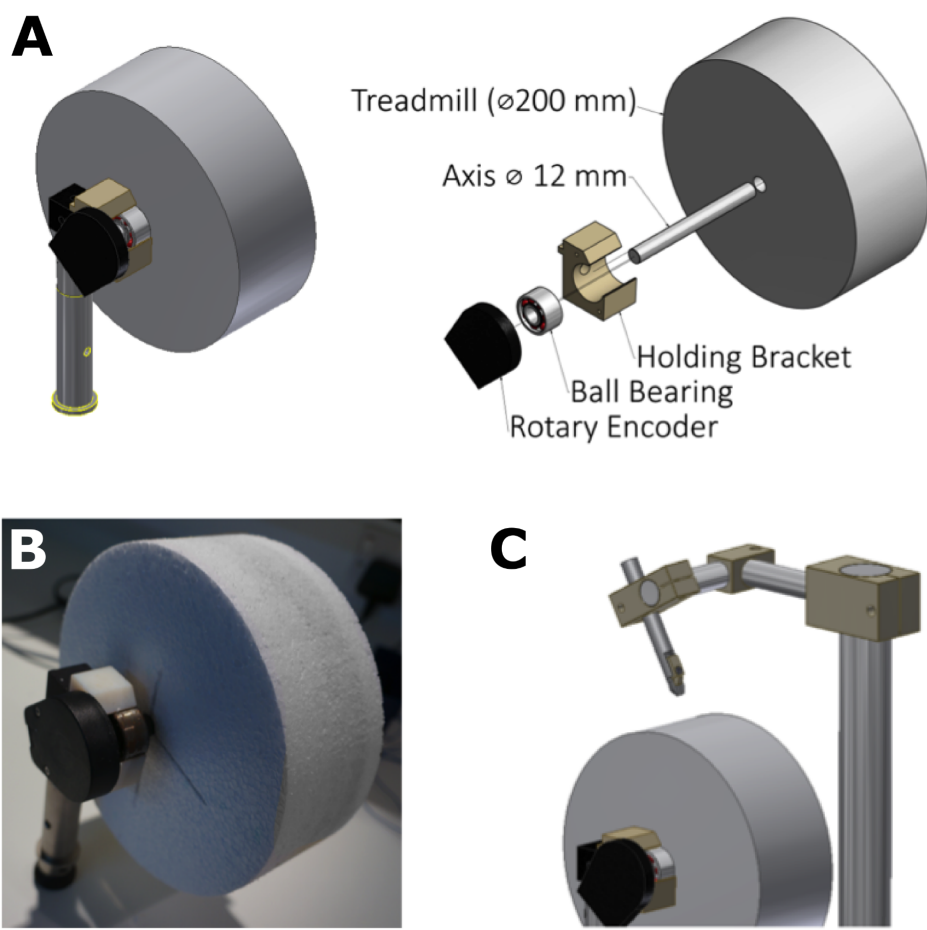


**Figure 16. Treadmill and rotary encoder.** (A) 3D-rendering of the treadmill attached to the rotary encoder and components of the treadmill assembly. (B) Photograph of the treadmill assembly. (C) 3D-rendering of the headmount in relation to the treadmill assembly.

*Head restraining.* To successfully immerse a mouse in virtual reality, they must take the place of the central camera object in the virtual environment. As the camera does not change its viewing direction or angle, the mouse does not either. This is achieved through fixing the position of the head in the focal point of the virtual environment. Most importantly, the mouse must be comfortable in order to be receptive to learning a goal-directed task. To best accommodate the aims of electrophysiological recording during a virtual reality task, a wide angled headpost (Osborne and Dudman 2014) was adopted to support enough room for a microdrive to sit within the hollow body, as shown in [Figure 17](#). A headmount (Ronan Tool Company, Inc) was assembled above the treadmill to allow the mouse to perch on the top of the treadmill, affording the mouse full control of its movement.

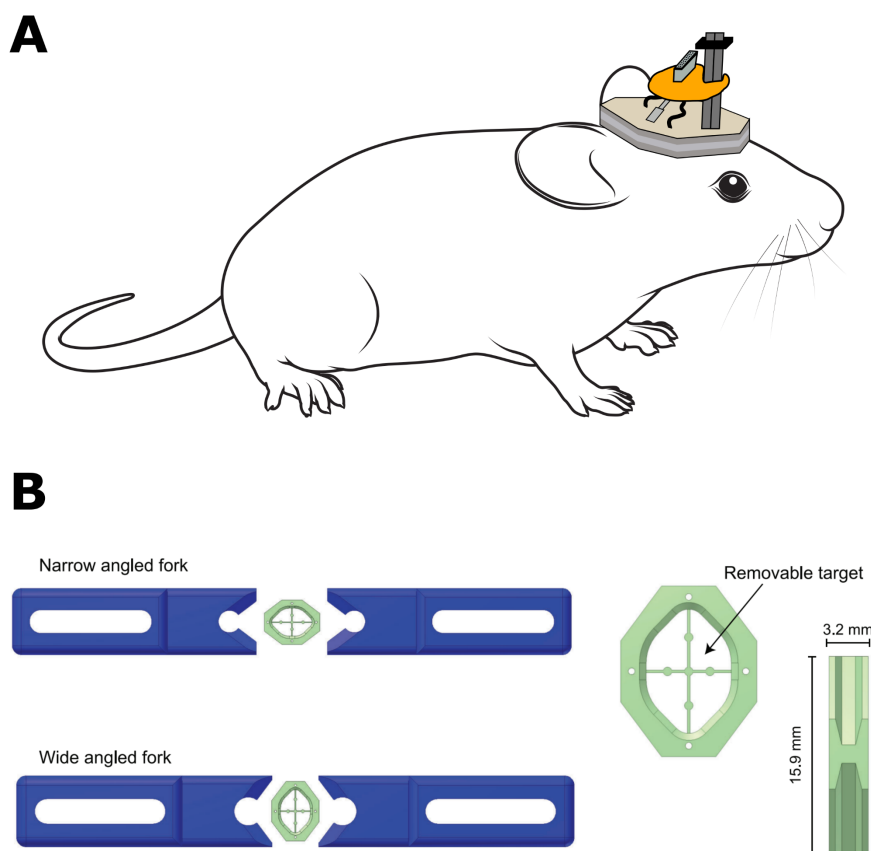


**Figure 17. Microdrive headpost design.** (A) Illustration of mouse with headpost and implanted microdrive. (B) Schematic of headpost mounting assembly and headpost design. Figure taken from Osborne and Dudman (2014).

*Electrophysiology.* The headstage adapter protruding from the microdrive was connected to an SPI cable (Intan Technologies, RHD2000 6-ft (1.8 m) standard SPI interface cable) and attached to an acquisition board (Open Ephys, 49). The SPI cable was dropped from the rig frame to remain out of view of the mouse.

*Feeding delivery.* Mice were given soy milk (Alpro, Soya Original) on successful trials during the task. This was delivered using a feeding needle (Kinesis Ltd) superglued to tubing (NResearch) attached to a container of soy milk. This container was suspended higher than the feeding needle such that without any interruption to the tubing, soy milk was continuously flowing out of the needle via the capillary effect. To gate the flow of soy milk, a pinch valve (NResearch, Full Opening Pinch Valve) was attached to the tubing creating a default state of no flow unless otherwise activated. Activation of the pinch valve was controlled via a valve driver (NResearch, CoolDriveSolo Universal Valve Driver) which was controlled by inputs from Blender3D during the task.

*Hardware connectivity.* A closed loop system was set up to create a virtual reality experience of running down a corridor and receiving soy milk rewards. The task was run through the Blender3D computer which communicated the visual display to the mouse through the projector and mirrors onto the concave screen. Motor information from the mouse was translated into an analogue voltage signal to the DAC channel of an Arduino Due microcontroller computer (Arduino) and read by the Blender3D computer to update the projected image proportional to the displacement signalled. When the movement conditions were met for the mouse to be rewarded, the Blender3D computer communicated to the pinch valve to open for 100 ms, thus allowing roughly 10  $\mu$ L soy milk to flow toward the mouse's mouth for that time. This movement information and the associating task variables were simultaneously copied as analogue voltage signals to the acquisition board with the recorded brain activity from the SPI cable connected to the mouse.

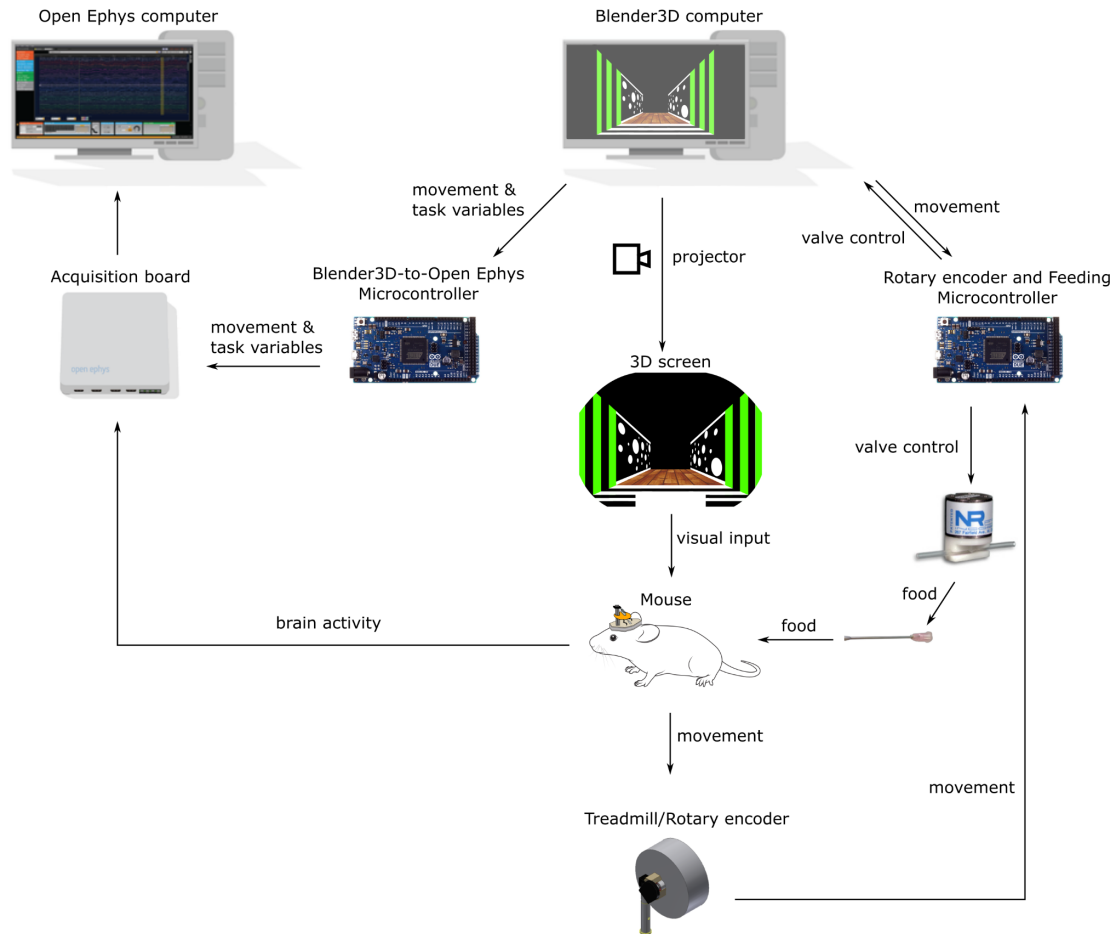
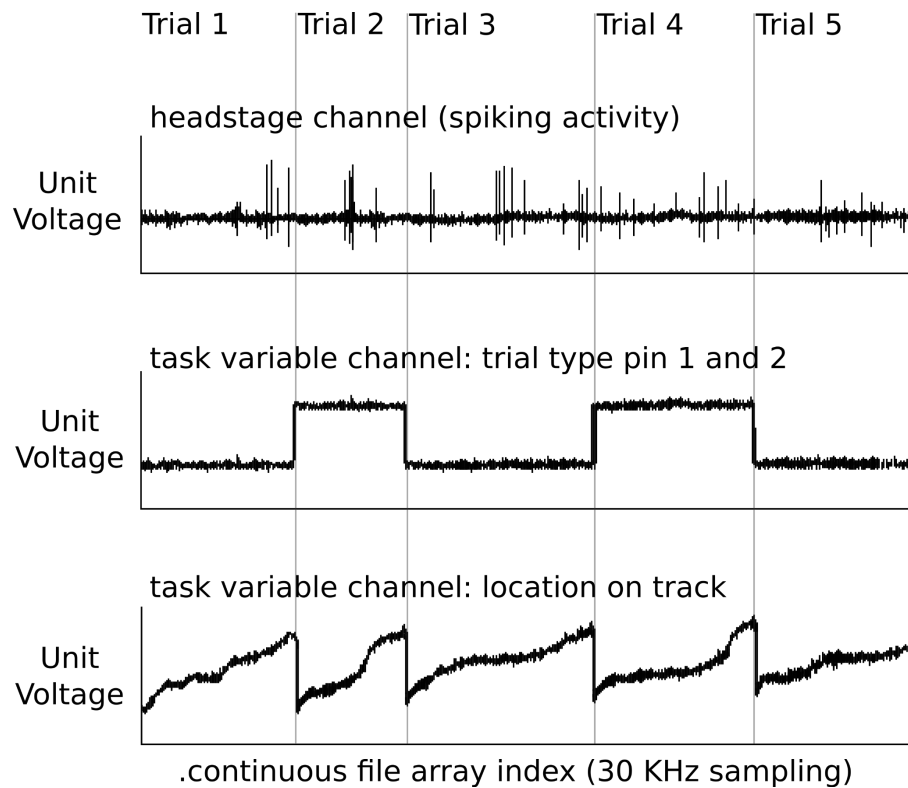


**Figure 18. Connectivity map for hardware components of the virtual reality task.**

*Data collection.* Electrophysiological and movement data were collected simultaneously to address the main thesis aims of uncovering the brain's solutions to spatial navigation problems. A single session's data is collected and stored into a single recording folder consisting of voltage trace signals saved as numerical arrays as the Open Ephys ".continuous" file format. There are 18 channels (16 electrodes + 2 ground screws) originating from the headstage adapter on the microdrive and 3 additional channels to store task variables (1 track location and 2 trial type indicators). The 3 task variable channels were received into the acquisition board through an I/O Board (Open Ephys) at the Blender3D 60 Hz sampling rate, then resampled by the acquisition board at 30 KHz. Track location was recorded as a voltage proportional to the current track location of the camera object and was later scaled by the track length in cm. Trial types were recorded on two binary voltage channels where a beaconed trial corresponded to [0,0], non-beaconed trial to [1,0] and probe trial to [1,1].

All channel files were then represented by a voltage trace sampled at 30 KHz over the course of roughly 30 minutes. These raw voltage files would be later used to reconstruct the spatial variables in the task (such as trial number, trial type, track location etc, instantaneous speed etc.) and the spike event timestamps, see [2.7](#) for more information. The different types of raw voltage traces are illustrated in [Figure 19](#) to provide an intuition of how data is stored and later reconstructed for post processing.

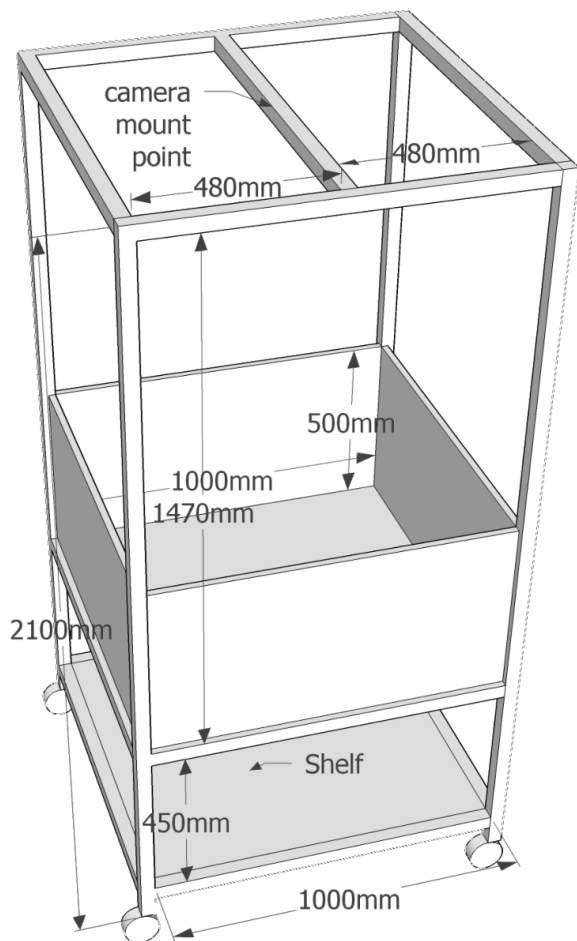
*Data storage.* Raw voltage files were transferred from the Open Ephys computer to the University of Edinburgh DataStore system for data processing purposes and long-term storage security.



**Figure 19. Open Ephys recorded variables for the virtual reality task.** Continuous Open Ephys files for different variables including (top) neural activity, (middle) trial type and (bottom) track location voltages. Grey vertical lines indicate the timestamp of a new trial.

### 2.4.3 Open field

A mouse was transferred to one of two open field arenas, both square arenas with side lengths 80 cm and 100 cm respectively. The two open field arenas were located in different animal facility floors and the choice between arena sizes was based on the availability of the experiment rooms alone. One one of the two arenas was only ever used for a single cohort. The arenas consisted of a metal box built from four removable metal walls (100 cm wide, 50cm high) and a metal floor (100 cm x 100 cm), housed in a custom metal frame (Frame parts from Kanya UK, C01-1, C20-10, A33-12, B49-75, B48-75, A39-31, ALU3; [Figure 20](#)). The interior walls and floor of the box was sanded, primed and spray-painted black. For the 80 cm wide arena, a custom-built box was constructed with four perspex walls (80 cm wide, 50 cm high) and a perspex floor (80 cm x 80 cm), surrounded externally with a single layer of chicken wire and lined internally with a matt white self-adhesive film. This setup was necessary to reduce electrical noise to an acceptable level for detecting neural spike activity. A camera (Logitech B525, 1280 x 720 pixels Webcam, RS components 795-0876) was mounted on the top of the metal frame viewing downwards toward the arena floor. A 3D printed commutator (Patrick Spooner of the University of Edinburgh, custom designed) suspended from the top of the frame was used to freely rotate a SPI cable (Intan Technologies, RHD2000 6-ft (1.8 m) Ultra-Thin SPI interface cable C3216) connected to the headstage adapter protruding from the mouse's microdrive. This afforded the mouse free movement throughout the arena with minimal resistance from the SPI cable. To reduce the weight of the cable felt by the mouse, the SPI cable was supported by elastic strings, suspended from the end of a thin metal pole freely rotating with the commutator. To illuminate the arena, a strip of LED lights was applied to each edge of the ceiling.

**A****B**

**Figure 20. Open field design.** (A) Schematic of the open field arena assembly. (B) Photographs of open field exterior (left) and interior (right).

*Motion tracking.* To record the location of a mouse, a camera mounted to the ceiling of the open field captured the surface of the arena. The location of the mouse was estimated as the midpoint between two polystyrene beads (one green, one red), mounted to the microdrive when in the arena. The outlines of these beads were detected on the camera image separately and midpoints averaged. Image processing was carried out using Bonsai tracking software and using a custom bonsai script (Lopes et al. 2015). The workflow of this Bonsai script is detailed in [Figure 21](#).

A sync pulse LED was also picked up by the camera, which was used to synchronise the location readings with the electrophysiological signal. An Arduino Due microcontroller emitted a signal to (1) the acquisition board and (2) to an LED, prompting a short burst of light that could be picked up by the camera, and used in later processing for synchronisation of the behavioural and electrophysiological data. The LED was switched on for 100 ms at random times throughout the session. This served the purpose of creating an irregular pattern of LED pulses (see [Figure 23](#)) that could be used to match the timing of the tracking and the electrophysiology data streams by finding the lag at which the correlation between both LED data streams were maximised.

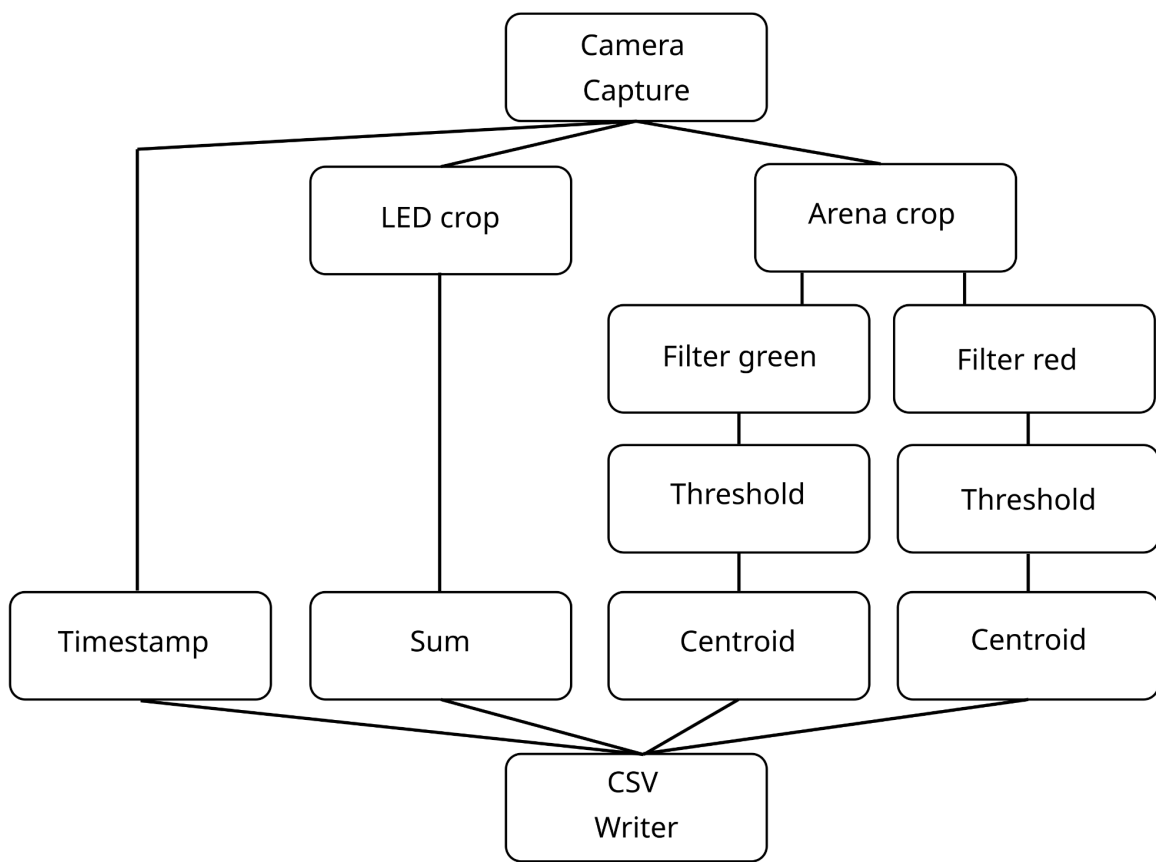


**Figure 21. Bonsai tracking workflow.** Two regions are tracked in parallel, the open field arena floor and the LED sync pulse. Mouse position is estimated by tracking green and red elements of the arena (coupled to the green and red beads mounted to the microdrive) and saving the midpoint (a.k.a centroid). LED sync pulses are captured by recording the luminosity of the cropped region around the LED. This is timestamped and saved in a .csv format for synchronising with the electrophysiology data.

*Electrophysiology.* The headstage adapter protruding from the microdrive was connected to a light weight SPI cable (Intan Technologies, RHD2000 6-ft (1.8 m) Ultra Thin SPI interface cable C3216) and connected to an SPI cable adapter board, (Intan Technologies, C3430). This adapter board connected to a second SPI cable (Intan Technologies, RHD2000 6-ft (1.8 m) standard SPI interface cable) which was attached to an acquisition board (Open Ephys, 49). The light weight SPI cable was dropped down from the commutator to remain out of view of the mouse.

*Hardware connectivity.* Electrophysiology signals were sent via SPI cables to an Open Ephys acquisition board. Movement of the mouse was captured by a ceiling mounted camera. To synchronise the timestamps of electrophysiological and spatial data, an arduino Due was programmed to spontaneously and briefly illuminate an LED light mounted to the edge of one of the open field walls. This LED sync pulse was sent to the acquisition board and the LED light was picked up by the camera.

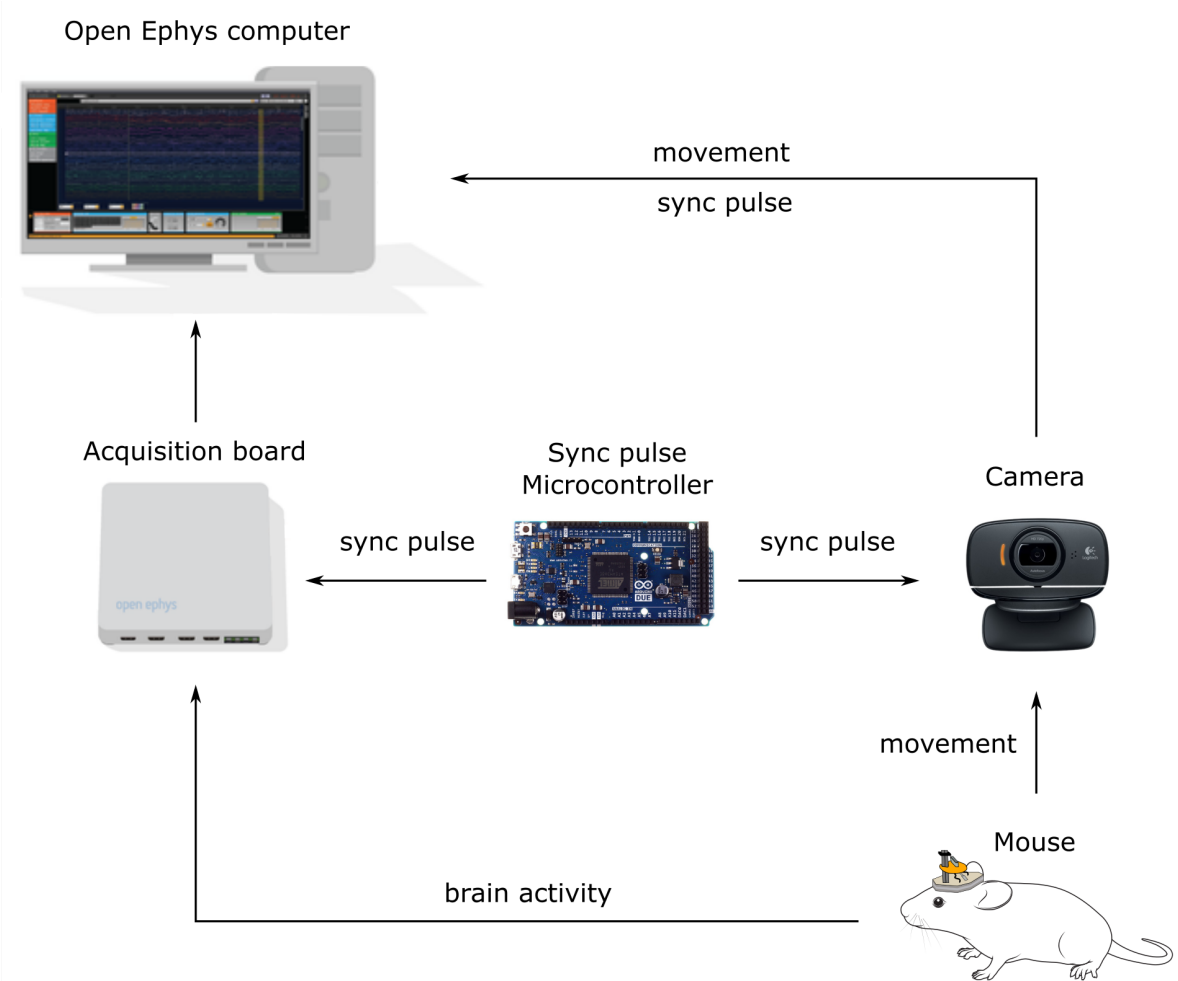


**Figure 22. Connectivity map for hardware components of the open field task.**

*Data collection.* Electrophysiological data was recorded much the same as described in [2.4.2](#). Movement and sync pulse data was captured by a mounted camera and saved via .csv files created through Bonsai tracking software. A single session's data is collected and stored into a single recording folder consisting of voltage trace signals saved as numerical arrays as the Open Ephys “.continuous” file format. There are 18 channels (16 electrodes + 2 ground screws) originating from the headstage adapter on the microdrive and 1 additional channel to store sync pulse data. The sync pulse channel was received into the acquisition board through an I/O Board (Open Ephys) at the Bonsai 30 Hz sampling rate, then resampled by the acquisition board at 30 KHz. All channel files were then represented by a voltage trace sampled at 30 KHz over the course of roughly 30 minutes. Sync pulse data saved separately by the Open Ephys and Bonsai software were later used to synchronise the movement data with the electrophysiological. The rest of the Bonsai data would be later used to reconstruct the spatial variables in the task (such as X location, Y location, head direction, instantaneous speed etc.) and Open Ephys data for the spike event timestamps, see [2.7](#) for more information. The different types of raw voltage traces are illustrated in [Figure 23](#) along with the Bonsai data ([Table 1](#)) to provide an intuition of how data is stored and later reconstructed for post processing.

*Data storage.* Raw voltage files and Bonsai tracking .csv files were transferred from the Open Ephys computer to the University of Edinburgh DataStore system for data processing purposes and long-term storage security.

Timestamp (time)	Red-X (pixel)	Red-Y (pixel)	Green-X (pixel)	Green-Y (pixel)	Sync pulse (amplitude)
1	10	34	11	33	0.0
2	12	30	13	29	1.0
3	15	30	16	29	0.0
4	17	31	17	30	0.0
5	12	32	14	33	0.0
6	9	31	10	31	1.0
7	7	25	8	25	0.0
8	8	23	7	22	1.0
...	...	...	...	...	...
N	13	40	14	39	0.0

**Table 1. Example Bonsai tracking data used to reconstruct the position of the mouse in the open field and synchronise this spatial data with the electrophysiological data.**

A midpoint is calculated for the red and green beads atop the mouse's microdrive with X and Y locations in pixels logged. For the sync pulse, the camera image is cropped around the LED and the sum of the pixel values within the cropped region is stored as a measure of LED amplitude. This summed signal is passed through a thresholding function that computes a binary value signifying if the LED sync pulse is illuminated (1) or not (0).

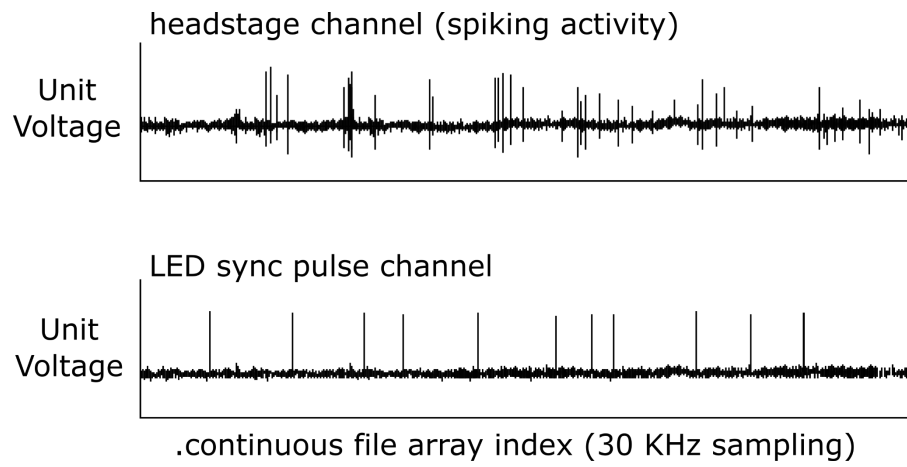


**Figure 23. Open Ephys recorded variables for the open field task.** Continuous Open Ephys files for different variables including (top) neural activity, and (bottom) LED sync pulses.

## 2.5 In vivo behavioural tasks

### 2.5.1 Overview

Mice performed two different spatial navigation tasks in a single day, (1) a goal-direction location estimation task in virtual reality and (2) a free exploration task in an open field arena. In this section, the behavioural aspects of the two tasks will be discussed.

A mouse was head-restrained on a treadmill with its vision and forward movement coupled in a closed loop to create a virtual reality environment. As it ran, it moved through a virtual corridor and once it had fully traversed the virtual corridor, it was teleported back to the start to repeat the process. Here, the term ‘virtual corridor’ and ‘virtual track’ are used synonymously. The objective of the task was to stop at a reward zone to receive a reward. This reward zone was either cued or non-cued and most importantly was marked a set distance away from a cued starting point. This was thus coined a virtual reality linear location estimation task (or shortened to linear location task). This task was designed to test a mouse’s ability to navigate towards a goal location using either the cue as a visual beacon or using its self-motion information and memory when this cue was absent. Self-motion information was available to the mouse in two ways, (1) self-generated motor information and (2) optic flow in the form of a repeating texture on the walls and floor of the arena (repeating every 20 cm). These textures could not alone be used to distinguish track location. To accurately execute the task, the mouse must principally use a path integration-based navigation strategy as no salient cues are available to the mouse when the reward zone is non-cued. With the mouse performing a path integration behaviour, simultaneous electrophysiological recording allowed the interrogation of the neural mechanism of path integration in the brain. The virtual reality task described in this section is the same that is described in Sarah Tennant’s PhD thesis and published work since (Tennant 2017; Tennant et al. 2018).

The mouse was then transferred to an open field arena after a 30 minute break in an enriching playground arena. The mouse ran around the square arena until the mouse had sufficiently sampled all locations within the arena. This afforded the detection of spatial-modulated cell types, in particular grid cells. As grid cells are defined by their observed firing properties in 2D environments, it was not possible to identify grid cells in VR sessions alone. With the positive identification of grid cells in the open field session, the utility of grid cells in the VR sessions could then be studied.

## 2.5.2 Virtual reality

### 2.5.2.1 Task design

Mice performed a linear location task for 30 minutes 5 days a week followed by 2 break days. They were transferred from their holding room to the experimental room and given 30 minutes of free-play in an enriching playground environment to minimise their stress. They were then head restrained and perched on a treadmill in the virtual reality system previously described. Mice ran through the virtual track and were teleported back to the beginning of the track to initiate another track run. Each track run was defined as a single trial. Two different trial types were used at the start of training, a cued trial, termed “beaconed” and a non-cued trial, termed “non-beaconed”. These terms reflected whether the track on a given trial had the reward zone marked by a cue or not. When a mouse’s speed dropped below a stopping threshold, the mouse was deemed to have stopped. If the mouse’s location was within the limits of the reward zone, a reward was dispensed from a feeding tube as detailed in [2.5.2.3](#).

To approximate the speed of the mouse, the elapsed distance was calculated over the previous 100 ms in real time in the Blender3D software. As the frame rate of Blender3D was 60 Hz, the elapsed distance was calculated by the location of the mouse on the track minus the location of the mouse on the track 6 frames prior. In cases where the mouse was teleported back to the start, this was accounted for. When the mouse’s speed dropped below a threshold of 4.7 cm/s, the mouse was deemed to have stopped. This seemingly arbitrary value was attained by trial and error over many experiments carried out by a handful of experimenters. It was agreed upon collectively as a good compromise between an accurate representation of a stopping action by the mouse and an achievable behaviour to learn in the timescale of days. A more stricter stopping threshold often resulted in mice not learning to stop within the reward zone.

Following two successive days of demonstrating a clear stopping preference for the reward zone as detailed in [2.5.2.8](#), a third trial type was introduced, whereby the reward zone was non cued and no reward was dispensed upon successful stopping at the reward zone, this was termed a “probe” trial. A timeline of the experiment is detailed in [Figure 24](#).

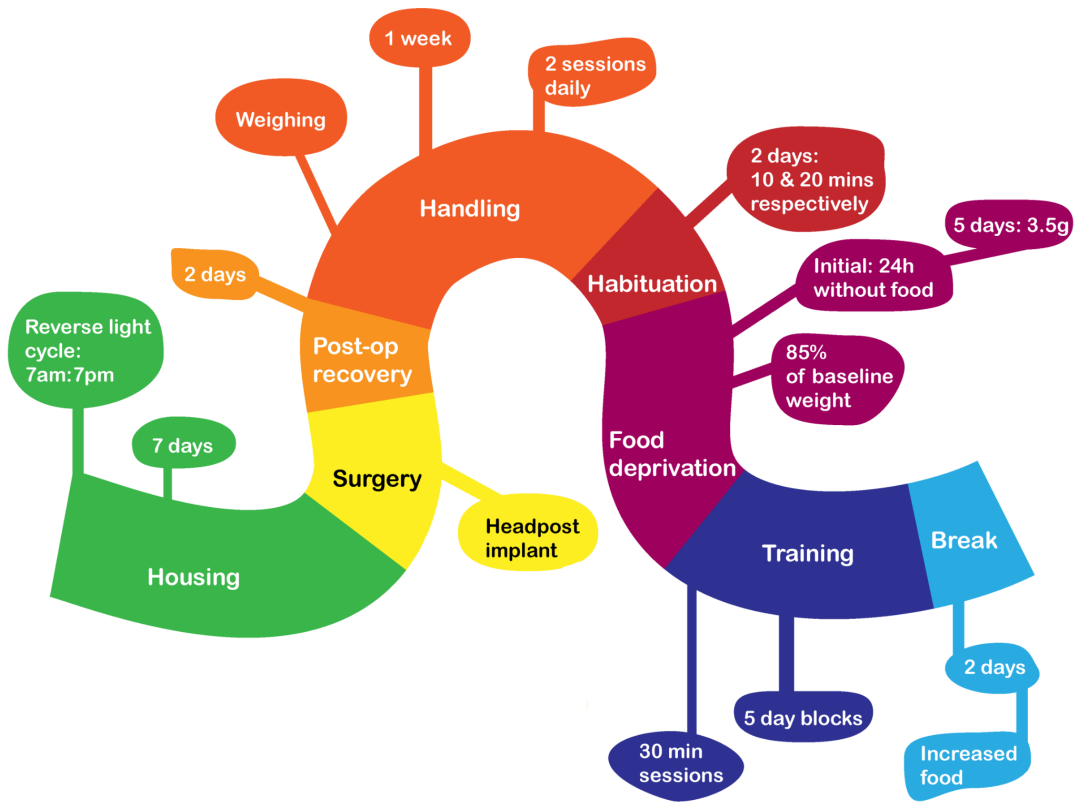
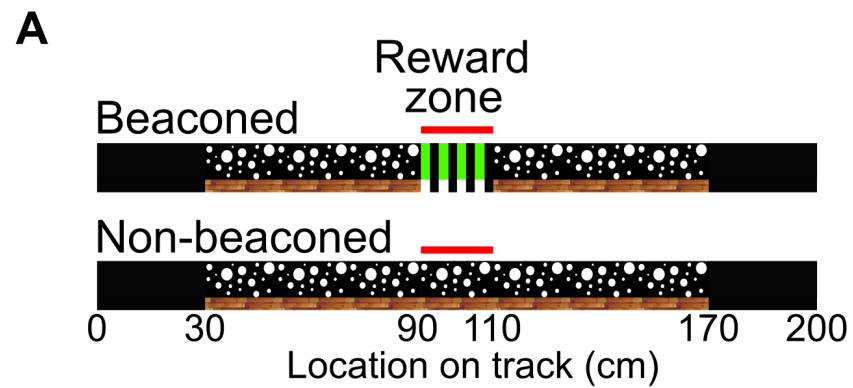


**Figure 24. Experimental timeline.** Taken and modified from Sarah Tennant's PhD thesis with permission.

### 2.5.2.2 Linear track

The track was designed and rendered in Blender3D. It consisted of a floor and two flanking walls similar to a corridor. The track was 200 cm and consisted of two 30 cm dark regions termed the black boxes at either end of the track and a textured region from 30 - 170 cm on the wall and floor. The textured wall pattern was made up of a repeated pattern of white circles on a black background with a rim of white at the top and bottom of the wall. The texture floor pattern was made up of a repeated pattern of wooden floorboards. These patterns repeated every 20 cm. This region was designed such that a mouse had no unique cue to estimate its location. To prevent the mouse using the end of the track as a cue, the visual range of the mouse was restricted to only 50 cm in front of the mouse at all times. To train the mice to stop at a particular location, a reward was available when the mouse stopped in a reward zone located between 90 - 110 cm and a visual cue was added to an identical track to mark the location of this reward zone. This cue consisted of a black-white grating on the floor and a black-green grating on the wall. [Figure 25](#) shows these two tracks as well as a point of view from the mouse's perspective.

A trial consisted of a mouse running the full length of the track. When the mouse reached the end of the track, its position in the virtual track was reset to the start to initiate another trial. These two tracks were used across three different trial types, termed beaconed, non-beaconed and probe trial types. Beaconed trials took place on the beaconing track whereas non-beaconed and probe trials took place on the non-beaconed track. Probe trials were identical to non-beaconed trials except no reward was released for stopping in the reward zone.



**B**

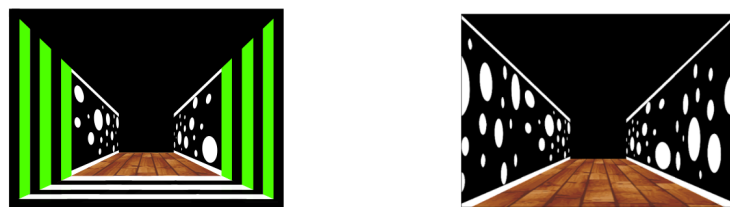


**Figure 25. Virtual reality track design.** (A) Track schematics for beaconing and path integration navigation behaviours, completed on the beaconed and non-beaconed tracks respectively. (B) Mouse point of view (POV) for beaconing and non-beaconed trials.

### 2.5.2.3 Reward

When the mouse speed was below the stopping threshold of 4.7 cm/s and the mouse's location was registered between the reward zone limits, a reward was dispensed in the form of soy milk (Alpro, Soya Original), as described in [2.5.2.1](#). This reward was combined with the playing of an auditory tone for 500 ms to reinforce the association between the rewarded location and the reward. During probe trials, no reward was dispensed nor was the reward tone played.

### 2.5.2.4 Animal housing

Prior to the microdrive implantation surgery, mice were group housed in a holding room, operating on a reverse light cycle. Here, lights were controlled on an automatic timer such that they were turned on at 7 pm and off at 7 am daily. No external sunlight was visible from either the holding room or experimental room. This maintained a reversed daily light cycle as mice are much more active during dark hours. This facilitated the experimenter to maintain regular sleeping hours. Daily experimental sessions typically took place between the hours of 10 am to 5 pm and similar timings were used for a given mouse each day.

Following microdrive implantation, mice were transferred to fresh cages and individually housed from this point onwards. Each mouse was housed in a cage measuring 30 cm long, 15 cm wide and 12 cm tall. Cages included wooden shavings scattered about the floor, cotton wool bedding, a cardboard igloo, a running wheel and two hammocks for enrichment.

### 2.5.2.5 Animal handling

To get the mouse accustomed to being handled, it was vital to spend time with each mouse. Experimenters wore gloves, fresh scrubs, hair nets, and face masks (due to Covid-19 regulations at the time of experimentation). Mice were handled for 20 minutes twice daily for 1 week following 2 days of post-operative recovery. On days 1 and 2 of handling, the experimenter laid their palm upwards in the mouse's cage to allow the mouse to climb and sniff around the hand. When the mouse became comfortable enough to sit on the hand, the mouse was gently moved between hands and back to the cage. This was repeated to reinforce the association between the experimenter's hands and the safety of returning to their home cage.

When scheduling allowed (e.g. when the experimenter was waiting for the mice to grow to a particular age before starting the experiment), mice were given extra handling sessions in the week before surgery. Group housed mice were transferred together to the playground arena to freely explore. Again, the experimenter's hands were introduced to the arena for

mice to climb and sniff when comfortable. It was observed that mice that were more comfortable being picked up were less visibly stressed on the first few days being head-restrained on the virtual reality treadmill. It was thus encouraged to spend an hour a day playing with the mice in the playground and importantly only engaging with a mouse once it was actively moving towards and climbing on the experimenter's hands and arms.

#### 2.5.2.6 Animal habituation

During animal handling, soy milk was offered out of the experimenter's glove to strengthen the association between the experimenter and food rewards. Head-restraining the mouse to the headmount above the treadmill is unfortunately a stressful scenario the first couple of times. To minimise this stress for the first training day, mice were head-restrained for 10 and 20 minutes for 2 days respectively. The virtual reality system was switched on and soy milk was available as reward such that the mouse could get accustomed to the environment it would be exposed to in the coming days and weeks.

#### 2.5.2.7 Food deprivation protocol

To motivate the mouse to learn the task swiftly, the food reward was made substantially more valuable to the mouse by depriving the mouse of food prior to the task. Food deprivation protocols were signed off by a named surgeon and adhered to strictly.

Weights were recorded daily at the same time each day starting immediately after postoperative recovery. Here, the weight of the mouse provided a key metric for monitoring the health of the mouse. To obtain a baseline body weight, an average weight was calculated from the five days preceding the start of food deprivation. The weight of the mouse did not include the microdrive or headpost. The weight of the microdrive and headpost were subtracted from all measurements to obtain a weight of the mice alone. Immediately after the second habituation session, the mouse was provided with a fresh cage and no food was given to the mouse for 24 hours. The food given to the mouse on the subsequent days was based on its baseline body weight as indicated by [Table 2](#).

<b>Baseline body weight (g)</b>	<b>Initial daily food allowance (g)</b>
< 17	3.1
17 - 19	3.3
19 - 21	3.5
21 - 23	3.7
23 - 25	3.9
25 - 26	4.0
26 - 27	4.1
> 27	4.2

**Table 2. The amount of daily food given to a mouse following 24 hours of food deprivation.**

The restricted allowance of daily food was given in order to maintain a weight of 85 % of the baseline bodyweight. This weight is a tolerable level for the mouse's wellbeing, but encourages the mouse to eat when food is immediately available to it. As the experiment takes place for up to 10 weeks, maintaining 85 % of the original baseline body weight would not account for the expected growth of the mouse over this time. To account for this, the expected daily growth of a large population of mice was obtained from The Jackson Laboratory. This data was available for male and female mice across a range of ages as shown in [Figure 26](#). This expected daily growth was then adjusted based on the baseline body weight of a given mouse. Firstly, the baseline body weight of the experimental mouse was compared to the mean population body weight, matched by age and gender, to make a body weight factor given by:

$$(3) \text{ Body weight factor} = \frac{\text{Mouse body weight}_{\substack{\text{Experimental} \\ \text{Age} = i, \text{Gender} = j}}}{\text{Mouse body weight}_{\substack{\text{Population Mean} \\ \text{Age} = i, \text{Gender} = j}}}$$

This factor was multiplied by the daily expected growth of the population to obtain a corrected daily growth for the experimental mouse. This corrected daily growth was added to the baseline body weight every day to obtain the growth-corrected baseline body weight. The daily food allowance was thus adjusted to maintain the mouse's body weight at 85 % the growth-corrected baseline.

The daily food allowance was altered throughout the experiment to maintain a high level of task engagement while also maintaining healthy body weights. To monitor the health of the mouse, a severity score was used to access and record the mouse's level of deprivation. A score of 0 - 3 was assigned based on criteria listed in [Table 3](#). A severity score of 1 was aimed for. At the end of the fifth training day per week, mice were provided with a fresh home cage and instead given 130 % of their daily food allowance to compensate for the food they did not receive in task rewards. On break days one and two, mice were given 115 % and 100 % of their daily food allowance respectively.

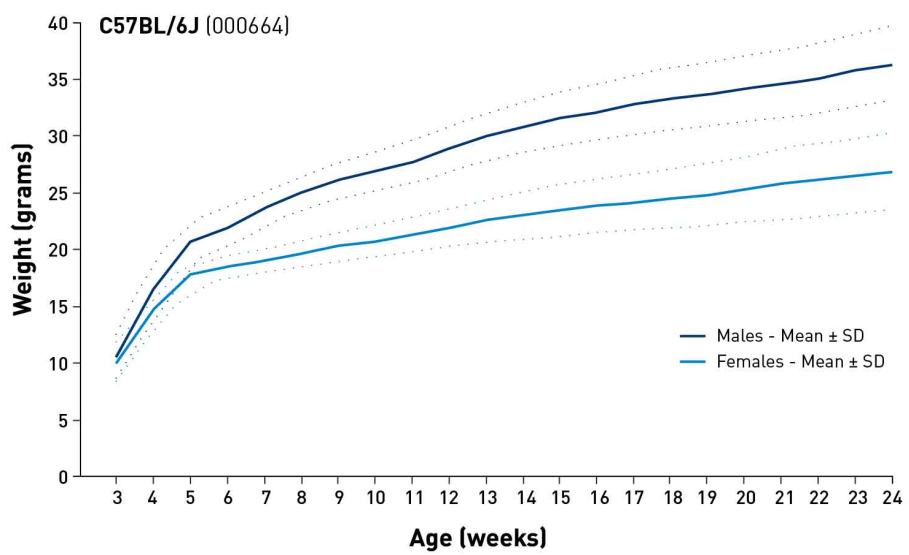


**Figure 26. Jackson Laboratory weight index for C57BL/6J mice.** Figure taken from the C57BL/6J strain datasheet provided by the Jackson Laboratory.

<b>Severity score</b>	<b>Behavioural criteria</b>	<b>Daily food changes</b>
0	<ul style="list-style-type: none"> <li>- Weight above 95 % baseline</li> <li>- Mouse does not eat immediately when offered food</li> </ul>	- 0.2 g
1	<ul style="list-style-type: none"> <li>- Weight between 85-90 % baseline</li> <li>- Very active behaviour <ul style="list-style-type: none"> <li>- Running on playground wheel</li> <li>- Nibbling fingers of experimenter</li> </ul> </li> </ul>	No change
2	<ul style="list-style-type: none"> <li>- Weight between 80-85 % baseline</li> <li>- Hyperactive behaviour <ul style="list-style-type: none"> <li>- Running frantically in playground</li> <li>- Biting down on the fingers of experimenter</li> </ul> </li> </ul>	+ 0.2 g
3	<ul style="list-style-type: none"> <li>- Weight less than 80 % baseline</li> <li>- Lethargic behaviour <ul style="list-style-type: none"> <li>- Slow movement</li> <li>- Hunched posture</li> </ul> </li> </ul>	2 x daily food (Constant monitoring, wetted food if necessary)

**Table 3. Severity scores used to assess the deprivation of a mouse.**

#### 2.5.2.8 Behavioural training

A mouse was trained in the linear estimation virtual reality task for 30 minutes per day, five days a week, with two days break. Comfort and performance was monitored daily. The behavioural training began with the mouse running beacons and non-beaconed trials in a ratio of 4:1 (4 beacons followed by 1 non-beaconed). Training days were broadly split into three distinct phases. These included (1) learning, (2) graduation, and (3) manipulation.

*Learning.* Learning encompassed the initial phase of training and ended when the mouse demonstrated a clear bias for stopping at the reward zone on both trial types. This bias was identified when the stop distribution peaked in the reward zone versus the rest of the track.

*Graduation.* When the mouse demonstrated this bias and was running a minimum of 75 trials for two days in a row, the mouse “graduated” to the second phase of training. Here, a third trial type was introduced. This trial type named probe was a non-beaconed trial however no reward was dispensed when the mouse successfully stopped in the reward zone. This was introduced to control for the effect of a reward signal in later analysis. Mice now ran trials with a ratio of 8:1:1. The order of these trials is summarised in [Table 4](#).

*Manipulation.* The final phase of training (Manipulation) introduced a number of manipulations to the standard experimental protocol. These included training days on longer tracks or using a different trial type order entirely.

*Experimental endpoints.* The behavioural portion of the experiment ended when any one of a number of conditions were met. These included:

- Poor performance - Mouse performing < 20 trials for two days after training day 10.
- Health reasons - Mouse visibly uncomfortable on the treadmill past training day 10, not eating food, haemorrhaging from microdrive.
- Poor electrophysiology - No curated clusters identified for 5 days.
- Experiment time cap - Mouse had completed the imposed cap of 50 training days.

Once a mouse had finished the experiment, it was fed ad-libitum until it was euthanized via lethal injection and tissue prepared for imaging by perfusion fixation (see [2.6.2](#)).

	<b>Learning</b>	<b>Graduation</b>	<b>Manipulation</b>
<b>Trial 1</b>	B	B	B
<b>Trial 2</b>	B	B	B
<b>Trial 3</b>	B	B	B
<b>Trial 4</b>	B	B	B
<b>Trial 5</b>	NB	NB	NB
<b>Trial 6</b>	B	B	B
<b>Trial 7</b>	B	B	B
<b>Trial 8</b>	B	B	B
<b>Trial 9</b>	B	B	B
<b>Trial 10</b>	NB	P	P
...	Repeat from Trial 1		

**Table 4. Trial type orders for learning, graduation and manipulation phases.** Trial orders repeated every 10 trials. B = beaconed, N = non-beaconed, P = probe.

### 2.5.3 Open field

Mice performed a free exploration task for 30 minutes, 5 days a week followed by 2 break days. These sessions occurred after a 30 minute session performing the virtual reality task followed by a 30 minute break in a playground environment.

#### 2.5.3.1 Task design

The open field task was considerably easier for the mouse, as no training was required per se. Mice were placed in the open field arena with a cable attached to their microdrive for recording the electrophysiological signal while the mouse was exploring the environment. Over the course of 30 minutes, the majority of mice explored the entire arena and sampled the same location in the arena multiple times. This was encouraged by minimising the light provided to the arena and minimising the noise created by the researcher. This created a safe environment for the mouse to explore more exposed regions of the arena. The arena was designed to be very plain and limited in environmental enrichment. No food was used to encourage exploration. The wall was single coloured, either white or black and had a single yellow cue card present on the middle of one of the walls. This cue card was used as a disambiguating cue for the mouse in the case the mouse could not determine its orientation within the arena. Of the two open field setups used (100 x 100 cm and 80 x 80 cm), the majority of the mice performed the open field task in the bigger arena (N = 13 vs N = 2, respectively).

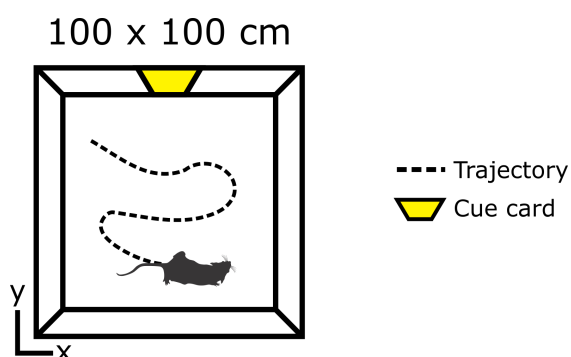


**Figure 27. Open field arena schematic**

The purpose of the free exploration task was to reproduce the experimental conditions for detecting classically defined spatial modulated cell types in the MEC including head direction cells, speed cells, border cells and grid cells (J. Taube, Muller, and Ranck 1990; Kropff et al. 2015; Solstad et al. 2008; Hafting et al. 2005). Detection of these cells was necessarily done in a 2D arena as it was not possible to compute scoring metrics to define grid, border and head direction cells from the virtual reality task.

## 2.6 Tissue Imaging

### 2.6.1 Overview

To be able to address questions of the function of spatial cells in MEC, one must verify that the neural spikes recorded do indeed originate from the MEC. In this thesis, three separate methods are used to estimate a recording location. These include (1) imaging the tetrodes or tetrode tracks within the brain, (2) looking for theta wave oscillations of the local field potential (LFP) and (3) looking for theta-modulated firing of individual neurons, also indicative of retrohippocampal. In this section, the process for imaging the tetrodes and tetrode tracks within the brain will be described. To determine tetrode locations either Cresyl violet staining or microcomputed tomography (microCT) was used.

For microCT, Brains were processed using a modified protocol designed for x-ray micro-computed tomography (micro-CT) imaging of whole rat brains (Masis et al. 2018). This process aims to image a whole brain with tetrodes intact and visible for tetrode localisation. Osmium tetroxide is used as a contrast agent to discern regions with high or low densities of neuron cell bodies which can be used to detect notable anatomical structures such as the hippocampus. The process is illustrated in [Figure 28](#). For Cresyl violet staining, brains were processed, sliced and then imaged sagittally. Inspecting sagittal cross-sections allowed the negative trace of the tetrodes to be seen. Tetrodes or tetrode tracks were localised relative to landmarks in version 2 of the Allen Reference Atlas for the mouse brain (<https://mouse.brain-map.org/static/atlas>).

### 2.6.2 Perfusion fixation

Mice were anaesthetised in a bell jar with several drops of isoflurane (Abbott Laboratories IL) pipetted onto a paper towel on the floor of the jar. Once pedal and eye reflex were no longer present, the mouse was injected with 0.1 mL pentobarbital. intraperitoneally. The mouse was pinned down to a corkboard and the heart was swiftly exposed by removing skin and the ribcage with fine scissors. Phosphate buffered saline (PBS; Fisher Scientific, 7001104410, 10 times diluted with distilled water) was intracardially perfused at 10 mL / minute and the liver was cut to allow blood to flow out of the body. Once liquid from the liver turned clear in colour, the perfusion solution was switched to 2 % (for micro-CT processed brains) or 4 % paraformaldehyde (for cresyl violet processed brains; PFA; Sigma Aldrich, 30525-89-4), 2.5 % (for micro-CT processed brains only; GA; Emsdiasum, 16220) in 1 M phosphate buffer (PB; Sigma Aldrich, P7994) for 5-10 minutes. The mouse was decapitated

and the head was post fixed in 2 % PFA, 2.5 % GA in 1M PB for 48-72 hours at 4°C while shaking at 50 rpm on an orbital shaker.

### 2.6.3 Micro-CT

#### 2.6.3.1 Tissue processing

After shaking for 48-72 hours, heads were washed in distilled water (ddH<sub>2</sub>O) three times and left on a rocker at room temperature (RT) for 1 minute between washes. A final wash was done with a 15 minute wait on the rocker. Solutions were made up to cover the brain with 10 mL additional volume above the brain (roughly 20 mL).

*Microdrive removal.* The outer cannula of the drive was cut at the base of the headpost, followed by the drive mechanism. This was done to reduce the amount of excess metal imaged by the scanner, which causes excessive light scattering and image noise. Brains were then excavated from the heads. Special care was taken to keep the microdrive and headpost attached to the top of the skull such that the tetrode did not move while still in the brain.

*Osmication.* Brains were placed in 20 mL 2 % Osmium tetroxide (10 mL 4 % OsO<sub>4</sub> diluted in 10 mL ddH<sub>2</sub>O, Emsdiasum, 19190) in 50 mL conical tubes. Tubes were sealed with parafilm and covered in aluminium foil. These were stored vertically in a large beaker on a rocker at 50 rpm under a fume hood at RT for 2 weeks. (SPECIAL NOTE: For any person reading this thesis with view of implementing this protocol, please note osmium tetroxide is an extremely deadly chemical, causing blindness with contact with eyes and is known to cause long term liver and kidney problems. Take extreme care and read safety protocols exhaustively before use).

*Embedding.* Brains were washed in ddH<sub>2</sub>O three times and left on a rocker at RT for 1 minute between washes, followed by a 15, 60, and 30 minute wash. Brains were dehydrated with increasing concentrations of ethanol, (20 %, 50 %, 70 %, 90 % and 100 %) on the rocker for 30 minutes each. Brains were then washed with 100 % acetone solutions on the rocker three times at 30 minutes between washes. To embed the brains in resin, increasing concentrations of a water-soluble epoxy resin, Durcupan was used (Sigma Aldrich, component A-44611, component B-44612, component C-44613, component D-44614). Solutions were slowly mixed to avoid bubbles. Brains were further washed with increasing concentrations of Durcupan component A (33 %, 50 %, 67 %) diluted in acetone and left shaking at RT for 2, 2.5 and 2 hours respectively. This was followed by a 12 hour wash in 10

mL component A, 10 mL component B and 100 µL component C on the shaker at RT. Brains were transferred to embedding moulds (Ted Pella, 27114) and a final wash was applied in a solution of 10 mL component A, 10 mL component B, 100 µL component C and 300 µL component D for 4 hours shaking at RT. All times during embedding were strictly adhered to because it was observed that acetone could, given enough time dissolve the dental cemental. This needed to be avoided as it is critical to keeping the remaining cannula in place (and thus the tetrodes). Brains were transferred to an oven and left to cure in resin at 60°C for 48 hours.

#### 2.6.3.2 Imaging

*Scanning.* Brains were scanned in a micro-CT scanner (Skyscan 1172, Bruker), with a ten megapixel detector. A Hamamatsu (100/250) x-ray source metal was used, scanned at 100 kV and 100 µA with a 1.45 second exposure time, and took 900 projections averaging 4 frames per projection. A Cu+Al filter was used to reduce the edge artefacts created by the edges of the brain.

*Reconstruction.* Samples were reconstructed into a Z-stack of images with NRecon (v 1.7.0.4) and saved in TIFF format. Stack images were rotated in X, Y and Z directions in Fiji to align sagittal slices to the Allen Brain Atlas. Tetrodes could be localised to a brain region by visually cross referencing sagittal CT slices with the atlas sagittal segmentation guide.

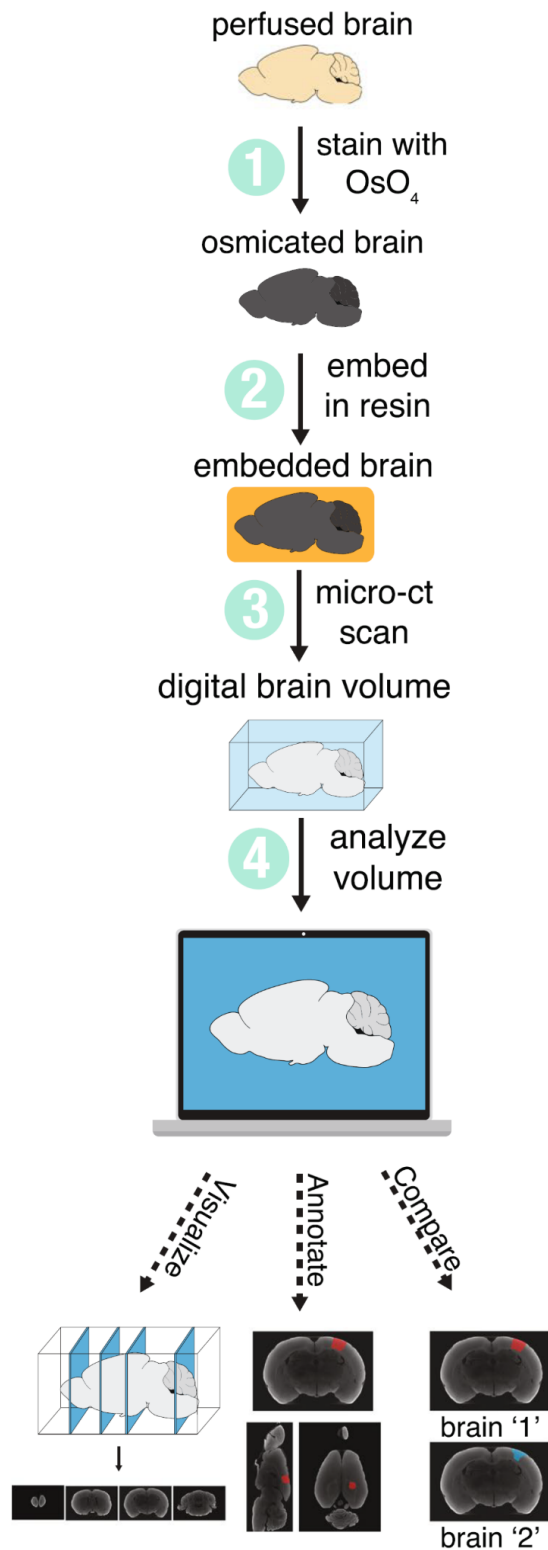


**Figure 28. Step for processing and analysing a brain using Micro-CT imaging.** Figure taken from Masis et al. 2018.

#### 2.6.4 Cresyl violet staining

Following perfusion fixation, brains were removed and placed in 4 % PFA in 0.1 M PB for 12 hours followed by 30 % sucrose in PBS for 48 hours. A freezing microtome was used to cut 50 µm sagittal slices, which were mounted on polarised slides. Sections were left to dry out for 24 hours before being based in xylene before rehydration in varying concentrations of ethanol (100 %, 90 % then 70 % for 1-2 minutes each). Sections were placed in Cresyl violet for 2 mins before additional washing and dehydration (70 % then 90 % for 1.5 minutes each followed by two 30 second washes in 100 %). Sections were then placed in xylene and mounted with Dibutylphthalate Polystyrene Xylene (DPX). Imaging of sections was performed with a slide scanner (Zeiss Axioscan Z1).

## 2.7 Data Processing and Analysis

### 2.7.1 Overview

Data was collected and analysed five days a week throughout the navigation experiments. In order to facilitate the training of the mice and the optimal collection of a variety of spatial-modulated cells, the previous day's session required a basic analysis. This basic analysis provided important feedback to the experimenter including a range of plots and graphs conveying the spatial behaviour of the mice and the cells recorded. To produce this analysis in a timely manner, a user-friendly Python repository was developed and is publicly available on GitHub ([https://github.com/MattNolanLab/in\\_vivo\\_ophys\\_openephys](https://github.com/MattNolanLab/in_vivo_ophys_openephys)). For detail on the data management of the pipeline see. (Gerlei 2019).

This section will detail the processing pipeline for raw spatial and electrophysiological data into single unit activity of putative neurons as is graphed in [Figure 29](#).

### 2.7.2 Pre-processing

To isolate neuron spikes from electrophysiological data, automated spike sorting was performed using MountainSort 3 (v 0.11.5 and dependencies) (Chung et al. 2017). For optimal performance, first the raw voltage channels were passed through a bandpass filter between 600-6000 Hz to remove noise outside the range of a typical action potential. Secondly, spatial whitening was performed over all 16 channels to remove correlated noise. This step removed voltage fluctuations recorded across all channels that are unlikely to originate from a single neural source but are rather movement-related or environmental noise.

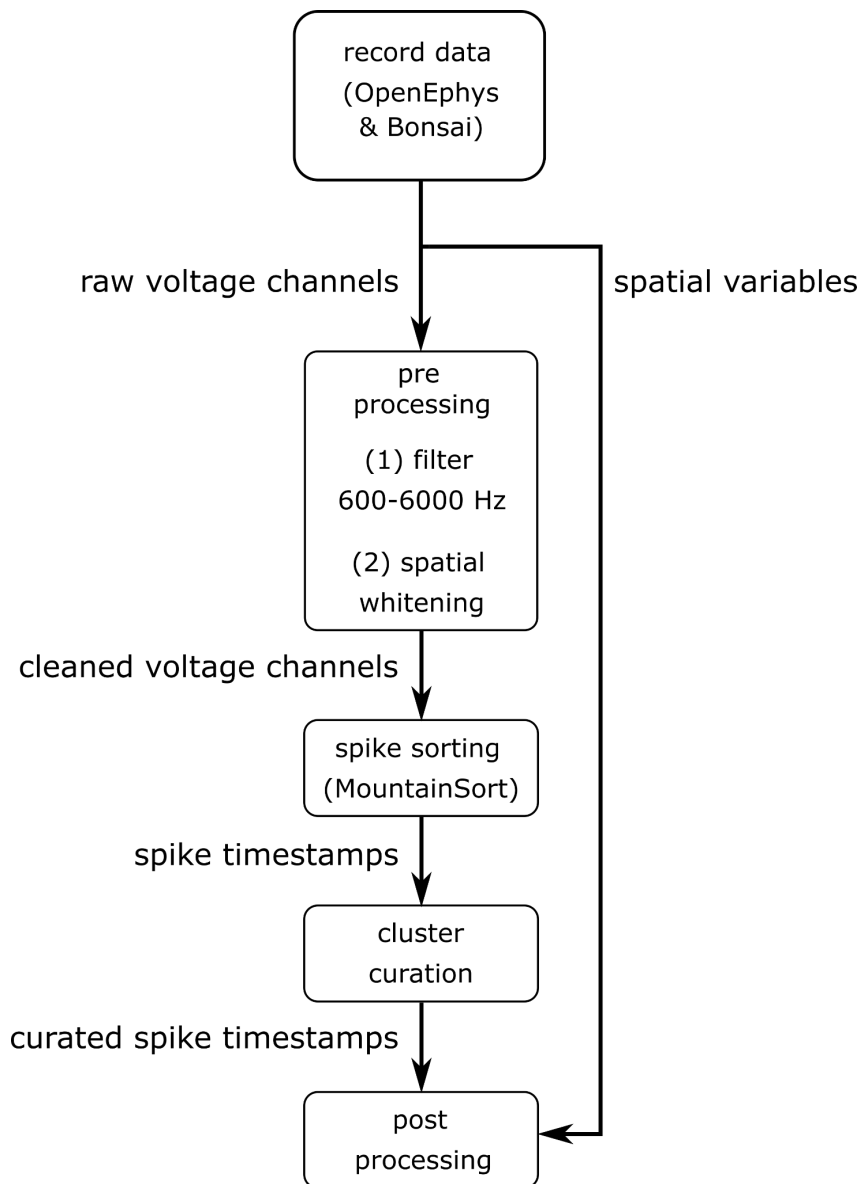


**Figure 29. Python pipeline for analysing electrophysiology recordings**

### 2.7.3 Spike sorting

Neural spike detection and clustering into separable neural units was performed by MountainSort 3. Neuron spiking events were defined as peaks in the cleaned voltage channels with an amplitude greater than three standard deviations above the mean and at least 0.33 ms apart from other events detected on the same channel.

Clustering of these events was performed using the ISO-SPLIT spike sorting algorithm (Chung et al. 2017). Firstly, the corresponding waveforms for neural events were extracted from the cleaned voltage channel and the first 10 principal components taken for clustering. The ISO-SPLIT algorithm is based on two key assumptions about cluster distributions in a feature space, (1) each cluster arises from a density function that, when projected onto any line is unimodal and has a single region of highest density and (2) any two clusters can be separated by a hyperplane in the feature space. The algorithm first over-clusters waveforms and then performs pair-wise checks, reclustering where necessary until all groupings meet the assumptions. The algorithm completes with a set of unique cluster labels for the detected spike events. These spike times and cluster labels are outputted for curation.

### 2.7.4 Curation

To remove clusters unlikely to have originated from true neuron spiking events, a set of validated metrics were used to evaluate cluster quality (Chung et al. 2017). Clusters that had isolation > 0.9, noise overlap < 0.05 and peak signal-to-noise ratio > 1 were accepted for further analysis. No constraint was placed on firing rate to accommodate the possibility of cells firing in one environment but not the other.

It was observed that artefacts originating from licking events often passed curation. As the waveforms of these artefacts were typically much larger in amplitude than other curated clusters, clusters with waveforms with peak amplitudes above 500  $\mu$ V were rejected from further analysis.

### 2.7.5 Post-processing

Spike timestamps and their associated cluster labels were passed into post-processing with the time-synchronised spatial variables to analyse the cluster's spatial firing properties. For daily analysis during the experiment, graphical plots were generated to provide feedback to the experimenter about the behaviour of the mice performing the spatial tasks and the firing properties of the curated clusters. For the VR task, this included speed profile plots across trial types, stop raster plots, waveform plots, spike raster plots, and firing rate plots. For the open field task, additional plots included trajectory maps, coverage maps and spatial autocorrelograms. This provided information about the mouse's motivation and task aptitude as well as whether the tetrodes were localised in a brain region populated with spatial-modulated cells.

Spatial metrics were also calculated daily to indicate the presence of grid cells, border cells, head direction cells, speed cells and theta-modulated cells (Hafting et al. 2005; Solstad et al. 2008; J. Taube, Muller, and Ranck 1990; Kropff et al. 2015; Kornienko et al. 2018). As grid cells are the main focus of this paper, tetrodes were lowered daily by 50 µm until a grid cell was found, this location was recorded for two days before it was lowered in search of more grid cells.

### 2.7.6 Remote computing services

*Eddie and Eleanor.* Remote computing services were utilised to process the data in this thesis using Eddie and Eleanor, a University of Edinburgh hosted linux computer cluster and research cloud service respectively. A 16 core CPU, 96 GB RAM virtual computer hosted by Eleanor was remotely controlled via a secure shell procedure (SSH) through a Python IDE, PyCharm V2019.2.4. Where highly parallel computer processing was required, such as when shuffling open field spike times to generate shuffled open field scores, Eddie was accessed via terminal and remote SSH. Both services had electronic access to the DataStore server where the raw data and analysed data was held.

## 2.8 Identifying spatial cells in open field and virtual reality environments

Spatial cells are classically defined by their spatial coding properties when recorded from animals exploring or completing a spatial task in a 2D environment. This creates an obvious challenge when the spatial task is solely 1D. To get around this issue, mice are recorded in spatial arenas in a single recording day, one 30 minute session in an open field arena and one 30 minute session head restrained on a treadmill running through a virtual linear track. The former provides a baseline recording for capturing grid cell activity with the primary function of classifying grid cells, whereas the latter provides a recording of grid cell activity while the mouse performs a 1D spatial memory task.

### 2.8.1 Concatenated spike sorting

There are two contrasting approaches to identifying spike clusters that originate from the same neural source between two separate recordings within electrophysiology. The first and most commonly used approach is cluster matching. Recording sessions are spike sorted independently from one another and the firing properties of the resulting curated spike clusters are statistically compared to determine whether the clusters can with confidence be ascribed to the same neural source. The second approach termed concatenated sorting, involves spike sorting both recording sessions together to cluster spikes within the same feature space across sessions. This method was preferred as it removed the parameterisation and statistical thresholding of firing properties required in cluster matching, (see Campbell et al. 2018).

Concatenated sorting begins with the concatenation of the raw voltage traces across electrodes. With a 16-channel (4 tetrode) design each channel voltage trace from the first session was appended with the corresponding channel in the second session, creating 16 voltage traces corresponding to roughly 60 minutes (30 minutes x 2 recording sessions). Preprocessing steps and spike sorting proceeded as described in [2.7](#). Spike clusters spanning both sessions were curated together before being split back into session-specific firing timestamps. This allowed the cluster IDs produced during spike sorting to be shared between open field and virtual reality neural recordings and provide a one-to-one mapping of the spatial firing properties between recording sessions. A grid cell recording processed with concatenated sorting is shown in [Figure 30](#).

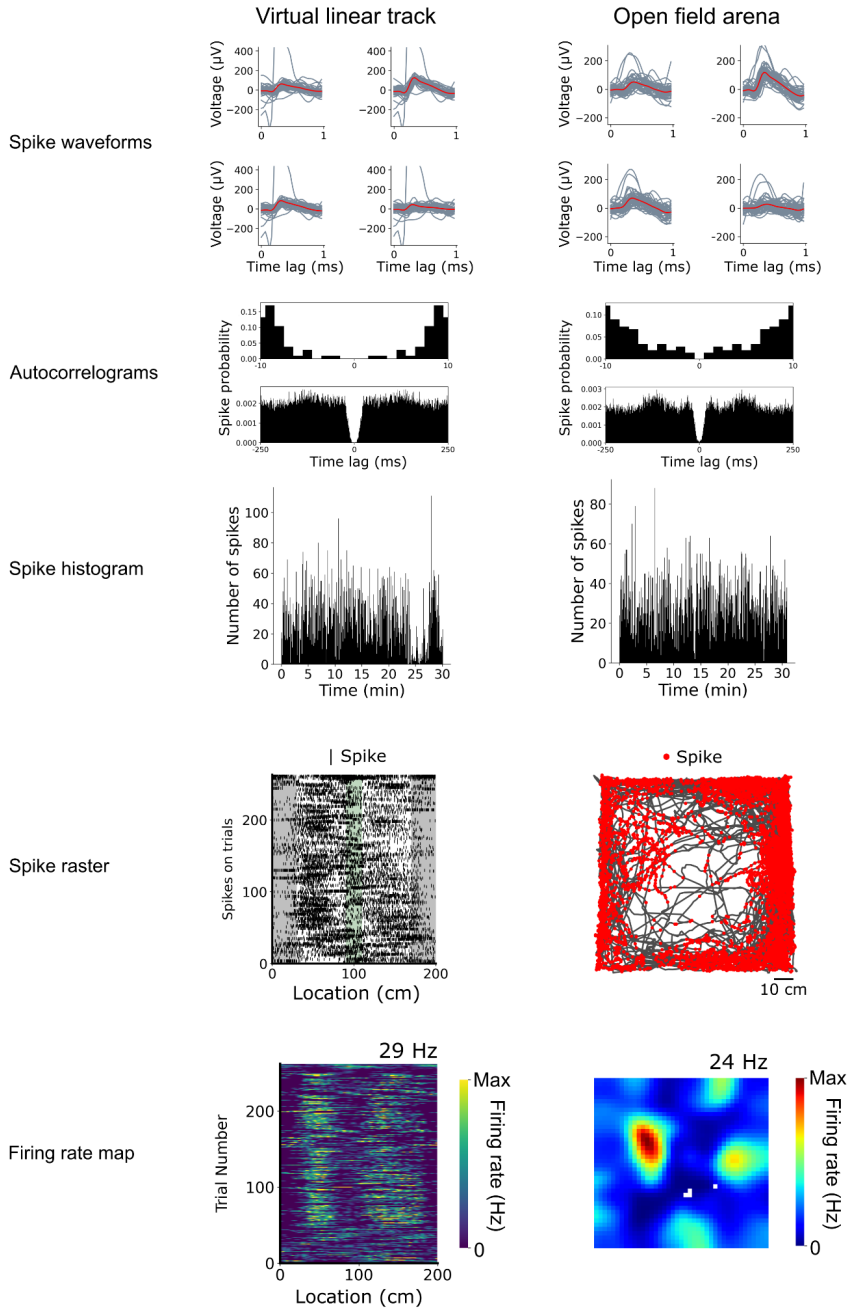


**Figure 30. Example grid cell from concatenated spike sorting of two different electrophysiological recordings.** Spike waveforms and autocorrelograms show the same waveform shape and temporal firing properties. This allows the spatial firing properties to be assessed with confidence that the spikes come from the same neural source. From top to bottom, plots are showing: 30 example spike waveforms from the cluster, the temporal autocorrelogram, spike histogram across the session, spike raster plot and firing rate map. For the firing rate maps, the colour bars are scaled between 0 and the max firing rate which is given above the plot.

## 2.8.2 Classification of cell types in the open arena

To classify cells based on their activity in the open arena, methods in (Diehl et al. 2017) were followed. Cells were classified into one of five hierarchically organised functional cell types: grid > border > spatial > head direction > non-spatial. Cells were assigned to the highest cell type in the hierarchy for which their corresponding identity metric was greater than the 99<sup>th</sup> percentile of the same scores from 1000 shuffled datasets. For example, a cell with grid score above the 99<sup>th</sup> percentile was classified as a grid cell irrespective of scores in other categories. To generate shuffled spike data, a single value from a uniform distribution between 20-580 seconds was drawn and added to the timestamp of each spike. Spike times that exceeded the recording length were wrapped around to the start of the session. Spike locations were recomputed from the shuffled spike times and spatial scores calculated similar to measured data. Using this method, 1000 shuffles per cell were generated and the 99<sup>th</sup> percentile of the scores used as a threshold for belonging to the five cell types.

Established scores were used for grid, border, head direction and spatial stability (Hafting et al. 2005; Solstad et al. 2008; Skagg et al. 1993). Grid scores were defined as the difference between the minimum correlation coefficient for rate map autocorrelogram rotations of 60 and 120 degrees and the maximum correlation coefficient for autocorrelogram rotations of 30, 90 and 150 degrees. The firing rate map was calculated by binning spikes into 2.5 cm bins and dividing by the total time occupied in each bin and then smoothed with a Gaussian kernel (standard deviation = 2 bins). Autocorrelograms were calculated by sliding the rate map over all X and Y bins and calculating a correlation score. Fields were detected in this autocorrelogram by converting it into a binary array using 20 % of the maximal correlations as a threshold. If the binary array had more than 7 local maxima, a grid score was calculated. Correlations between the rotated autocorrelograms were then calculated using only a ring containing the 6 local maxima closest to the centre of the binary array and excluding the maximum at the centre. The ring was detected based on the average distance of the 6 fields near the centre of the autocorrelogram (middle border = 1.25 \* average distance, outer border = 0.25 \* average distance).

To calculate border scores (Solstad et al. 2008), firing fields were identified from the firing rate map by collecting neighbouring bins with firing rates greater than 30 % the maximal firing rate and covering at least 200 cm<sup>2</sup>. For each putative field, the mean firing distance  $d_m$  was computed as the average distance to the wall for each bin, divided by the mean firing rate of the field. To obtain a value between 0 and 1,  $d_m$  was normalised by the shortest distance from the centre of the arena to the wall. The maximal coverage  $c_m$  of a field was

measured as the maximum proportion of field bins occupying any of the four edges of the firing rate map. The border score was then given by

$$(4) \quad b = \frac{c_m - d_m}{c_m + d_m}$$

To calculate head direction scores, the head direction recorded at times corresponding to firing events were binned into 360 bins between 0 and  $2\pi$  and was normalised by the duration of time spent occupying each directional bin. This polar histogram was then smoothed with a rolling sum with a window size of 23 degrees. The head direction score is the length of the mean vector of this polar histogram. To obtain this length, the X and Y components are computed by first calculating dx and dy in a unit circle (radius = 1) in steps of 1 degree as

$$(5) \quad dx = \frac{\cos(\text{angle})}{\text{radius}}, \quad dy = \frac{\sin(\text{angle})}{\text{radius}}$$

The head direction score is then given using the Pythagorean theorem by

$$(6) \quad \sqrt{(\Sigma \text{polar Histogram} \cdot dx)^2 + (\Sigma \text{polar Histogram} \cdot dy)^2}$$

For assessing spatial stability, two separate metrics were used, spatial information and the within-session spatial correlation to identify spatial cells (Diehl et al. 2017; Hafting et al. 2005; Sargolini et al. 2006; Boccaro et al. 2010; Hardcastle et al. 2017). The spatial information per spike was calculated as

$$(7) \quad \sum_{i=1}^N P_i \left( \frac{R_i}{R} \right) \cdot \log_2 \left( \frac{R_i}{R} \right)$$

where i indexes a position bin in the firing rate map, N is the number of bins,  $P_i$  is the occupancy probability,  $R_i$  is the firing rate in the bin, R is the mean firing rate. The within-session spatial correlation is calculated by computing the Pearson correlation between the firing rate map computed from the first half session and the second half session. Bins that were not visited in both halves were excluded from the calculation.

# Self-localisation behaviours in a VR linear location task

## 3.1 Introduction

To investigate the functional roles of spatial cells in self-localisation behaviours, a behavioural task that distinguished beaconing and path integration-based behaviours was required. Tennant et al. (2018) introduced a virtual reality-based linear location estimation task that requires mice to estimate their location along a linear track and execute stops at a specific location to receive a soy reward. Mice could complete this task via beaconing when salient visual cues marking the reward zone were available. Alternatively, mice could adopt a path integration-based strategy as the reward zone was always a fixed distance from the beginning of the track. When the salient visual cue was not present, a path integration-based approach remained the only viable strategy for effective localisation of the reward zone.

The task boasts valuable qualities which makes it well suited to address questions surrounding biological solutions to path integration. The introduction of virtual reality technologies provides the tools for experimenters to design environments where the completion of a spatial navigation task is only possible by employing path integration-based strategies. This is achieved in the VR linear location task by creating an intentionally ambiguous track made up of repeating textures as shown in [Figure 25](#). As the track repeats the same textures from track locations 30 - 170 cm, the estimation of self-location must be computed as an iterative update by integrating speed estimates over time from a previously-visited landmark. This is because no unique cues exist along the track (except on beacons trials) to correct the mouse's self-location estimate. This would not be the case for a real linear track as unique cues can not be easily ruled out, even if designed and prepared meticulously. These cues could take the form of imperfections in the material used to make the track, odour cues left by the mouse itself such as urine or even non-perfectly uniform lighting across the length of the track. In the virtual track design however, these issues do not arise. Material imperfections are only possible on the concave projector screen or the treadmill, but these cannot be associated with any specific location on the track. Odour cues are possible on the treadmill however the circumference of the treadmill (~63 cm) and the virtual track length (typically 200 cm) are not compatible for tracking any specific track location.

Tennant et al. (2018) found most mice learnt the self-localisation task within the space of two weeks, stopping selectively at the reward zone on both beacons and non-beacons trials. This was verified with replications of the study by myself in this chapter. Mice performed

better on beaconsed trials compared to non-beaconsed trials suggesting while mice were adopting a path integration-based strategy (at least on non-beaconsed trials), the visual cue available on beaconsed trials was being utilised. Performance typically fluctuated throughout training and between trial types, presumably due to changes in engagement fuelled by reward motivation and attention. The variation in trial outcomes afforded comparisons of spatial firing properties under different behavioural outcomes.

The goal for this chapter is to demonstrate mice learn to use a path integration and beaconsing navigation strategy to solve a linear location task and to outline changes I made to the behavioural task to increase the information provided about path integration based behaviours. The behavioural protocol taken from work by Tennant et al. (2018) adopted an interleaved trial delivery of beaconsed and non-beaconsed trials at a ratio of 4:1. As work in this thesis looks to address the activity of spatial cell types during both beaconsed and path integration-based behaviour, this ratio was amended in favour of more non-beaconsed trials than beaconsed trials. Under this scheme, mice completed more non-beaconsed trials however completed a smaller percentage of the total non-beaconsed trials. This afforded a greater sampling of the behaviour on non-beaconsed trials which provided a greater statistical power to compare neural activity under different trial outcomes in the following chapters.

## 3.2 Methods

Materials and methodologies used for this experiment are as described in Chapter 2. While behavioural analysis is the sole focus of this chapter, it is important to note the analysis presented comes from mice which have been surgically implanted with a tetrode microdrive and have undergone the same behavioural training procedures.

### 3.2.1 Subjects

15 male wild type C57BL/6NCrl mice were obtained (Charles River) and surgically implanted between the ages of 10-15 weeks. Male mice were chosen over females as the increased size of males afforded more space on the skull to implant and attach the tetrode microdrive. Data from 12 of these mice are shown in the chapter. One mouse was culled during habituation due to the microdrive being loose and becoming a danger to the animal's wellbeing. Two further mice were excluded because they were showing visible signs of distress on the VR treadmill and did not improve. Mice were trained and handled alone by the author, Harry Clark. In [3.3.2](#), an additional 6 mice (making 18 in total) were used as a baseline measurement for the default trial type ratio. These mice were trained by Sarah Tennant (1), Junji Hua (1), Wannan Yang (2) and myself, Harry Clark (2).

### 3.2.2 Data analysis

Behavioural analysis was performed in Python 3.8 and statistics calculated using the Scipy and Statsmodal modules. It should be noted that only fully balanced within-subject designs are supported in Statsmodal (v 0.14.0) for ANOVA calculations, as such, data is ejected for unbalanced data samples. For example, if mice did not complete 30 training sessions, data was ejected from the last day in which there was a completed training session for all mice.

### 3.2.3 Quantification of spatial behaviours

The linear location task can be thought of in terms of a reinforcement learning paradigm. Mice are encouraged to stop at a specific location to receive a reward and may receive many rewards by completing more trials throughout the experiment. To speed up the learning of a rewarded location on the track, a beaconsed cue is placed at the reward zone for the majority of trials. To quantify this spatial learning, stops (as defined in [2.5.2.1](#)) and speed profiles are used to disambiguate a spatial behaviour over naive exploration. A mouse performing a clear stopping strategy is one that stops at specific locations on the track over many trials, such that compiling the stops into a histogram reveals peaks above random chance. This chance level threshold is calculated by shuffling the location of all stops to

random locations and computing the histogram peak. This is repeated 1000 times and peak amplitudes collated. The 99<sup>th</sup> percentile is taken as the chance level threshold and is computed independently for each trial type. Only fully completed trials are included. [Figure 31](#) shows the spatial learning profile of an example mouse (M11). While enumerating stops is a helpful metric, additional reward-related stops are often picked up when the mouse is receiving the reward. To overcome this, the first stop of each trial is taken and enumerated in [Figure 32](#). Speed profiles are also used to investigate task performance, as the selectivity for the reward zone can be measured by weighting the relative speeds within and outside the reward zone, as shown in [Figure 33](#).

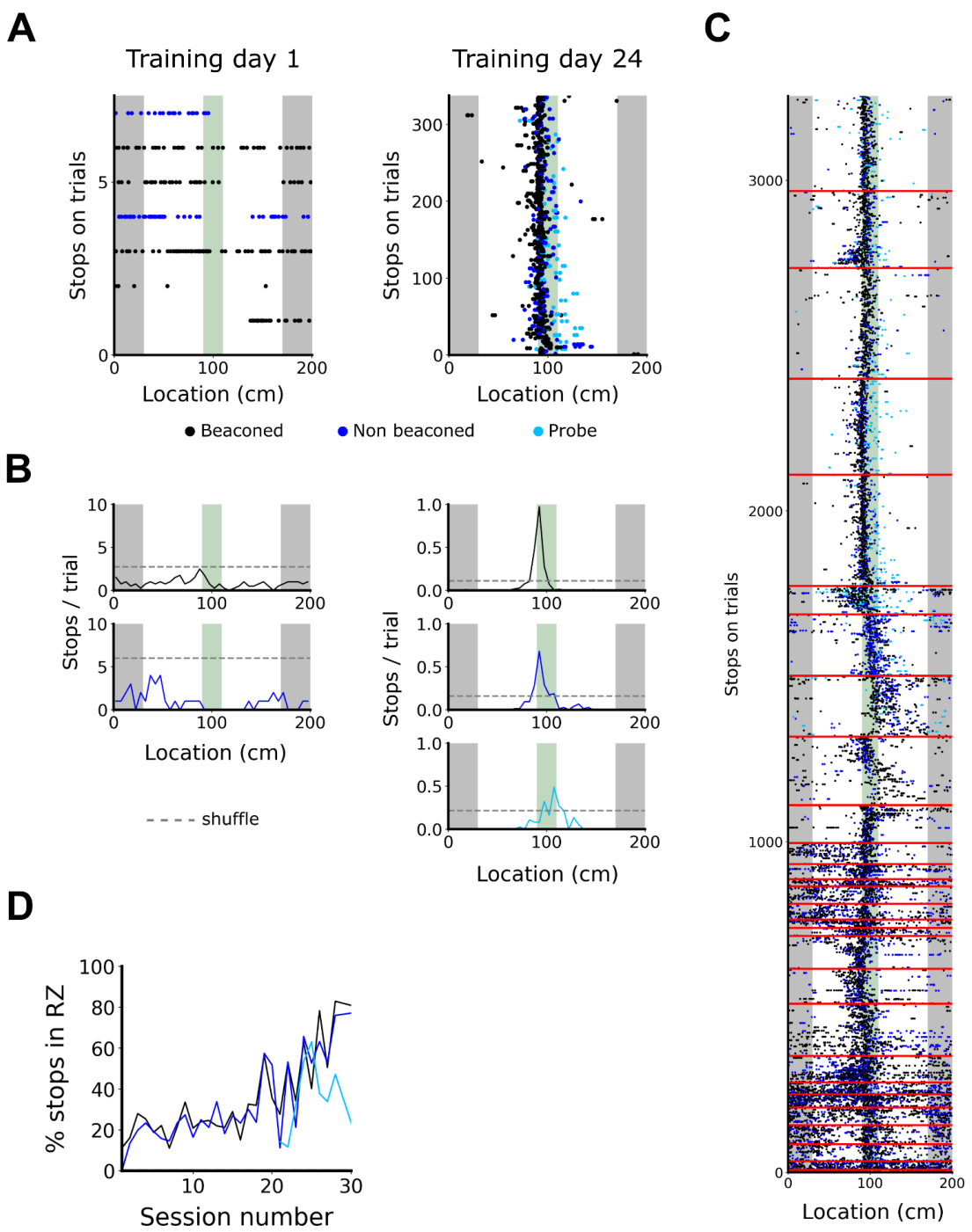


**Figure 31. Stopping behaviour of an example mouse M11.** (A) Stop raster and (B) stop histogram on training day 1 and 24. Grey line denotes the shuffled 99<sup>th</sup> percentile for histogram peaks. (C) Stop raster from training day 1 to 30, red horizontal lines denote the start of a new training day. (D) Percentage stops registered within the reward zone as a function of training day.

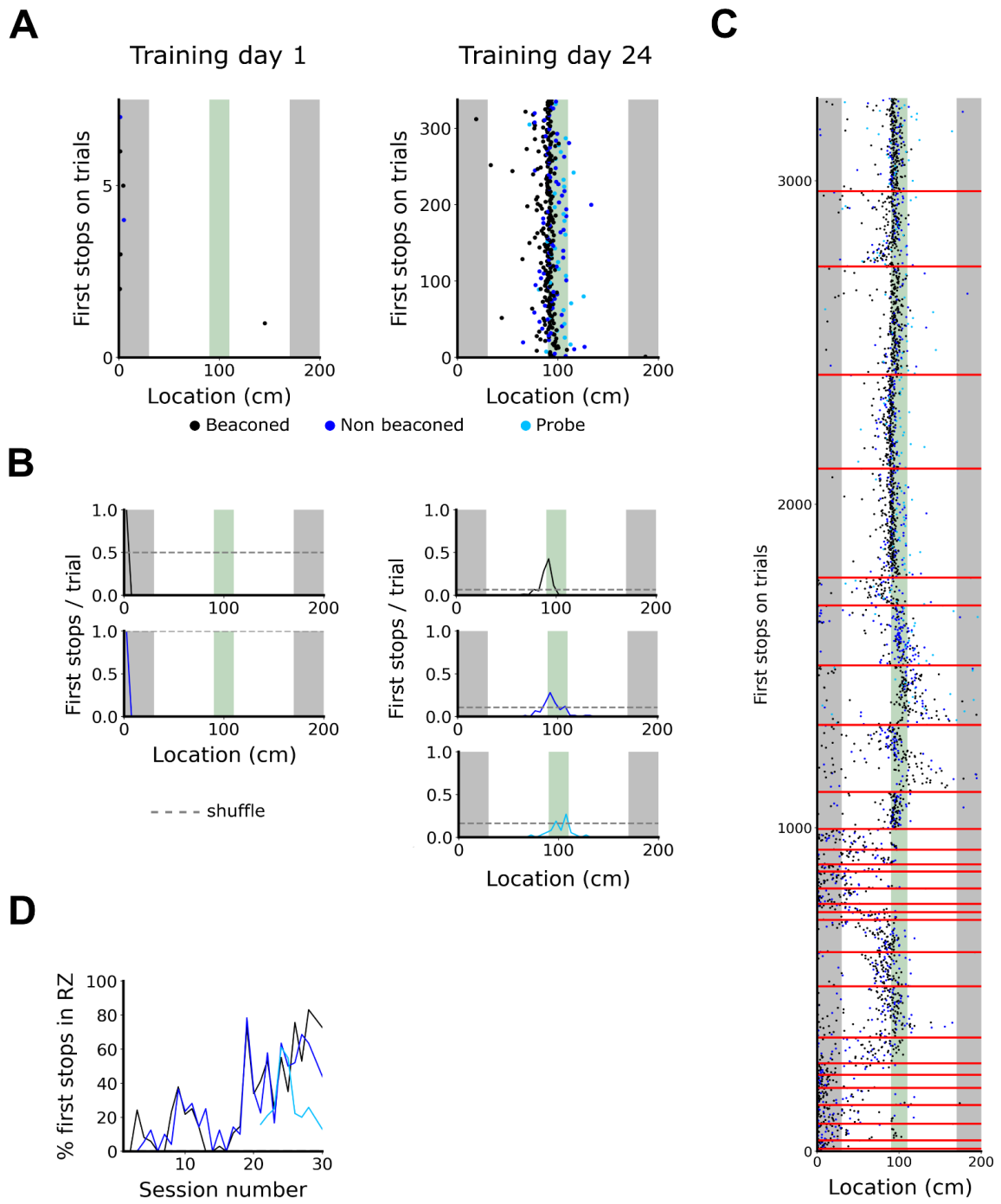


**Figure 32. First stop behaviour of an example mouse M11.** (A) First stop raster and (B) first stop histogram on training day 1 and 24. Grey line denotes the shuffled 99<sup>th</sup> percentile for histogram peaks. (C) First stop raster from training day 1 to 30, red horizontal lines denote the start of a new training day. (D) Percentage first stops registered within the reward zone as a function of training day.

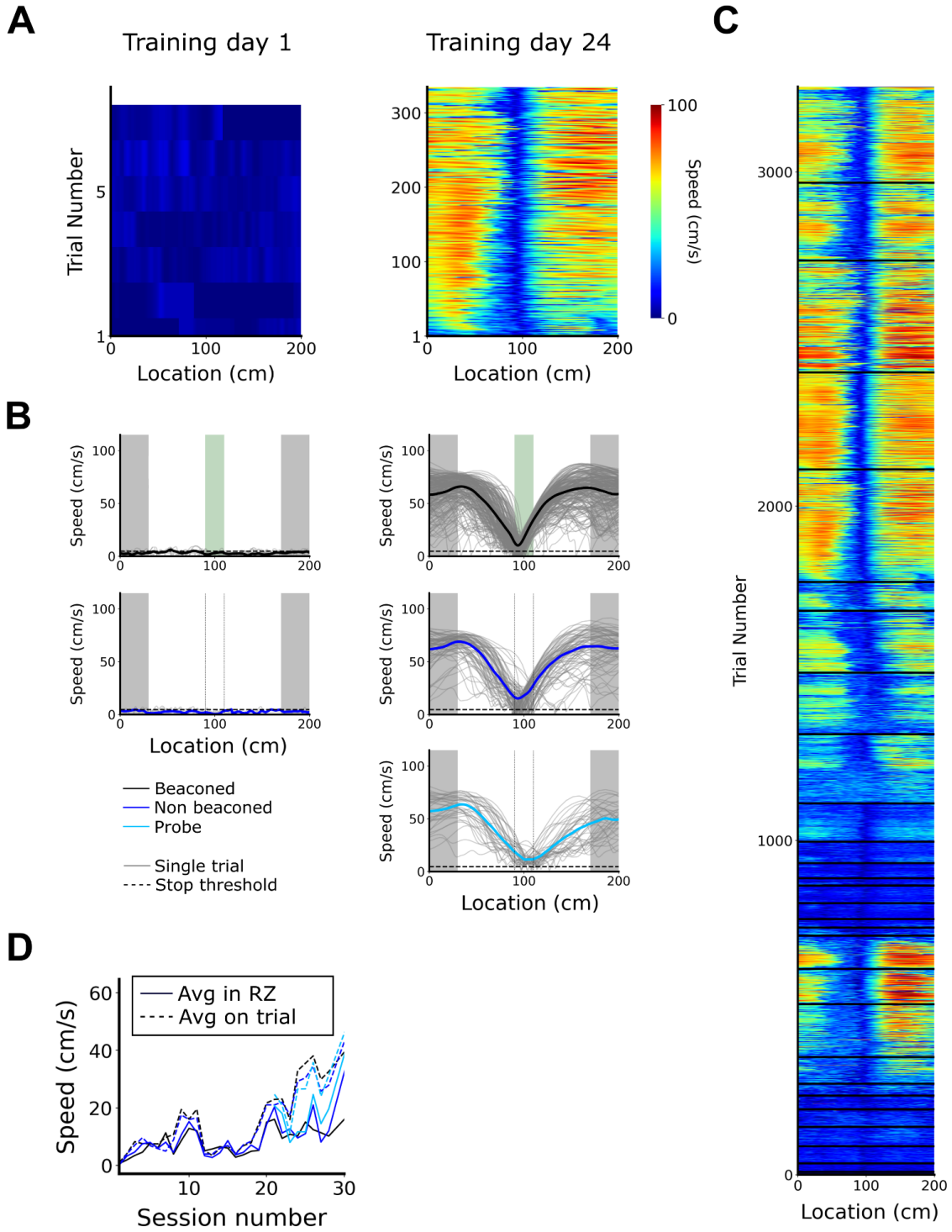


**Figure 33. Speed profiles of an example mouse M11.** (A) speed heatmap and (B) average speed profiles on training day 1 and 24. (C) Speed heatmap from training day 1 to 30, black horizontal lines denote the start of a new training day. (D) Average trial speed across training days (left) and the differential between the track speed and speed in the reward zone (right). Note that based on the variation of the stops, and the smoothing of the speed profiles, the mean minimum speed can appear above the stop threshold.

It is clear this mouse quickly learns a stopping strategy within several days which is biassed to the reward zone for both beaconed and non-beaconed trials. At the beginning of training, trial speeds are slow, and in the case of this example mouse, is below the stop threshold on the first day of training. As such, most locations along the track qualify as the mouse having stopped. By training day 24, the mouse achieves an average trial speed of approximately 40 cm/s. When comparing the average trial speeds with the average speed within the reward zone, it can be seen these two metrics drift apart throughout training, demonstrating the mouse is adopting a stopping strategy biassed to the reward zone. The discrepancy between trial speeds and reward zone speeds is also present on probe trials, showing the difference cannot be a feature of the dispensing of a reward. Engagement in the task fluctuates over the course of training and within training sessions. As can be seen in [Figure 31](#), [32](#) and [33](#), trial speeds at the beginning of sessions are typically slow and many stops are registered. As more trials and sessions are completed, the mouse runs quicker which can generally be explained by the mouse getting more comfortable running on a treadmill while head-fixed. The mouse also learns to stop exclusively within the reward zone which shows the mouse has learnt the task structure.

### 3.2.4 Classification of trial outcome

Using the registered stops and speed profiles, the performance of any given trial can be quantified. This is important for addressing functional associations between spatial cell types and spatial behaviours because engagement in the task changes throughout a session based on variables unbeknownst to the experimenter. Possible factors include comfort, energy levels or motivation for the reward.

A single trial is classified as a hit when a stop is registered within the reward zone or a miss when a stop is registered outside of the reward zone or not at all ([Figure 34](#)). This however, does not accurately capture all the nuances of task engagement. A mouse moving below the stop threshold will register a stop within the reward zone without demonstrating any navigational selectivity to the reward zone. Similarly, a trial in which a mouse narrowly misses the reward zone would be categorised equally to a trial in which the mouse runs at full speed through the reward zone. To better classify trials based on task engagement, miss trials were split into near-hits (tries) and run-throughs (runs). Initially classified misses were split by comparing their average speeds in the reward zone to hit trials. The 95<sup>th</sup> percentile of average speeds in the reward zone for hit trials in a single session was used to discriminate between tries (< 95<sup>th</sup> percentile speed) and run trials (> 95<sup>th</sup> percentile speed).

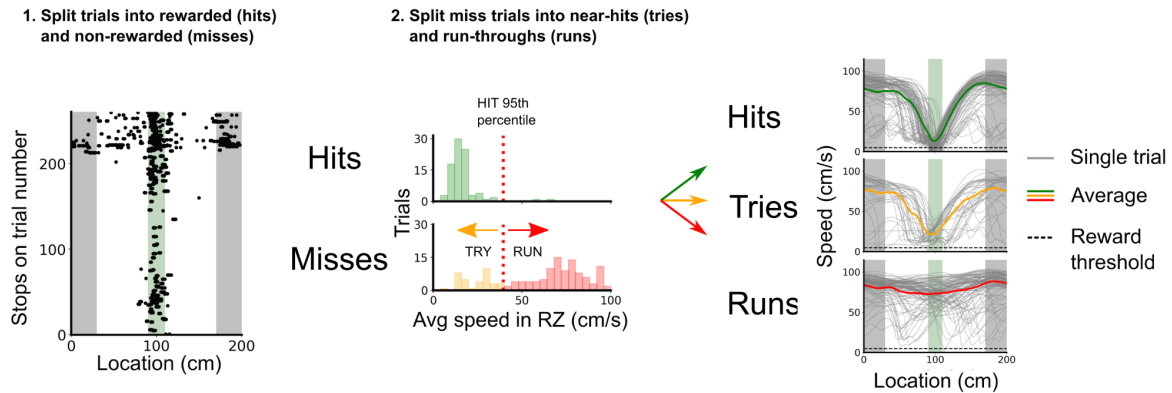


**Figure 34. Example classification of trial outcomes.** Trials are classified into hits, tries and runs, based on stopping locations and the speed profile on a given trial. First, trials are classified into hits and misses based on whether a stop was registered in the reward zone or not. Next, a distribution of the average speeds in the reward zone is drawn for hit and miss trials, the 95<sup>th</sup> percentile of the hit average speeds in the reward zone is used to split the miss trials into near hits (tries) and run-throughs (runs). Finally, slow trials are removed to better discriminate trial outcomes based on the mouse's engagement.

It is important to note that at low running speeds, a hit trial does not correspond with a spatially selective stopping strategy for the reward zone. For example in Figure 31 and 32, the example mouse runs below the stopping threshold on training day 1. As these trials qualify as hit trials, it benefits the evaluation of task performance to consider which hit trials are slow or fast. Figure 35A shows the distribution of trial speeds outside of the reward zone. The speed profiles of the corresponding bins are shown in Figure 35B. This shows the slowest hit trials do not necessarily correspond to a spatial selective stopping strategy. To overcome this, hit trials corresponding to an average track speed greater than 20 cm/s were considered as fast hit trials, whereas hit trials with average track speeds less than 20 cm/s were considered as slow hit trials.

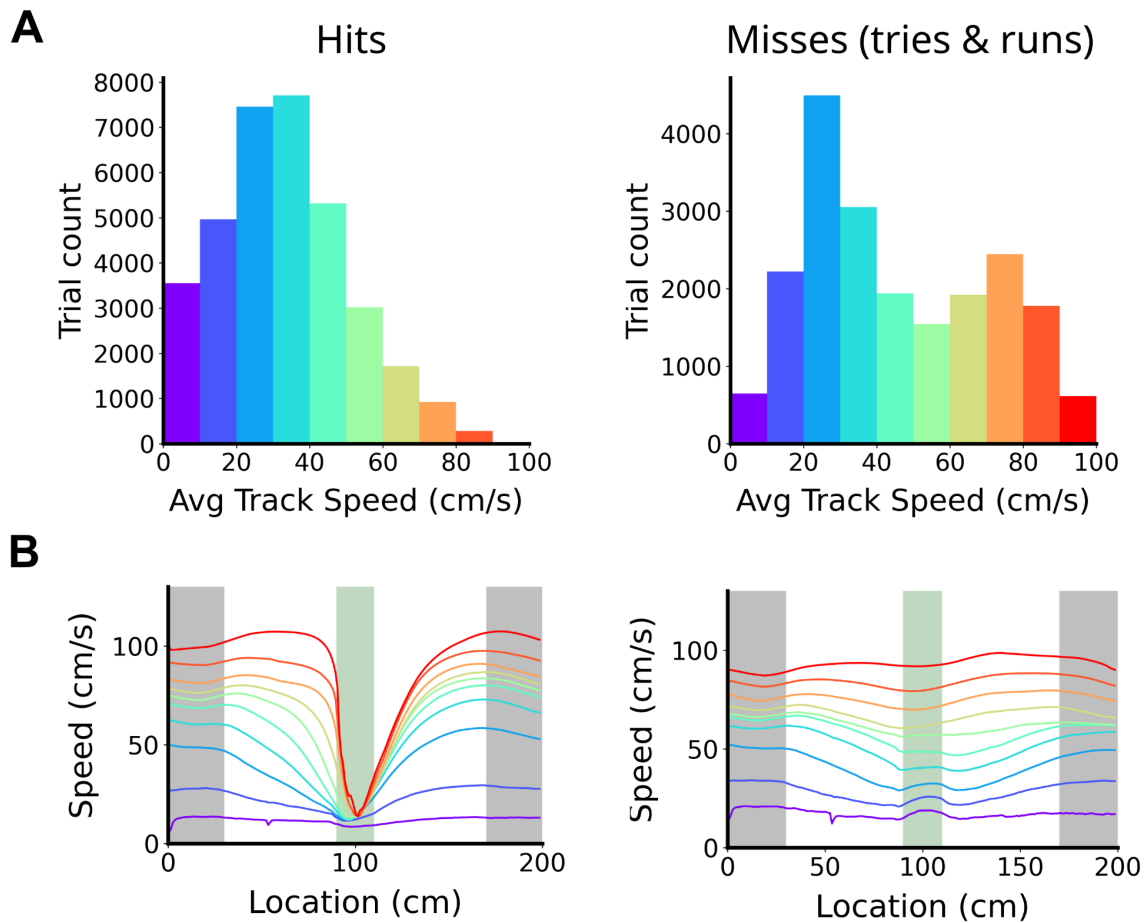


**Figure 35. Distribution of trial speeds.** (A) Distribution of average track speeds for hit and miss trials and the (B) average speed profile binned by the average track speed (shown with the corresponding colour as in A). Below 20 cm/s, the hit speed profiles do not reflect a clear spatial preference for the reward zone. Average track speeds above 20 cm/s are considered fast hits in some analyses.

### 3.3 Results

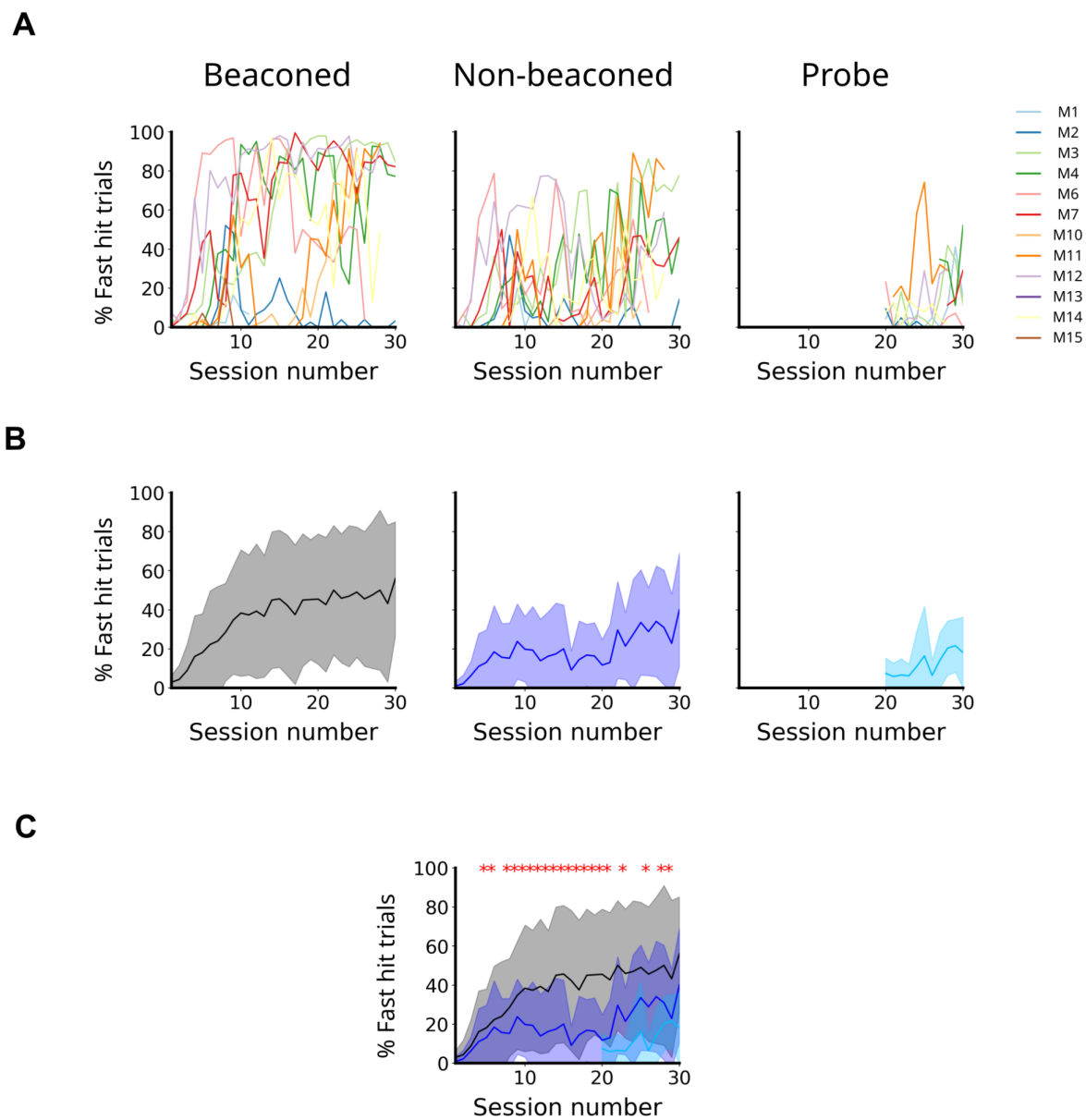
#### 3.2.5 Mice learn to solve a linear location estimation task

##### 3.2.5.1 Performance summary

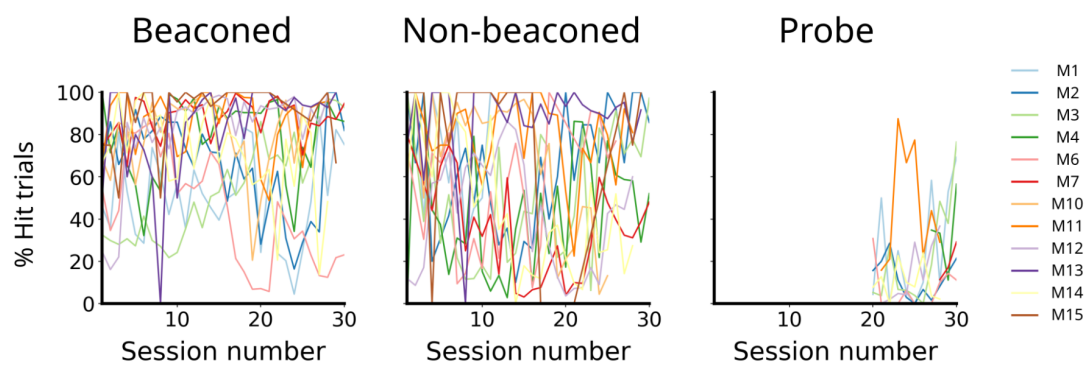
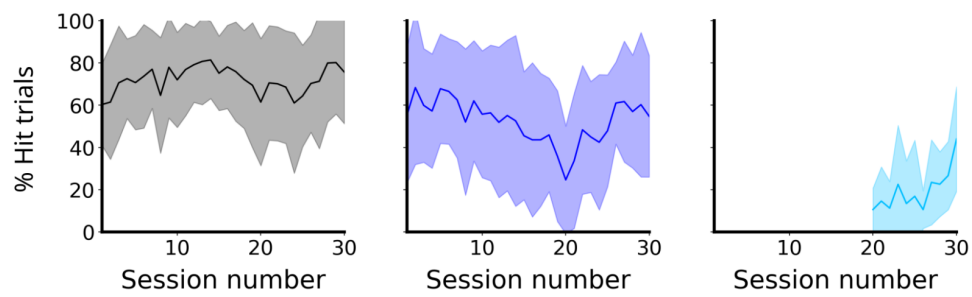
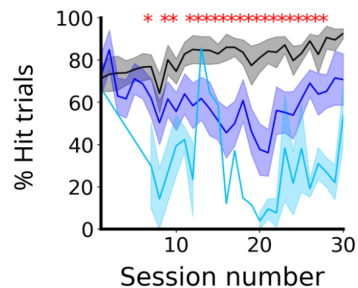
To address whether mice learn the linear location task over the course of training, a repeated-measures one-way ANOVA was used to test the effect of session number on the proportion of fast hit trials. For both beaconsed and non-beaconsed trials, there was a significant effect on the percentage of fast hit trials in a session as a function of training day (beaconsed,  $DF = 24, 168, F = 6.2, P < 1e-12$ ; non-beaconsed,  $DF = 24, 168, P = 0.008, F = 1.9$ ). The proportion of fast hit trials was used as the metric to quantify task performance over any hit trials as mice typically begin the experiment running at low speeds and achieve many hit trials by simply running below the stopping threshold, which as explained in [3.2.4](#) does not necessarily reflect a selective stopping strategy to the reward zone. Consistent with this, using the proportion of hit trials as a metric for task performance yielded a non significant effect of training day (beaconsed,  $DF = 24, 168, P = 0.65, F = 0.87$ ; non-beaconsed,  $DF = 24, 168, P = 0.46, F = 1.0$ ). [Figure 36](#) and [37](#) shows the proportion of fast hit trials and hit trials changes as a function of training day. Probe trials were not analysed as they were introduced at different time points within the experiment based on the animal's performance however are shown for completeness .

The strategies implemented throughout training might change based on the mice's understanding of the task structure and or their motivation. Beaconsing is a valid solution to stopping on beaconsed trials whereas path integration is the only viable option during non-beaconsed and probe trials. The proportion of fast hit trials was significantly greater on beaconsed than non-beaconsed trials when compared across all training days ( $F = 1144.0, P < 1e-28, N = 309$ , Wilcoxon sign-rank test). To compare between trial types for each training day, multiple Wilcoxon sign-rank tests were used. It was found that throughout the majority of training, performance was greater on beaconsed trials compared to non-beaconsed trials. These tests reveal two features of learning between these different trial types, (1) mice learn the beaconsed task quicker than the non-beaconsed task and (2) once performance plateaus, performance on beaconsed trials is greater than on non-beaconsed trials. The former point can be explained by mice being trained on more beaconsed trials than non-beaconsed trials, whereas the latter might be explained by the beaconsed task being easier to execute as multiple strategies can be utilised.

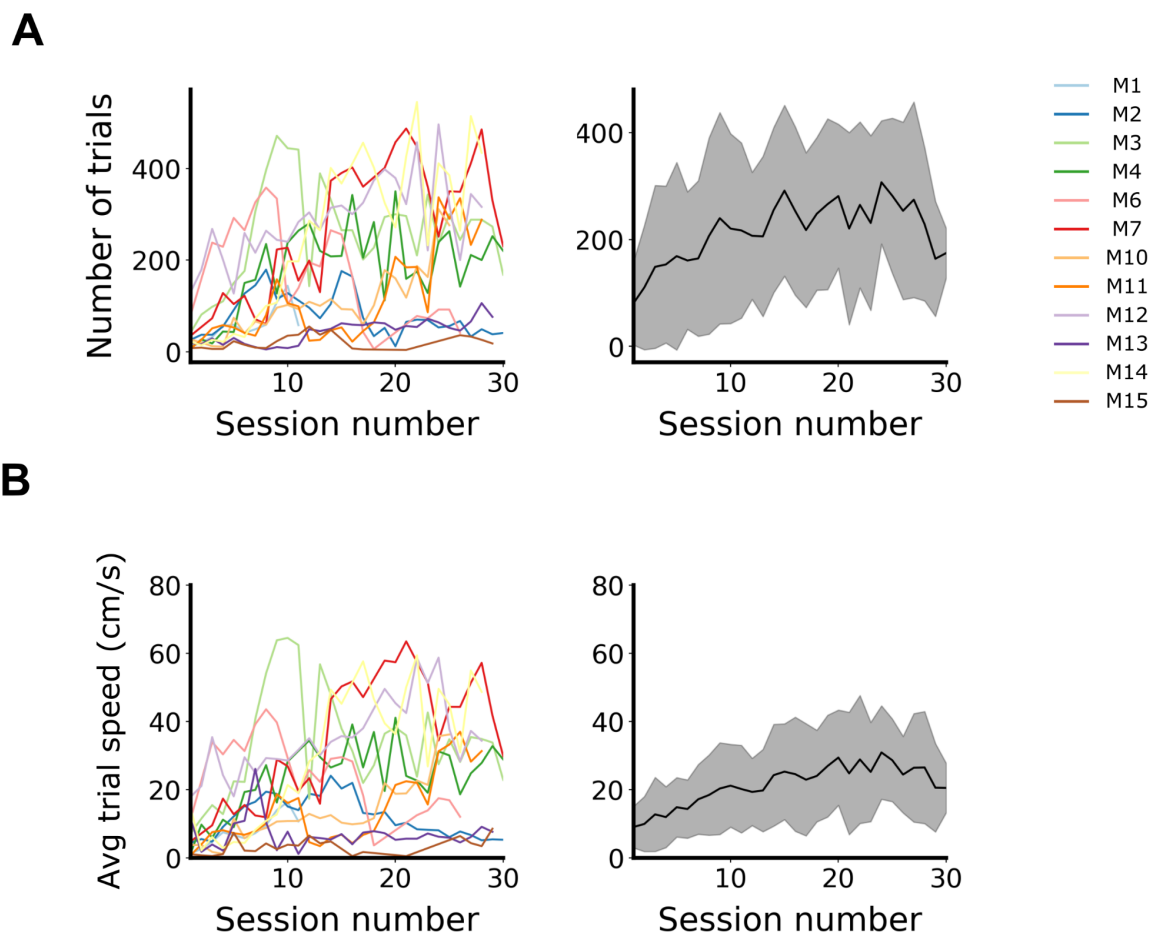
Combined with improved fast hit percentages, [Figure 38](#) shows a clear increase in trials attempted. This might reflect improved mobility on the treadmill as mice became more comfortable running on a treadmill while being head-fixed and presumably attempted more trials to maximise the soy milk rewards as the session length was not constrained to a set number of trials but rather a maximum time of 30 minutes. This was confirmed with a repeated-measures one-way ANOVA to test the effect of session number on the number of trials attempted ( $DF = 24, 168, F = 5.3, P < 1e-10$ ).



**Figure 36. Proportion of fast hit trials across training.** This is shown (A) by mouse, (B) averaged across mice for beacons, non-beaconed and probe trials. (C) Average plots from B are overlaid. Shaded regions represent the standard deviation across animals. Red stars indicate where beacons and non-beacons percentage hit trials are significantly different ( $P < 0.05$ , Wilcoxon sign-rank test).

**A****B****C**

**Figure 37. Proportion of hit trials across training.** This is shown (A) by mouse, (B) averaged across mice for beaconed, non-beaconed and probe trials. (C) Average plots from B are overlaid. Shaded regions represent the standard deviation across animals. Red stars indicate where beaconed and non-beaconed percentage hit trials are significantly different ( $P < 0.05$ , Wilcoxon sign-rank test).

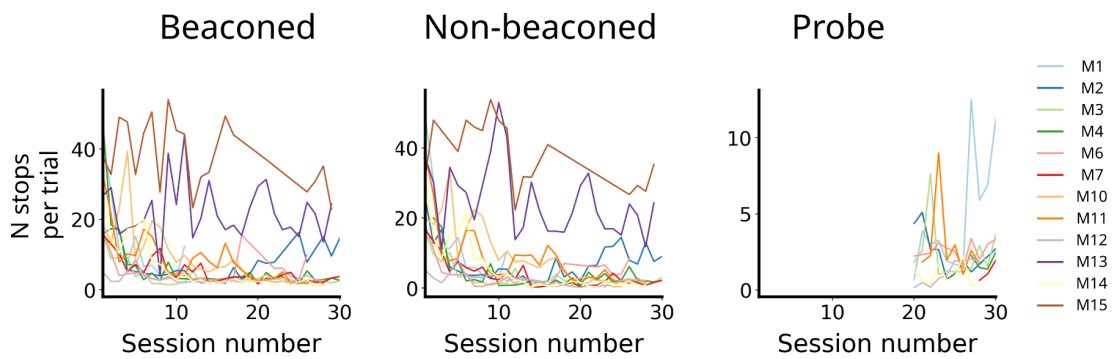
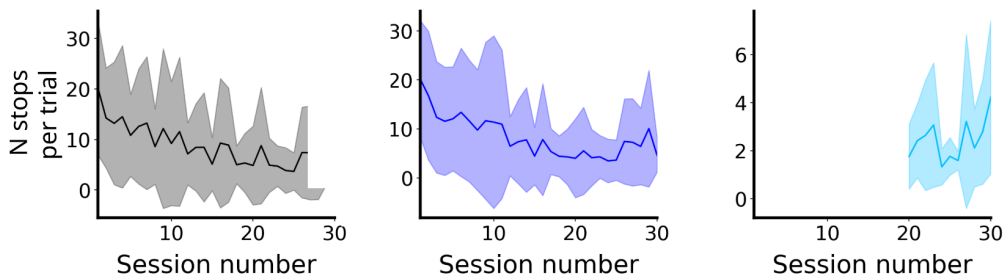
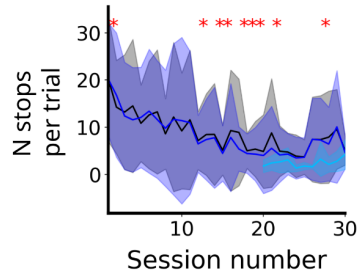


**Figure 38. Trials and trial speeds across training.** (A) Number of trials completed and (B) Average trial speeds as a function of training day by mouse (left plots) and averaged across mice (right plots). Shaded regions represent the standard deviation of across animals.

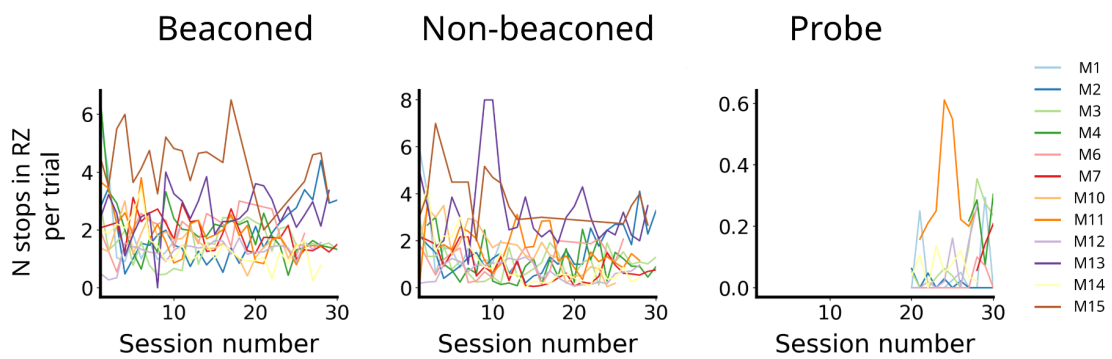
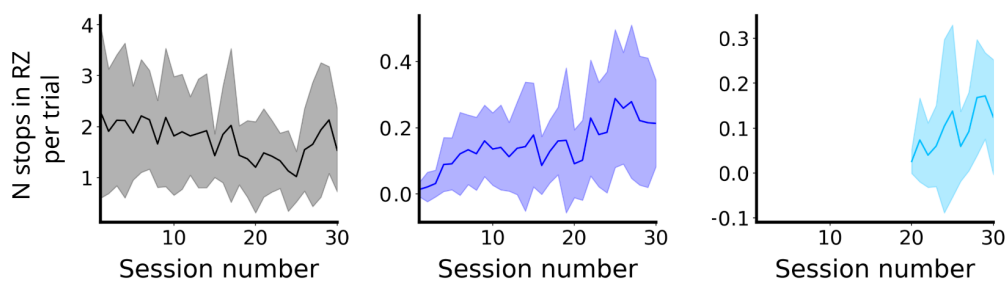
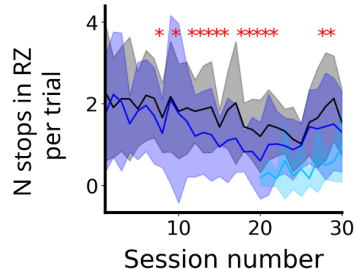
### 3.2.5.2 Mice optimise a stopping strategy over learning

Over what time frame of learning do mice learn the linear location task? To address this, the numbers and relative proportions of stops and first stops within the reward zone were compared across training days and trial types. Consistent with increased trial numbers and average trial speeds over training, the number of registered stops was significantly different across training days (repeated-measures ANOVA, beaconed:  $DF = 24, 268, P < 1e-9, F = 4.9$ , non-beaconed:  $DF = 24, 268, P < 1e-12, F = 6.1$ ; [Figure 39](#)). This was not as clearly shown for stops registered in the reward zone (repeated-measures ANOVA, beaconed:  $DF = 24, 268, P = 0.23, F = 1.2$ , non-beaconed:  $DF = 24, 268, P = 0.04, F = 1.6$ ; [Figure 40](#)), suggesting the stops were maintained across training in the reward zone but not the rest of the track. This is supported by an increased proportion of stops being localised to the reward zone (repeated-measures ANOVA, beaconed:  $DF = 24, 268, P < 1e-12, F = 5.9$ , non-beaconed:  $DF = 24, 268, P < 1e-7, F = 4.3$ ; [Figure 41](#)). Taken together, mice learn to minimise the number of stops attempted on a trial and selectively stop primarily within the reward zone. A truly optimal stopping strategy would see the mouse stop once in the reward zone without any anticipatory stops before the reward. Consistent with this optimisation, the percentage of first stops within the reward zone increases over training (repeated-measures ANOVA, beaconed:  $DF = 24, 268, P < 1e-6, F = 3.8$ , non-beaconed:  $DF = 24, 268, P = 0.015, F = 1.8$ ; [Figure 42](#)). This is seen by the reduction in pre-reward zone stops between early and late training days ([Figure 42C](#)).

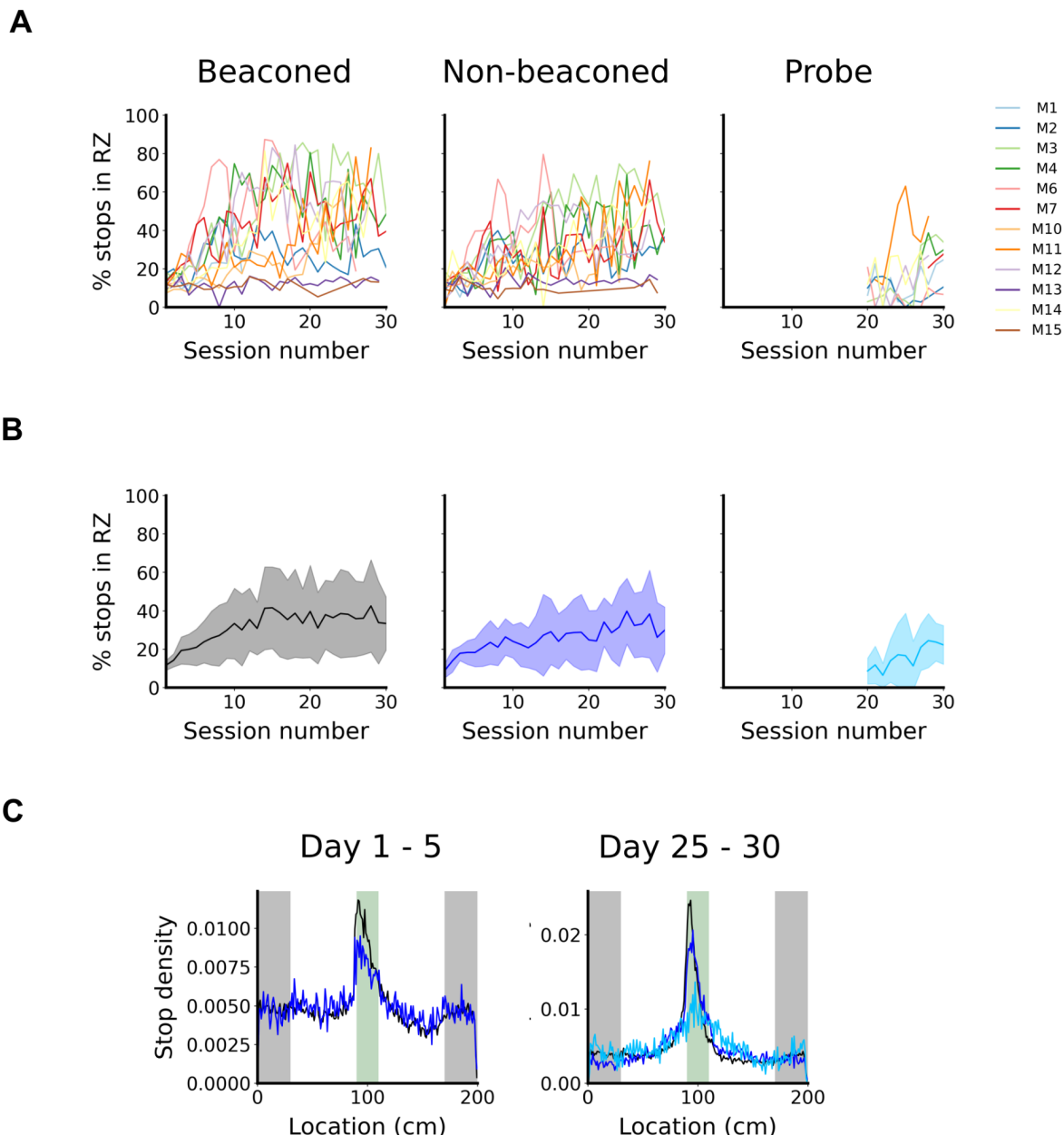
To compare the performance of mice across trial types over the course of training, metrics were compared by day using a Wilcoxon sign-rank test. Mice typically attempted more stops on beaconed trials. This is consistent with the greater proportion of hit and fast hit trials in beaconed compared to non-beaconed trials, showing mice performed better on beaconed trials. The differences between beaconed and non-beaconed performance narrowed towards the end of training ([Figure 36](#)), which is consistent with the late rise of first stops within the reward zone ([Figure 41](#)). This shows mice can stop with a selectivity for the reward zone on non-beaconed trials on par with beaconed trials given sufficient training.

**A****B****C**

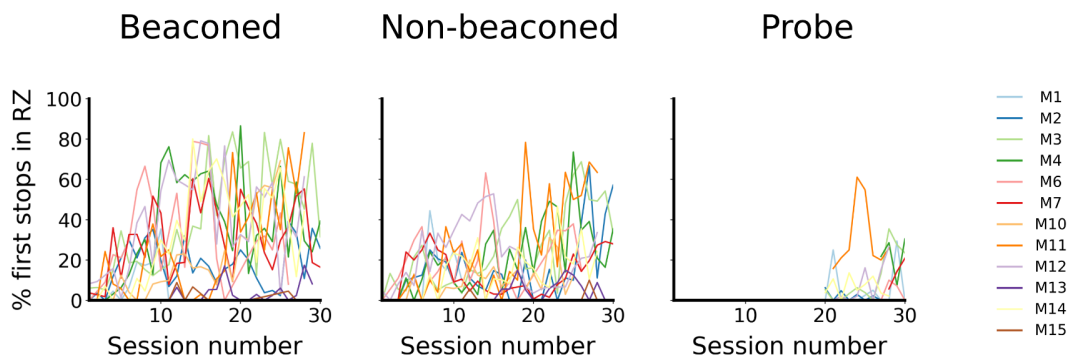
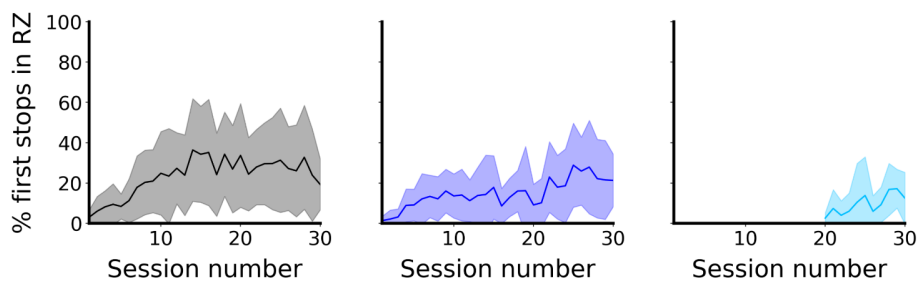
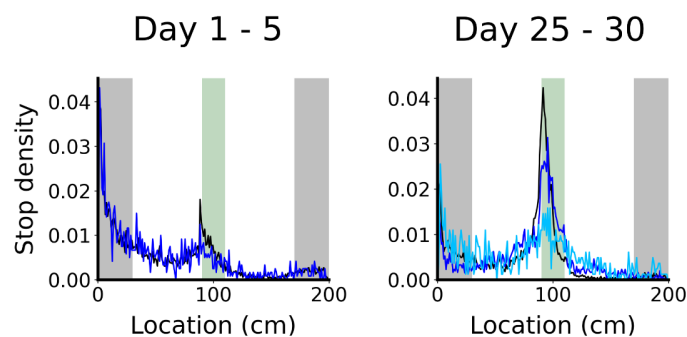
**Figure 39. Stops per trial as a function of training day.** This is shown (A) by mouse and (B) averaged across mice for beaconed, non-beaconed and probe trials. (C) Average plots from B overlaid. Shaded regions represent the standard deviation of across animals. Red stars indicate where beaconed and non-beaconed percentage hit trials are significantly different ( $P < 0.05$ , Wilcoxon sign-rank test).

**A****B****C**

**Figure 40. Stops per trial within the reward zone as a function of training day.** This is shown (A) by mouse and (B) averaged across mice for beacons, non-beacons and probe trials. (C) Average plots from B overlaid. Shaded regions represent the standard deviation of across animals. Red stars indicate where beaconed and non-beaconed percentage hit trials are significantly different ( $P < 0.05$ , Wilcoxon sign-rank test).



**Figure 41. Percentage stops registered within the reward zone as a function of training day.** This is shown (A) by mouse and (B) averaged across mice for beacons, non-beacons and probe trials. (C) Histogram of stops from training days 1-5 (left) and 25-30 (right).

**A****B****C**

**Figure 42. Percentage first stops registered within the reward zone as a function of training day.** This is shown (A) by mouse and (B) averaged across mice for beaconed, non-beaconed and probe trials. (C) Histogram of stops from training days 1-5 (left) and 25-30 (right).

### 3.2.5.3 Mice do not rely on the treadmill for distance estimation

Do mice use visual or olfactory cues provided by the treadmill to guide distance estimation? The circumference of the treadmill is approximately 63 cm, while the distance from the end of the black box to the start of the reward zone is 60 cm. As such, mice could take note of the visual or olfactory cues that exist on the treadmill when they are leaving the black box and stop when they notice these noted cues. To test this possibility, I looked at the stop histograms on sessions in which the mouse was trained on different tracks that did not have this similar correspondence between the treadmill circumference and the distance to the goal. If mice utilised these treadmill cues then mice should stop at the same track location even if different track lengths are used. This would appear as a peak at roughly 93 cm on the stop histogram (30 cm for the black box and 63 cm for one cycle of the treadmill). After the initial training on a 200 cm track, several trained mice were switched to a longer track for two training sessions. The length of these longer tracks and location of the reward zone followed the increased track lengths in (Tennant et al. 2018)

Four different track lengths are shown in [Figure 43](#). As can be seen, no clear peak appears for any of the three alternative track lengths and as such I could reject the possibility of mice using treadmill cues to guide stopping behaviour.

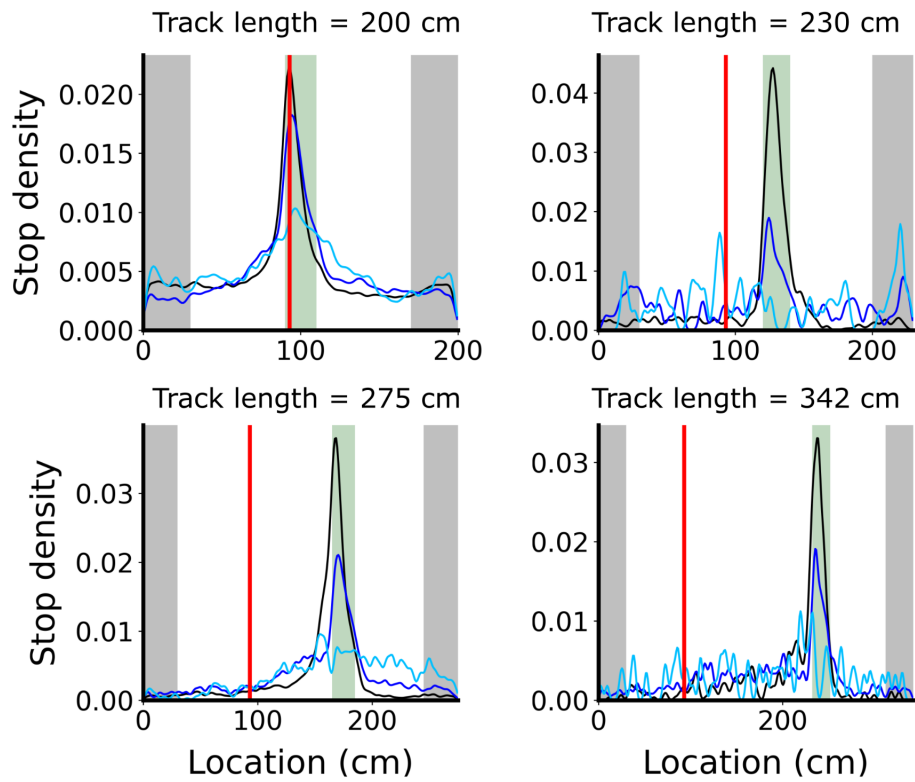


**Figure 43. Stop histograms of trained mice on different track lengths.**

Stops were compiled across the last 5 training days for track length 200 ( $N = 18$  mice, 90 sessions) and all sessions for greater track lengths. ( $N = 5$  mice, 29 sessions). The red vertical line indicates the location of the peak corresponding to a stopping strategy consistent with mice using treadmill cues (visual or olfactory).

### 3.2.6 Task improvements: Improving non-beaconed task engagement

#### 3.2.6.1 Motivation

The default task operated with a trial type ratio of 4 beaconed trials followed by 1 non-beaconed trial. Probe trials were introduced once every 2 non-beaconed trials as soon as the mouse demonstrated a clear stopping preference for the reward zone on non-beaconed trials for two successive days. It was often observed that mice ceased stopping on non-beaconed trials as though they had given up attempting to gain rewards on these trials. Such a strategy would make sense if a large proportion of the rewards available in a training session were obtainable on beaconed trials. If mice abandon efforts to successfully complete non-beaconed trials in favour of only completing beaconed trials, this suboptimal policy although warranting less reward on average, can guarantee rewards when stops are initiated by beaconing with the visual cue, which might be adequate for the mouse. As the aims of this thesis are focussed on understanding how mice utilise spatial cells to inform their stopping on beaconed trials as well as non-beaconed trials it was important to address this behaviour and to encourage continued engagement on non-beaconed trials throughout the experiment.

To illustrate the gain/loss trade-off of engagement in the two different trial types, it is useful to consider the expected reward (ER) allocation from each trial type within a training session ([Figure 44](#)). The two parameters in which to vary the proportion of rewards available include the trial type ratio and the relative reward dispensed on each trial. The reward dispensed on different trial types can be varied by adjusting the length of time the reward valve is open. For example, if the valve is open for twice as long on non-beaconed trials compared to beaconed trials, then roughly twice as much reward is available on non-beaconed trials. Assaying these parameters shows what proportion of the total reward available from the training session can be obtained from non-beaconed trials. [Figure 44](#) shows that using the default parameters, only 20 % of the total expected rewards available in the training session are obtainable from non-beaconed trials. Following the introduction of probe trials, this drops to 11 % as rewards are withheld on probe trials and mice have no way of knowing whether they are on a non-beaconed trial or probe trial. [Figure 45](#) shows the task performance of mouse M14 whereby non-beaconed performance increased and then subsequently dropped before I intervened and amended the expected reward available from non-beaconed trials on training day 15. Weighting the total reward more in favour of non-beaconed trials improved the performance of non-beaconed trials in the later stages of training.

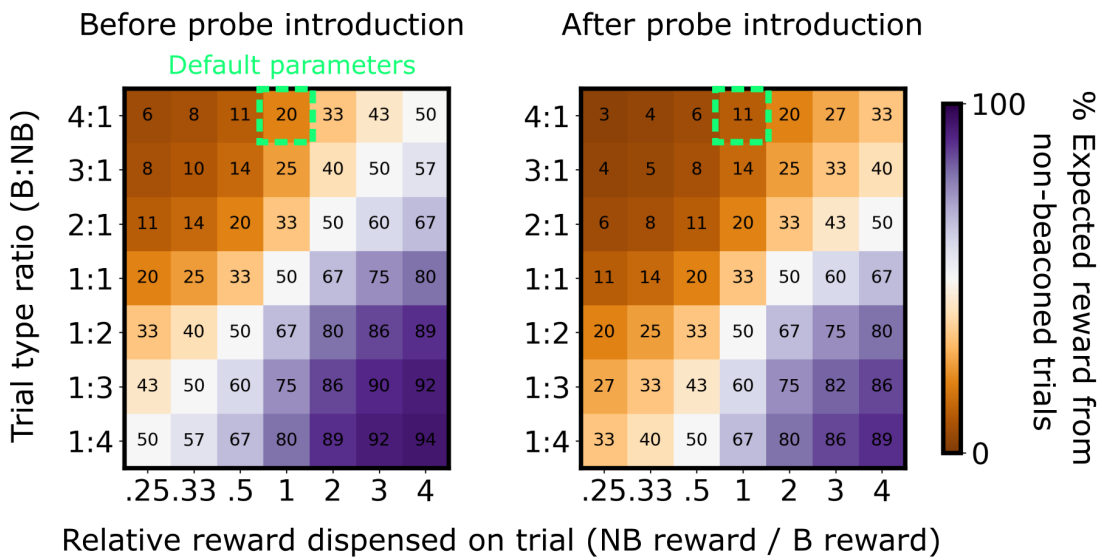


**Figure 44. Expected reward allocation across a training session for non-beaconed trials.** Trial type ratio and the relative reward dispensed is assayed and the proportion of the total expected reward over a single training session is calculated for non-beaconed trials ( $ER_{NB}$ ). The remainder of the expected reward is obtainable on beaconed trials. Percentages as defined by the colour bar are annotated onto the parameter heatmap. The green boxes indicate the default parameters from the original task design (Tennant 2017; Tennant et al. 2018).

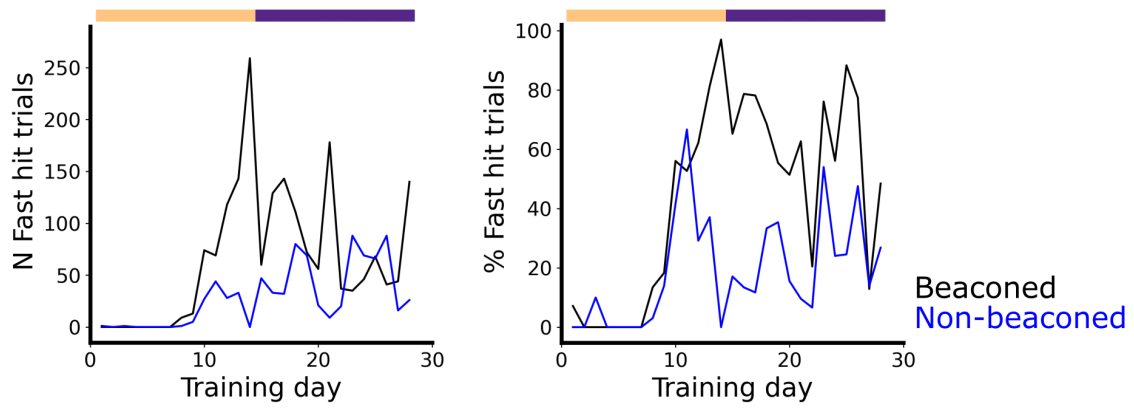


**Figure 45. Performance of training for mouse M14 with a change of reward allocation.**

The mouse completes more beaconsed and non-beaconsed trials over training however the number and percentage of successful non-beaconsed trials drops by day 15 suggesting the mouse abandoned a path integration strategy in favour of a cue-response stopping strategy. The trial type ratio used for these training sessions was 2:1 (beaconsed: non-beaconsed trials). To increase the proportion of total reward available from non-beaconsed trials, from day 15, the reward dispensed on non-beaconsed trials is 3 times greater than on beaconsed trials. The percentage expected reward from non-beaconsed trials is colour-coded for reference to the heatmap in [Figure 44](#).

### 3.2.6.2 The effect of expected reward allocation on task performance

To test manipulations of the expected reward allocation that might result in the improved engagement of non-beaconed trials, the reward allocation was altered in two different ways across 2 mice cohorts. In the first manipulation, the trial type ratio was amended in favour of non-beaconed trials, such that an increased proportion of the total session reward was available from non-beaconed trials compared to the default parameters. In the second manipulation, both the trial type ratio was amended in favour of non-beaconed trials, and the reward dispensed on non-beaconed trials was increased to three times the amount dispensed on beaconed trials. To quantify the task performance across these manipulations, the number and percentage of fast hit trials was compared across manipulation groups and statistically compared with cohorts which operated with the default parameters. A single value of the number and percentage of fast hit trials was calculated for each mouse by averaging across the last five days of training. To obtain a performance baseline from the default parameters, additional mice were pooled from the same experiment however data was collected by different experimenters.

Trial type ratio manipulations (abbreviated TTR) and trial type ratio plus the relative reward dispensed between trial types (abbreviated TTR+R) both increased the number of fast hit trials compared to the default group for non-beaconed but no significant effect on beaconed trials numbers (beaconed trials, default vs TTR: DF = 8, P = 0.35, T= 7.0; default vs TTR+R: DF = 8, P = 0.47, T= 8.0; non-beaconed trials, default vs TTR: DF = 8, P = 0.0095, T = 0.0; default vs TTR+R: DF = 8, P = 0.0095, T= 0.0; Mann-Whitney U tests). There was no clear differences between TTR and TTR+R manipulation groups (beaconed trials, TTR vs TTR+R: DF = 6, P = 0.35, T= 7.0; non-beaconed trials, TTR vs TTR+R: DF = 6, P = 0.68, T = 10.0; default vs TTR+R: DF = 6, P = 0.2, T= 3.0; Mann-Whitney U tests).

Comparing the percentage of fast hit trials between groups revealed a marginal effect of the manipulations compared to the default group on both trial types (beaconed trials, default vs TTR: DF = 8, P = 0.17, T= 5.0; default vs TTR+R: DF = 8, P = 0.038, T= 2.0; non-beaconed trials, default vs TTR: DF = 8, P = 0.038, T = 2.0; default vs TTR+R: DF = 8, P = 0.18, T= 5.0; Mann-Whitney U tests). Again no differences were found between TTR and TTR+R manipulation groups (beaconed trials, TTR vs TTR+R: DF = 6, P = 0.35, T= 7.0; non-beaconed trials, TTR vs TTR+R: DF = 6, P = 0.69, T = 10.0; default vs TTR+R: DF = 6, P = 1, T= 8.0; Mann-Whitney U tests).

Taken together, these results suggest amendments to the default parameters improves engagement of non-beaconed trials both in terms of the numbers and to a lesser extent the percentage of completed fast trials, while not affecting the engagement of beaconed trials. As analysis discussed later in this thesis benefits from the increased trial numbers while the mice are engaged in both path integration and beaconing behaviours, the manipulations to the default parameters are a useful improvement to the task design. Amendments to the trial type ratios in favour of more non-beaconed trials naturally increase the number of possible fast hit trials and this was indeed the case, however amendments to the relative reward dispensed between trial types did not change the number or percentage of fast hit trials suggesting this manipulation is not strictly necessary. It should be noted that changing the relative weighting of rewards could complicate further analysis as this change between trial types might affect the brain state and neural activity of the animal. This is possible because the visual cue is visible (or not in the case of non-beaconed trials) from 10 cm out of the black box at the start of a trial. This means the mouse has access to information about the trial type for the vast majority of the distance up to the rewarded location, which possibly affords the mouse to alter its strategy for a given trial type to maximise its rewards. If the reward weighting is different, this might factor into the mouse's strategy, which complicates comparisons between trial types given that the different trial types should be used to compare behaviour and neural activity on the basis of the navigational strategies available to the mouse and not the extent to which the mouse is rewarded. For future experiments, it is suggested from this work that manipulating the total expected reward from non-beaconed trials is best changed by altering the trial type ratio.

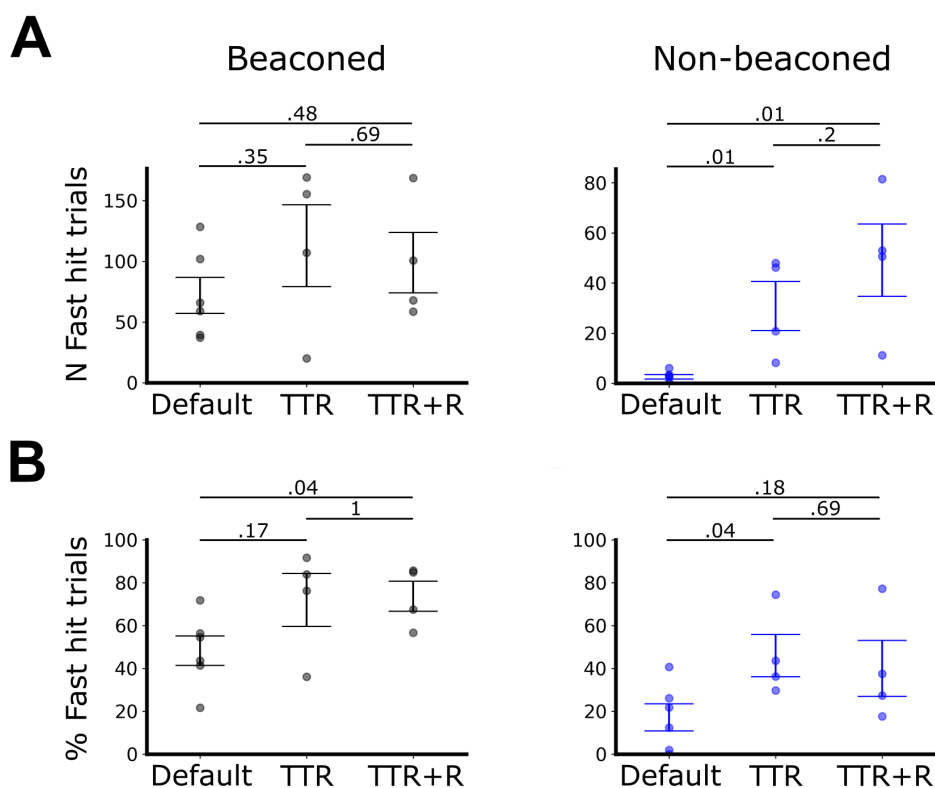


**Figure 46. Comparison of task performance of the default trial type ratio (TTR) and the relative reward (R) between beaconsed and non-beaconsed trials.** P values are annotated above the comparison. Each data point indicates the average session statistic across the last 5 days of training from a single mouse. Manipulations of the reward allocation were made over the course of several cohorts. The default group comprised 6 mice tested by experimenters Sarah Tennant (1), Junji Hua (1), Wannan Yang (2) and myself, Harry Clark (2). The TTR and TTR+R groups both comprised 4 mice each tested by myself, Harry Clark. In total, the task performance of 14 mice is shown. Mice that did show a clear learning profile over the course of 30 training days were excluded from the analysis. These mice typically failed to run sufficiently fast enough to qualify any trials as fast hit trials. ERNB from each group are as follows: Default = 20 %; TTR = 33 %, TTR+R = 60 %.

### 3.3 Discussion

To establish the linear location task captures self-localisation behaviours like beaconing and path integration, as previously reported (Tennant 2017; Tennant et al. 2018), I looked to repeat the task and validate the original findings. I found the majority of mice were able to learn to stop at the reward zone for both beaconed and non-beaconed trial types within 10 days. These results were consistent with the original findings establishing the task as a measure for self-localisation behaviour. To address whether an alternative strategy might be employed other than path integration is an important issue and will be discussed below.

As the default task operated with a far greater number of beaconed trials compared to non-beaconed trials, I asked whether the task design could be amended to accommodate more non-beaconed trials in order to increase the statistical power to address the functional roles of spatially-modulated cells in path integration behaviours. I found mice were able to perform the task with a greater proportion of non-beaconed trials and found this did not affect the performance of beaconed trials. These results indicate that future experiments should take advantage of these amended task designs where questions of path integration wish to be addressed.

#### 3.3.1 Technical challenges

With the increased numbers of experimenters addressing linear location estimation within the lab, it became apparent a second experimental rig was required to accommodate everybody. As the experimental rig required an open field setup within the same animal house and preferably the same room, I took it upon myself to build and set up a second rig. The first experiment tested on this rig was a success with mice performing the task within 10 days, thus negating any unknown variables from the learning process of the mice.

#### 3.3.2 Do animals path integrate in a VR linear location estimation task?

The linear location task was designed to train mice to estimate their distance travelled and stop when a particular distance was traversed from the start of the virtual track. Marking the rewarded location with a sensory cue or not provides a clear experimental manipulation for comparing beaconed and path integration behaviours. While it might appear a clear experiment to capture beaconed and path integration-based behaviour, it is worth considering whether other navigational strategies could be employed in place of beaconing or the error-ridden process of path integration. At the beginning of each trial, mice traverse out of a black box region into the textured track. After travelling 10 cm out of the black box, if the mouse is on a beaconed trial, the mouse will be able to see the visual cue marking the

reward location. From this point the mouse could choose to navigate with a beaconed strategy and even disregard any other strategy. These alternative strategies include path integration and time or step-counting. As discussed previously, path integration is inherently prone to errors and would lead to more errors than beaconing. Time or step counting involves the navigating animal to remember the duration of travel or the number of steps required to reach the reward zone, and has been shown in rodents (Light et al. 2019). Both strategies are prone to similar errors in the imperfections and variabilities of timekeeping and gait respectively. Therefore, it stands to reason that when a beacon is available, the animal will resort to beaconing navigation as it affords the possibility of a low uncertainty method.

On non-beaconed trials, beaconing no longer becomes a viable strategy. The remaining strategies available include path integration and time or step-counting. As all of these strategies are prone to accumulating errors, which is consistent with the distance-dependent stopping error reported in the original study (Tennant et al. 2018). As mice stop at distances consistent with path integrating with motor-based self-motion signals (Tennant et al. 2018), step-counting cannot be ruled out. A timing-based strategy would result in a consistent time to reward in each trial throughout a session. Work from Teris Tam showed in a representative session, the time to the reward can vary considerably suggesting a timing based-strategy was not preferentially observed (Tennant et al. 2022).

On both trial types, path integration is a valid strategy and cannot be easily separated from beaconing on beaconed trials. This is because information crucial to drive path integration is available to the mouse at all times (e.g. optic flow, motor efferent information). In order to draw comparisons of the behaviour and neural activity between trial types, it is important to consider the additional information provided by the visual beacon may influence the navigational strategy away from one based on path integration, while without the visual beacon, this influence is in effect absent. Thus, the comparisons that can be made between trial types are not strictly based on beaconed versus path integration navigation, but are rather weighted on the credibility of the navigational strategy available.

# How do grid representations relate to task performance?

## 4.1 Introduction

Since the discovery of grid cells in rats freely exploring an open arena (Hafting et al. 2005), this has been followed up in other environments such as linear tracks (Derdikman et al. 2009; Pérez-Escobar et al. 2016) and cue-rich virtual tracks (Domnisoru, Kinkhabwala, and Tank 2013; Campbell et al. 2018). These examples showed the allocentric coding capabilities of grid cells as firing fields mapped to the same environment locations across traversals of an open arena and laps of linear and virtual tracks. Grid cell activity can in some conditions spontaneously remap (Low et al. 2021) and it has also been observed that grid cell activity can represent egocentric or allocentric codes (Jacob et al. 2019), but what is unclear is whether anchoring of grid codes to spatial cues that facilitates allocentric coding is necessary for solving behavioural problems. Grid cells are thought to support path-integration operation by integrating speed and head direction inputs. As such, grid cells should operate with very minimal spatial cues in which to function as path integrators. Using a task designed to encourage mice to utilise both beaconing and path integration-based navigation, the functional relevance of spatial coding of grid cells can be investigated. This chapter addresses whether grid cells contribute to successful performance of the task. If so, then their activity should be locked to the track on successful trials. Moreover, if performance errors result from failures in grid coding then this should be apparent as discrepancies between grid representations and track location on miss trials.

To begin addressing the function of grid cell activity on a linear track, first, a true grid cell must be classified based on its  $60^\circ$  rotational symmetry in a 2D environment. To do so, mice performed two tasks on the same recording day, an open field exploration task, used to identify grid cells followed by a VR linear location estimation task used to evaluate the relationship between grid cell firing and behavioural performance. Neural activity recorded as electrode voltage traces was concatenated between these two recording sessions such that spike sorting was performed across recording sessions on the same day. This provided an objective approach for cross-session spike identification and subsequent classification of grid cells for both tasks. Next, grid cell activity in the linear location task was classified based on its spatial coding scheme. A method was devised to quantify the spatial coding schemes consistent with continuous attractor dynamics. It was found that grid cells encoded both allocentric and egocentric coding schemes and individual grid cells were not always locked to a single spatial code. Where coding changes did occur, it was found that jointly recorded

grid cells were also more likely to change their spatial code coherently. This suggests that at least within grid modules, spatial coding schemes are a functional output of the medial entorhinal cortex. Finally, whether spatial codes were linked to particular spatial behaviours was addressed. It was found that allocentric coding was more common in mice performing the task with high fidelity, particularly on trials in which path integration was the only viable solution. This provides evidence that grid cell activity is linked to path integration behaviours.

## 4.2 Methods

### 4.2.1 Subjects

15 male wild type C57BL/6NCrl mice were obtained (Charles River) and surgically implanted between the ages of 10-15 weeks. Mice were the same as presented from in Chapter 3. Data from 12 of these mice are shown in this chapter, as explained in [3.2.1](#). Mice were trained and handled solely by the author, Harry Clark.

### 4.2.2 Data analysis

Preprocessing, spike sorting, and post-processing was completed as detailed in Chapter 2: Methods and Materials. Spatial firing analysis was performed in Python 3.8 and statistics calculated using the Scipy and Astropy modules.

### 4.2.3 Calculating spatial periodicity

#### 4.2.3.1 Possible coding schemes

The current best explanation for the  $60^\circ$  rotational symmetry in firing activity postulates grid cells form a network that follow continuous attractor dynamics (McNaughton et al. 2006). In this framework, neurons are organised in a neural sheet by their spatial phase, and exert short range excitation and long range inhibition (with a mexican hat architecture) or short range inhibition and long range excitation (with an inverted Lincoln hat architecture). Activity can be translated across the neural sheet in accordance with the animals movement in the environment which can be expressed by directional and speed signals from head direction and speed cells respectively. As grid fields are stable across time (Hafting et al. 2005), allothetic cues likely play a role in anchoring field positions to the environment such as the environmental boundaries (Hardcastle, Ganguli, and Giocomo 2015). If these anchoring dynamics are extrapolated to a grid cell firing on a virtual reality track where trials are run and then animals are teleported back to the beginning, field positions would remain fixed and grid cells would potentially break their periodic firing to realign to the track and its cues ([Figure 47](#)). On the other hand, if an animal moves forward continuously without the impedance of a barrier, it follows that a grid cell may continue its periodic firing indefinitely, without realignment. While early evidence has suggested grid cells encode the allothetic position on a virtual track (Domnisoru, Kinkhabwala, and Tank 2013), whether this is a stable feature of the grid cell system is unclear. Moreover, the extent to which specific navigation strategies guide the coding scheme is a completely untouched question.

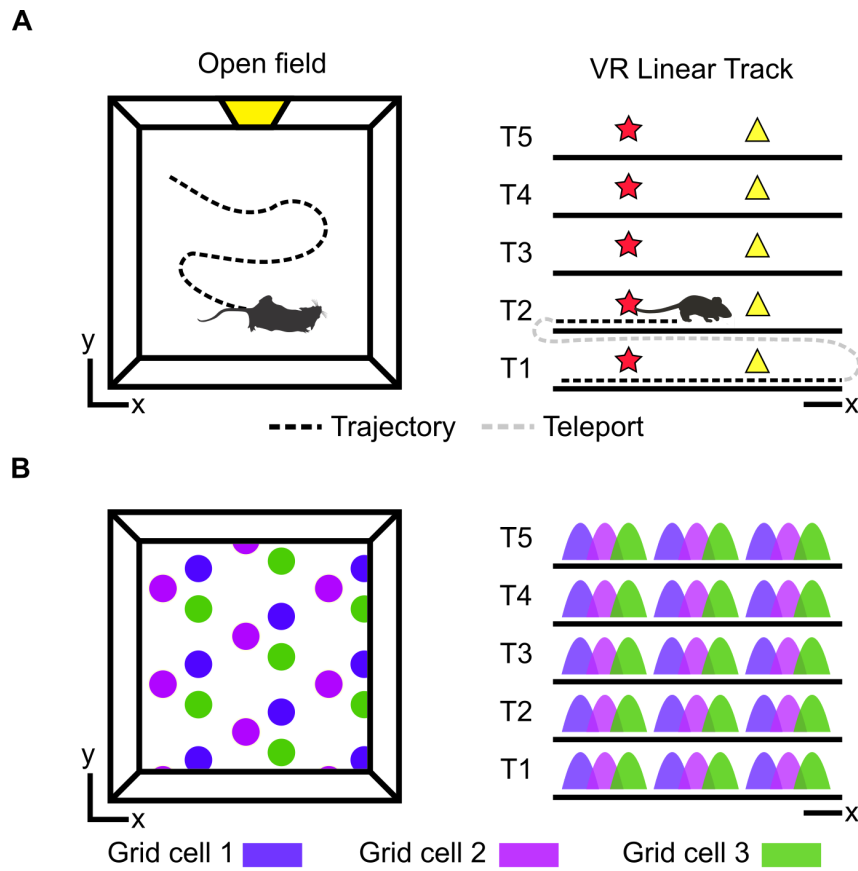
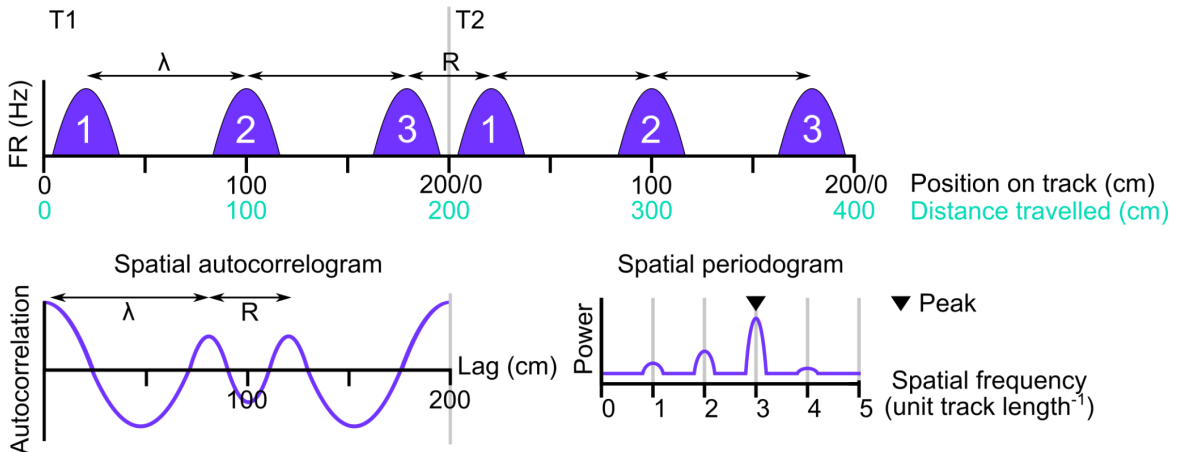


**Figure 47. The dogmatic view of grid cell firing in open arenas and virtual tracks.** (A) mice explore open arenas and virtual reality tracks with clear landmark cues (yellow and red markers). (B) Grid fields remain stable over time and thus thought to anchor to locations in both open arenas and virtual linear tracks.

#### 4.2.3.2 Quantification of spatial periodicity

Quantification of the spatial periodicity that will be used to distinguish position or distance coding from aperiodic coding can be achieved by estimating the periodicity of a cell's firing rate as a function of track position. If a cell periodically fires at the same locations across a range of trials, then it will be well modelled by a sinusoidal wave with a spatial frequency  $f$  that corresponds to a firing rate profile with  $f$  oscillations per track length, which can be interpreted for grid cells to be the number of firing fields observed per track length. If a cell fires periodically but its firing is not anchored to specific track positions, the firing can again be well modelled by a sinusoidal wave, however the phase of the oscillations will fluctuate between trials as the periodic firing rolls over on consecutive trials. The best fit sinusoidal wave with spatial frequency  $f$  will approximately represent the average number of oscillations (or firing fields) per track length. As the number of oscillations remain constant for position coding due to track anchoring, the approximated spatial frequency will be constrained to integer values, whereas the best fit spatial frequency for distance coding without track anchoring will not. Taken together, the spatial frequency at which a sinusoid best fits the firing rate of a measured cell can be used to distinguish between position and distance coding.

### Allocentric coding - Position



### Egocentric coding - Distance

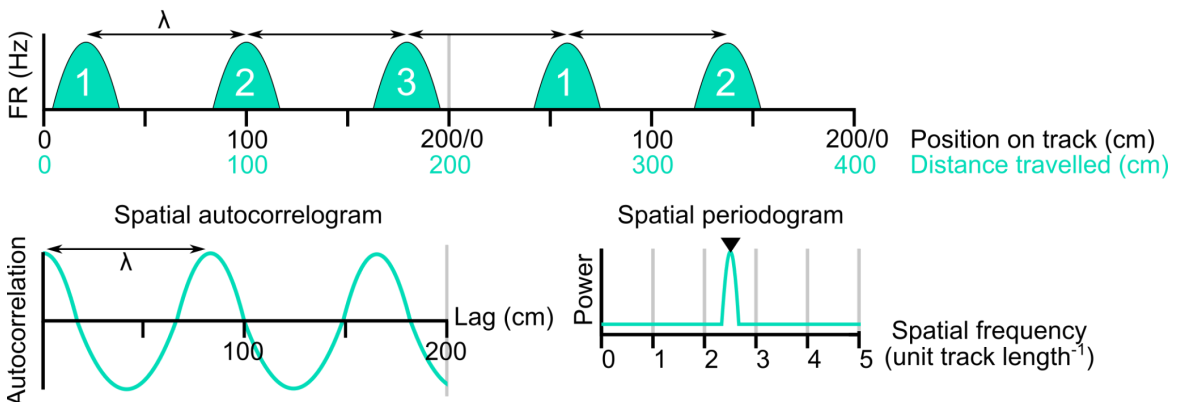


**Figure 48. Possible coding schemes consistent with continuous attractor models.**

Spatial periodograms predict integer peaks for allocentric coding grid cells. In an allocentric coding scheme, a grid cell fires with field spacing  $\lambda$  and resets its firing every trial by anchoring its fields to the same location. A realignment lag  $R$  would be observed in the spatial autocorrelogram. The number of fields remains constant on each trial and thus is approximated with an integer power in the spatial periodogram (see [Figure 49](#)). In an egocentric coding scheme, a grid cell fires with field spacing  $\lambda$  and continues to fire at regular intervals without anchoring. Unless field spacing and the track length are integer divisible, the number of fields per trial varies, and thus the peak of the spatial periodogram approximates the average number of fields per trial and will not be an integer frequency.

To quantify a cell's spatial periodicity, the Lomb-Scargle method of least-squares spectral analysis (LSSA) was used to generate a periodogram in the spatial domain (Lomb 1976; Scargle 1982). Similar to Fourier analysis, LSSA is a method that approximates the composition of a signal into a linear combination of sinusoidal waves.

For a given set of data values (in this case a cell's firing rate)  $h_i = 1, \dots, N$  at respective observation points  $p_i$  (the corresponding track locations scaled between 0 and 1) the Lomb-Scargle periodogram is constructed first by computing the data's mean and variance by

$$(8) \quad \bar{h} \equiv \frac{1}{N} \sum_{i=1}^N h_i$$

$$(9) \quad \sigma^2 \equiv \frac{1}{N-1} \sum_{i=1}^N (h_i - \bar{h})^2$$

secondly , for each spatial frequency  $\omega \equiv 2\pi f > 0$  of interest, compute a time-offset  $\tau$  by

$$(10) \quad \tan(2\omega\tau) = \frac{\sum_j \sin(2\omega\tau_j)}{\sum_j \cos(2\omega\tau_j)}$$

Finally the normalised Lomb-Scargle periodogram (spectral power as a function of  $\omega$ ) is defined by

$$(11) \quad P_N(\omega) \equiv \frac{1}{2\sigma^2} \left\{ \frac{[\sum_j (h_j - \bar{h}) \cos(\omega(p_i - \tau))]^2}{\sum_j \cos^2(\omega(p_i - \tau))} + \frac{[\sum_j (h_j - \bar{h}) \sin(\omega(p_i - \tau))]^2}{\sum_j \sin^2(\omega(p_i - \tau))} \right\}$$

These equations were taken from (Press and Rybicki 1989) and edited to show spatial observation data points rather than time.

LSSA was chosen over computing the Fourier transform as it can handle unequally spaced data and the spectral precision is not constrained by the length of the data samples. For grid cells that fire periodically but also sporadically such that their firing fields might appear out of phase with each other, it became apparent that computing a frequency spectrum over the full signal would not be optimal. Instead, a spectral estimate was computed every 10 cm with a sample length equal to 3 track lengths. Spectral estimates were concatenated to create a spatial periodogram across the session and averaged across trial samples to generate the average spatial periodogram. Peaks in this periodogram could then be used to classify a cell's spatial firing properties to the position and distance coding schemes. The peak of the average periodogram can be interpreted as the best fitting sinusoidal component for the signal. The spatial frequency of this component is equivalent to the average number of firing oscillations occurring in a single trial and the power is proportional to the relative weight of the component in the signal. A summary of the method is provided in [Figure 49](#). Spatial frequencies  $> 5$  were discarded from further analysis as no grid cells were found with grid spacings  $< 40$  cm.

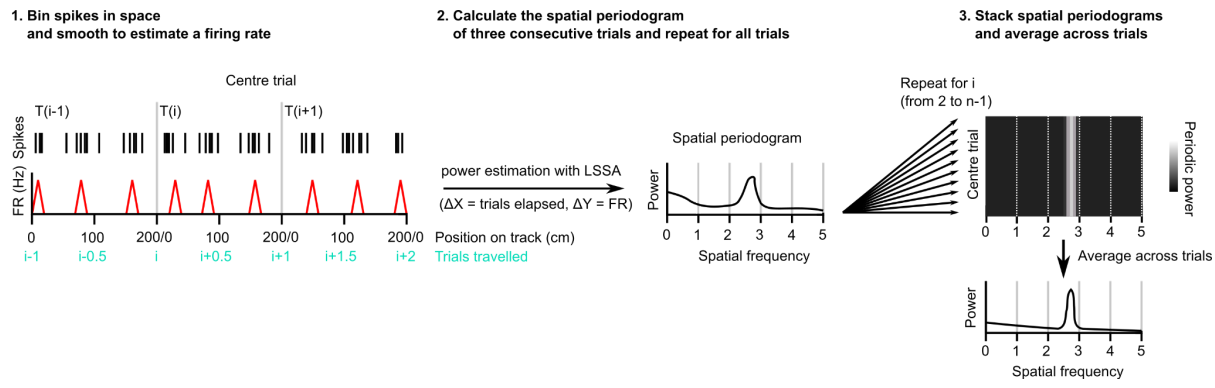


**Figure 49. Procedure for extracting a spatial periodogram for a set of spike timestamps.** A single cell's spikes are binned in space (1 cm bin size) and smoothed using a Gaussian kernel (standard deviation = 2 cm). LSSA was computed on a signal equivalent to 3 track lengths long using the Lomb-scargle implementation in the Astropy Python module ( $\Delta x$  = distance elapsed in trials,  $\Delta y$  = firing rate). The signal was advanced 10 cm and repeated for the whole session. All spatial periodograms are concatenated and averaged across trials to generate the average spatial periodogram.

#### 4.2.3.3 Classifying spatial periodicity using a field shuffle method

The average spatial periodogram generated as explained in [4.2.3.2](#) provides a useful metric for quantifying the spatial periodic firing properties of a cell on repeated trials of a linear track. But how can this be used to statistically classify a cell as spatially periodic? What if the cell is temporally periodic? And is that sufficient to falsely classify a cell as spatially periodic given the potential for coupling between space and time? To address these questions, a procedure was designed to compare the spectral peaks between the measured cell and a false alarm threshold signifying the likelihood of the peak power being greater than chance-level periodicity. This was inspired from the field shuffle procedure used for grid cells in 2D (Barry and Burgess 2017). Available analytical and numerical approximations of a false alarm threshold were not suitable for statistical comparisons as these methods generated false alarm thresholds based on signals derived from Gaussian noise with no periodic components (Baluev 2007). Furthermore, as neural signals are known to have temporal dynamics such as burst firing or theta-modulated firing, it was important these features were incorporated into the firing properties of a shuffled cell as much as possible. To overcome these issues, a bootstrapping method was devised by generating 1000 shuffled instances of the cell's firing from which to compare against the measured cell. Measuring the spatial periodicity of these 1000 shuffles generated a distribution of peak powers. A false alarm threshold was then derived from the 99<sup>th</sup> percentile of the peak power distribution. If the cell's peak power was greater than the false alarm threshold, the peak power could be rejected as a false alarm and the cell could be classified as spatially periodic.

To generate a shuffled instance with disrupted spatial periodicity while preserving any local temporal firing, first, firing fields were identified in a highly smoothed version of the cell's firing rate map (Gaussian kernel, standard deviation = 4 cm). To identify fields, the peaks and troughs of the highly smoothed firing rate map were first identified, with a minimum peak distance of 20 cm, smaller peaks were removed until the condition was satisfied (see `scipy.signal.find_peaks`). Fields were defined as the detected trough to trough. The field positions were reallocated in an unsmoothed rate map to random positions, preserving the spatial organisation of the field and subsequently bins not attributed to a firing field filled the remaining gaps. The shuffled unsmoothed rate map was then smoothed (Gaussian kernel, standard deviation = 2 cm) and spatial periodogram calculated as in [4.2.3.2](#). This was repeated 1000 times and the 99<sup>th</sup> percentile calculated from the distribution of shuffled peak power. A cell that had a peak that exceeded this 99<sup>th</sup> percentile was classified as spatially periodic. The procedure is summarised in [Figure 50](#). If the cell was spatially periodic, it was either consistent with an allocentric position encoding if the frequency at its peak power was within 5 % of an integer spatial frequency or egocentric distance coding if it was outside 5 %

of an integer spatial frequency. Using this threshold theoretically fixes the false positive rate of true distance-encoding cells classified as position-encoding to 5 %, as distance-encoding cells can have peaks at any spatial frequency. This was considered sufficient for the purposes of classifying the vast majority of periodic signals correctly. [Figure 51](#) illustrates the spatial periodograms computed from different cells with spatial firing properties. For spatially periodic cells, the measured spatial periodogram peak is greater than the false alarm threshold. It is worth noting that while multiple peaks may fall above the false alarm threshold, this does not equate to the signal being well modelled by these additional spatial frequencies. Spectral analysis is an approach used to approximate the signal composition from a set of sinusoidal waves. When signals do not correspond with perfect sinusoidal waves, a linear combination of sinusoidal waves is estimated to best fit the signal, which may fall within the spatial frequency range of interest. Therefore, it is important to appreciate that only the peak spatial frequency is taken to estimate the periodicity of the signal.

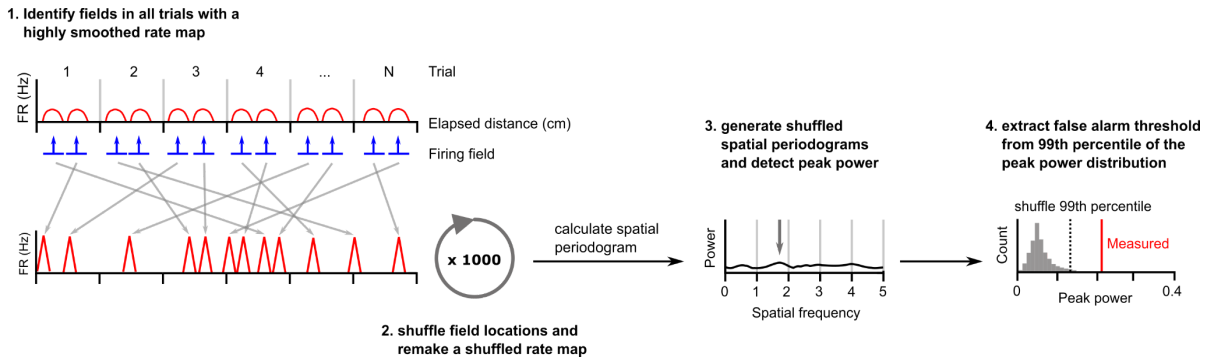


**Figure 50. Procedure for estimating a false alarm threshold using a field shuffle for a given cell.** A single cell's spikes are binned in space (1 cm bin size) and smoothed using a Gaussian kernel (standard deviation = 4 cm). Firing fields are detected and field bins reallocated in an unsmoothed rate map. Bins not attributed to a field are allocated to the remaining gaps. This rate map is then smoothed with a Gaussian kernel (standard deviation = 2 cm). An average spatial periodogram is calculated and peak power detected. This is repeated 1000 times and a false alarm threshold assigned from the 99<sup>th</sup> percentile of the shuffled cell's peak power distribution.

## Simulated example cell types

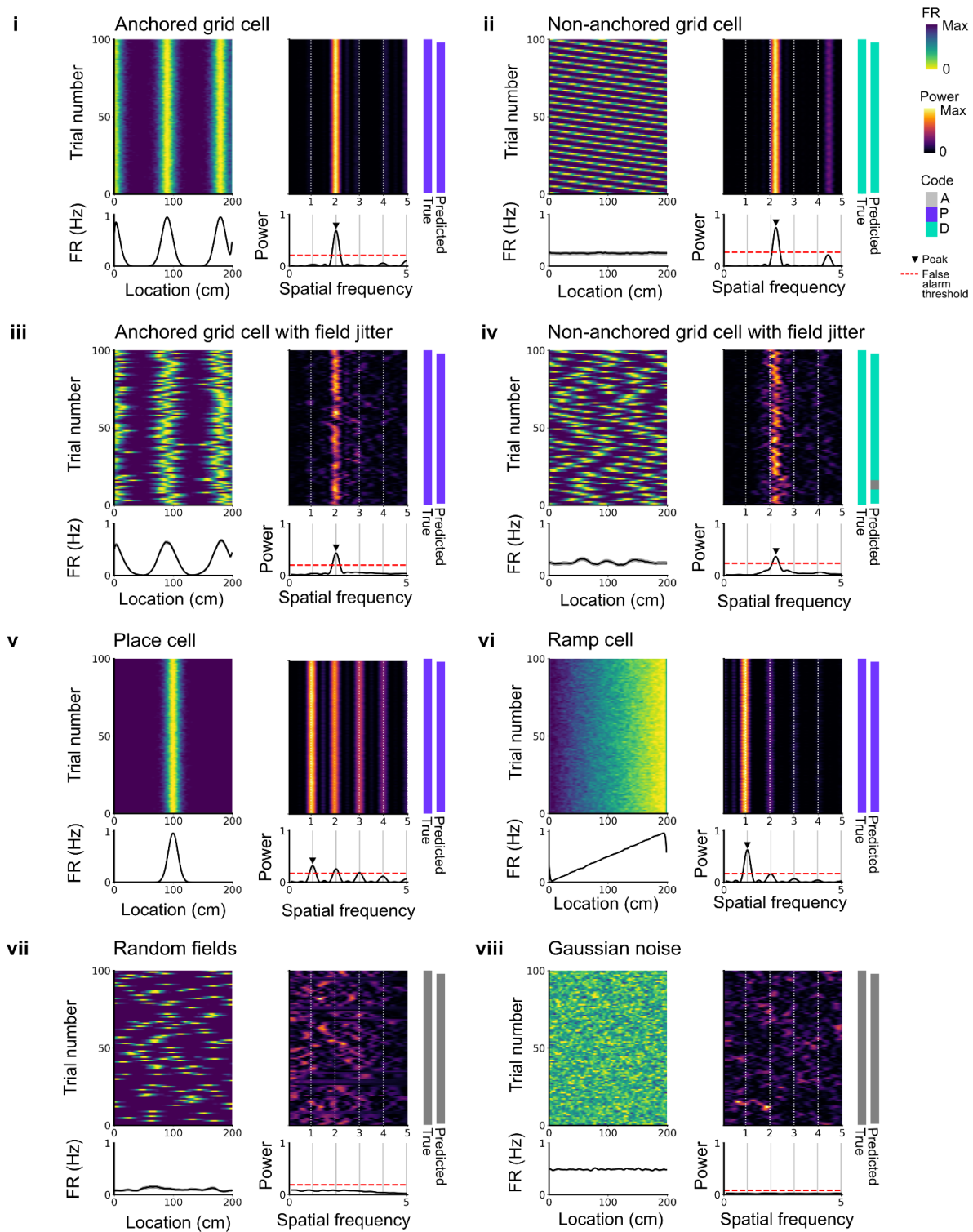


**Figure 51. Eight example cells to illustrate the expected measured periodicity for different cell types.** From top to bottom shows the spike raster by trial, firing rate map by trial, spatial periodogram by trial and the trial-averaged spatial periodogram. From left to right, the example cells include (i) a perfect allocentric grid cell, (ii) a perfect egocentric grid cell, (iii) a allocentric grid cell with field jitter , (iv) an egocentric grid cell with field jitter, (v) a perfect place cell, (vi) a ramp-like cell, (vii) randomly positioned fields and (viii) Guassian noise. Within each example shows the firing rate map across trials (top left within the example panel), the average firing rate map (bottom left), the spatial periodogram (top right), the average spatial periodogram (bottom right) and the classification labels (true and predicted; far right). Cells that are spatial periodic in nature, either over some spatial interval or are additionally locked to features of the track will show a peak in the trial-averaged spatial periodogram above chance level. Spatial firing patterns which are not periodic in nature will show a peak in the trial-averaged spatial periodogram below chance level.

#### 4.2.3.4 Classifying spatial periodicity across a single session

To classify cells throughout the recording session, rolling windows of the spatial periodogram were averaged over 200 data samples which equated to 10 trials (20 samples per 200 cm track with 10 cm steps). Similar to classifying across the entire session, the peak of the average spatial periodogram from a single window was identified. The peak power and the frequency at which this occurred were extracted. To determine if the peak reflected a periodic signal that occurred above chance level, it was compared with an adjusted false alarm threshold. As the heights of average periodogram peaks are extracted for each field shuffle to generate a distribution from which the false alarm threshold is approximated, peak heights vary depending on the number of samples in the periodogram. [Figure 52](#) shows how the false alarm threshold changes as a function of the number of periodograms used to compute the average periodogram from a representative recording. As the number of samples within the rolling window increases, the false alarm threshold decreases. This is a common feature across all cells. The adjusted false alarm threshold must therefore reflect the same number of samples to have the same statistical purpose. To compute this adjusted false alarm threshold, for each field shuffle, the first 200 samples are used to compute the average periodogram, thus matching the number of samples used in the rolling window calculation. The 99<sup>th</sup> percentile of peak powers from 1000 field shuffles is used as the adjusted false alarm threshold.

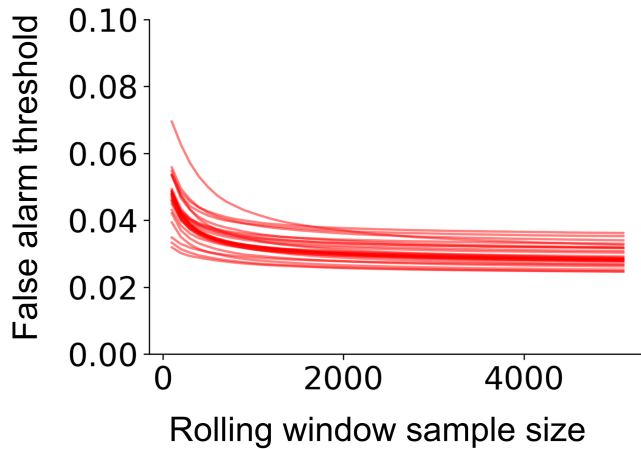


**Figure 52. False alarm threshold as a function of the rolling window sample size from a single recording,  $n = 30$  cells.** The false alarm threshold is defined by the 99<sup>th</sup> percentile of the distribution of the peak power of the average spatial periodogram for 1000 shuffled instances of a cell's firing rate profile across the full session. The rolling window sample size is defined as the number of samples of spatial periodograms over which the average spatial periodogram is computed. The false alarm threshold decreased asymptotically in all cells with an increase in rolling window sample size.

#### 4.2.3.5 Validation of periodicity classification

To evaluate classification of cells as positional or distance coding we simulated cell types including grid cells, place cells, ramp cells and aperiodic cells ([Figure 51](#)). For each cell type, we simulated an agent moving with a constant velocity of 10 cm/s across 100 trials of a 200 cm long linear track and recorded the locations visited with a sampling rate of 1000 Hz. For each cell-type the probability of firing at any given location was defined by a probability density function (PDF) with a maximum range of 0 to 1, with 1 equating to a guaranteed firing event. The average firing rate was set by multiplying this normalised PDF by a scalar variable  $P_{\max}(\text{spike})$  which by default was set to 0.1. Firing events were then assigned to each sampled location based on the scaled PDF. Firing rate maps and subsequent spatial periodograms were created as described previously.

PDFs for grid cells were created by positioning Guassians kernels at equidistant locations along the track, with kernel standard deviation equal to 0.1 multiplied by a given grid spacing between the kernels. To simulate positional grid codes, the Guassian kernels were positioned at the same track location on each trial, whereas to simulate distance grid codes the kernels were positioned independently from the track with distances equal to the grid spacing. To simulate field jitter, a displacement of the kernel position was drawn from another Guassian distribution with  $M = 0$  cm and  $SD = 0$  cm (for no jitter) or 10 cm (for default jitter). A random variable denoting jitter was drawn for each field and was used to shift the field. The PDF for the place cell example was made up of a singular Guassian kernel ( $M = 100$  cm,  $SD = 10$  cm) positioned at the centre of the track and was repeated every trial. The PDF for the ramp cell example consisted of a linear ramp from the start of the track (0 cm) to the end of the track (200 cm). The PDF for the “random field” cell was created by first generating the PDF for the place cell example and then passing this through the field shuffle as explained above. The PDF for the noisy cell example was a uniform distribution.

To generate PDFs of grid cells alternating between positional and distance codes, representations of each type were generated and merged based on the type of alternation. For the simulations that alternated in blocks of trials, the initial trial was randomly assigned to either the anchored PDF or the non-anchored PDF with equal probability, for all subsequent trials there was a 10% chance of alternating to the other PDF (e.g. anchored to non-anchored or non-anchored to anchored). For simulations that alternated at the level of single trials, every trial was randomly assigned to either the anchored PDF or the non-anchored PDF, with equal probability.

To gauge the accuracy and any underlying bias in our classification of periodic firing at the level of individual cells, we simulated 500 anchored grid cells and 500 non-anchored grid cells with grid spacings uniformly distributed between grid spacings of 40 - 400 cm and compared the true labels of these simulated cells with the predicted classifications. To determine what spatial frequency tolerance to use in our classification, we classified the simulated dataset across a range of spatial frequency thresholds to graph at which spatial frequency tolerances we could maximise prediction accuracy and minimise the estimation bias between position and distance encoding classifications. This was repeated using a range of  $P_{\max}(\text{Spike})$  and jitter SD values. To simplify the analysis, no field shuffle was computed on simulated data within this particular analysis and therefore no false alarm threshold was used. This effectively forced our classifier to label cells position or distance without the possibility of an aperiodic label. The prediction accuracy of our classification was calculated as the percentage of true position and distance-encoding grid cells with a correct prediction label. The prediction bias was calculated as the difference between the number of cells predicted as position-encoding and the number of cells predicted as distance-encoding. Figure 53 shows the prediction accuracy is above 80% under a range of firing parameters when a spatial frequency tolerance close to zero is used.

Similarly, to gauge the accuracy and underlying bias in our classification of periodic firing at the level of individual trials, we simulated 100 grid cells with grid spacings uniformly distributed between grid spacings of 40 - 400 cm that could alternate between position and distance encoding either in blocks of trials or every trial (see above) and compared the true labels of these simulated cells and trials with the predicted classifications. To determine how many spatial periodograms to average over (or if any), we classified the simulated dataset across a range of rolling window sizes to graph at which rolling window size we could maximise prediction accuracy and minimise the estimation bias between position and distance encoding classifications. Again this was repeated. This was repeated using a range of  $P_{\max}(\text{Spike})$  and jitter SD values and no field shuffles were computed. The prediction accuracy of our classification was calculated as the average percentage of true position and distance-encoding trials with a correct prediction label. The prediction bias was calculated as the difference between the true difference between the number of position and distance encoding trials and the predicted difference between the number of position and distance encoding trials. Figure 54A shows several examples of grid cells switching between position and distance either in trial blocks or at the level of individual trials. Figure 54B shows the prediction accuracy initially increases and then decreases as a function of the number of periodograms used in the rolling classification. Based on this analysis, it is clear the

classification of recorded grid cells will be more accurate if grid cells could indeed switch periodic coding schemes in blocks rather than at the level of individual trials.

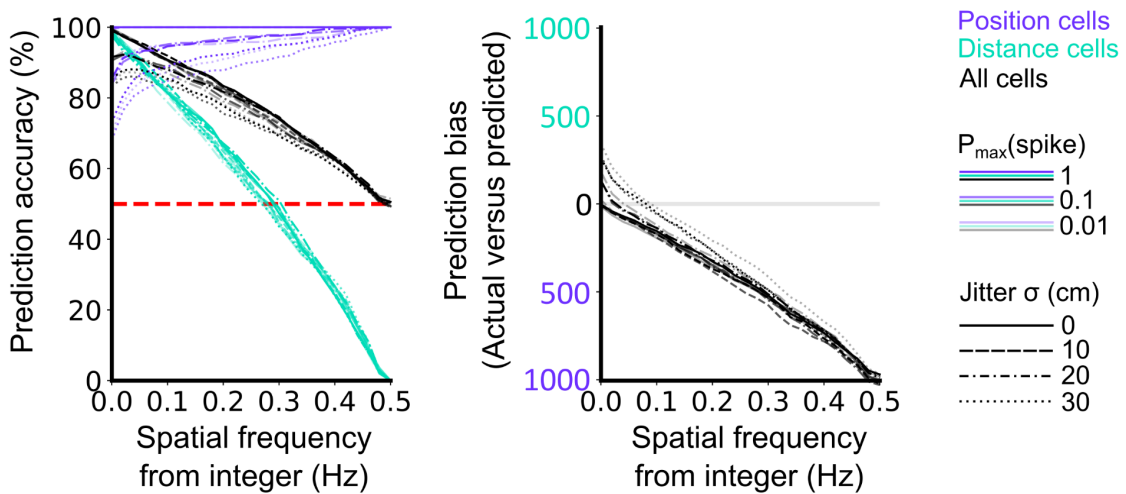


**Figure 53. Classification accuracy and bias on the level of cell as a function of spatial frequency.** 1000 grid cells were simulated as per section 4.2.3.5. Classifications were made on each set of simulations by comparing the spatial frequency at which a peak occurred within the average spatial periodogram. The difference between this spatial frequency and the closest positive integer was calculated as used to classify the cell into the position cell class by being smaller than or equal to a given spatial frequency threshold or into distance cell class by being greater than this threshold. Prediction accuracy (left) and bias (right) are shown as a function of the spatial frequency from a positive-integer used for the spatial frequency threshold.

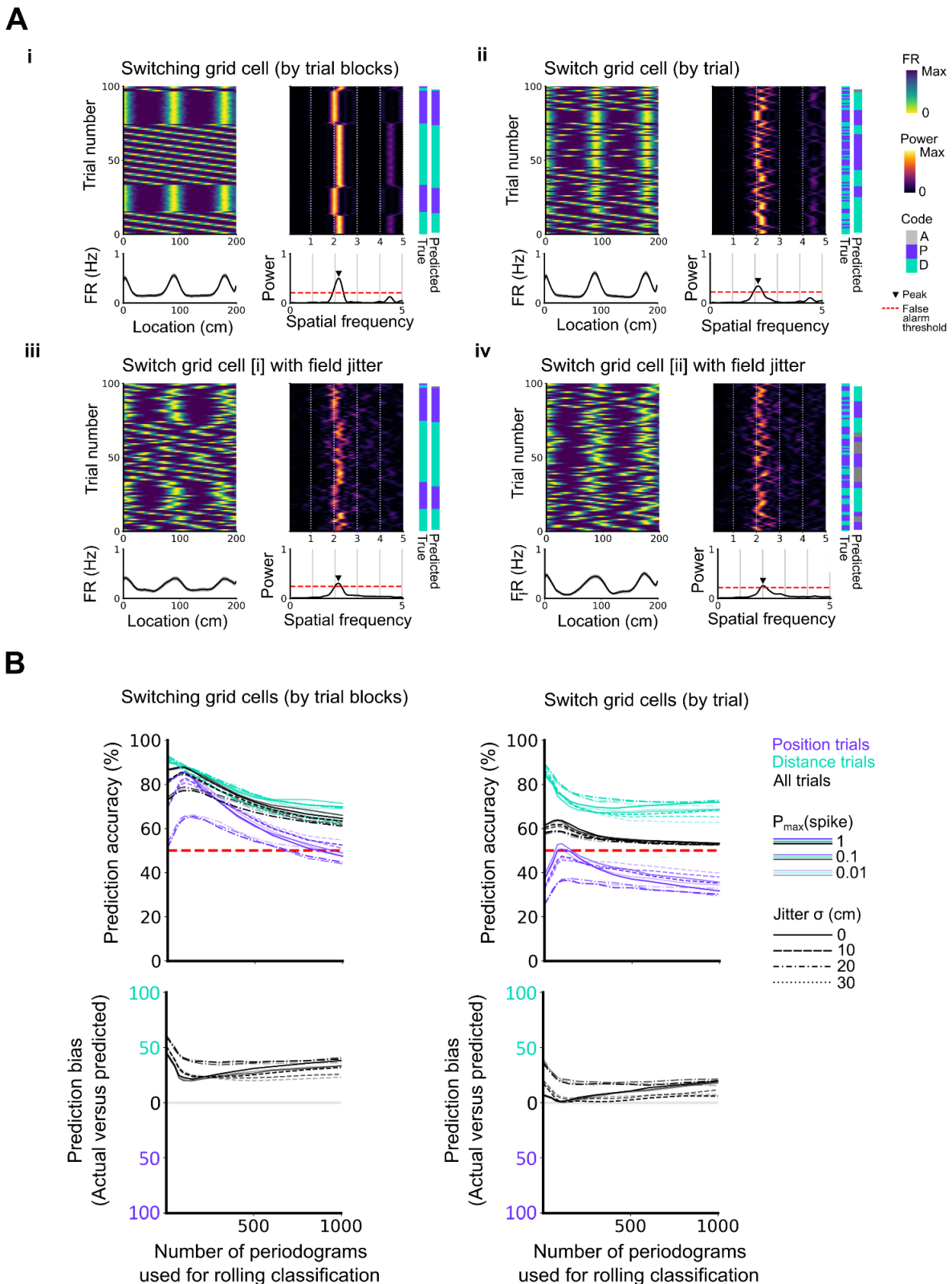


**Figure 54. Classification accuracy and bias on the level of trial as a function of rolling window size.** (A) Four example grid cells which switch between anchored and non-anchored periodic firing. Within each example shows the firing rate map across trials (top left within the example panel), the average firing rate map (bottom left), the spatial periodogram (top right), the average spatial periodogram (bottom right) and the classification labels (true and predicted; far right). (B) 100 grid cells were simulated with grid spacings between 40-400 cm (randomly assigned individually) and classified into position or distance encoding cells based on the peak spatial frequency measured from their average spatial periodograms. Each grid cell was simulated as a periodic set of firing fields following on a linear track of length 200 cm and with 100 trials. Either cells were simulated as position encoding by anchoring field locations to track locations on each trial or by continuously the periodic field locations without explicit track anchoring. In each simulation, there was an equal probability of anchoring or not anchoring. 1000 simulations were repeated over different spike rate probabilities and over different field jitters (as defined by the standard deviation of the field locations from their preassigned locations). Classifications were made on each set of simulations by comparing the spatial frequency at which a peak occurred within the average spatial periodogram. If the difference between this spatial frequency and the closest positive integer was smaller than or equal to 0.05 the cell was classified as position-encoding and distance-encoding otherwise. Prediction accuracy (left) and bias (right) are shown as a function of the number periodograms used to compute rolling classifications. Each line shows the average prediction accuracy or bias across the 100 grid cells for a given parametrisation of the simulation.

## 4.3 Results

Mice with neural implants targeting the MEC were recorded while performing an open field exploration task and a VR linear location task. Only cells that fired in both environments and recorded from mice that ran a minimum of 10 trials on a 200 cm track were analysed. Grid cells were recorded from nine mice across three separate cohorts (9 / 12) and 252 sessions ( $21.0 \pm 8.6$  per mouse; [Table 5](#)). Of the 2063 neurons recorded from qualifying sessions, 2050 fired in both environments, 103 were grid cells (5 %; vs 1% expected from the grid cell classification method based on shuffling with a 99<sup>th</sup> percentile grid score threshold; see [2.8.2](#)). The vast majority of grid cells recorded are positively assigned to the MEC (99.0 %; 102/103; [Table 5](#); [Figure 63](#)). As a result, claims made concerning grid cells are primarily with respect to MEC grid cell populations.

### 4.3.1 Grid cells encode position and distance on a linear track

What spatial coding schemes are employed by grid cells on the linear track? In order to address this, the firing rate profiles of each cell were classified into periodic (position and distance codes) and aperiodic schemes by comparing the spatial periodogram of the firing rate profile against chance-level (see [4.2.3.2](#) and [4.2.3.3](#)).

Virtually all grid cells were found to be spatially periodic, with 97% (100/103) of the corresponding spatial periodograms containing a peak power greater than the false alarm threshold derived from the field-shuffled analysis. The majority of grid cells were found to be position encoding (68/103) while a significant proportion were found to encode distance (32/103). A handful of grid cells were not classified to position or distance coding (3/103). Several examples are shown in [Figure 55](#). In comparison to non-grid cells, position encoding grid cells were observed in similar proportions as position encoding non-grid cells (66% grid cell position encoding vs 67% non-grid cell position encoding). Distance encoding grid cells however were observed in greater proportions to non-grid cells (31.1% grid cell distance encoding vs 17.6% non-grid cell distance encoding). This left a small proportion of aperiodic cells in the grid cell population while there was a significant proportion in the non-grid cell population (2.9% grid cell encoding aperiodically vs 15.7% non-grid cell encoding aperiodically).

To characterise the cells in each coding population, features of the periodicity and firing such as the peak power, the peak width and the mean firing rate were compared between groups. Peak width was defined as the difference between trough to trough within the average spatial periodogram that contained the peak. Of the two periodic coding populations, peak power

was significantly greater in position encoding neurons than distance ( $DF = 98, P = 0.0007, T = 1549.0$ , Mann-Whitney U test), showing the periodic firing patterns of position encoding neurons was better explained by a single sinusoidal component than for distance encoding neurons. As distance encoding neurons are not locked to cues on the track, the code might be more susceptible to accumulating positional errors that could broaden the peak in the spatial periodogram. It is therefore possible the differences in peak power between coding schemes reflect the spatial irregularities of firing fields of distance encoding neurons. Consistent with this idea, distance encoding neurons in general had a wider distribution of peak widths compared to position encoding neurons ( $DF = 98, P = 0.0001, KS = 0.46$ , Kolmogorov-Smirnov test). Mean firing rates weren't drastically different between encoding neurons (position vs distance,  $5.0 \pm 3.9$  vs  $3.9 \pm 2.6$ ,  $DF = 98, P = 0.21, T = 1257.0$ , Mann-Whitney U test) however aperiodic encoding grid cells did fire less than position or distance encoding grid cells (position vs aperiodic,  $5.0 \pm 3.9$  vs  $1.0 \pm 0.9$ ,  $DF = 69, P = 0.011, T = 185.0$ ; distance vs aperiodic,  $3.9 \pm 2.6$  vs  $1.0 \pm 0.9$ ,  $DF = 33, P = 0.02, T = 10.0$ , Mann-Whitney U tests). This suggested aperiodic coding of grid cells could be explained by cells that fired significantly less on the linear track.

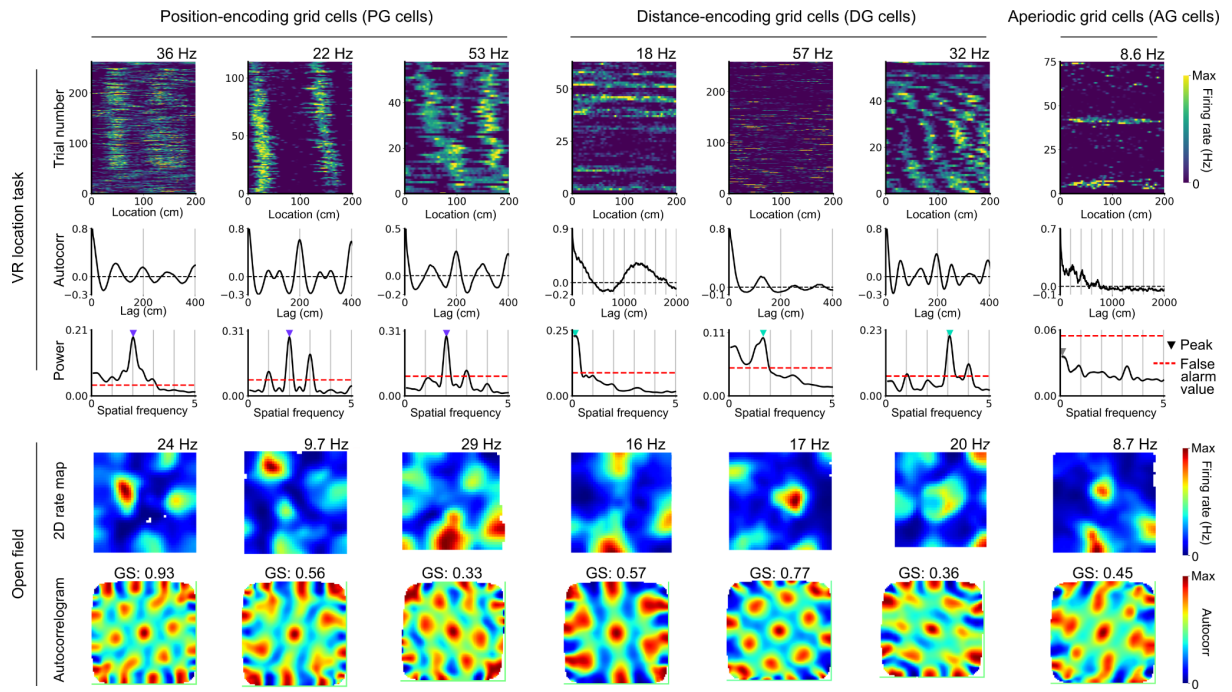


**Figure 55. Grid cells encode track location using allocentric and egocentric coding schemes.** Three example cells from allocentric and egocentric coding cells (position and distance respectively) and a single example of a cell encoding neither schemes. From top to bottom plots show: VR firing rate map across trials, VR trial-averaged firing rate map, VR spatial autocorrelation, VR session-averaged spatial periodogram, open field firing rate map and open field spatial autocorrelogram. Shaded regions indicate the standard error of the mean for the VR trial-averaged firing rate map and VR session-averaged spatial periodogram. The red line indicates the false alarm threshold estimated from a field analysis shuffle and peaks are labelled with a triangle. X-axis scales are adjusted on VR spatial autocorrelogram for several examples to visualise the long-range periodic signal.

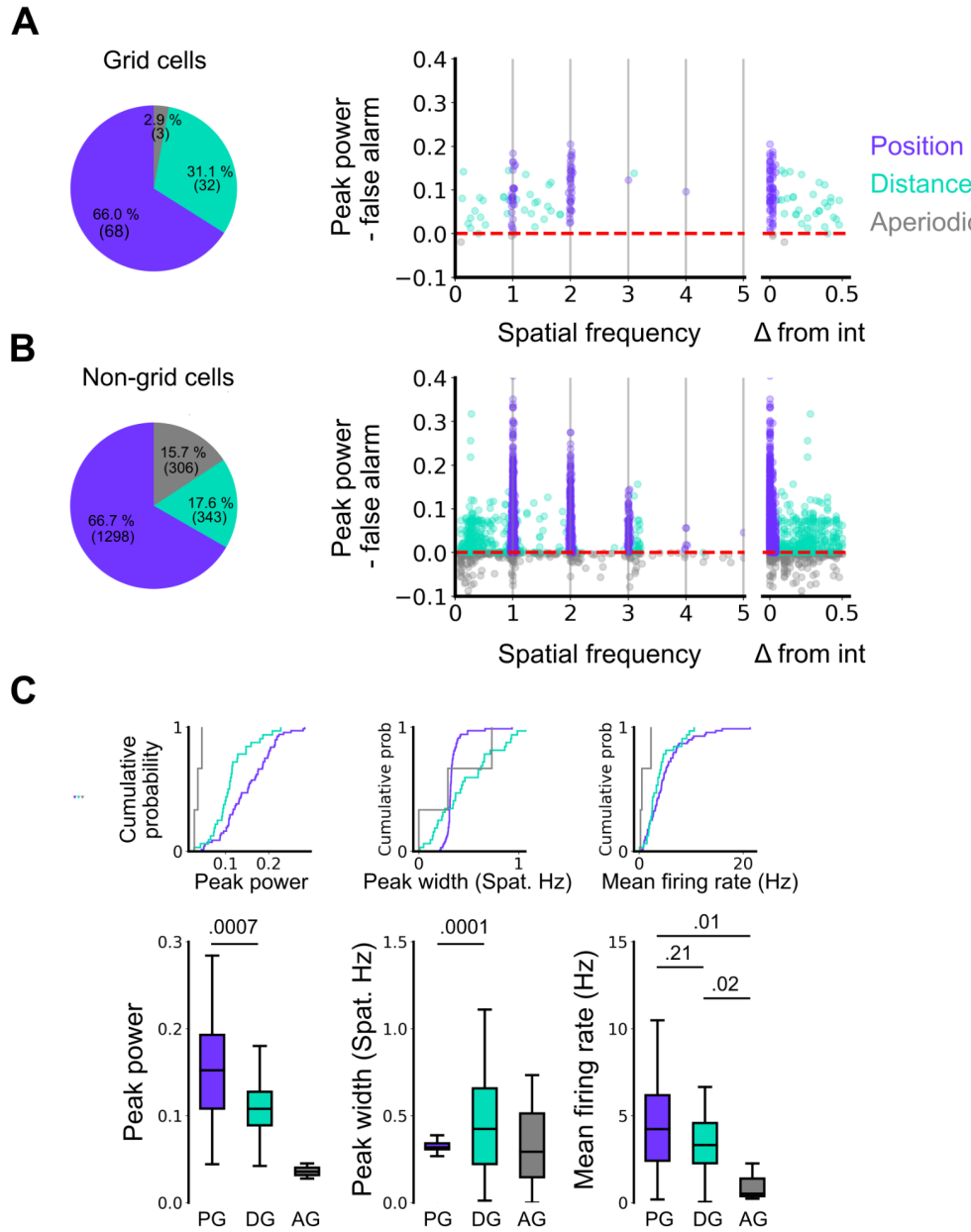


**Figure 56. Population statistics of position and distance encoding neurons.** (A) Percentage of grid cells classified to position, distance and aperiodic groups (left), the distribution of recorded grid cells' peak spatial frequency and power minus the field shuffle false alarm threshold (middle) and the corresponding distribution where the difference from an integer ( $\Delta$  from int) is the difference between the spatial frequency and the nearest positive integer (right). The Y value indicates the difference between the peak power and the false alarm threshold. Red dashed line indicates the false alarm threshold. (B) Same as A for the non-grid cell population. (C) Comparison of peak power, peak width and mean firing rate between position, distance and aperiodic encoding grid cells with (top) cumulative histograms and (bottom) box plots.

#### 4.3.2 Grid cells are not locked to a single coding scheme

Is position or distance coding by grid cells stable within a session ([Figure 57A](#)) or can the spatial code change within it? ([Figure 57B](#)). For example, a change between position and distance coding might be prompted by the gain or loss of cue anchoring dynamics. Initial analyses have shown both position and distance codes are exhibited by grid cells, but whether these differences reflect unique populations of grid cells or reflect changes at the level of spatial firing dynamics is not clear. To test this, I calculated a rolling average of the spatial periodogram across trials and computed the peak powers and their corresponding spatial frequencies to classify the spatial coding of a cell throughout the session. All trials of each trial type were included in this analysis. If grid cells are locked to a single coding scheme then their classification will be stable across the session. On the other hand, if grid cells can switch between coding schemes, their classifications too will change throughout the session. To quantify this, I assigned neurons that encoded a single coding scheme for greater than 85 % of the session to a stable coding group and cells that encoded a single coding scheme for less than 85 % of the session to an unstable coding group. I found most cells originally assigned as position and distance cells were unstable when classified on a rolling basis and these cells commonly switched between position and distance codes (76/103; 73.8 %). This is illustrated in [Figure 57D](#), as a large proportion of position-encoding grid cells (PG) and distance-encoding grid cells (DG) cells were found to encode the alternative periodic coding scheme (i.e. PG cells encoding distance and DG cells encoding position for significant portions of the session), while PG and DG cells did not encode aperiodic coding schemes for significant portions of the session. A minority of cells did exhibit stable periodic codes (27/103; 26.2 %). Examples of each type are shown in [Figure 57C](#).

To test whether codes change at behaviourally-relevant timescales (compatible with changes in behaviour), I quantified the proportion of a session in which a grid cell continuously coded a single periodic code into coding blocks. I then compared the true block lengths against block lengths measured when trials were shuffled and rolling classifications were recomputed ([Figure 58A](#)). If coding is maintained across a sequence of trials, the distribution of true block lengths will be skewed to longer block lengths compared to the shuffled trials blocks. Alternatively, if coding switched every trial or at a timescale shorter than the typical duration of a trial, the block lengths between the true and shuffled trials would be similar. Only cells that exhibited unstable periodic coding were used in this analysis. I found the distribution of true block lengths was significantly different from the shuffled trial blocks length

(Figure 58B; DF = 1765, 2359, P = 0.0003, Ks = 0.066, Kolmogorov-Smirnov test) consistent with coding remaining stable over behaviourally-relevant timescales.

Taken together, this analysis shows that classification on the level of cells fails to capture the fluidity of the recorded grid coding as single grid cells can switch between position and distance codes within a session. These switches could reflect changes in task behaviour or task perception as these switches occur on the scale of tens of trials which is consistent with behaviourally-relevant changes.

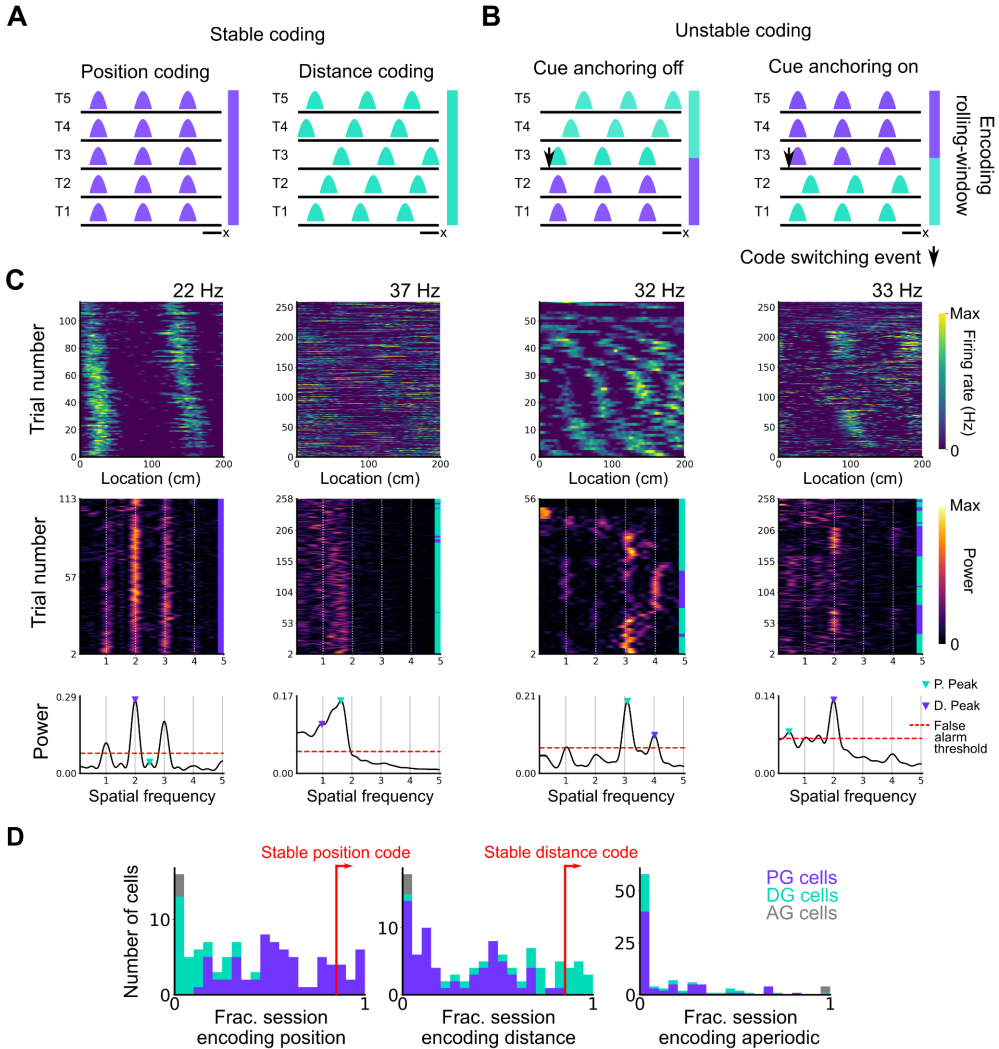


**Figure 57. Grid coding throughout a training session.** (A,B) Grid cells either maintain a coding scheme or remap within a session (top). Remapping events occur when the coding scheme changes within the session. These remapping events can be hypothesised by the gating of speed and visual information to grid cells (bottom). (C) Examples of neurons exhibiting constant positional coding, constant distance coding and remapping events. From top to bottom, plots show the firing rate map across trials, spatial periodogram across trials and the session-averaged spatial periodogram. Average periodograms are computed across trials corresponding to position and distance coding separately. (D) Histograms of the fraction of a recording session grid cells were encoding position, distance or neither. Colours in the histogram indicate the initial classification of the neurons to the position, distance or unclassified groups. The red line indicates the point at which a grid cell can be considered to encode position or distance stably.

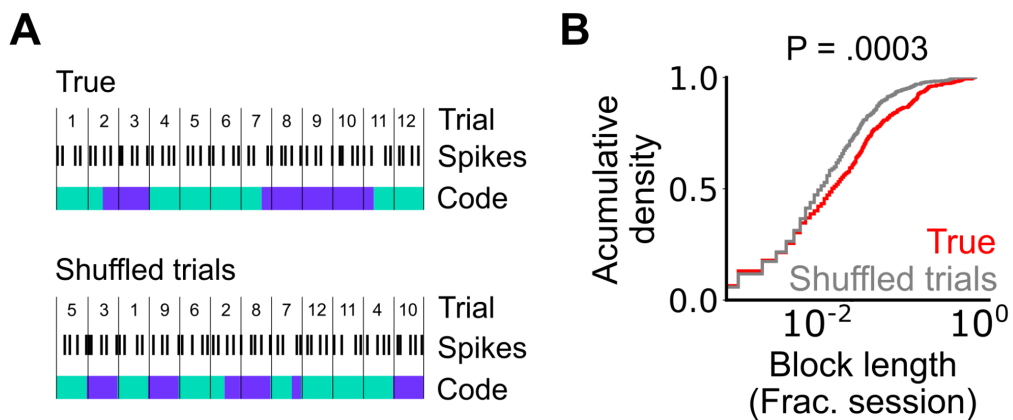


**Figure 58. Comparison of the length of periodic coding blocks.** (A) Schematic illustrating how coding blocks are recomputed from shuffling spikes at the level of trials. Spike locations are reallocated to a new position in the firing profile based on the random shuffling of trials. With these new spike locations, the rolling classification is recomputed and coding blocks can be measured. (B) Cumulative histogram of block lengths for the observed grid cells (red) and the same grid cells with the trial order shuffled and blocks recalculated (grey). P value for the Kolmogorov-Smirnov test is labelled above.

#### 4.3.3 Pairs of grid cells switch between periodic coding schemes coherently

Does the spatial coding of one grid cell coincide with the spatial coding of another? In other words, do grid cells switch between periodic coding schemes coherently? Individual grid modules are well modelled by continuous attractor dynamics (K. Yoon et al. 2013; Gardner et al. 2022). Consistent with this, neurons maintain phase relationships across environments (Caswell Barry et al. 2007; Waaga et al. 2022) and are similarly maintained in sleep (Trettel et al. 2019; Gardner et al. 2019; 2022). In line with this coherence, I predicted pairs of grid cells recorded within the same recording session would change coding schemes at the same points during a session. To test this, I compared the positions of the coding blocks with a shuffled arrangement of the coding blocks within the population of remapped grid cells ([Figure 59B](#)). I computed an agreement score as the proportion of the session where codes between a pair of grid cells overlapped. An agreement matrix in [Figure 59C](#) illustrates the agreement between all pairs of grid cells from a single recording and the corresponding agreement when the blocks are shuffled and an average computed across 100 shuffles. Shuffling the coding blocks and computing an average across shuffles provides an estimate of the expected agreement score if grid coding is independent of other grid cell coding. Agreements were compared between the observed and shuffled grid cell pairs and revealed the observed agreements were significantly greater than the corresponding shuffled agreements ( $DF = 121$ ,  $P < 1e-18$ ,  $T = 290.0$ ; Wilcoxon sign-rank test). This result is consistent with the coherent remapping of grid cell modules as previously observed (Caswell Barry et al. 2007; H. Stensola et al. 2012). Interestingly, grid cells 28 and 31 appeared to be less coherent with all other simultaneously recorded grid cells. Grid cell 28 was the only cell classified as a distance-encoding cell whereas grid cell 31 was classified as a position-encoding cell. The lack of coherence might be explained by these cells belonging to different grid modules, as both cells differed from a spatial frequency of 2 at which the peak power was observed. Grid spacings as calculated from the corresponding open field session did indicate that grid cell 31 had a larger grid spacing than the remaining recorded grid cells but this was not the case for grid cell 28 (Grid spacing:  $GC_{28} = 58.1$  cm vs GC session average =  $66.8 \pm 11.8$  cm,  $GC_{31} = 77.0$  cm vs GC session average =  $63.6 \pm 11.1$  cm). If grid cell 31 does indeed belong to a different grid module, this further highlights coherent remapping might be a feature of independently remapping grid modules (Caswell Barry et al. 2007; H. Stensola et al. 2012) however many more neurons across multiple grid modules will need to be recorded from in order to deliver strong evidence for this.

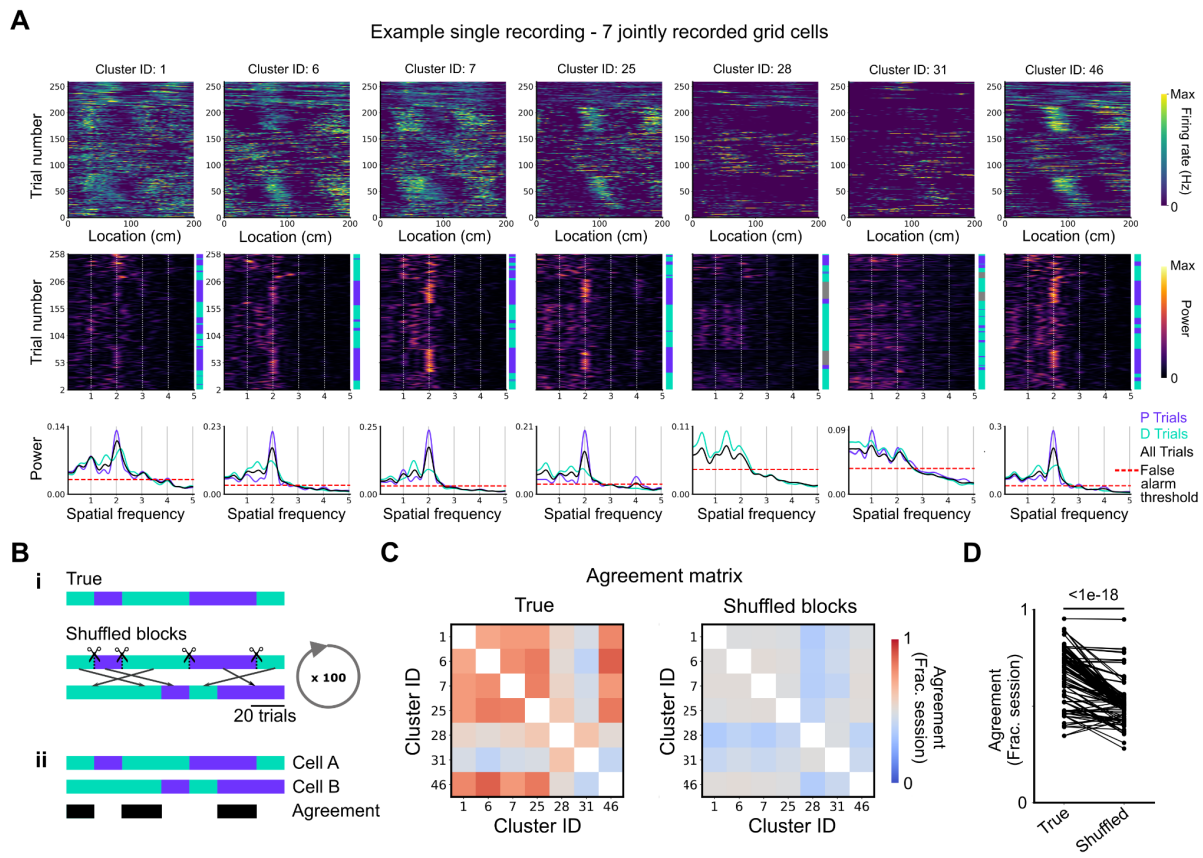


**Figure 59. Grid cells switch between coding schemes coherently.** (A) Joint activity of 7 simultaneously recorded grid cells. From top to bottom, plots show the firing rate map across trials, spatial periodogram across trials, and the average spatial periodogram. (B) (I) Encoding blocks are shuffled by positioning whole encoding blocks at random positions and (II) an agreement score calculated based on the proportion of the session where coding blocks overlap between two cells. This is repeated 100 times per shuffle and average agreement score calculated (C) Agreement matrix for the coding scheme across a session for the example cells in A for the true comparison and between shuffled blocks. (D) Agreements between the true grid pairs and the block shuffled pairs test whether coding blocks agree within a session between pairs of grid cells above chance level (122 grid pairs across 18 sessions). Only cells without a stable coding scheme were compared (< 85 % of a stable coding scheme; Wilcoxon sign-rank test).

#### 4.3.4 Grid coding is associated with path integration-dependent behaviours

Are the periodic coding schemes of grid cells associated with spatial behaviours presented by the animal? First, a ‘by-cell’ analysis was considered. Stopping behaviour was collated from all sessions in which stable position coding and distance encoding grid cells were found. Histograms of these stops indicated there was no apparent difference between position and distance coding grid cells for beacons trials but there was a large difference for non-beaconed trials ([Figure 60A](#)). To quantify these differences, the percentage of correct trials, the amplitude of the peak of the stop histogram within the reward zone and the location of the peak were all compared between coding schemes for each trial type. Sessions which contained at least one stable position encoding grid cell were no more successful during the beacons trials than sessions which contained at least one stable distance encoding grid cell ( $DF = 18$ ,  $P = 0.057$ ,  $T = 75.0$ , Mann-Whitney U test). This was not the case on non-beaconed trials, as sessions which contained at least one stable position encoding grid cell were more successful than sessions which contained at least one stable distance encoding grid cell ( $DF = 18$ ,  $T = 92.0$ ,  $P = 0.001$ , Mann-Whitney U test). This was further reflected when comparing the peak of the stopping histogram within the reward zone which corresponds to how frequently across all trials the animal successfully stopped in the reward zone (beacons trials,  $DF = 18$ ,  $P = 0.32$ ,  $T = 76.0$ ; non-beaconed trials,  $DF = 18$ ,  $P = 0.002$ ,  $T = 82.0$ , Mann-Whitney U test). The peak location of the stopping histogram did not differ between coding schemes for either trial type (beacons trials,  $DF = 18$ ,  $P = 0.06$ ,  $T = 40.5$ ; non-beaconed trials,  $DF = 18$ ,  $P = 0.44$ ,  $T = 31.5$ , Mann-Whitney U test).

As the majority of grid cells displayed some level of remapping, a ‘by-trial’ analysis was considered to address whether position and distance coding were aligned to success or failures. To test this, the spatial behaviours from both beacons and non-beaconed behaviours were compared across trials in which grid cells were found to encode position and distance. Trials were grouped by three different factors, (1) trial type, (2) trial outcome, and (3) the dominant coding scheme observed by the grid cell. In this analysis, all grid cells were included rather than the small subset of stable encoding grid cells. Similar to the ‘by-cell’ analysis, the stopping histogram appeared to show no apparent differences in stopping behaviour on beacons trials but possibly differences on non-beaconed trials ([Figure 60B](#)). Beacons trials in which grid cells encoded position were no more successful than beacons trials in which grid cells encoded distance ( $DF = 80$ ,  $P = 0.3$ ,  $T = 1198.0$ , Wilcoxon sign-rank test). On the other hand, non-beaconed trials in which grid cells encoded position were significantly more successful than non-beaconed trials in which grid cells encoded distance ( $DF = 80$ ,  $P < 1e-4$ ,  $T = 586.5$ ; Wilcoxon sign-rank test). Comparing the

peak amplitude of the stopping histogram within the reward zone revealed more successful stops occurred on position-encoding trials than distance-encoding trials for non-beaconed trials but wasn't the case on beaconed trial (beaconed trials,  $DF = 81$ ,  $P = 0.57$ ,  $T = 1541.0$ ; non-beaconed trials,  $DF = 81$ ,  $P = 0.0007$ ,  $T = 943.0$ , Mann-Whitney U test). Again, the peak location of the stopping histogram did not differ between coding schemes for either trial type (beaconed trials,  $DF = 81$ ,  $P = 0.88$ ,  $T = 1216.0$ ; non-beaconed trials,  $DF = 81$ ,  $P = 0.83$ ,  $T = 1216.0$ , Mann-Whitney U test). Several example remapped grid cells are shown in [Figure 61](#). From these examples, it is clear engagement in non-beaconed but not beaconed tasks align with positional coding of grid cells suggesting anchoring of track cues is required for successful non-beaconed trials.

To complement the 'by-trial' analysis, it was considered what proportion of different trial outcomes corresponded to particular coding schemes. To address this, trials were classified in both the trial outcome and the coding scheme of a recorded grid cell. The percentage of trials that were classified as a particular coding scheme was calculated for each trial outcome. [Figure 62](#) shows that as the quality of the trial outcome increases (hit > try > run), the proportion of trials that correspond to position-encoding also increase in non-beaconed but not beaconed trials. Conversely, the proportion of trials that correspond to distance-encoding decreases as a function of trial outcome in non-beaconed trials but not beaconed trials. Using a one-way ANOVA, trial outcome was found to be a significant factor in the variation of the proportion of position-encoding in non-beaconed trials but not in beaconed trials (beaconed,  $DF = 32$ ,  $P = 0.6$ ,  $F = 0.51$ ; non-beaconed,  $DF = 76$ ,  $P < 1e-7$ ,  $F = 20.2$ ).

Taken together, these results indicated that the spatial behaviours displayed were indeed different between sessions containing position and distance encoding grid cells as well as at the level of trial, though only for non-beaconed trials. As path integration is required for successful stopping on non-beaconed trials, these results provide evidence that positional coding of grid cells is associated with successful path integration operations.

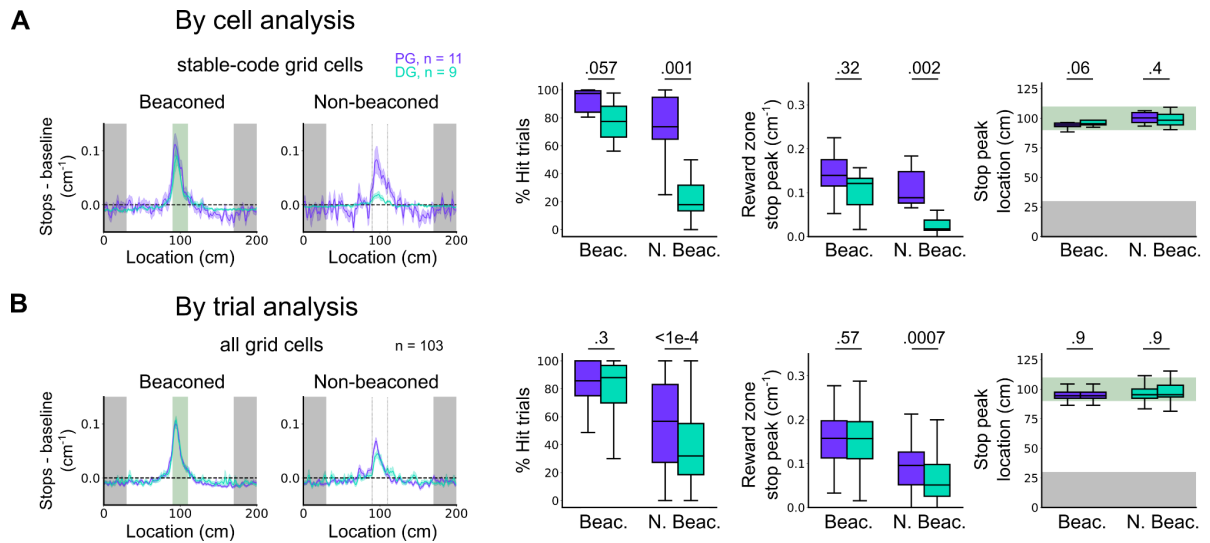


**Figure 60. Comparison of spatial behaviour during position and distance encoding trials.** (A) Cells assigned to the stable position and stable position group were compared by each trial type by their (left to right) stopping histogram, hit percentage, peak amplitude of stops in the reward zone and location of the stopping peak. (B) Same as in A but in this analysis, all grid cells were included and trials partitioned based on whether the grid cell was encoding position or distance. Shaded region of the stop histogram shows standard error of the mean across cells.

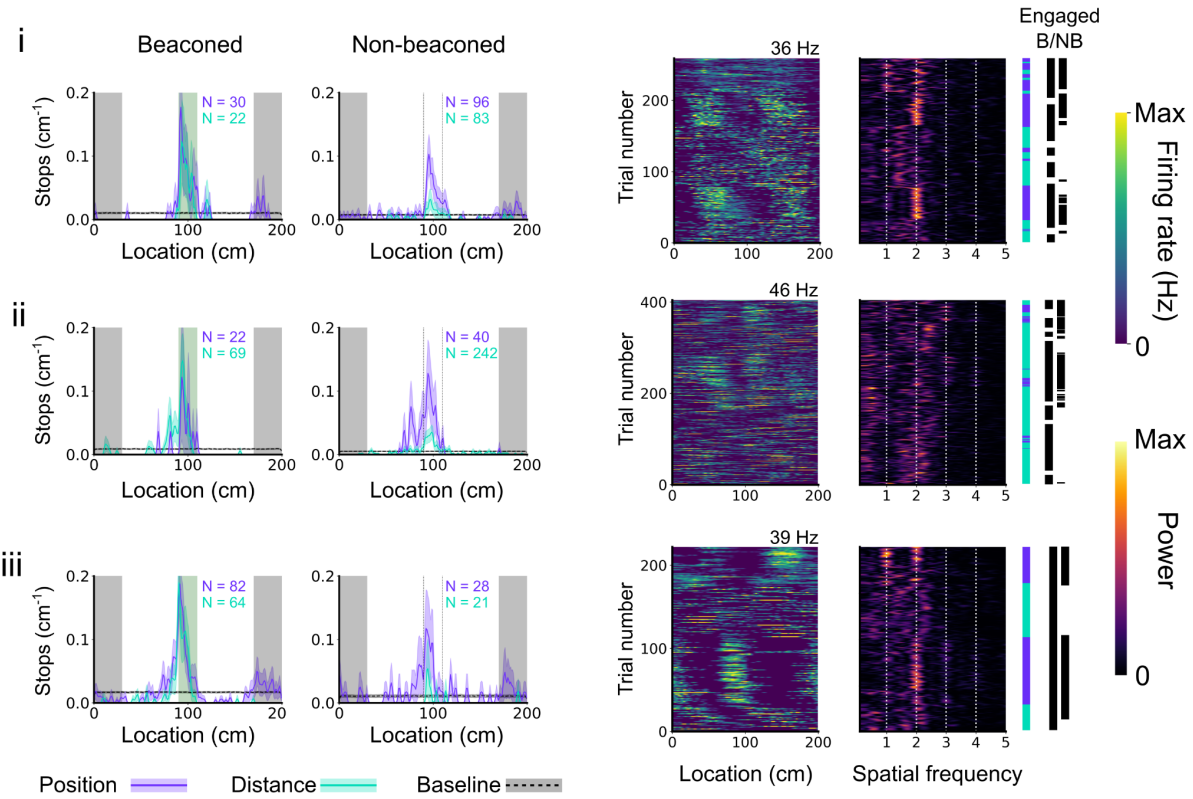


**Figure 61. Stopping behaviours during grid cell position and distance encoding trials.**

Three example grid cells from three separate sessions are shown. From left to right, plots show the stop histogram during position and distance encoding beacons trials, likewise with non-beaconed trials, the firing rate map across all trials, the spatial periodogram with rolling-window classifier, the active engagement in the task showing beacons and non-beacons trials separately. The number of trials used to construct the stop histograms are labelled on each histogram. Animals are considered engaged in the task if they do not exceed a streak of 3 successive failed trials for a given trial type. Shaded regions of the stop histogram indicate the standard error of the mean across trials. Peak firing rates are given for the firing rate maps.

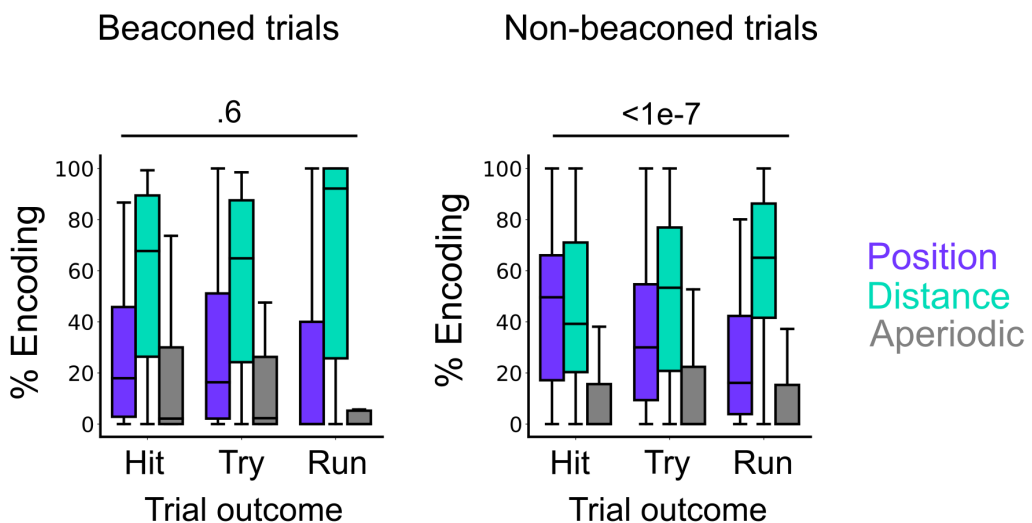


**Figure 62. Proportion of hit, try and run trials corresponding to position, distance or aperiodic coding schemes.** Trials from sessions with at least one recorded grid cell were grouped based on trial outcome. For each grid cell, the percentage of trials classified to position, distance or aperiodic coding was calculated for each trial outcome. To test the influence of trial outcome on the occurrence of a particular coding scheme, a one-way ANOVA was computed across the percentage encoding for the position coding scheme (beaconed,  $DF = 32$ ,  $P = 0.6$ ,  $F = 0.51$ ; non-beaconed,  $DF = 76$ ,  $P < 1e-7$ ,  $F = 20.2$ ; shown in figure), Consistent with positional but not distance or aperiodic coding being beneficial for path integration behaviours, quantifying the influence of the trial outcome on the occurrence of distance and aperiodic coding, showed distance coding was detrimental to accurate path integration but not beaconing (beaconed,  $DF = 32$ ,  $P = 0.08$ ,  $F = 2.6$ ; non-beaconed,  $DF = 76$ ,  $1 < 1e-6$ ,  $F = 16.8$ ; not shown in figure), while aperiodic coding was not found to be linked to trial outcomes (beaconed,  $DF = 32$ ,  $P = 0.14$ ,  $F = 2.1$ ; non-beaconed,  $DF = 76$ ,  $P = 0.6$ ,  $F = 0.51$ ; not shown in figure).

#### 4.4 Discussion

Following the identification of grid cell firing on the virtual reality track, I asked what coding scheme was being utilised throughout the linear location task. I found the vast majority of recorded grid cells (97.1 %; 100/103) demonstrated periodic spatial firing which could either be assigned to a positional firing scheme (68/103), which corresponds to periodic firing that was anchored and reset by features of the track or a distance encoding firing scheme (32/103), which corresponds to periodic firing that did not anchor or reset with features of the track. The first recordings of grid cells on virtual tracks suggested all grid cells would anchor to salient features of the track (Domnisoru, Kinkhabwala, and Tank 2013), however my findings are the first to demonstrate grid cells are not strictly anchored to track cues but rather remap between position and distance codes. The remainder of grid cells did not demonstrate any periodic firing signal (2.9 %; 3/103). Whether this small percentage reflects a true subset of grid cells that lose periodic firing properties when recorded in a virtual linear location estimation task is unclear. These cells might reflect a subset of false positive grid cells, or may indeed be true grid cells. Recording from more grid cells either with high density probes or in greater numbers of mice will add power to address whether grid cells can lose their periodic firing in virtual environments. Alternatively, an altered experimental design could be employed whereby an open field recording session takes place before and after the linear location task. Only cells that qualify as grid cells in both open field sessions would be considered true grid cells. This conservative classification would more likely eliminate false positive grid cells and afford an analysis of the periodic firing of true grid cells.

Of the grid cells that exhibited periodic firing, the majority (64 %; 64/100) were found to remap between position and distance codes (<85 % of the session occupied by a single coding scheme) while the remainder were found to maintain the same coding scheme throughout the session (>85 % of the session occupied by a single coding scheme). Whether this remapping occurs in open field settings is less clear as many more salient cues are available. Accumulations of grid coding errors away from boundaries of open field arenas (Hardcastle, Ganguli, and Giocomo 2015) may reflect a loss of cues in which to anchor to, which in turn may reflect the distance coding scheme observed in this chapter. In virtual track studies, Low et al. (2021) employed a similar task analogous to the beacons linear location task shown in this thesis. They found cells in the entorhinal cortex remapped between multiple stable position coding schemes and also unstable coding schemes which may have been the observed distance coding scheme. The authors reported the remapping events were instigated by changes in running speed. Contrary to their findings, I found remapping between position and distance coding schemes was consistent with the level of task

engagement for the non-beaconed trials but not beaconed trials. As the task used by Low et al. (2021) lacked non-beaconed trials, the authors could not look at the same path integration-specific behaviours. Low et al. (2021) also found remapping events occurred at the same time for concurrently recorded entorhinal cells. Consistent with these results, I found grid cell pairs recorded together remap at the same time. Taken together, these results are consistent with the coherent spatial firing properties of individual grid modules, however whether individual grid modules can remap independently of other modules remains to be seen as this requires high density neural probes to record from numerous grid cells that span across different modules. This was not addressed by Low et al. (2021) but could easily be looked at within the high density probe dataset they collected.

#### 4.4.1 Technical challenges

I came across several issues during the analysis described in this chapter which warrants discussion for any researcher looking to build upon these analyses. To address the spatial firing properties of grid cells during the linear location task, mice were trained in the linear location task and placed in an open field arena to freely explore. After this, I required a method of identifying neurons across these environments following spike sorting. I added a feature to the electrophysiology analysis pipeline established by Sarah Tennant and Klara Gerlei, to concatenate and spike sort any number of recording sessions together. Spikes were assigned to clusters across all recording sessions which avoided the need for parameterized methods of cluster-matching.

Once all grid cells were identified and their spatial firing properties could be analysed on the virtual track, a method was required to classify the coding scheme utilised. Jacob et al., (2019) devised an analysis to classify grid cells to either allocentric firing or integrated firing analogous to the position and distance codes discussed in this chapter. This method required calculating a correlation value of the firing rate profile across trials to compute the allocentric firing correlation and comparing this to a egocentric firing correlation which is calculated by computing a firing correlation with a recomputed length of each trial which is consistent with the period between firing fields. I looked to simplify the classification between position and distance coding by employing commonplace statistics in the study of periodicity, such as quantifying periodicity by estimating the Fourier transform of the periodic signal. I found computing periodic signals that were anchoring to specific track locations would reflect sinusoid components of the Fourier transform which were close to integer values, consistent with fields that perfectly repeated each trial. To classify between position and distance coding, the maximum of the estimated Fourier transform was used as a metric for the best

fitting sinusoid. A maximum peak above chance level significantly away from an integer value was deemed sufficient to classify a cell as distance encoding. This significance value was set at 0.05, and might require further investigation to validate the method described.

#### 4.4.2 Behavioural and computational roles

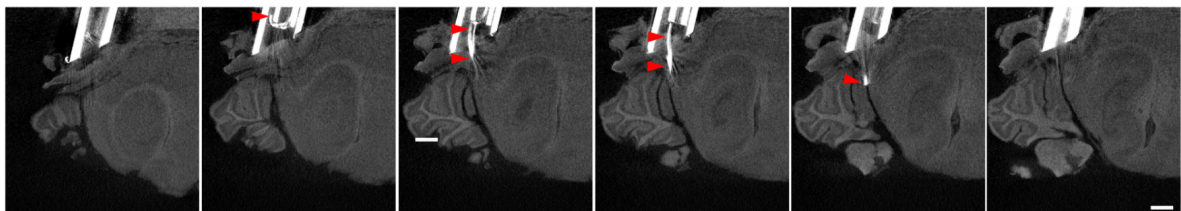
Analysing the spatial coding on a trial-by-trial basis revealed grid cells switch between position and distance coding schemes regularly. It was found that when grid cells were positional coding, mice performed better than when grid cells were distance encoding. This was only the case for non-beaconed trials but not beaconed trials suggesting the positional coding of grid cells is beneficial to path integration but not beaconing behaviours. Consistent with findings from Gil et al. (2018) who showed grid cells were disrupted in a group of mice that performed worse at a path integration task but not at a beaconed variation of the same task, the finding in this chapter links positional coding of grid cells to accurate path integration. Tennant et al. (2018) also found deficits in path integration behaviours in the linear location task following the inactivation of stellate cells in the MEC, which are one of the anatomical cell-type of grid cells (Domnisoru, Kinkhabwala, and Tank 2013). As grid cells were not directly recorded, it remains unclear what spatial firing properties were disrupted to cause the impaired spatial behaviours.

Based on the findings to date, this thesis provides evidence that anchoring of grid fields specifically enhances stopping behaviour on path-integration but not beaconing-based navigation. I hypothesise the positional coding scheme exhibited by grid cells is the default coding scheme while the animal is actively engaged in a path integration behaviour. Under this scheme, the mouse takes notice of salient features of the environment to anchor the grid code and provide a consistent phase code across multiple grid modules from which an accurate location estimate can be readout. One might expect mice to perform equally well using a distance encoding grid code as distance information is stored within the periodicity of a distance code, however anchoring of this grid code appears to be important for accurate path integration. When not actively engaged in path integration, the grid code maintains periodic firing but is not anchored to salient features of the track. A high accuracy is still possible on beaconed trials as no position estimate needs to be readout from the grid system to receive a reward. Instead, mice simply need to associate the reward zone cue with the reward.

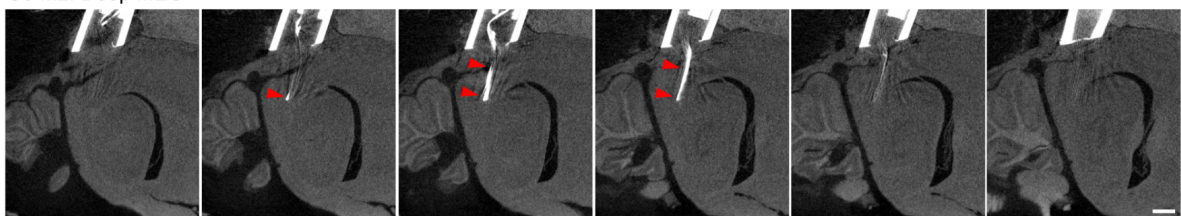
## 4.5 Appendix

### 4.5.1 Tetrode localisation

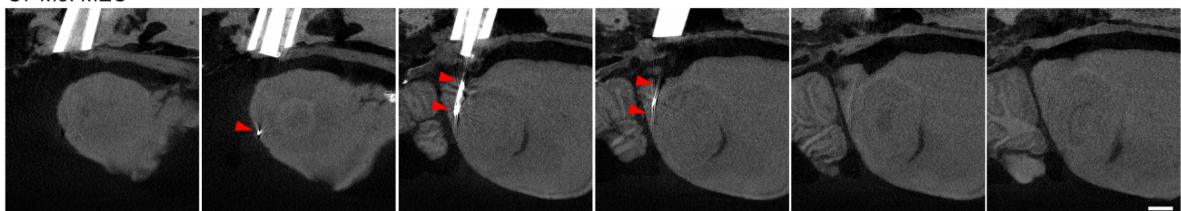
C6 M1: MEC



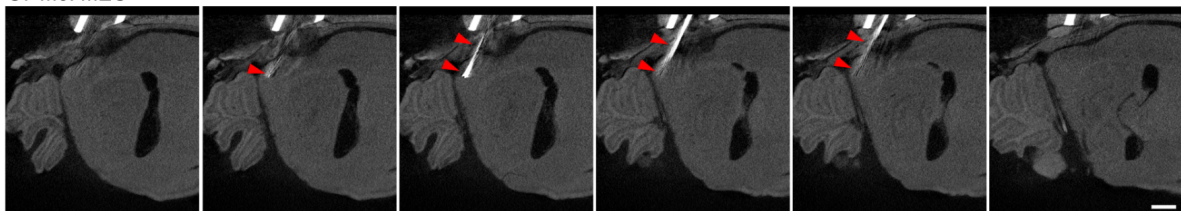
C6 M2: Deep MEC



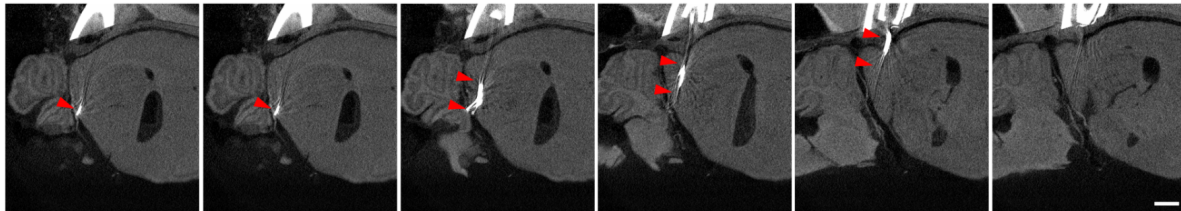
C7 M3: MEC



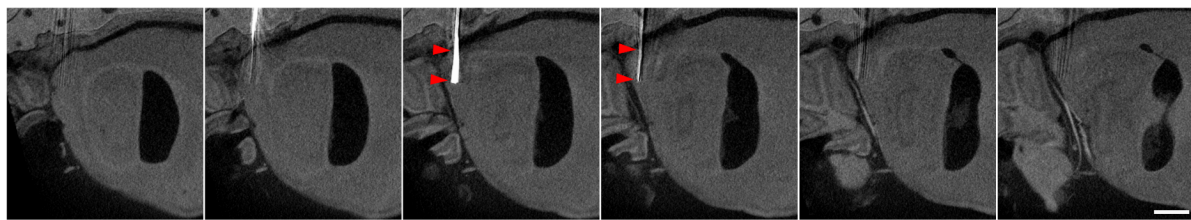
C7 M6: MEC



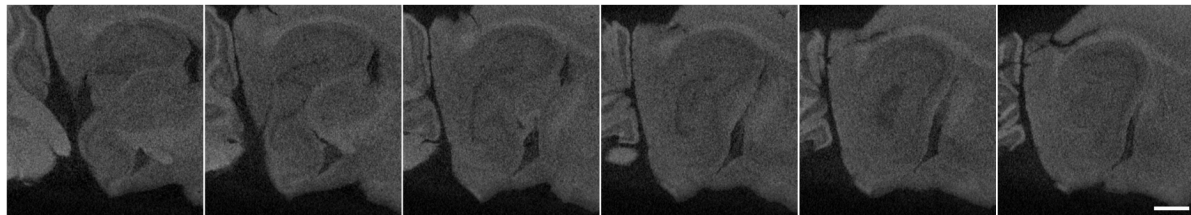
C7 M7: MEC



C7 M11: MEC



C7 M12: Unclassified



C7 M13: MEC



C7 M14: MEC

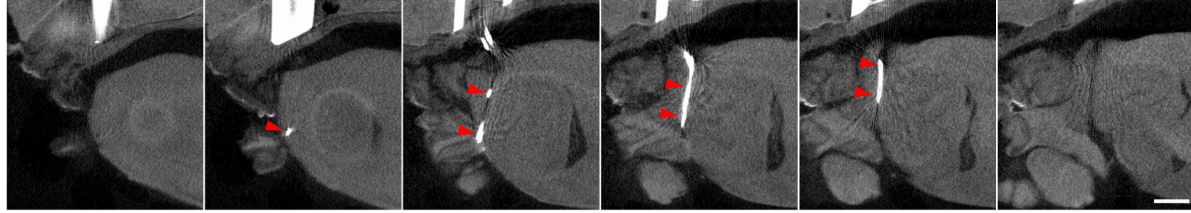


**Figure 63. Tetrode localisation.** Micro-CT images used for assessment of tetrode locations in nine mice. For each animal, sagittal slices are presented lateral to medial from left to right and the classification of the tetrodes target is shown at the top left. This classification is based on the terminal location of the tetrode and the distance travelled during the experiment (see Methods). Mouse M4 was processed from cresyl violet staining and tetrode track localisation however had no visible tetrode tracks in any slice and are not shown. Two further mice M10 and M15 sustained significant damage duration preparation for microCT imaging and were not imaged. Mouse M12 was imaged without the headpost (and tetrodes) attached, no negative trace of the tetrode tracks were clearly seen. In all images red triangles point to the putative tetrode tracks. Scale bar denotes 1 mm.

Mouse	N cells	N sessions	N grid cells (%)	Tetrode location
M1	53	11	3 (5.7)	MEC
M2	24	9	0 (0)	Deep MEC
M3	258	26	7 (2.7)	MEC
M4	23	17	0 (0.0)	Unclassified
M6	233	21	1 (0.4)	MEC
M7	202	23	4 (2.0)	MEC
M10	67	16	1 (1.5)	Unclassified
M11	573	35	53 (9.2)	MEC
M12	118	21	1 (0.8)	Unclassified
M13	172	25	7 (4.1)	MEC
M14	298	37	26 (8.7)	MEC
M15	42	11	0 (0.0)	Unclassified
Average	171.9. $\pm$ 152.2	21.0 $\pm$ 8.6	15.1 $\pm$ 8.6 (2.9 $\pm$ 3.2)	
Total	2063	252	103	

**Table 5. Summary of recorded grid cells and estimated tetrode locations.** Tetrode locations were estimated from microCT images as in [Figure 63](#). For average measurements, standard deviations are provided.

# Spatial representation by ramping activity of neurons

## 5.1 Introduction

While grid cells are thought to play a key role in path integration computations, how an animal can plausibly read this coding scheme into an unambiguous self-location representation is less clear. Current models suggest a representation of space can be recalled from the activity of collective modules of grid cells (Stemmler, Mathis, and Herz 2015; Fiete, Burak, and Brookings 2008; Bush et al. 2015), however such models require previously unobserved intermediate spatial representations. One such cell type is predicted to represent space with a firing rate proportional to the distance to a goal location (Stemmler, Mathis, and Herz 2015; Fiete, Burak, and Brookings 2008; Bush et al. 2015). If such cells do exist, they would appear as cells with ramping firing rate profiles in the VR linear location estimation task detailed in Chapters 2 and 3. This chapter will investigate these prospective ramp cells and their possible role in spatial representation.

The first question to ask is do these ramping firing rate profiles exist in spatial cortices? And if so, do these representations reflect a relationship with location? These representations were found in roughly 40 % of the recorded cell population in the medial entorhinal cortex, parasubiculum and presubiculum. Within this population, the majority of cells were most strongly influenced by position. These positional-encoding ramp cells were found to encode reward locations uniquely from non-rewarded parts of the track through an interruption of the ramping activity. This was maintained in trials where the cue was not visible and also when the mouse was not engaged in the task suggesting this interruption represents a spatial memory of the reward zone that can be recalled while the mouse is path integrating towards the goal. These cells were found to be largely non-overlapping with populations of classically defined spatial-modulated cell types (grid, border, head direction cells), suggesting a collaborative role with useful representations during the task (such as grid cells).

Work detailed in this chapter was a collaboration between the authors of the publication “Spatial representation by ramping activity of neurons in the retrohippocampal cortex” (Tennant et al. 2022). I contributed to all parts of the analysis detailed in this chapter.

## 5.2 Methods

### 5.2.1 Subjects

13 male wild type C57BL/6NCrl mice were obtained (Charles River) and surgically implanted between the ages of 10-15 weeks. Two mice were excluded as tetrodes were found to be within visual cortices and not the targeted retrohippocampal regions. Of these 11 mice, 1 mouse was trained by Sarah Tennant, 2 by Junji Hua, 2 by Wannan Yang and 6 from myself.

### 5.2.2 Data analysis

Preprocessing, spike sorting, and post-processing was completed as detailed in Chapter 2: Methods and Materials. Analysis of the spatial firing properties was performed in Python 3.8. Statistical analysis and population-level analysis was performed in R (v 4.1.2).

### 5.2.3 Measuring ramp-like spatial codes

#### 5.2.3.1 Possible coding schemes

Neural coding for space was discovered in place cells (O'keefe and Nadel 1978) as a subset of hippocampal cells were shown to fire when a rat was at a particular location within its environment. As the rat moved away from the place cell's firing field, the cell's firing rate dropped to zero. This discrete coding scheme has also been observed in dorsal MEC neurons with multiple firing fields (Fyhn et al. 2004) and in grid cells of the MEC and pre/parasubiculum (Hafting et al. 2005; Boccara et al. 2010). Discrete coding schemes provide a solution to self-localisation within an environment when there are sufficient neurons to tile the available space. The combination of firing rates within this population can then provide a position estimate (Fiete, Burak, and Brookings 2008; Stemmler, Mathis, and Herz 2015; Bush et al. 2015). In contrast, a continuous code scheme can theoretically be used to encode using a single neuron. Such representations have been observed in striatal neurons which ramp in anticipation of reward locations (Howe et al. 2013). Continuous coding schemes might also be a key component to the readout of location from grid modules (Stemmler, Mathis, and Herz 2015; Fiete, Burak, and Brookings 2008; Bush et al. 2015). In these models, an intermediate spatial cell fires proportionally to the distance to a goal location. In the linear location task, this would appear as distinct ramp codes occurring up to the reward zone, with some configuration occurring at the reward zone. These representations are illustrated in [Figure 63](#) showing ramp-like codes increase or decrease their firing rates up to the reward zone, before switching the polarity or resetting the ramp.

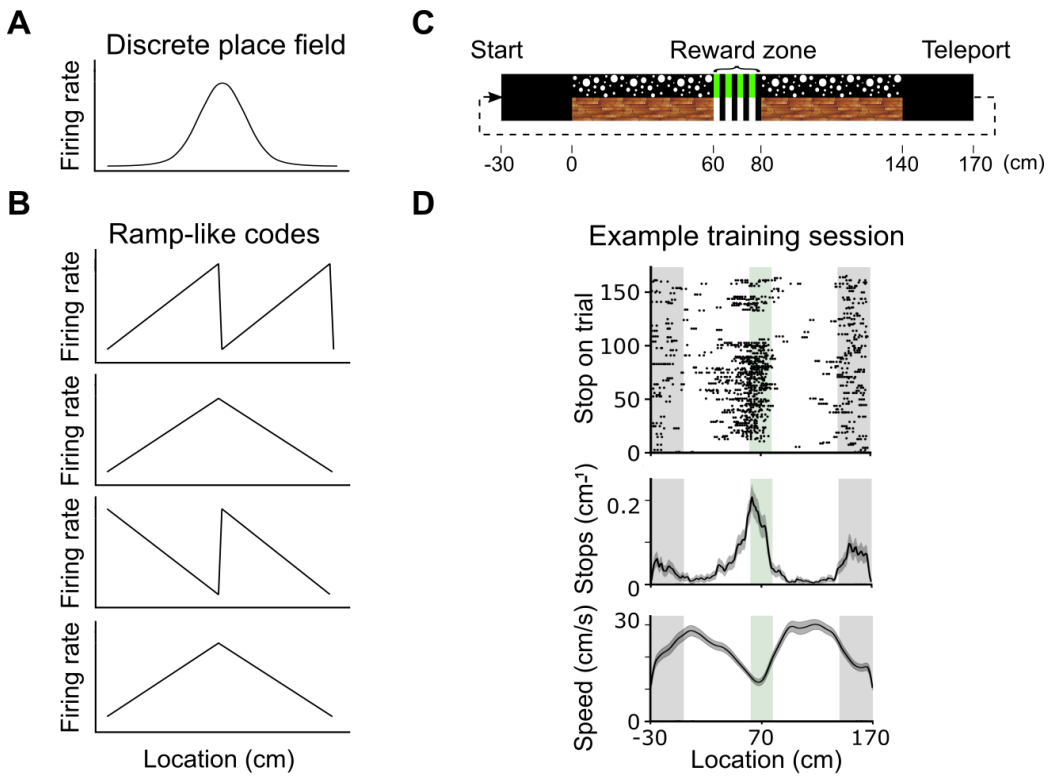


**Figure 64. Neural codes for location.** (A) Discrete and (B) continuous coding schemes on a linear track. (C) Schematic of the virtual reality linear track. (D) Spatial behaviour from an example training session, showing from top to bottom, the stop raster, stop histogram and average speed profile. Shaded regions indicate the standard error of the mean across trials.

### 5.2.3.2 Classifying spatial ramp-like neural activity

To investigate whether ramp-like firing profiles exist in spatial cortices, linear regression was performed on the unsmoothed trial-averaged firing rate profiles from neurons of mice performing the linear location task. The analysis initially focused on trials in which the mouse received a reward on beaconed trials. Linear regression was calculated on pre-reward zone and post-reward zone regions of the track (0-60 cm, 80-140 cm respectively) separately. To statistically determine whether modal fits were consistent with spatial ramping properties, each neuron was compared to a shuffled dataset generated from a trial-independent cyclic shuffling procedure, as detailed in [Figure 64](#). A cyclic shuffle implemented at the trial level was necessary as it was found a standard cyclic shuffle (typically used to classify spatial cells in the open field, see [2.8.2](#)) did not appropriately remove the spatial correlations between trials, presumably because trial times can be similar within a session. Moreover, it was found that the process of smoothing firing rate maps introduced false-positive ramping neurons (not shown). As a consequence, all analysis performed in this chapter is done using unsmoothed firing rates in both space and time. Where firing rate profiles are illustrated in figures, the smoothed firing rate maps are shown.

Neurons were classified as having ramping activity with positive or negative slopes if the linear model was significant (corrected  $P < 0.01$ ), and the slope was outside the 5-95 % intervals of the shuffled data.  $P$  values obtained from the linear model were corrected for multiple comparisons using the Benjamini & Hochberg method (Benjamini and Hochberg 1995). Neurons not meeting these criteria were allocated to the unclassified group. This yielded six possible combinations of ramping before the reward zone with subsequent classifications after the reward zone (+ +, + -, +un, - -, - +, -un).

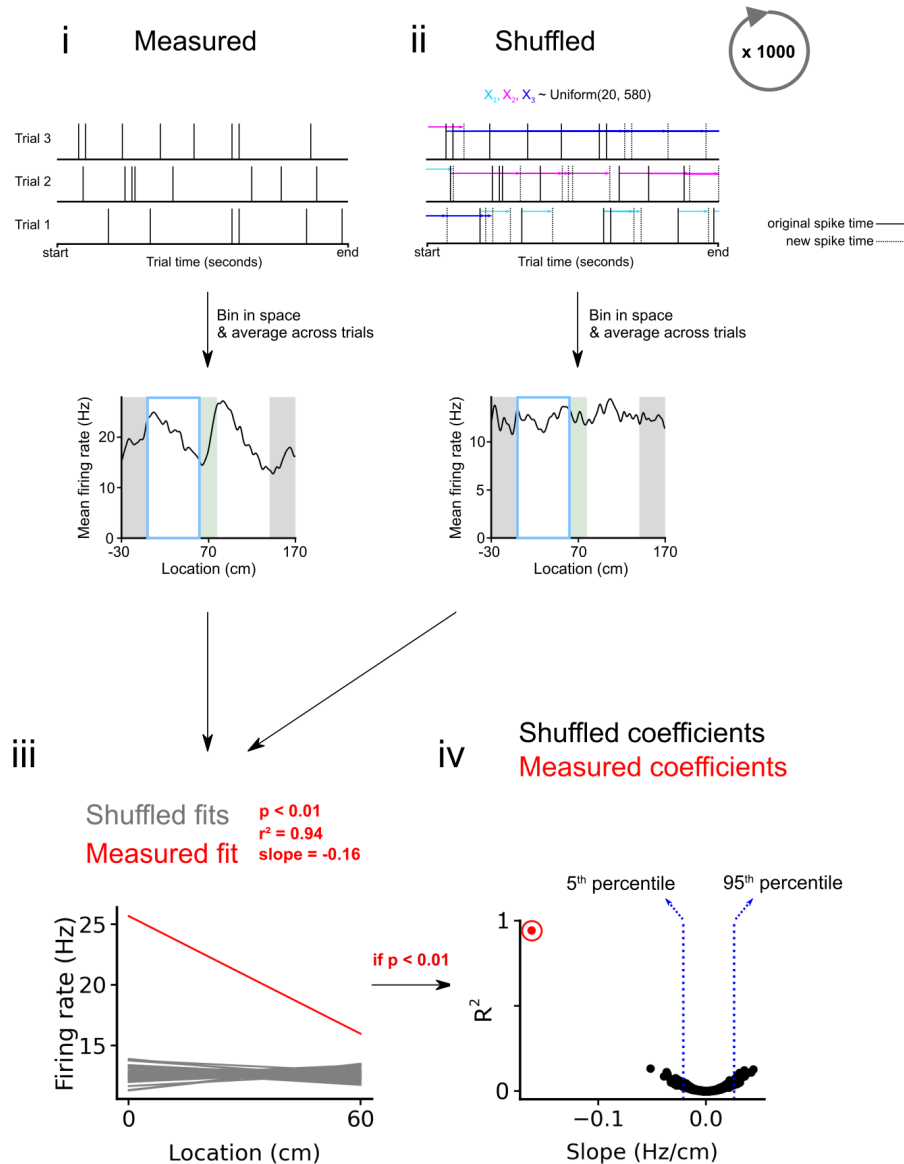


**Figure 65. Trial-dependent cyclic shuffle procedure.** (i) A neuron's spike times are binned in 1 cm spatial bins and firing rates calculated as the number of spikes divided by the time spent in the bin. Firing rates are averaged across trials to produce a firing rate profile across the 200 cm track. (ii) The same procedure is applied 1000 times to generate shuffled rate maps. For each shuffle, a single random time between 20-580 seconds is drawn for each trial and added to spike times in that trial. (iii) The pre-reward zone or post-reward zone regions of the firing rate profile are modelled with a linear regression for the cell and the corresponding shuffles. (iv) If the cell's linear regression  $p$  value is less than 0.01 and the slope is outside the 5-95<sup>th</sup> percentile of the shuffled distribution, the cell is classified as ramping based on the sign of the cell's slope.

#### 5.2.4 Generalised linear mixed effect model for position, speed and acceleration

For each neuron, all variables were binned into 100 ms blocks and bins when the animal's speed was < 3 cm/s were removed (Góis and Tort 2018). The average speed and acceleration of the animal across the whole recording was calculated, and bins in which speed or acceleration was 3 standard deviations above or below the average for that variable were removed. This step was done to remove unrealistic speeds or accelerations that were caused as a consequence of calculating speed around the track teleport. A Poisson GLMER model with the configuration 'Rate ~ Position + Speed + Acceleration + (1 + Position | Trials)' and log linker function was fit using the lme4 package (version 1.1-12) in R (Bates et al. 2015; [Figure 70A](#)). The ANOVA function provided by the car package (version 3.0-9) was used to calculate significance values for each model coefficient (Fox and Weisberg 2019). To classify neurons as being modulated by position (P), speed (S), acceleration (A), or a combination thereof, a significance threshold of 0.01 was used and corrected for multiple comparisons using the Benjamini & Hochberg method (Benjamini and Hochberg 1995). For example, a neuron with corrected P < 0.01 for position and acceleration and  $\geq 0.01$  for speed coefficients was classified as a PA neuron.

#### 5.2.5 Measuring theta index and local field potentials

Theta index was calculated following methods in (Kornienko et al. 2018). Spike times were transformed into instantaneous firing rates. A power spectrum was then estimated using Welch's method. The theta index was defined as

$$T = \frac{\theta - \text{baseline}}{\theta + \text{baseline}}$$

where  $\theta$  is the mean theta band power (6-10 Hz) and baseline is the mean power of two adjacent frequency bands (3-5 and 11-13 Hz). Local field potential was calculated by estimating the power spectrum across the raw voltage trace from each channel using Welch's method. This power spectrum was averaged across all 16 channels to produce an average power spectrum.

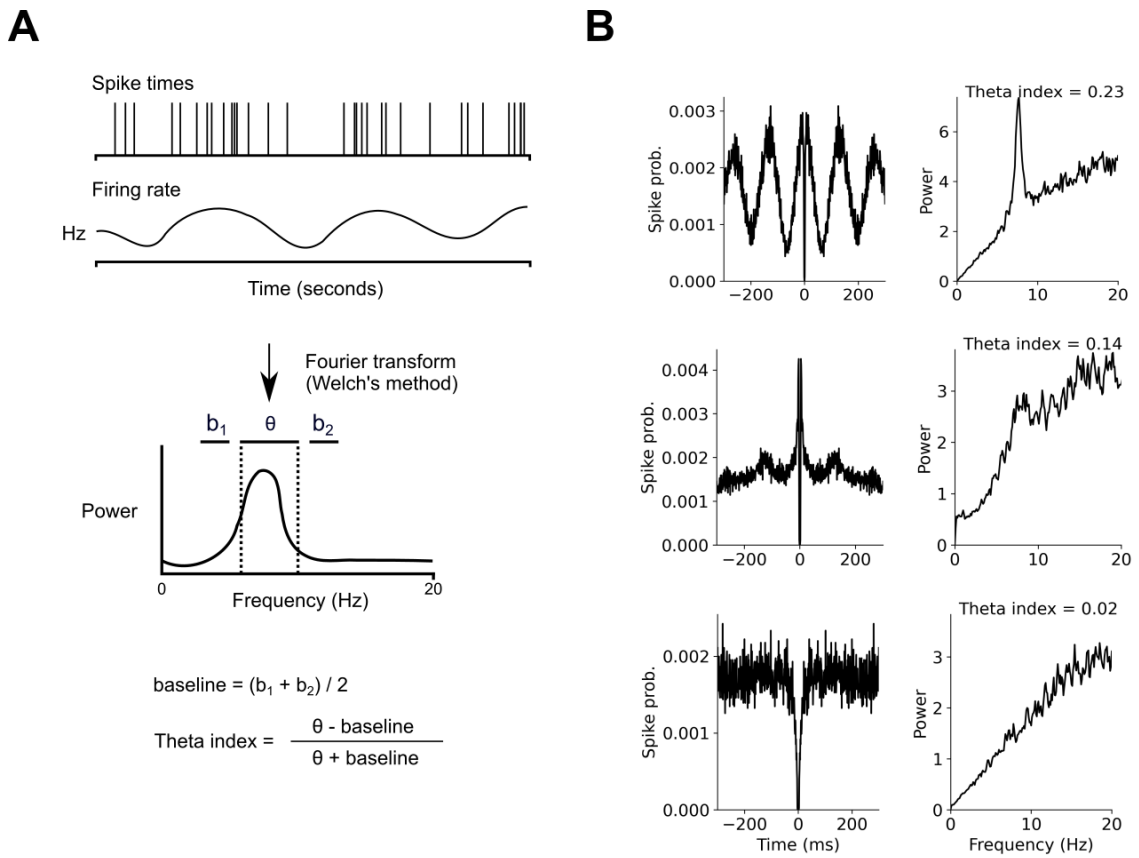


**Figure 66. Measuring the theta index of a neuron's spike timing (A) Schematic illustrating the procedure for calculation of the theta index.** Firing indices were transformed into instantaneous firing rates from which a power spectrum was estimated using Welch's method. The theta index was defined as  $(\theta - \text{baseline}) / (\theta + \text{baseline})$ , where  $\theta$  is the mean power in the theta band (6–10 Hz) and baseline ( $b$ ) is the mean power of two adjacent frequency bands 3–5 Hz ( $b_1$ ) and 11–13 Hz ( $b_2$ ). (B) Autocorrelograms (left) and power spectra (right) for three simultaneously recorded neurons that exemplify strong (top), moderate (middle) and low (bottom) theta indices.

## 5.3 Results

### 5.3.1 Encoding of location by ramping activity

Slopes before and after the reward zone were calculated and compared to the corresponding shuffled data. Only sessions with more than 30 successful trials were included in all further analysis and initially only reward beaconed trials were included. Following this behavioural criterion, 1395 neurons were identified after spike sorting from 187 sessions ( $196.5 \pm 7.7$  trials / session, 17 sessions / mouse, range 6-25). Out of the 1395 neurons, 546 neurons (39 %) had significant ramping activity before the reward zone (224 +ve sloping, 322 -ve sloping). Of the shuffled data, only 2 % of the firing rate maps showed significant ramping slopes before the reward zone ( $n = 28235 / 1395000$ ). Neurons with ramping activity were found in all animals with similar proportions (mean:  $60.7 \pm 4.99$  %, range: 45.8 - 77.4 %).

It was possible that ramping activity manifested from drifting discrete firing fields and subsequent averaging over trials. To rule this out, the ramp slopes and average firing rate profiles were calculated for the first and second half of the session. For ramping neurons, slopes and firing rate profiles correlated highly between half sessions (pre-reward zone slope,  $r^2 = 0.88$ , post-reward zone slope,  $r^2 = 0.77$ ; firing rate profile,  $r^2 = 0.47 \pm 0.28$ ). Neurons without any ramping slope pre or post reward zone had significantly lower half-session correlations (pre-reward zone slope,  $r^2 = 0.25$ , post-reward zone slope,  $r^2 = 0.21$ ; firing rate profile,  $r^2 = 0.23 \pm 0.26$ , respectively: DF = 1, P < 1e-14, F = 164.4, ANOVA; DF = 1, P < 1e-14, F = 63.0, ANOVA; DF = 1103, P < 1e-15, T = 14.6, T-test).

Several examples are shown in [Figure 67](#) for neurons with significant ramping activity before and after the reward zone. Firing rates from each cell were z-scored and averaged across cells within ramping classifications to show the average firing rate profile for a ramping group. A heat map for all neurons within each ramp group is shown in [Figure 68](#). Depending on how the ramp codes might be utilised in the brain, ramp codes that reset might predominate over ramp codes that switch polarity, or vice versa. Of the six ramp groups based on ramping activity before and after the reward zone (+ +, + -, +un, - -, - +, -un), each of these groups were well represented with no clear bias of a single ramping group predominating. Furthermore, ramp slopes before the reward zone did not predict ramp slopes after the reward zone ([Figure 69](#)). This suggests all ramp-like codes are represented in the brain.

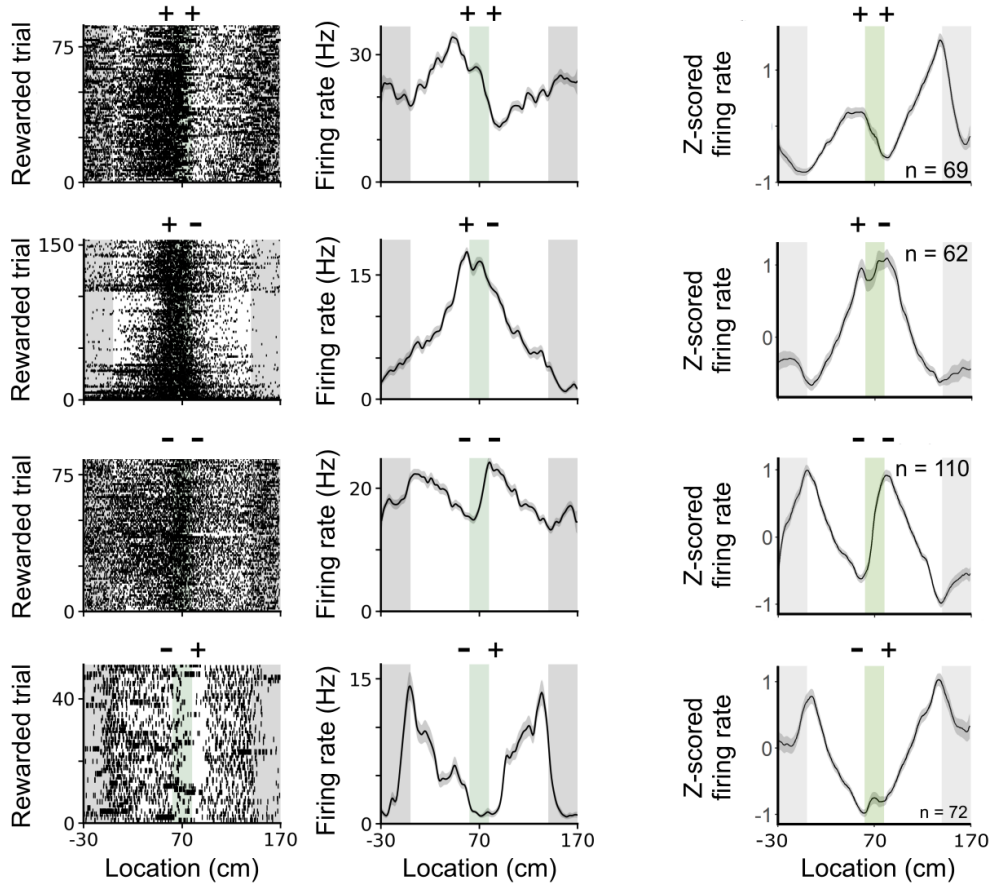


**Figure 67. Example ramp cells and population averaged ramp cells.** From left to right, spike rasters and average firing rate maps for example neurons from four ramp classes (+ +, + -, - -, - +), and the corresponding population averaged firing rate. Shaded regions indicate the standard of error across trials (example cells) and cells (population-averaged).

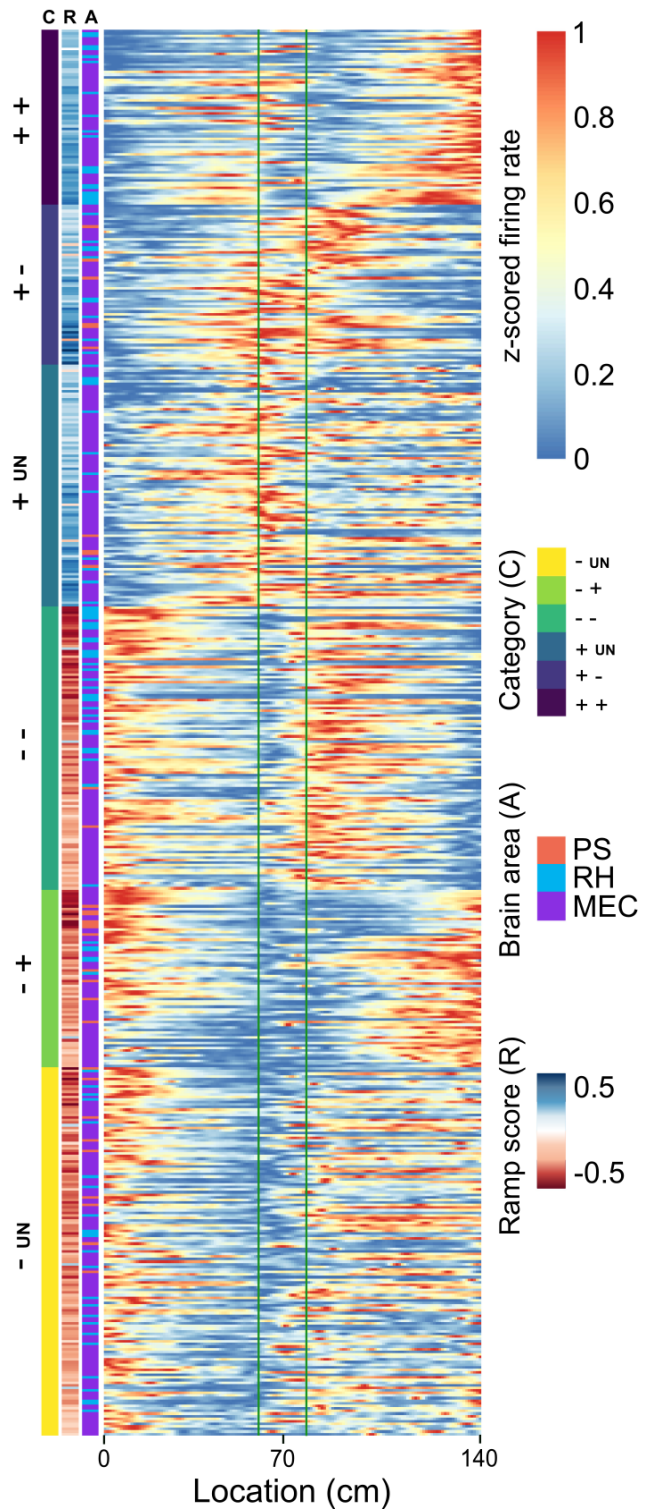


**Figure 68. Normalised firing rate maps of all ramping neurons.** The black box regions of the track are not shown. Neurons are ordered hierarchically by ramp category, ramp score and the brain area in which the neurons were recorded from.

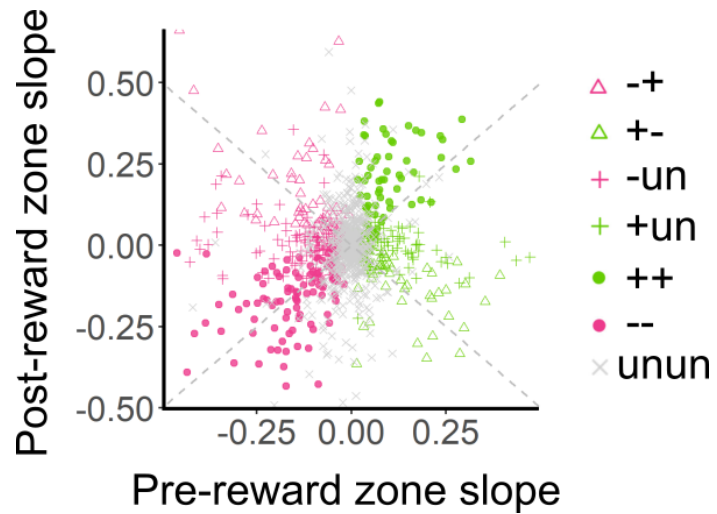


**Figure 69. Pre-reward zone slope as a function of post-reward zone slope.** Dashed lines indicate points at which slopes would be identical on both track segments or with a flipped sign.

### 5.3.2 Interruption of ramp-like firing profiles encode rewarded locations

For ramp-like codes that maintain the same ramp direction on each track segment (+ + and - - groups), firing rates at the reward zone may either deviate from the sloping trajectory or continue along the same ramping trajectory. By looking at the example neurons and z-scored firing rate maps, it was clear some level of resetting of the firing rate was taking place. To quantify this, the firing rate slope before the reward zone was extrapolated to the beginning of the post-reward zone region to predict the firing rate of ramping neuron based on its pre-reward zone ramping activity. This was compared with the y intercept of the post-reward slope to generate an offset (predicted - measured firing rate). For both - - and + + ramp groups, the offset was significantly non-zero suggesting ramping activity was being reset at the reward zone (+ +:  $P < 1e-12$  n = 67; - -:  $P < 1e-15$ , n = 109, one sample T-test vs mean = zero). This is consistent with a ramp code that encodes portions of a journey up to salient landmarks or features of an environment, like visual cue or reward. This interruption of the firing rate may encode the location of reward locations within the environment.

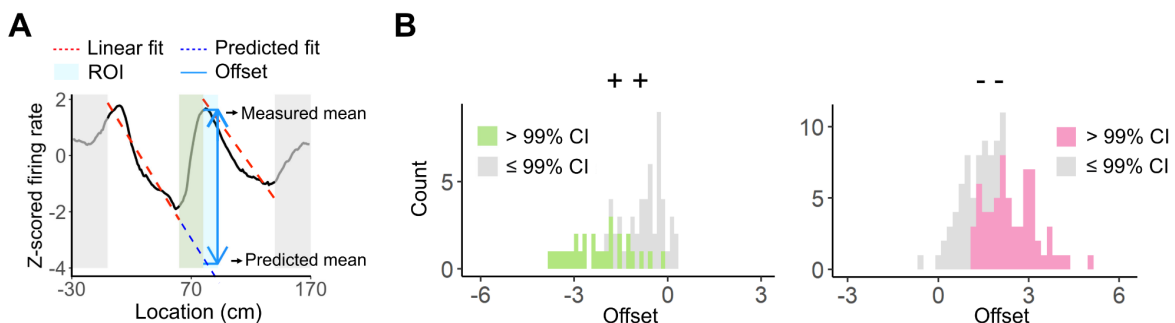


**Figure 70. Interruption of ramp codes around the reward zone.** (A) Pre-reward zone slopes are extrapolated to predict the firing rate at the beginning of the post-reward zone region and used to compute an offset by comparing the predicted fit based on the pre-reward zone slope and measured fit from the post-reward zone slope. (B) Histogram of offsets for + + and - - ramping neurons. Coloured bars indicate individual neurons for which the offset was outside 99 % confidence of intervals of the neuron's predicted value.

### 5.3.3 Differential influence of position, speed and acceleration

Does ramping activity of the firing rate encode position along the track? To address this, it was important to consider all possible kinematic variables as the encoded variables by the ramping neurons. For example, speed and position are tightly coupled in this experiment as a mouse performing the task will run fast and slow down to stop within the reward zone. The speed profile of this mouse would ramp similarly to location on the track. To determine what influence position, speed and acceleration have on ramping neurons, firing rates in the pre-reward zone region were fitted with a generalised linear mixed effect model that included position, speed and acceleration as fixed effects and trial number as a random effect.

For the majority of ramping neurons, firing rates could be best accounted solely by position or conjunctively with position as the dominant coefficient alongside speed and / or acceleration ( $n = 340/546$  neurons with ramping activity before the reward zone; [Figure 70C](#)). For both negative and positive ramping neurons, the position coefficients were larger than those for acceleration ( $P < 1e-15$ , Bonferroni corrected paired T-test) and speed ( $P < 1e-16$ , Bonferroni corrected paired T-test).

Interestingly, all possible combinations of position, speed and acceleration encoding neurons were present in the ramping and non ramping populations. Example neurons from the position or conjunctive-position encoding groups are shown in [Figure 71](#). It is important to note, that while the GLMER fit unsmoothed kinematic variables to unsmoothed firing rates, smoothed firing rates are visualised below.

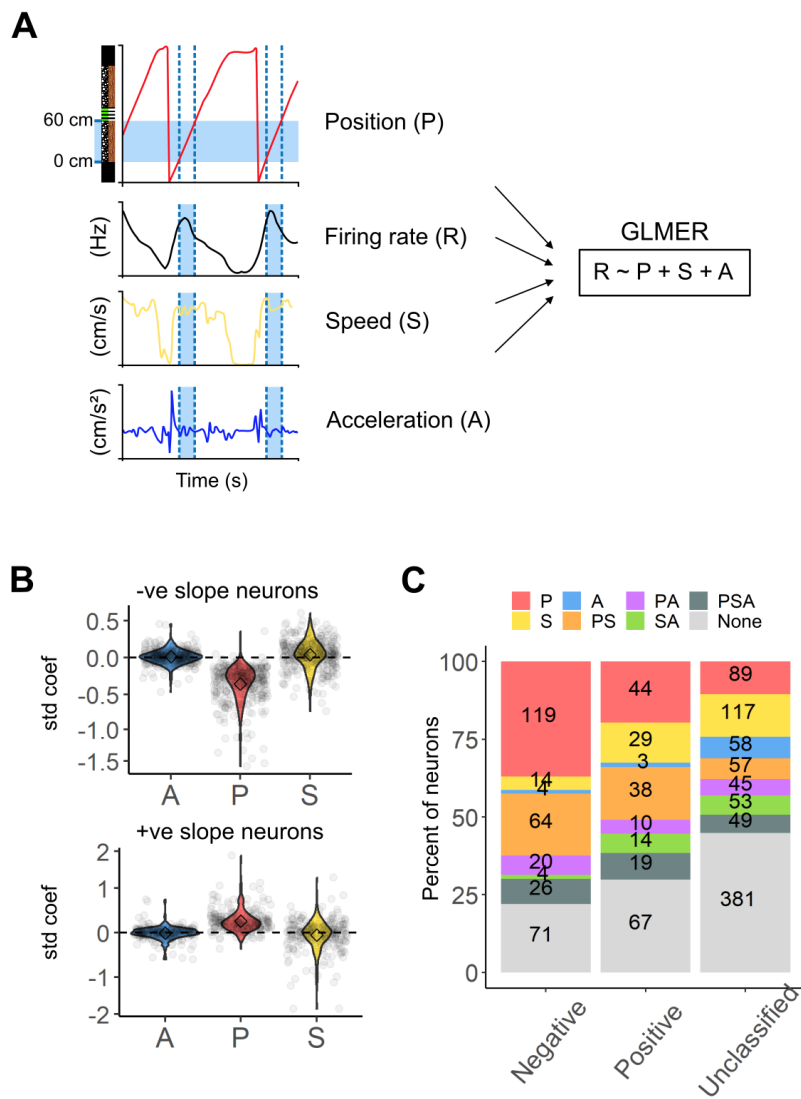


**Figure 71.** (A) Generalised linear mixed effect models that include speed (S), acceleration (A) and position (P) as fixed effects were fit to the firing rate in the track region approaching the reward zone. The track region over which the model was fitted is indicated by the blue shaded bar. Trial number was included as a random effect. (B) Standardised coefficients, which index the relative strength of each fixed effect variable, obtained from the model fits for neurons with negative (upper) and positive (lower) ramp slopes on the track segment before the reward zone. (C) Proportions of neurons for which each combination of P, A and S coefficients were significant at a threshold of  $P < 0.01$  (Wald's chi squared test) for neurons classified as having a positive slope, negative slope or as unclassified.

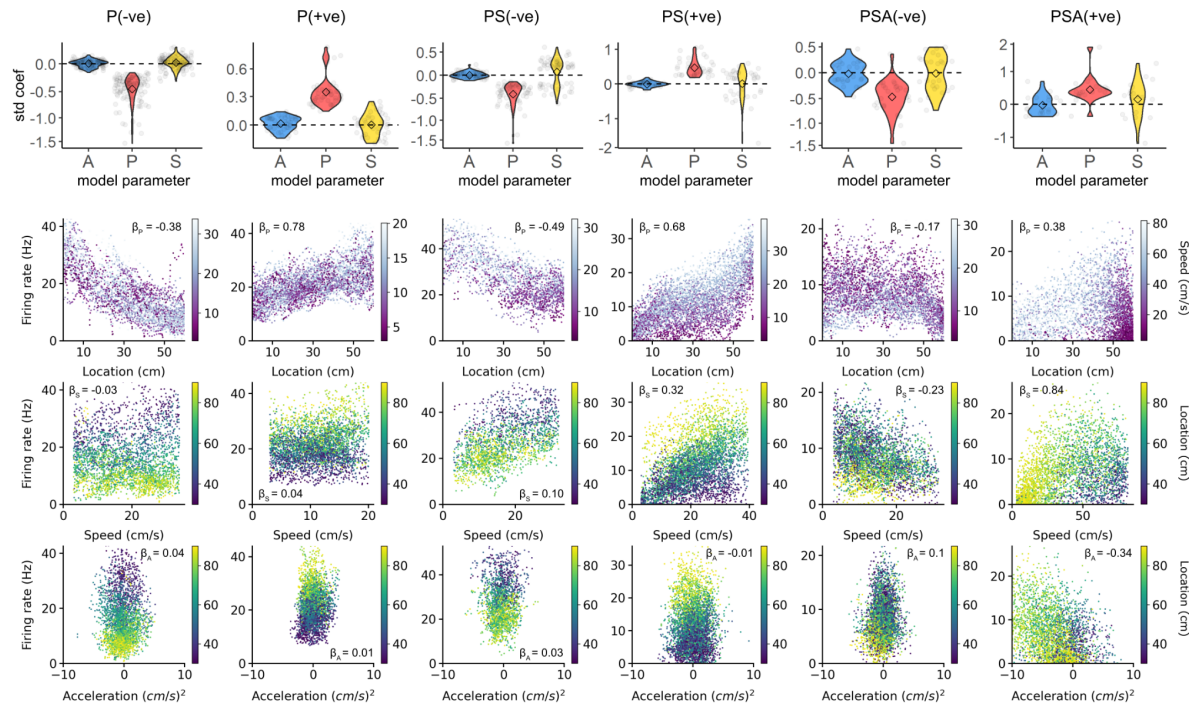


**Figure 72. Distribution of standardised coefficients (upper row) and example data (lower rows) for neurons with positive (+ve) or negative (-ve) ramp slopes and classified as modulated solely by position (P), by position conjunctively with speed (PS), and position conjunctively with speed and acceleration (PSA). Example data shows firing rate as a function of position (second row), running speed (third row) and acceleration (lower row). Firing rates as a function of position are colour coded by speed (cm/s) while firing rates as a function of speed or acceleration are colour coded by position along the track (0 - 60 cm).**

### 5.3.4 Ramp codes across trial outcomes

The ramping activity shown up to this point, has been from neural activity recorded on beaconed trials in which mice have received a reward and have therefore stopped within the reward zone. This begs the question, is ramping activity related to the spatial behaviour of the animal. To address this, trials were split up by behavioural outcomes including hit, try and run trials, as previously detailed in [3.2.4](#). On hit trials, mice receive rewards by registering a stop within the reward zone. Unrewarded trials are split based on the average speed recorded in the reward zone into try trials, in which the reward zone speeds were close to hit trials or run trials, in which the reward zone speeds were distant from reward zone speeds observed on hit trials. [Figure 72](#) shows the average speed profile of hit, try and run trials across mice. A high speed is maintained throughout the track for run trials consistent with the animal ignoring the reward zone on that particular trial. Try trials exhibit an initial decrease in speed but do not reach the minimum observed in hit trials. This is consistent with the spatial behaviour of a mouse either missing the reward zone or slowing down with the intention of stopping but not.

To assess whether ramping activity was present on unrewarded trials, ramp slopes and offset were calculated for the average firing rate profiles of position-encoding neurons (P, PS, PA, PSA) on try and run trials and compared with the ramping activity on hit trials ([Figure 73](#)). Position-encoding neurons from each ramping group showed similar ramping properties across all trial outcomes in both example neurons and in the population-averaged firing rate profiles ([Figure 72D](#)). Trial outcome had no significant effect on either pre-reward zone slope or post-reward zone slope (pre-reward zone +ve slopes: DF = 2, 164, P = 0.12, F = 2.1; pre-reward zone -ve slopes: DF = 2, 308, P = 0.93, F = 0.069; post-reward zone +ve slopes: DF = 2, 308, P = 0.04, F = 3.2; post-reward zone -ve slopes: DF = 2, 164, P = 0.65, F = 0.427; repeated measures ANOVA) and all pre-reward zone slopes maintained a non-zero slope across all trial outcomes (P < 1e-9, Bonferroni corrected one sample T-test vs mean = zero). Offsets in the firing rate profile around the reward zone were affected by the trial outcome for + + and - - ramp groups. (+ +: DF = 2, 56, P < 1e-4, F = 12.4; - -: DF = 2, 102, P < 1e-7, F = 21.9), but for all outcomes the offsets differed from zero (P < 1e-6, Bonferroni corrected T-test).

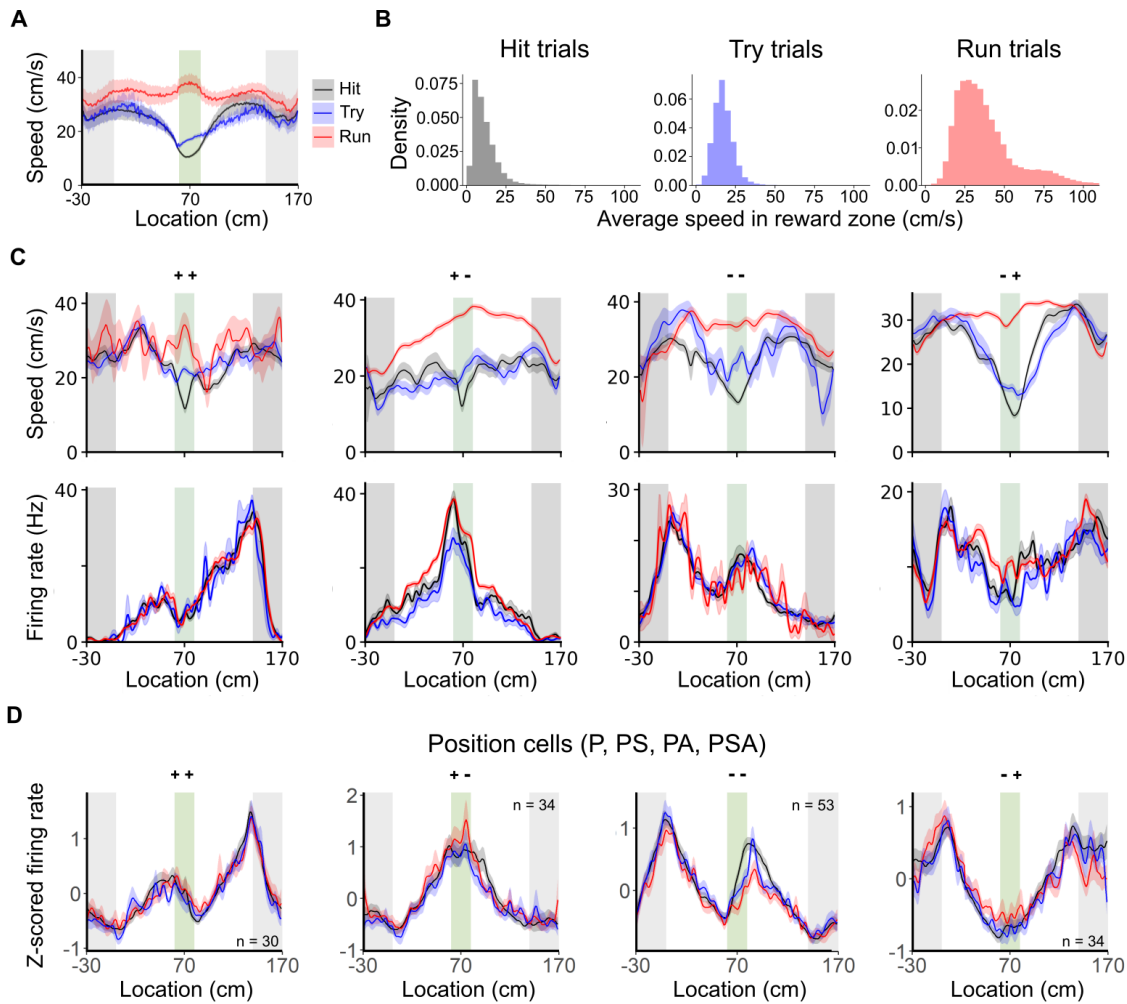


**Figure 73. Ramping activity as a function of trial outcome.** (A) Population average of mean running speed as a function of position for each trial outcome across all animals ( $n = 11$ ). Shaded regions correspond to the standard error of the mean across animals. (B) Trial level distribution of mean running speeds within the reward zone for hit, try and run trial outcomes. (C) Examples of running speed (upper) and firing rate (lower) as a function of track position. Note that for some animals the average running speed in the hit group can be greater than zero because the stopping location varies between trials. Shaded regions correspond to the standard error of the mean across trials. Neurons were classified (+ +, + -, - -, - +) according to their firing rate profiles on beacons trials. (D) Population averaged firing rates as a function of position on hit, try and run through trials for positionally modulated neurons (P, PS, PA, PSA groups). The neurons were classified on hit trials as having + -, - +, + + and - - firing rate profiles. Shaded regions correspond to the standard error of the mean across cells.

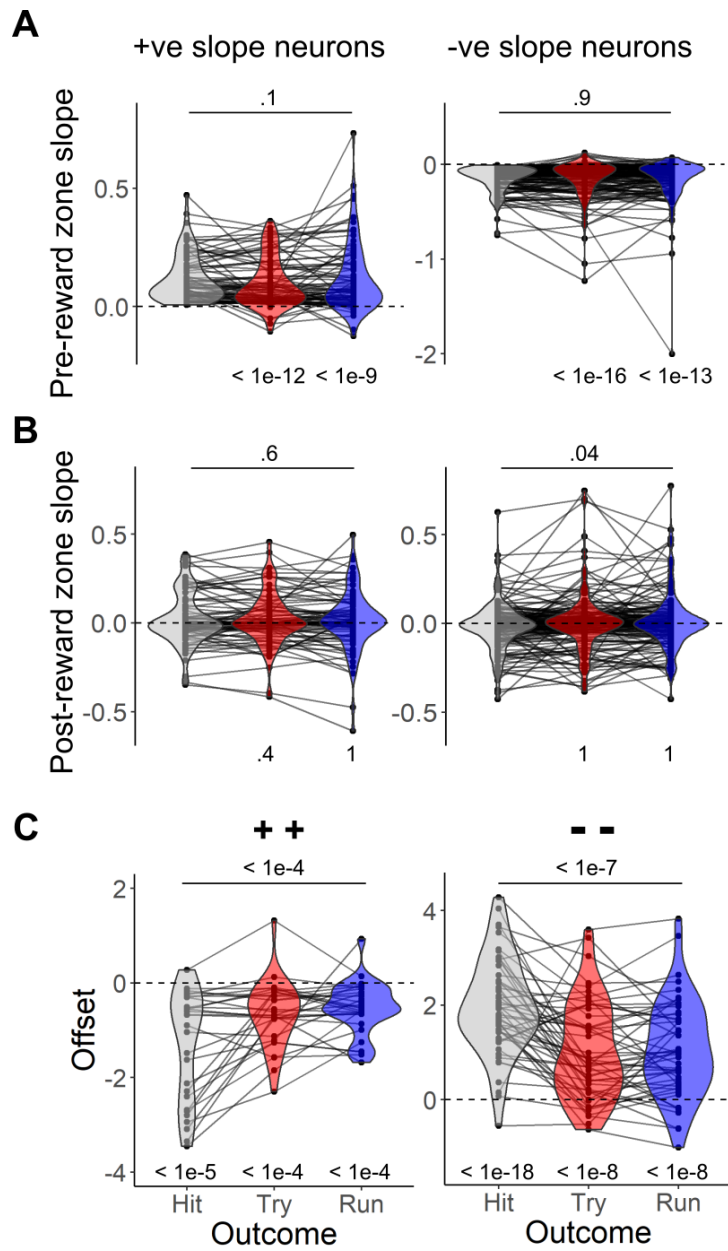


**Figure 74. Ramping slopes and slope offsets as a function of trial outcome.** (A) Pre-reward zone slopes of neurons that had a positive and negative ramp in the pre-reward zone region of the track. (B) Post-reward zone slopes of the same neurons. (C) Offsets of a subset of the ramping neurons (+ + or - - groups).

### 5.3.5 Ramp codes across trial types

Are ramp codes related to the available cues on the track? If so, ramping slopes and offsets would be diminished with the removal of track cues. If ramp slopes and offsets are maintained when cues are removed, they may result from recall of a spatial memory of the track structure. The track on probe trials had no visible reward zone and no reward was dispensed for a stop within the reward zone ([Figure 74](#)). Probe trials were interleaved between beacons trials, 1/10 trials were probe trials, following a repeating pattern of 4 beacons trials, 1 non-beaconed trial, 4 beacons trials and 1 probe trial. Mice registered more stops within the reward zone ([Figure 74B](#)) than the rest of the track on beacons trials but less so than on probe trials.

To assess whether ramping activity was present on probe trials, ramp slopes and offset were calculated for the average firing rate profiles of position-encoding neurons (P, PS, PA, PSA) on probe trials and compared with the ramping activity on beacons trials. Position-encoding neurons from each ramping group showed similar ramping properties across trial types in both example neurons and in the population-averaged firing rate profiles ([Figure 74D](#)). Trial type had a significant effect on pre-reward zone slopes ([Figure 76A](#), +ve slopes: DF = 36, P = 0.03, T = 2.3; -ve slopes: DF = 45, P = 0.01, T = -2.6; paired Student's T-tests) and some effect on post-reward zone slopes ([Figure 76B](#), +ve slopes: DF = 36, P = 0.09, T = -1.7; -ve slopes: DF = 45, P = 0.0007, T = -3.7; paired Student's T-tests). Regardless, pre-reward zone slopes were significantly non-zero (P < 0.0001, Bonferroni corrected one sample T-test vs mean = zero). Furthermore, slopes were well correlated between trial types (pre-reward zone: adjusted  $r^2$  = 0.50, P < 1e-14; post-reward zone: adjusted  $r^2$  = 0.45, P < 1e-12). This was also seen at for ramp offsets of + + and - - ramp groups, offsets were significantly affected by trial type (+ +: DF = 2, 56, P = 0.0003, F = 12.4; - -: DF = 2, 102, P < 1e-7, F = 21.9) but were significantly non-zero (+ +: P = 0.04; - -: P = 0.0008, Bonferroni corrected one sample t-test vs mean = zero). Offsets between trial types were again well correlated (adjusted  $r^2$  = 0.3938, P < 1e-10). Results suggest track cues do play some role in setting the firing rate slopes and offsets, although are not required for ramping activity and the corresponding offsets at suspected rewarded locations. This is consistent with ramping neurons encoding position from a recalled track structure with cues reinforcing the recalled memory when available.

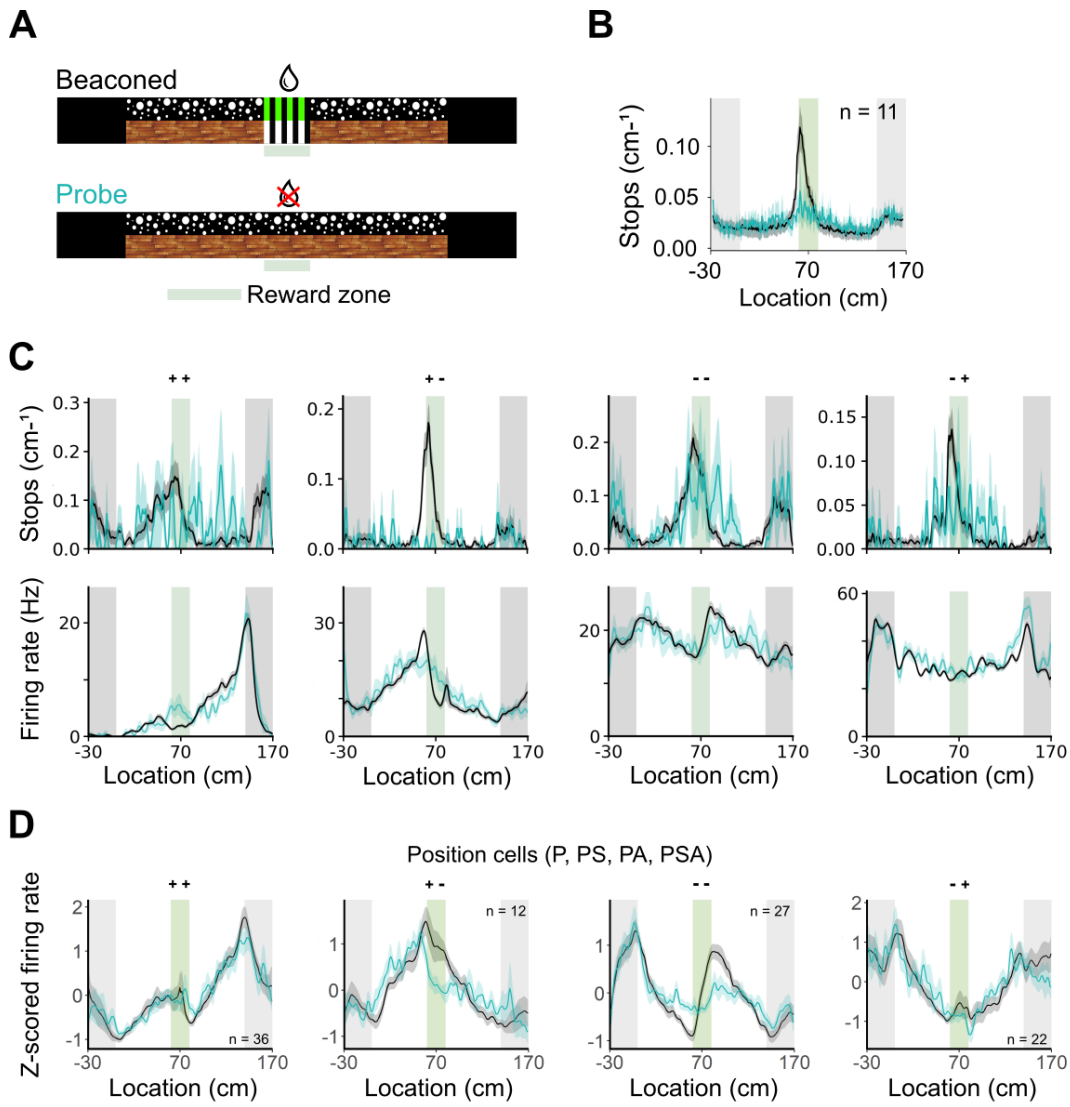


**Figure 75. Ramping activity as a function of trial type.** (A) Schematic of track configuration. Beaconed trials contain two cues on the track, the visual cue of the reward zone and the reward itself. Probe trials contain neither. (B) Population mean of behaviour from trained mice on beaconed and probe trials, showing the mean stops (per cm) as a function of position on the track. Shaded regions correspond to the standard error of the mean across animals. (C) Examples from beaconed trials (black) and probe trials (blue) of stop histogram (upper row) and mean firing rate (lower row) as a function of track position. Shaded regions correspond to the standard error of the mean across trials. Neurons were classified (+ +, + -, - -, - +) according to their firing rate profiles on beaconed trials. (D) Mean firing rates as a function of track position on beaconed trials and probe trials for the populations of neurons classified with + +, + -, - -, - + firing rate profiles.

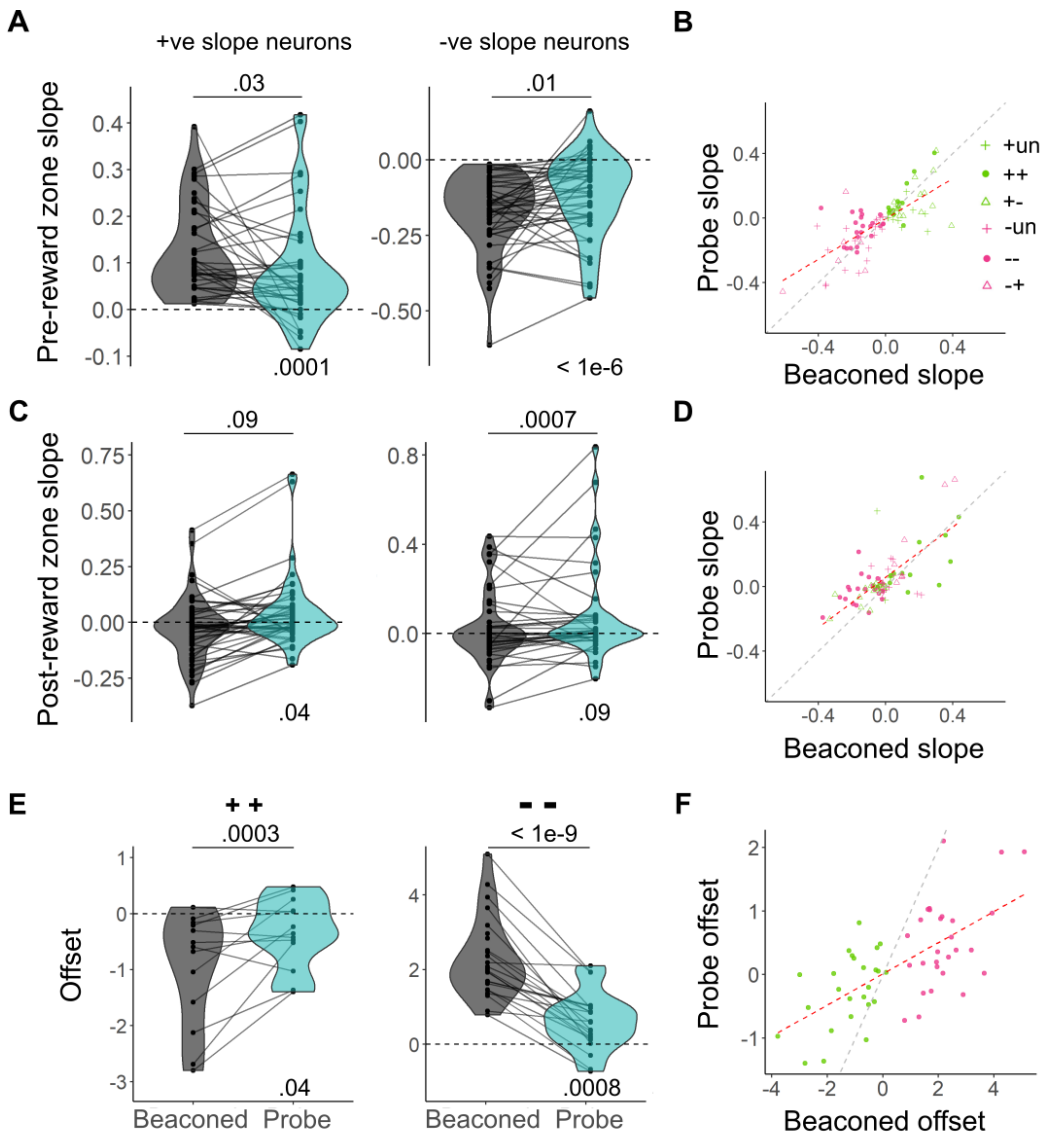


**Figure 76. Ramping slopes and slope offsets as a function of trial type.** (A) Pre-reward zone slopes of neurons that had a positive and negative ramp in the pre-reward zone region of the track. (B) Beaconed slopes as a function of probe slopes in the pre-reward zone region of the track. (C) Post-reward zone slopes for the same neurons. (D) Beaconed slopes as a function of probe slopes in the post-reward zone region of the track (E) Offsets of a subset of the ramping neurons (+ + or - - groups). (F) Beaconed offsets as a function of probe offsets. For B,D,F: Grey dashed line indicates unity, red dashed line indicates the line of best fit.

### 5.3.6 Ramp cells in the open field

Do ramp cells overlap with spatial modulated cell types such as grid or border cells? As ramp cells increase or decrease their firing rate proportional to the distance to a goal location, it's possible that ramping neurons are in fact a subset of border cells with defined border fields at salient points on the track (Campbell et al. 2018), or grid cells with grid spacings and field locations reminiscent of a ramp-like code, possibly tuned to rewarded locations (Butler, Hardcastle, and Giocomo 2019). To address this, mice performed the linear location task before completing a free exploration task in an open field to record activity of neurons in both spatial paradigms. Electrophysiological recordings were concatenated and spike sorted together to track the neural firing between set ups (see [2.8](#)). If ramp cells were in fact a subset of the border, grid or any other spatial cell population, neurons would show significant ramping activity on the linear track while also classifying as grid, border, or other spatial cells based on their spatial firing properties in the open field. All 11 mice undertook both the linear location task and open field recordings daily, however only cohort 7 (C7) is used within this analysis as electrophysical noise levels from the open field recordings in previous cohorts were not suited for the concatenated sorting procedure used to identical clusters in both settings. This was because all other cohorts were recorded before low noise levels were achieved with the open field setup.

Of the 340 positionally-encoding cells, 201 of these cells had a corresponding open field recording. Only 10 of these cells classified as border cells, 7 as grid cells and 18 as head direction cells. The vast majority overlapped with non-specific spatial cells (145/201) and a small proportion was classified as non-spatial in the open field (21/201). Examples from each ramp group (+ +, + -, - +, - -) are shown in [Figure 77](#). These cells show features of spatial firing properties but do not fall into any classically defined spatial firing category consistent with the large proportion of ramping cells classified as spatial. Conversely, examples of classically defined spatial cells (grid, border, narrowly-tuned head direction and broadly-tuned head direction) are shown with their spatial firing properties on the virtual linear track. To quantify this, the overlap between cell classifications in the open field and virtual linear track was measured by calculating the proportion of cell-types in the VR that corresponded with a particular cell-type in the open field, and vice versa. [Figure 79A](#) shows the proportion of border, grid and pure head direction cells were similar among ramping and non-ramping neurons while [Figure 79B](#) shows the proportion of ramping and non-ramping neurons were similar among each open arena cell type. This data suggests ramp cells are largely non-overlapping with grid and border populations but do correspond to spatial cells in the open field.

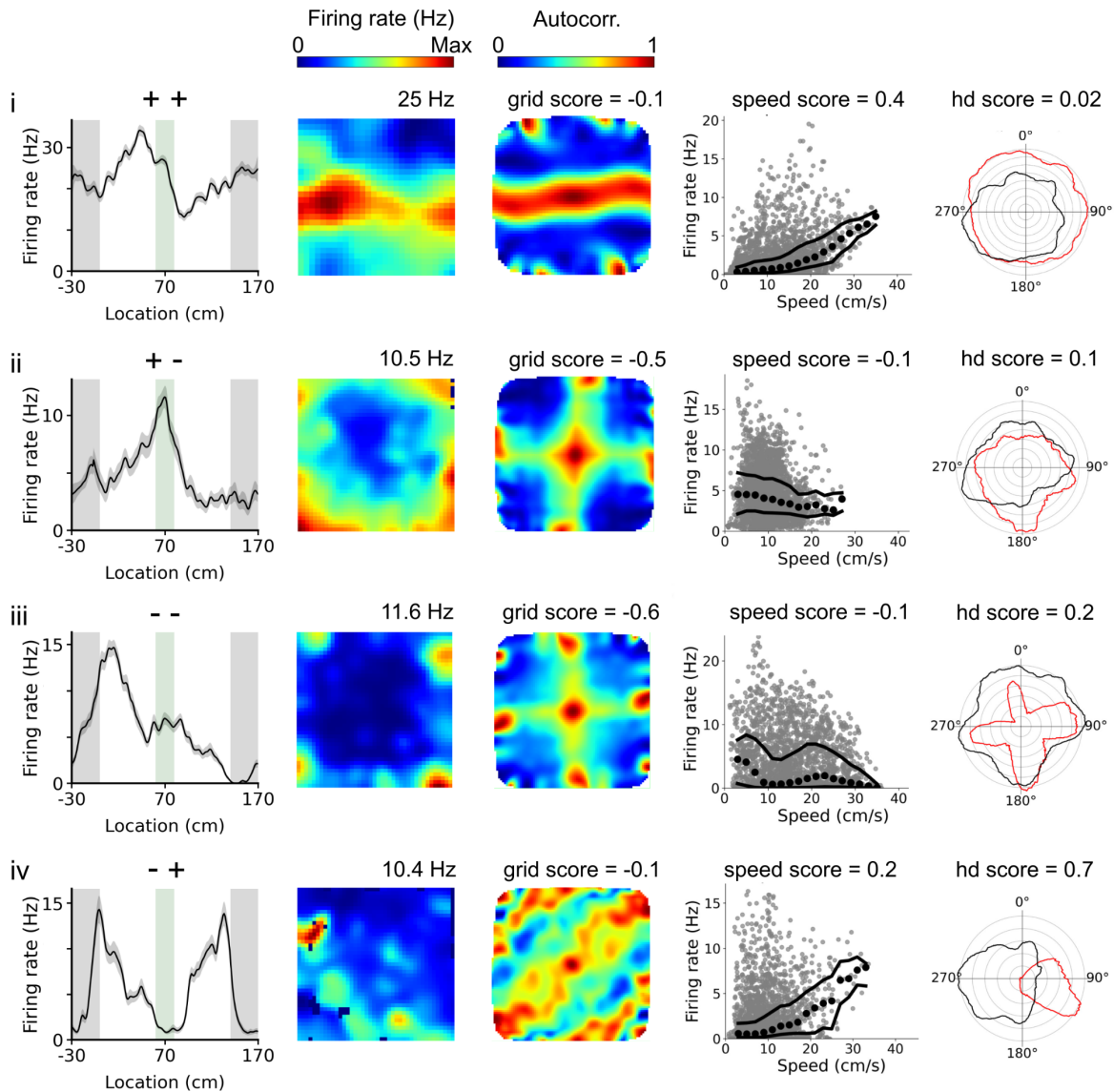


**Figure 77. Examples of the open field spatial firing properties of ramping neurons.**

From top to bottom shows spatial firing of (i) ++, (ii) +-,(iii) -- and (iv) -+ ramping neurons in the virtual linear track and the open field. Panels show (from left to right): average firing rate profiles on the virtual track as a function of position; spatial heat maps of firing rates in the open arena; spatial autocorrelograms of the open arena firing rate; firing rate in the open arena as a function of speed; and polar plots of average firing rate in the open arena as a function of head direction (red) and movement (black). Maximal firing for which the spatial heat maps are normalised up to are shown above the spatial heat maps.

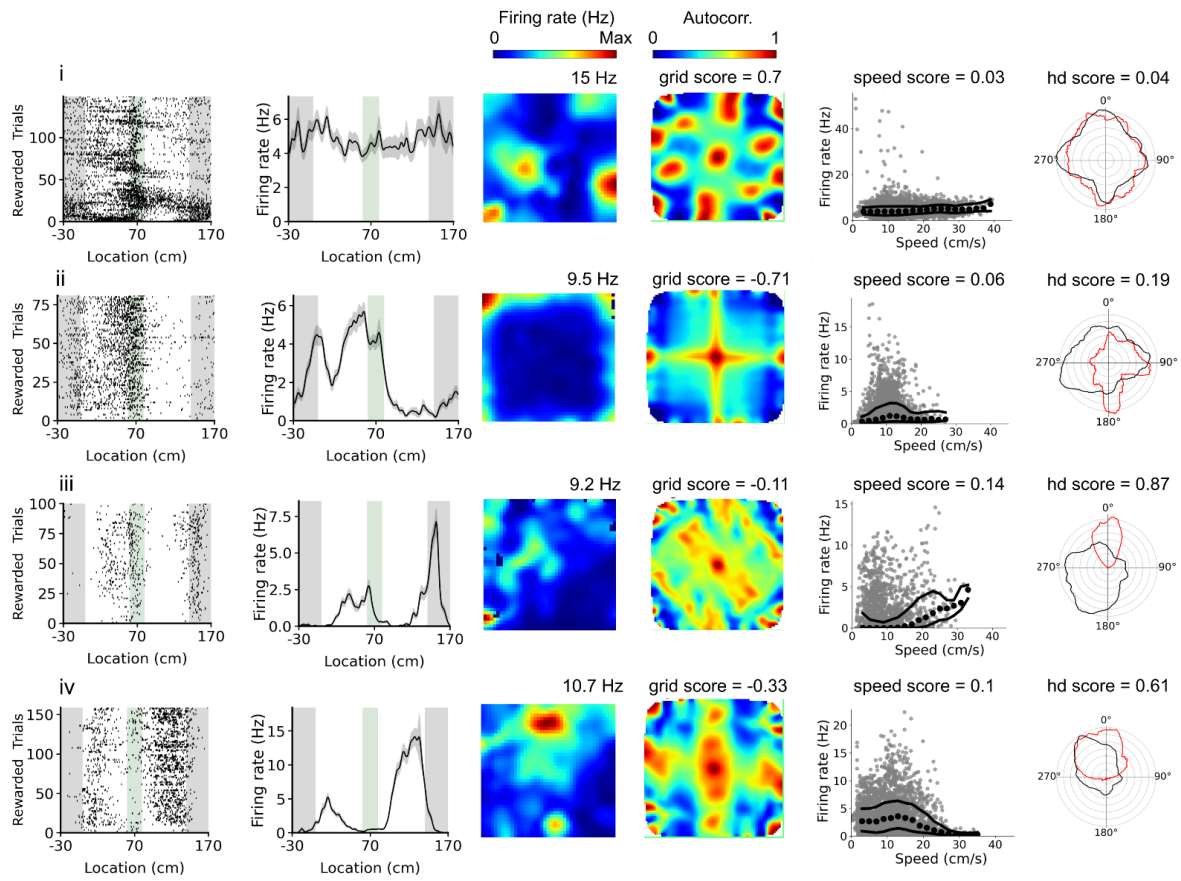


**Figure 78. Examples of the virtual linear track spatial firing properties of classically-defined spatially modulated cell types.** From top to bottom shows spatial firing of a (i) grid cell, (ii) border cell, (iii) narrowly-tuned head direction cell and a (iv) broadly-tuned head direction cell in the virtual linear track and the open field. Panels show (from left to right): spike locations as a function of position; average firing rate profiles on the virtual track as a function of position; spatial heat maps of firing rates in the open arena; spatial autocorrelograms of the open arena firing rate; firing rate in the open arena as a function of speed; and polar plots of average firing rate in the open arena as a function of head direction (red) and movement (black). Maximal firing for which the spatial heat maps are normalised up to are shown above the spatial heat maps.

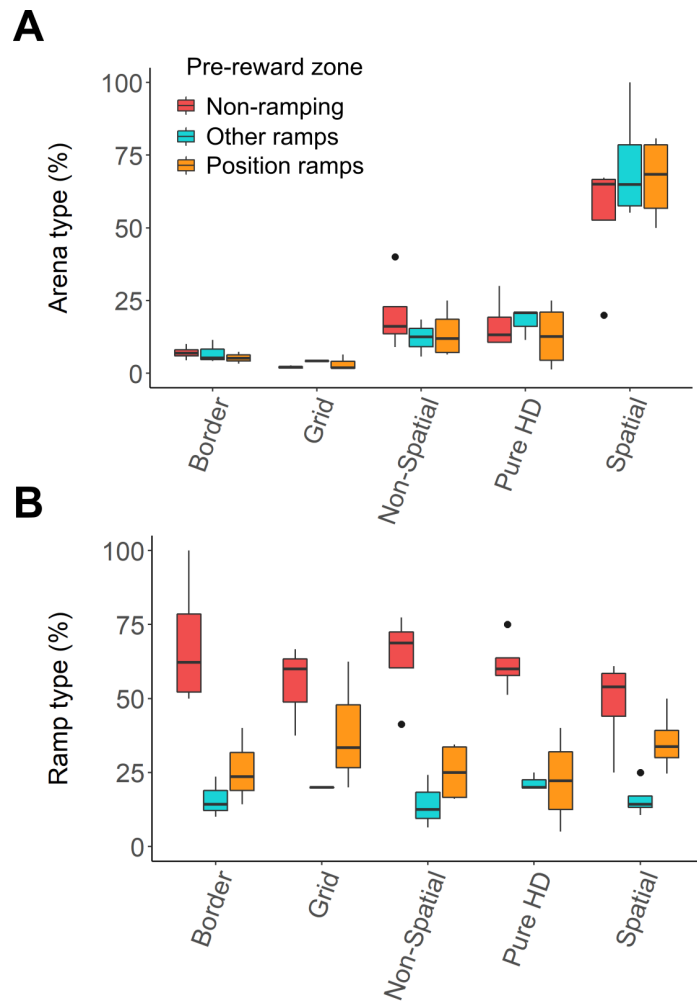
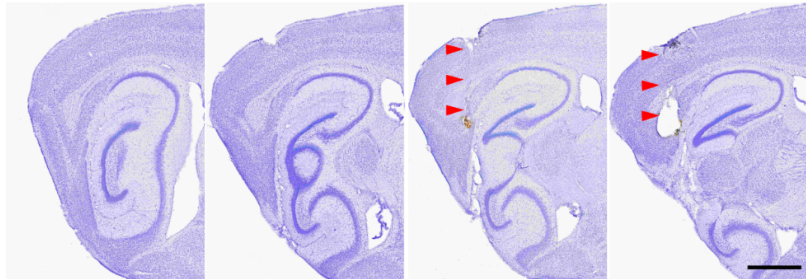


**Figure 79. Proportions of overlap between cell types in the virtual linear task and open field.** (A) Proportion of each open arena cell type (border, grid, head direction, non-spatial, other spatial) among neurons with activity on the linear virtual track classified as position-dependent ramping (P, PA, PS, PSA-encoding with positive or negative ramps in the pre-reward zone region), other ramping (S, A, SA-encoding with positive or negative ramps in the pre-reward zone region), and non-ramping (no positive or negative ramps in the pre-reward zone region). (B) Proportion of neurons classified on the linear virtual track classified as position-dependent ramping, other ramping, and non-ramping among neurons classified as border, grid, head direction, non-spatial, other spatial. In (C) and (D), boxes show the median, 25<sup>th</sup> and 75<sup>th</sup> percentiles, and whiskers extend to the largest value 1.5 times the interquartile range from the box. Points outside this range are plotted individually.

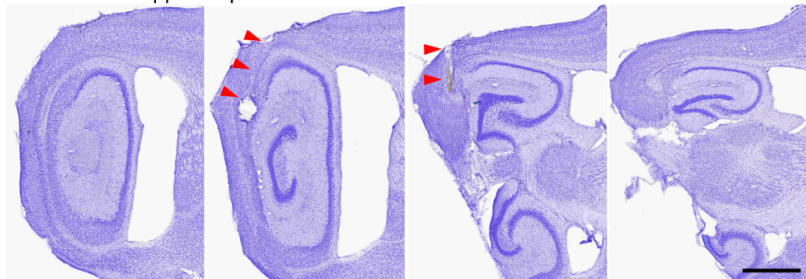
### 5.3.7 Ramp cells are found within the retrohippocampus

Where are ramping cells found in the hippocampal formation? For the purpose of this thesis, only mice with tetrodes localised to this area were analysed. To determine the location of tetrodes, brains were processed and imaged using Micro-CT based imaging or cresyl violet staining (see [2.6](#)). Tetrodes were assigned either to the MEC ( $n = 5$  mice), the pre/parasubiculum ( $n = 2$ ), or when the location was ambiguous between these areas to retrohippocampal cortex ( $n = 3$ ; [Figure 80](#)). Presubiculum and parasubiculum were not differentiated as the borders between these regions are not well defined. Localisation of the tetrodes to the retrohippocampal region was confirmed by a clear theta modulation of the local field potential and theta-locked firing consistent with previous findings from these areas ([Figure 81, 82](#); Chrobak and Buzsáki 1998; Colgin et al. 2009). The animal from which we were unable to localise the tetrodes anatomically, but had strong theta-modulation of the local field potential and theta-locked firing was assigned to the retrohippocampal group.

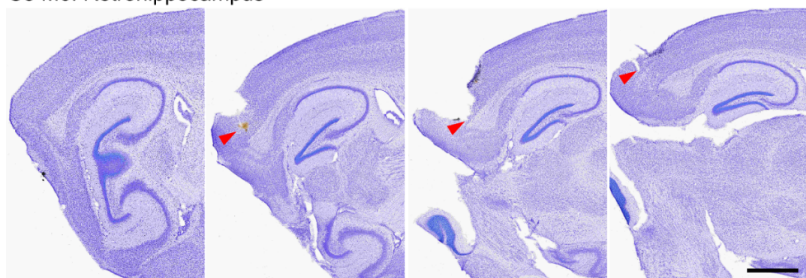
C2 245: Presubiculum



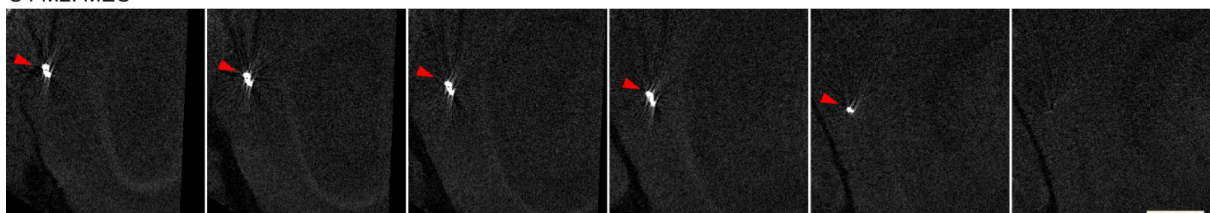
C3 M1: Retrohippocampus



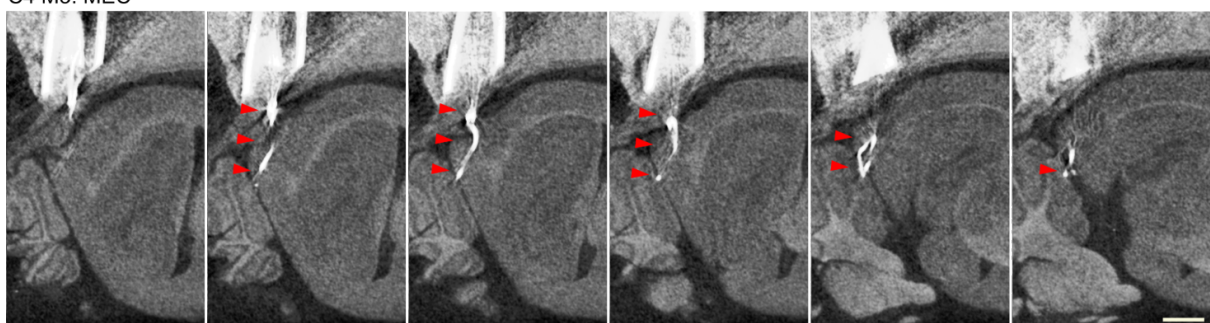
C3 M6: Retrohippocampus



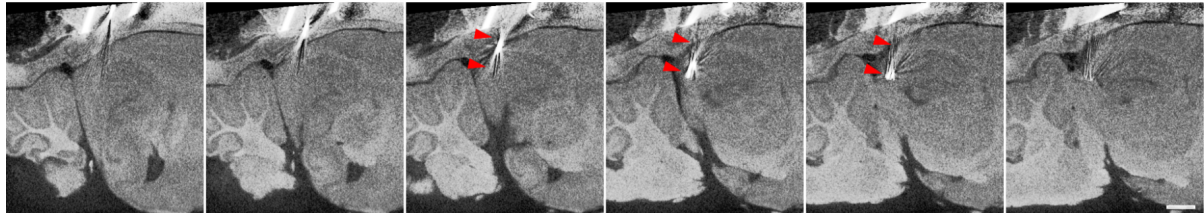
C4 M2: MEC



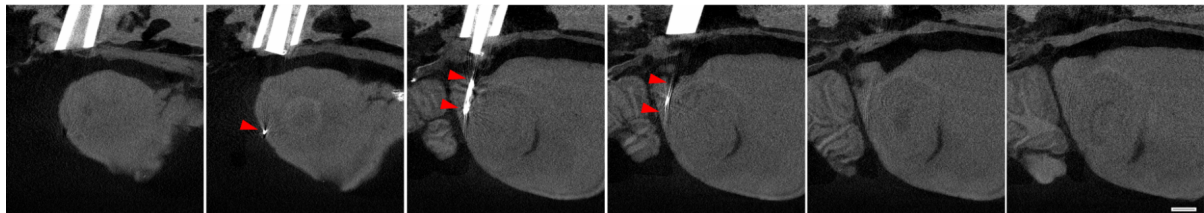
C4 M3: MEC



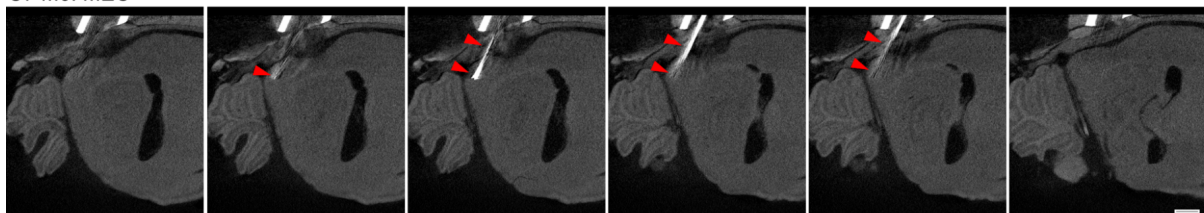
C5 M2: Presubiculum



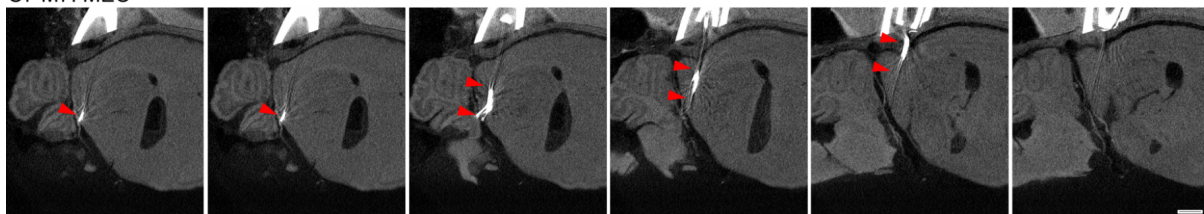
C7 M3: MEC



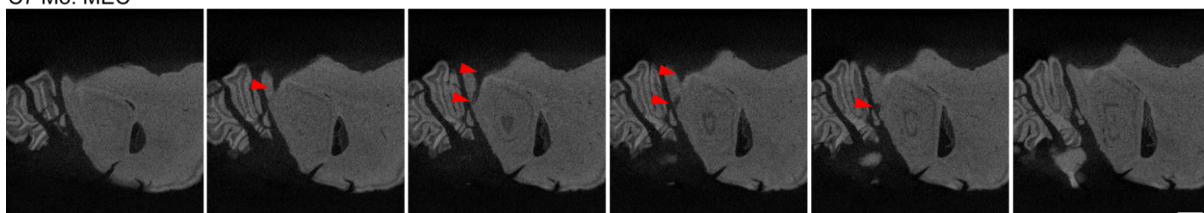
C7 M6: MEC



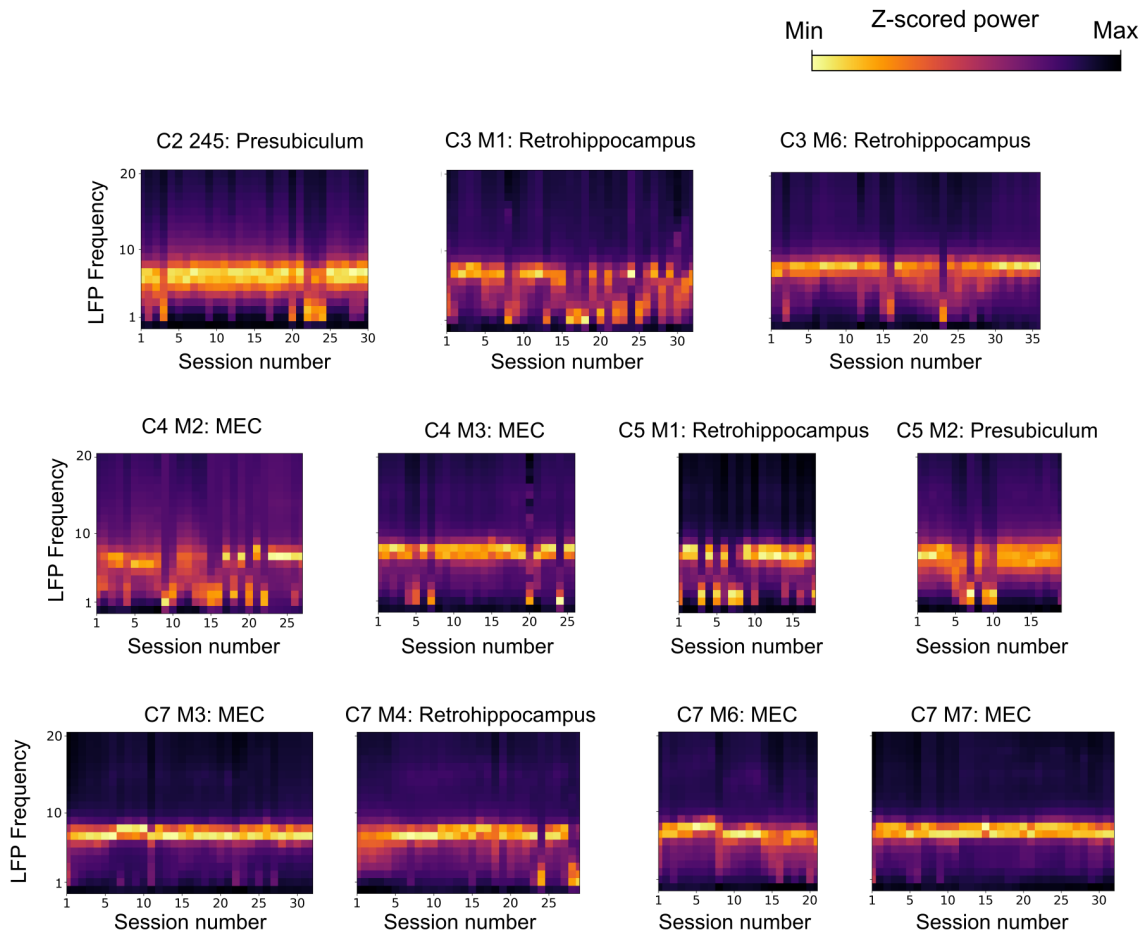
C7 M7: MEC



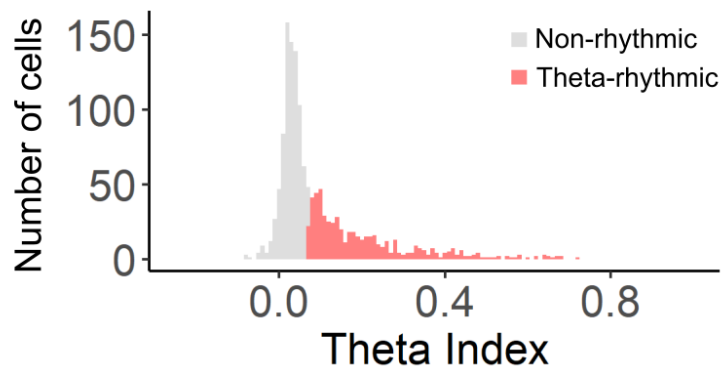
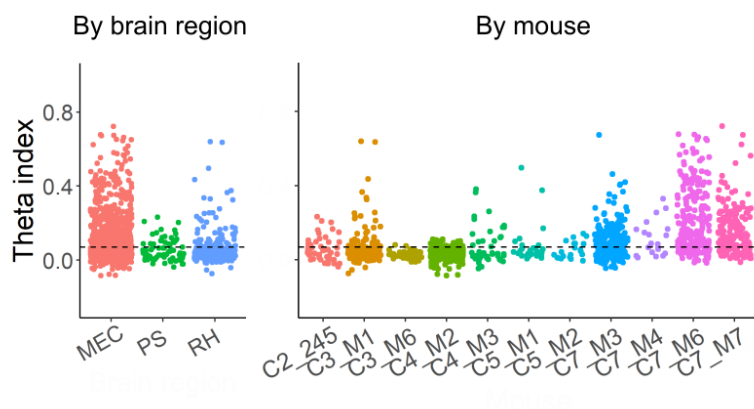
C7 M8: MEC



**Figure 80. Tetrode localisation.** Cresyl violet stained brain sections used for assessment of tetrode locations in three mice and Micro-CT images used for assessment of tetrode locations in six mice. For each animal, sagittal slices are presented lateral to medial from left to right and the classification of the tetrodes target is shown at the top left. This classification is based on the terminal location of the tetrode and the distance travelled during the experiment (see Methods). Two mice had no visible tetrode tracks in any slice and are not shown. In all images red triangles point to the putative tetrode tracks. The number of neurons recorded in each mouse was: C2 M2: 47 neurons; C3 M1: 181 neurons; C3 M6: 56 neurons; C4 M2: 314 neurons; C4 M3: 48 neurons; C5 M2: 21 neurons; C7 M3: 266 neurons; C7 M6: 243 neurons; C7 M7: 204 neurons. No histology: C5 M1: 31 neurons; C7 M4: 23 neurons. Scale bar denotes 1 mm.



**Figure 81. Heat maps of the local field potential as a function of training day.** Mouse IDs and tetrode localisation are given above. Colours denote the magnitude of the LFP power.

**A****B**

**Figure 82. Theta indices of recording neurons.** (A) Histogram of the theta index across all cells (top) and (B) scatter plots showing the theta index grouped by tetrode location (left) and mouse (right). Cells were classified as having theta-rhythmic firing (red in the histogram) when their theta index was  $> 0.07$  (indicated by a black dashed line; Kornienko et al. 2018).

### 5.3.8 Ramping activity is similar across retrohippocampal regions

Ramping neurons were found in both MEC and pre/parasubiculum areas, all with similar proportions. In both regions there was a slight bias towards negatively ramping neurons. Of the ramping neurons, position-encoding neurons were abundant in each region. Less conjunctive position encoding neurons were found in pre/parasubiculum areas however this region was not as well sampled as MEC neurons. Slopes were also similar for ramping neurons.

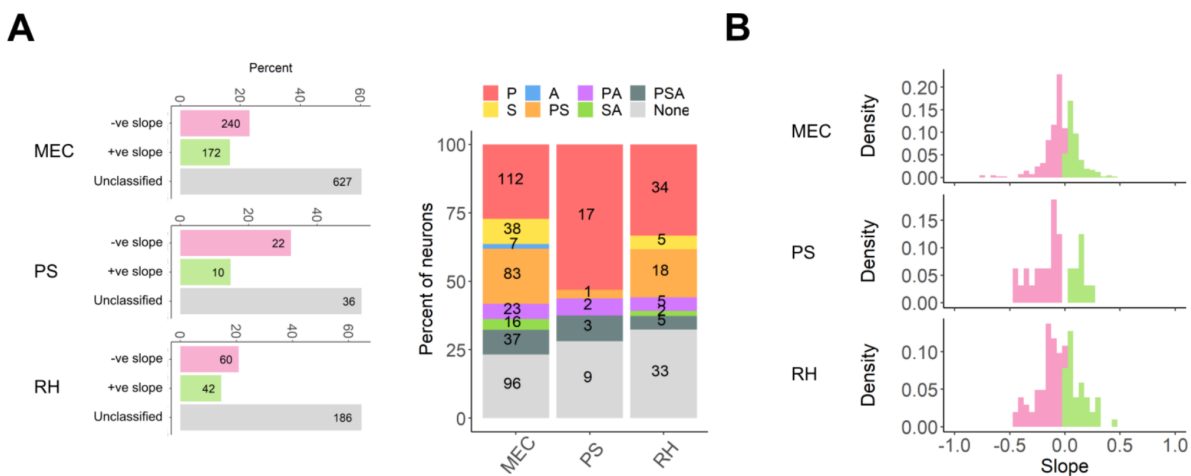


**Figure 83. Summary of ramping activity in the retrohippocampus.** (A) Proportions of cells classified as having positive, negative or unclassified slopes in the pre-reward zone region for MEC, PS and RH neurons. (B) Proportion of ramping neurons (positive or negative slopes in the pre-reward zone region) for which each combination of P, A and S coefficients were significant at a threshold of  $P < 0.01$  (Wald's chi squared test) as a function of tetrode location. (C) Distribution of pre-reward zone ramp slopes for ramping neurons for MEC, PS and RH neurons.

### 5.3.9 Theta modulation of ramp cells

The theta oscillation (4–12 Hz) in local field potentials in the hippocampal formation is closely associated with spatial functions. Individual neurons show phase precession in place and grid cells (John O’Keefe and Recce 1993; Hafting et al. 2005). Whether ramp cells show similar theta-modulated firing would suggest whether these cells are implicated in similar spatial-coding networks. Theta indices were calculated for each neuron as detailed in 5.2.5. Ramping neurons were found in both non-rhythmic and theta rhythmic cell populations, all with similar proportions. In both groups there was a slight bias towards negatively ramping neurons. Of the ramping neurons, position-encoding neurons were abundant in each group. Slopes were also similar for ramping neurons.

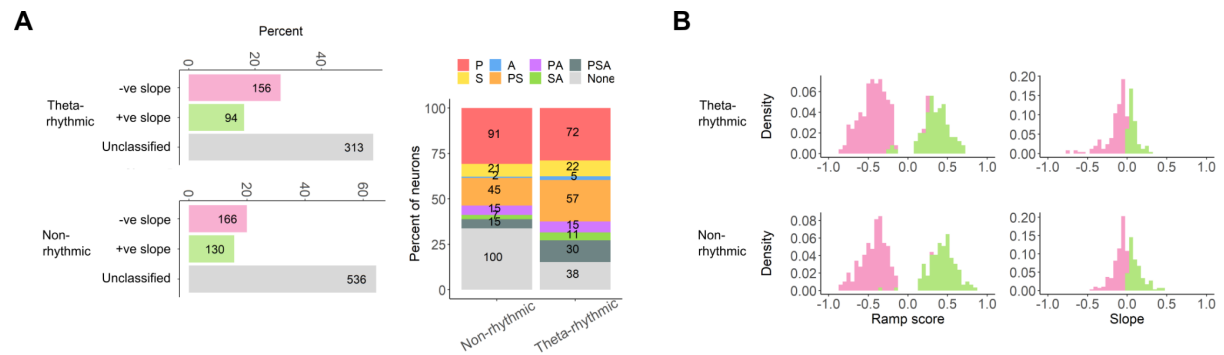


**Figure 84. Summary of theta modulation in ramping neurons.** (A) Proportions of non-rhythmic (NR) cells and theta rhythmic (TR) cells as having positive, negative or unclassified slopes in the pre-reward zone region. (B) Proportion of ramping neurons (positive or negative slopes in the pre-reward zone region) for which each combination of P, A and S coefficients were significant at a threshold of  $P < 0.01$  (Wald’s chi squared test) as a function of theta modulation. (C) Distribution of pre-reward zone ramp slopes for non-rhythmic and theta rhythmic neurons.

## 5.4 Discussion

These results show retrohippocampal neurons exhibit ramping neural activity on a virtual linear track while mice perform a spatial memory task. Ramping activity changes around the rewarded location with a reset of the ramp or a switch in polarity. From these ramping neurons, it was found position was the most influential kinematic variable over speed and acceleration. Ramping activity might still be explained by time however a time analysis revealed most ramping neurons could be better explained by position rather than time (Tennant et al. 2022). These ramp slopes were not generally affected by the spatial behaviour of the mouse on any given trial but offsets in the ramp code were, suggesting the encoded reward location is reinforced by the reward. Without a visual cue or reward present, ramp slopes and offsets were maintained albeit at reduced magnitudes, again suggesting track cues play a role in strengthening position representations along the track, possibly by anchoring the code to a salient landmark which over many trials is more consistent present at the same locations and therefore stronger.

### 5.4.1 Technical challenges

I came across several issues during the analysis described in this chapter which warrants discussion for any researcher looking to develop upon these analyses. When putting together a statistical method for classifying a ramp-like firing rate profile, a standard tool for the interpreting neuroscientist is a well designed shuffle analysis. A common shuffling procedure is the cyclic shuffle, which generates shuffled data per neuron by drawing a single random time interval and adding this to all spike timestamps to generate new spatial firing profiles while maintaining temporal dynamics. This works in environments where time additions do not frequently correspond to predictable locations like open field arenas when the animal is randomly foraging. However, on a linear track I found the implementation of a cyclic shuffle procedure reproduced ramp-like profiles in shuffled datasets suggesting the random addition of a single value onto each timestamp did little to break the ramp-like profiles across trials. A mouse running similar trial times could account for this and this prompted me to adjust the cyclic shuffling procedure by drawing a random time interval for each trial. This alone did not remove significant ramp-like profiles in the trial-averaged firing rate map. I found the process of smoothing with a Gaussian kernel systematically created false positive ramp-like profiles. With this in mind, I altered the entire analysis by removing all Gaussian smoothing except from visualisation in the presented plots and figures.

To address whether ramp cells overlapped with well characterised spatial cells like grid and border cells, similarly to Chapter 3, mice were trained in the spatial memory task and placed

in an open field arena to freely explore. Electrophysiological recordings were concatenated and spike sorted together. All mice reported in this chapter completed tasks in the two different environments, however unlike Chapter 4, electrophysiological noise was much higher in open field sessions compared to VR sessions in all but one cohort because these cohorts were recorded from a suboptimal open field setup, in terms of electrical shielding. Due to this, only this one cohort was used to compare the spatial firing properties in both environments. In the open field recordings with high noise level, very few spatial-modulated cells were found even though tetrode identification revealed the recording location was localised in retrohippocampal regions. This suggested the noise levels were too high to capture these cells and it was decided to leave these cohorts out of the open field analysis.

#### 5.4.2 Relationship to neural activity in other brain areas

Is there evidence for ramp codes in other regions of the brain? LaChance, Todd, and Taube (2019) found cells in the postrhinal cortex to encode the distance to the centre of an open field arena. This resembled a continuous code unlike discrete codes observed in place and head direction cells. Ramping activity has also been observed in the striatum that signals the time to receive a reward in rats and monkeys (Lavoie and Mizumori 1994; Fiorillo, Tobler, and Schultz 2003, respectively) and scales to reward magnitude (Howe et al. 2013). I found ramps were insensitive to the presence of a reward although no experiments were done to evaluate if rewards were critical to the formation of the positional ramps. In the prefrontal cortex (PFC), ramping activity was also shown to encode expected reward (Watanabe 1996; Hikosaka 2000; Kobayashi et al. 2002) which scales with reward magnitude (Leon and Shadlen 1999). In persistent firing neurons of the PFC, this code can be multiplexed with stimulus-dependent encoding such that neurons represent the memory of the stimulus. For example, Brody (2003) showed persistent neurons encoded the frequency of a motor stimuli presented to macaques as a function of firing rate during stimuli presentation and over the course of a delay, which resembled a similar ramp code. Taken together, ramp codes serve as a useful representation to signal the progression to a salient feature or response within a task, whether this is a location or a stimulus associated or not with a reward.

### 5.4.3 Behavioural and computational roles

Are these neural representations utilised to solve the spatial memory task? The results show that positional representations are encoded within ramping neurons which could benefit the animal during path integration. However, direct evidence for their causal role in spatial navigation will require targeted manipulation of these cells or a closed-loop task design which can interrogate the activity of ramping neurons in real time. One possible experiment might involve manipulating the gain of the VR to probe how the ramping activity maps to track locations while the proprioceptive input is placed in conflict with the visual features of the track. If ramping activity could be entrained to ramp up or down to rewarded locations either marked by a visually-defined reward location or a distance-defined reward location, this would provide direct evidence for the utility of ramping representations driving navigation. Indirect evidence for their function has been provided by Ian Hawes who created an artificial reinforcement learning agent with a recurrent neural network architecture. Ramping units (artificial neurons within the network) emerged in the recurrent layers of an agent trained to learn a similar task. Performance was disrupted upon lesioning the output of ramping units but performance was preserved upon lesioning outputs of non-ramping units (Tennant et al. 2022). These simulations suggest ramping units are more useful representations than non-ramping units in an analogous linear location task.

Whether these representations manifest over the course of training or are present from the beginning may further address issues of causality. This was not possible to address within the current task design. Tetrodes were lowered over the course of training towards the targeted retrohippocampal areas so it was difficult to address whether ramps were not found for reasons of learning or tetrode locations. Future experiments with high-density silicon probes will help elucidate the manifestation of this ramping activity.

Current theories support ramping position codes as intermediate outputs to grid cells by providing a metric of travelled distance from salient landmarks (Stemmler, Mathis, and Herz 2015; Bush et al. 2015; Fiete, Burak, and Brookings 2008). Under these circumstances, the learned track structure is stored within synaptic weights onto grid cells. As discussed in [1.4.4](#), positional ramping neurons can be utilised as a readout system from the grid code during vector navigation. If this is the case, investigating the activity of grid and ramp cells in conjunction will address whether these cell types are part of a coherent internal model of location estimation. For example, if ramp codes are associated with grid cells, spatial information would be lower during distance-encoding epochs compared to position-encoding epochs. Unfortunately, grid cells were not recorded in great numbers within the experiment.

To that end, further experiments included in this thesis have recorded greater grid cell numbers and will be the main focus of the next chapter.

## Discussion

The aim of the thesis was to investigate the coding schemes of grid cells and putative readout cells while a mouse navigated using beaconing and path integration-based self-localisation strategies. To address this aim, tetrode neural implants were targeted to retrohippocampal regions in mice. These mice performed a linear location task that required either beaconing and path integration-based navigation to solve. Grid cells were found in the MEC while ramp cells were found all throughout retrohippocampal areas including the MEC, presubiculum and parasubiculum. A range of behaviours were captured which covered different trial outcomes of a linear location task that required both beaconing and path integration to solve. This allowed for an analysis of the neural activity in which I could ask, to what extent can spatial coding be explained in terms of active engagement of beaconing and path integration-based behaviours? I modified our lab's existing analysis pipeline ([https://github.com/MattNolanLab/in\\_vivo\\_ophys\\_openephys](https://github.com/MattNolanLab/in_vivo_ophys_openephys)) to accommodate spike sorting across multiple sessions. With this modification, cells could be tracked across sessions recorded on the same day. This allowed the investigation of spatial cells identified in the open field session to be studied in the virtual reality session and vice versa.

Grid cells were found to fire periodically on the linear track, as predicted by grid firing in open field arenas, which reflected an allocentric code for position. However, it was clear grid cells were not consistently anchored to track cues. This inspired me to develop an analysis which could classify whether a cell's periodicity was consistent with anchoring to track cues or not. If the periodic firing fields anchored to track cues, the firing fields appeared at roughly the same locations on each trial. If the periodic firing fields did not anchor to track cues, the firing fields appeared at different locations on each trial. When grid firing is locked to track cues, the grid code can convey a reliable allothetic estimate of position within the environment. On the other hand, when grid firing is not locked to track cues, the grid code can convey an egocentric metric of distance travelled information (Figure 48). Are either or both position and distance coding schemes compatible with navigation using beaconing and path integration behaviours? I found grid cells frequently remap between these two coding schemes but the position code is more frequently utilised when the mouse is successful in trials that require path integration but not necessarily beaconing. The findings are consistent with previous studies linking grid cell activity to path integration behaviours (Allen et al. 2014; Kunz et al. 2015; Gil et al. 2018; Tennant et al. 2018). More specifically, I show accurate path integration and not beaconing is associated with the positional coding of grid cells, consistent with findings of Gil et al. (2018), who showed disrupted grid representations in mice coincides with a poor performance of a path integration but not beaconing.

The experiments in this thesis also contributed to the characterisation of recently discovered ramping representations of location by retrohippocampal neurons. This previously undiscovered cell type in the retrohippocampus fired proportionally as a function of distance from a salient location on the track and was shown to encode position along the track by the cell's instantaneous firing rate. This continuous coding scheme contrasts the discrete coding schemes found in similar regions of the brain such as place and grid cells. Ramp-like codes were maintained independently of trial outcome and trial type suggesting that the ramp code results from memory recall of the track structure. These positional ramp cells were largely non-overlapping with previously defined cell-types in the open field setting, being most defined as non-specific spatial cells, but no more frequently than non-positional ramp cells. As these cells did not overlap with grid cell populations, it remains possible that ramp cells offer a solution to the readout of positional estimates from the theorised population code for location conveyed by the grid cell system (Fiete, Burak, and Brookings 2008; Stemmler, Mathis, and Herz 2015).

In the following discussion, I will detail the implications and limitations of the thesis findings and put forward experiments that will address the next steps towards understanding the neural systems of self-localisation.

## 6.1 What role do grid cells play in self localisation?

The analysis in Chapter 4 provides evidence that grid cell firing is associated with the behaviour of mice while performing path integration-based but not beaconing navigation strategies. This corroborates the long-standing hypothesis that grid cells are utilised in path integration for the purpose of self-localisation (Hafting et al. 2005; McNaughton et al. 2006). Grid cells were found to fire in a spatially-periodic fashion when recorded from mice on a linear track. Spatially-periodic firing of grid cells could either be anchored to the virtual track, in which case the grid cell encoded position in an allocentric frame of reference, or it could be independent of track position, in which case the grid cell encoded distance in an egocentric reference frame ([Figure 48](#), [55](#)). Both schemes are consistent with active path integration computations, with both presumably requiring sufficient velocity input integrated over time to evoke the next firing field, although positional coding alone was found to be more beneficial to mice engaging in trials that required path integration-based navigation.

What distinguishes position and distance coding is the ability to anchor spatial firing to external salient cues. What role does grid anchoring play in path integration? In order to stop at specific locations along the linear track with path integration, distance travelled must be tracked over time from a starting point. As path integration is prone to accumulating errors, reducing the distances that need to be tracked by resetting this starting point greatly reduces the size of the error in the distance travelled estimate. If grid fields anchor to salient landmarks of the track when they are available, these errors are reset. This resetting is compatible with experiments in which the availability of cues were reduced and grid cell activity compared. Chen et al. (2016) showed grid cells were less spatially stable and periodic in darkness than in illuminated environments, whereas Pérez-Escobar et al. (2016) showed removing visual landmarks from a linear track greatly reduced the spatial periodicity of recorded grid cells. This thesis suggests that the grid position code is associated with accurate path integration and that the distance code may not be required for accurate path integration. Consequently, it becomes apparent that central to accurate path integration is in fact grid anchoring. Without anchoring the grid code to salient cues, grid fields tend to drift spatially as path integration errors grow. External spatial input is thus required to stabilise grid representations as has been found in path integration models (Pastoll et al. 2013; Solanka, Van Rossum, and Nolan 2015; Shipston-Sharman, Solanka, and Nolan 2016). In the context of grid vector population codes (Fiete, Burak, and Brookings 2008; Stemmler, Mathis, and Herz 2015), anchoring ensures locations are encoded with the same vector code across trials, without phases within the vector changing their mapping to specific locations across trials. Without anchoring, the location of grid fields fluctuates across trials. This results

in the phase vector code varying across trials even when the mouse is at the same track location on different trials. This would be difficult to be read out by downstream neurons without dedicated neural circuits that could track phase changes across trials. Further, if phases from individual grid modules change at different rates, this vector becomes even more difficult to decode. To test the role of grid anchoring in accurate path integration against the allocentric grid position code, I propose an altered version of the linear location task that puts the two in conflict. In this task, a dynamically positioned cue defines the starting point of which to path integrate to a non-cued goal location. If grid anchoring is critical to accurate path integration, trials in which the mouse stops at the correct reward location will coincide with trials in which the grid code is anchored to this dynamically positioned starting cue. On the other hand, if the allocentric grid position code is critical to accurate path integration, accurate path integration trials will coincide with trials in which the grid code is anchored to all track cues except the dynamically positioned starting cue. Similar to the current task, beaconed trials could be used to initialise the association between the distance and the rewarded locations as well as control for the differences in neural activity during beaconing and path integration-based navigation.

What mediates cue anchoring of grid cells? Spatial input from place cells is sufficient to stabilise grid representations in path integration models (Pastoll et al. 2013; Solanka, Van Rossum, and Nolan 2015; Shipston-Sharman, Solanka, and Nolan 2016). Furthermore, inactivation of the hippocampus has been shown to disrupt grid cell periodicity (Bonnevie et al. 2013) supporting the idea that place cells provide the spatial input critical for cue anchoring. In the scenario that alternative cells perform path integration, grid cells might be used to interface between these path integrators and the sensory information that anchors the incoming path integration input. To date, no studies have yet to show a closeup analysis of the spatial input to grid cells, leaving the door open to the possibility for another putative path integrator to facilitate the operation before synapsing onto grid cells. More broadly, cue anchoring might be mediated by the visual attention of the animal. Increased attention is associated with an increase in the signal-to-noise ratio of neurons that represent the attended stimuli (Lindsay 2020) as well as increased spiking coherence in the gamma band (Fries et al. 2008). Long silicon probes targeted to both visual regions and the MEC (which is possible due to their proximity in mice) could be used to measure these signals against grid anchoring dynamics during the linear location task.

How might this grid positional coding afford an accurate self-localisation estimate? Unlike the distance coding scheme, position encoding grid cells can confer a reliable estimate of location using the phase vector population code (Fiete, Burak, and Brookings 2008;

Stemmler, Mathis, and Herz 2015), as described in 1.4.4. With the grid phase vector encoding position, self-location estimates can be readout and compared to the grid phase vector corresponding to the reward location to guide stopping behaviour through vector navigation (Bush et al. 2015). Mechanistically, grid cells have themselves the machinery necessary to perform path integration operations (Burak and Fiete 2009; McNaughton et al. 2006). However, in an alternative scenario suggested by Bush et al. (2015), positional-decoding might be carried out by other cells that convey spatially periodic information such as band cells (Bush et al. 2015) or VCOs (Burgess, Barry, and O'Keefe 2007). Interestingly, the non-grid cell population presented in 4.3.1 (Figure 56) also contained distance encoding cells which are consistent with the periodicity signature of band cells and VCOs. If grid cells were to receive input from these putative path integrator cells, a close look at the information flow between simultaneously recorded pairs of periodic grid and non-grid cells could be used to address this possible scenario. Under either of these frameworks, individual grid cells or upstream cells perform path integration with updates of their firing in accordance with self-motion signals which results in the translation of the grid phases for individual grid modules. These phases form a population phase vector code across modules that is then readout into a self-location estimate from which goal-directed navigation can be guided.

To summarise, this thesis further provides evidence that grid cells bear the fruit of path integration operations but it remains unclear whether grid cells actively perform path integration or are downstream of cells that facilitate path integration operations. Accurate path integration during positional grid coding support models proposing grid cells convey an allocentric representation of space. What is clear is that anchoring dynamics that separates periodic grid coding into a position and distance code appears to mediate accurate self-localisation when path integration is required. The majority of computational models (both hand-designed or trained) support grid cells as the sole actuator in path integration operations without the need for intermediate periodic components (McNaughton et al. 2006; Burak and Fiete 2009; Sorscher et al. 2020), however without further investigation into the exact inputs received by grid cells, little can be concluded to pinpoint the illusive path integrator.

## 6.2 What role do ramp cells play in self localisation?

Chapter 5 detailed the discovery of putative readout cells in the form of a continuous code for location, which resembled ramping firing activity that mapped onto locations along segments within the linear track. These representations were maintained across trial types and different levels of task engagement such that ramp slopes were greater than chance-level. This suggested the representation reflected a recalled structure of the track, which could in theory be used by the mouse to readout self-location estimates and guide navigation. However, slopes were found to be significantly smaller during probe trials compared to beaconsed trials. This suggests that at least for some neurons, sensory information from the reward zone improves the ramp profile over both key regions of the track. Slopes did not change in respect to the trial outcome on beaconsed trials, while this was not investigated on non-beaconsed trials because of low trial numbers. This invariance to trial outcome suggests that the track structure remained embedded as a spatial memory regardless of whether the mouse actively engaged in the task or not. Slope offsets between sloping groups - - and + + were influenced by both trial type and trial outcome. If offsets are aligned to stopping location on a trial-by-trial basis, the increased variability in stopping locations across trial outcomes would explain such differences. This could also help explain similar changes in slope offset found between trial types as trial outcome was not controlled for in this comparison. This could easily be tested by calculating the best fitting slopes on each trial and asking whether intersections of these slopes align to stopping locations. Taken together, ramp cells reflect a representation of self-location that is compartmentalised to specific regions of the linear track and is improved by sensory cues similarly to grid cells on linear tracks (Pérez-Escobar et al. 2016).

Whether these representations are actively recruited in self-localisation behaviours still remains unclear. Beaconsing behaviour does not strictly require a self-location readout if mice utilise a cue-response strategy to stop. As ramp slopes are influenced by the presence of the beaconsing cue, any self-location estimate encoded in the ramp cell representation could be corrected upon first sight of the cue regardless of engagement. Under this scenario, ramp cells encode the self-location estimate but do not dictate whether the mouse actively chooses to use it (at least in the case for beaconsing). As for path integration behaviours, these were not well captured within the cohorts recorded in the study. Addressing how these cells responded to different levels of task engagement on non-beaconsed trials (and thus during path integration behaviours) was not possible due to relatively low numbers of non-beaconsed trials in the experimental design used. Nevertheless, evidence linking ramping activity to path integration behaviour comes in the form of computational modelling

performed by Ian Hawes, who showed when an artificial neural network was trained to complete a similar version of the linear location task, network units were found to hold very similar ramping profiles (Tennant et al. 2022). This suggested the formation of spatial memories by ramping representations of space offers a solution to the readout of path integration computations. Removal of the outputs from these ramping units disrupted accurate path integration behaviours. While this evidence supports the claim that ramp cells facilitate path integration behaviours, whether the ramp network is truly a solution to path integration or an artefact of a highly selective hyperparameter space (Schaeffer, Khona, and Fiete 2022) requires an extensive meta analysis to determine if this solution is singular and or rare. To address the relationships between ramping activity and path integration behaviours, further *in vivo* experimentation is needed with a focus on collecting data from more non-beaconed trials, which is now possible with the improvements discussed in Chapter 3, and was implemented in the cohorts used in Chapter 4.

How might ramps contribute to accurate path integration? Although not addressed empirically within the study, an allocentric self-localisation estimate (e.g. from the grid code) is consistent with accurate path integration. It follows that ramping code could convey a self-location estimate to guide stopping behaviour in the linear location task. Unlike the grid readout mechanisms involving ramp-like cells, I found ramp cells were compartmentalised to segments of the track, consistent with encoding proximity to event boundaries like in the bat hippocampus (Sarel et al. 2017). To test this, the same ramp analysis could be performed on similar neural recording experiments from mice on linear tracks to see if neural ramps align with event boundaries (e.g. track segments between salient cues or rewards). For cells that maintained their slope sign across each region of the track, these cells resembled cells in the striatum that encoded the expected reward as a function of proximity to the reward (Howe et al. 2013). To test if the expected reward plays a role in the mediation of neural ramps, reward size can be altered or removed entirely. Furthermore, mice start the experiment without a reward-bias for the reward zone. Recording the evolution of neural ramping over the course of the experiment would reveal how these ramps emerge as a consequence of learning with or without a reward. To achieve this, switching to chronically implanted silicon probes over tetrode implants offer the possibility to record a large neural population and importantly from the same brain regions over the course of the experiment.

### 6.3 Joint grid-ramp system for self-localisation?

Whether grid cells and ramp cells functionally interact within the same neural architectures remains to be seen. The discovery of ramp cells aligns with the theorised presence of readout cells for the grid cell system (Fiete, Burak, and Brookings 2008; Bush et al. 2015; Stemmler, Mathis, and Herz 2015). In these models, input from grid cells drive ramping activity. Alternatively, ramping activity might arise independently of grid firing. For example, ramp cells emerged without grid-like activity in the recurrent neural network of a reinforcement learning agent trained in the analogous linear location task (see 5.4.3; Tennant et al. 2022).

If grid cells do indeed communicate positional information to ramp cells, ramping activity would be affected by the disruption of the grid code. Selective manipulations of grid cells could be used to identify this link. From an analysis perspective, relationships between the ramp and grid cells might already be possible from available neural recordings. In the grid vector phase model of encoding location, grid cells are required to encode position rather than distance nor aperiodically. This predicts ramping activity would be impaired while grid cells are not actively encoding position (as defined in 4.2.3.2). If however, ramping activity is not coupled to positional coding of grid cells, this will support the alternative hypothesis for the independent emergence of positional ramping activity. Moreover, in the case grid cell input drives ramping activity before error-correction properties of the grid population code take effect (Sreenivasan and Fiete 2011; Stemmler, Mathis, and Herz 2015), it can be predicted that ramping activity would exhibit correlated trial-by-trial variability with grid cells. Correlating the variability in grid fields across trials or ‘jitter’ with the trial-to-trial variability of ramp cells would be a simple test to address this, similarly to how grid cell jitter has been shown to be correlated with other jointly recorded grid cells (Nagele, Herz, and Stemmler 2020).

Are ramp and grid cells found at the same anatomical locations in the retrohippocampus? Here I have shown ramp cells are located at multiple locations across the retrohippocampus. Grid cells have also been recorded at all anatomical locations where ramp cells reside (MEC, presubiculum and parasubiculum; Hafting et al. 2005; Boccara et al. 2010). Similar anatomical localisation supports the hypothesis that grid cells are well placed to convey positional information to ramp cells. However, whether grid and ramp cells are anatomically colocalized remains to be seen. Neural recordings from this thesis are available to address this question. If they are anatomically local, positional ramp cells should be found on the same tetrode as jointly recorded grid cells.

To better understand the interconnectivity of ramp and grid cells as a coherent neural network, several lines of analysis have been suggested. Analysis looking at the joint activity of ramp and grid populations is currently limited within the current data available. This is because of the relatively few cells that can be jointly recorded with a 16-channel tetrode array. Future experiments will employ more channels with the aspiration to (1) record both ramp and grid cells and (2) within large enough numbers and across multiple locations to make inferences with regards to population activity.

## 6.4 Wider applications of the research findings

### 6.4.1 Models for self-localisation and beyond

Arriving at a computational model of how mammals navigate in complex environments is a long term objective for the neuroscience community. Discoveries to date have delivered a platter of neurons that facilitate metrics for speed, place, heading and border information (O’keefe and Nadel 1978; Solstad et al. 2008; Lever et al. 2009; J. Taube, Muller, and Ranck 1990; Kropff et al. 2015) as well as algorithmic solutions to self-location, path integration and vector navigation (Hafting et al. 2005; McNaughton et al. 2006; Fiete, Burak, and Brookings 2008; Burak and Fiete 2009; Bush et al. 2015; Stemmler, Mathis, and Herz 2015). The major gap in knowledge currently stands in reconciling these cells and mechanisms with task specific behaviours and measuring the predictions spawned from the mechanistic solutions to self-localisation and navigation in general. This thesis provides a clear proof of concept for using the linear location task to appropriately capture spatial cells while animals engage (or not) in path integration or beaconing behaviours. This task is invaluable for future experiments that seek to close the loop between behaviour and neural activity. Further, this thesis provides a biological constraint to grid-based navigation models or at least a testable prediction with respect to the grid anchoring relationship with path integration performance. With further validation of ramping representations providing a readout mechanism of a grid code, this may also be added as a biological constraint onto state-of-the-art models that propose grid cells as a general solution to self-localisation. While artificial networks can be trained to decode grid codes directly (Fiete, Burak, and Brookings 2008), closer realisations of biological networks will require a separate readout mechanism.

As discussed in [1.3.4](#), the grid cell system may not simply operate within a feature space of physical distances but rather encodes states within continuous feature spaces however abstract. An extension of this work would predict ramp-like codes would exist as a potential readout mechanism in these abstract feature spaces. This would be testable with the neural

recording and ramping analysis of retrohippocampal cells while mice perform a continuous choice task similar to the linear location task, such as the frequency choice task (Aronov, Nevers, and Tank 2017). My findings suggest that anchoring of grid codes to salient features of an environment would be required for successful performance of abstract tasks. To test this, an experiment can be designed in which a mouse performs a task in an abstract 2D feature space while recording grid activity. This experimental design extends from similar experiments in humans, whereby grid-like representations were observed while humans performed navigated 2D abstract feature spaces (Constantinescu, O'Reilly, and Behrens 2016). A possible experiment would see a mouse head-fixed in a virtual reality setup, however the projected environment could be made of 2 coaxial variables, such as the size of a projected bar in the X and Y dimensions. A continuous change of the length of these two variables would be synonymous to movement through a 2D environment. If a reward was released at only certain coordinates in this feature space, a similar mapping of grid representations would theoretically emerge with neural recording of grid cells and sufficient sampling of the feature space. Results from this thesis would predict that when the mice was not actively licking for a reward in the correct location of the feature space, the grid structure would not be readily seen in a session-wide rate map, but would be present if the mouse was doing well at the task as the positional locking would be present and thus more grid-like than a non-anchored representation.

Artificial intelligence may also benefit from these findings, as researchers seek to build artificial agents and robots to self-reliantly navigate complex spaces. Modern artificial intelligence has taken a leaf out of the book of neuroscience by employing features of neurons or network-wide arrangements of neurons such as deep learning, which employs the compartmentalised function of single neuron activity in receiving and propagating signals as well as how these neurons are arranged in numerous functional layers within distinct neural systems. Robots and artificial agents suffer much the same sensory deficits as humans, without appropriate or insufficient sensory stimuli, they are blinded and must make best-guesses to inform their future actions until more informative sensory information is available. As has been proposed by Banino et al. (2018), grid cells may form a unique solution to navigating novel environments. My findings suggest accurate navigation in sensory-poor environments warrants an environment-locked grid code. Should artificial intelligence researchers pursue future grid cell models of navigation, systems which query the environment locking of grid cells may be required. Furthermore, while it is well within the capabilities of artificial agents to decode position directly from the grid code, the discovery of ramp cells suggests a designated readout might be beneficial to downstream operations in the action-observation cycle key in all artificial agents.

#### 6.4.2 Diagnosis of Alzheimer's disease

My finding that positional coding of grid cells is associated with accurate path integration behaviours sheds new light on the links between navigational deficits observed in patients suffering from Alzheimer's disease (Coughlan et al. 2018). Degraded grid representations which have been reported in Alzheimer's model in mice (Fu et al. 2017; Jun et al. 2020) might be explained by early neural atrophy found in the entorhinal cortex that either reduces the population of grid cells or removes vital connectivity that provides the important anchoring dynamics required for positional coding in grid cells, or indeed both. In either context, my finding provides a crucial validation of the long suspected links between grid cell activity and path integration. Researchers have been developing navigational tasks in hope of providing diagnostic markers for the early detection of AD before short-term memory deficits are observed (Coughlan et al. 2018). For example, performance in the supermarket task whereby patients are played a video of a first-person route around a supermarket before choosing the direction to the starting location was shown to be a highly indicative marker of AD compared with other forms of dementia (Tu et al. 2015). Patients with mild cognitive impairment (MCI) with other biomarkers for AD (MCI+) were well distinguished from MCI patients without these biomarkers (MCI-) in a simple triangulation task in virtual reality (Howett et al. 2019). Discrimination between MCI and AD patient groups has also been reported in a similar triangulation task in real world navigation (Mokrisova et al. 2016).

My results suggest path integration accuracy can be explained by grid cell activity on a 1D linear track task and need not require navigation in 2D environments to differentiate between impaired or unimpaired path integration. Implementation of the linear location task described in this thesis might offer a simpler and more high throughput test for path integration behaviour. As the environment is simple and minimal in terms of sensory cues, it offers no alternative strategies for completion other than path integration by estimation of self-location from a set reference point. Furthermore, the task benefits from being simple to explain and control for the participant which is imperative when assaying elderly patients/participants. Early studies from our lab have looked into the implementation of a joystick-controlled version of this linear location task using the Oculus-Rift head mounted virtual reality system and has been demonstrated to be achievable from many participants who have volunteered for a number of undergraduate research projects looking into the suitability of the task.

The discovery of ramp-codes in the retrohippocampus also suggests neural atrophy of the entorhinal cortex might affect this population of spatial cells. If these cells are indeed used in combination with grid cells to encode self-location, disruption of these representations should be expected in AD mice models similarly to degradation in grid representations (Fu et al.

2017; Jun et al. 2020). If grid cells do lie at the heart of the atrophy that presents the earliest symptomatology of Alzheimer's disease, the connections that provide the vital cue anchoring signals might explain the observed degraded grid representations. If these connections were disrupted first, continuous attractor dynamics would remain relatively intact and could be tested for with a test that assays spatial periodicity rather than estimation of absolute locations.

## Conclusions

This thesis extends the field of self-localisation by demonstrating how spatially-modulated cell types in the retrohippocampus encode representations of positional estimates within an environment. Grid cells were found to encode either a position or distance code, with the former encoding more frequently while animals were actively engaged in path integration behaviours but not beaconing. A possible readout cell, the ramp cell, was found in all retrohippocampal regions where grid cells are also found. Ramp cells were found to encode a rate-coded continuous representation of space encoding position on segments of the linear VR track. The representation was maintained across trial types and different levels of task engagement suggesting the representations reflect recall of the track structure. My results indicate grid cells play a key role in path integration in order to update self-location estimates in the brain, while ramp cells might provide a clear readout of self-location estimates by downstream brain areas. Future studies will need to consolidate these claims by addressing grid and ramp codes at the population level and the network interactions between these two cell types, possibly with the forthcoming availability of stable and high density neural probes (Steinmetz et al. 2021).

## Bibliography

- Ainge, James A., Matthijs A.A. van der Meer, Rosamund F. Langston, and Emma R. Wood. 2007. ‘Exploring the Role of Context-Dependent Hippocampal Activity in Spatial Alternation Behavior’. *Hippocampus* 17 (10): 988–1002.  
<https://doi.org/10.1002/hipo.20301>.
- Allen, Kevin, Mariana Gil, Evgeny Resnik, Oana Toader, Peter Seeburg, and Hannah Monyer. 2014. ‘Impaired Path Integration and Grid Cell Spatial Periodicity in Mice Lacking GluA1-Containing AMPA Receptors’. *The Journal of Neuroscience* 34 (18): 6245–59. <https://doi.org/10.1523/JNEUROSCI.4330-13.2014>.
- Aronov, Dmitriy, Rhino Nevers, and David W. Tank. 2017. ‘Mapping of a Non-Spatial Dimension by the Hippocampal-Entorhinal Circuit’. *Nature*.  
<https://doi.org/10.1038/nature21692>.
- Baluev, Roman V. 2007. ‘Assessing Statistical Significance of Periodogram Peaks’. <https://doi.org/10.48550/ARXIV.0711.0330>.
- Banino, Andrea, Caswell Barry, Benigno Uria, Charles Blundell, Timothy Lillicrap, Piotr Mirowski, Alexander Pritzel, et al. 2018. ‘Vector-Based Navigation Using Grid-like Representations in Artificial Agents’. *Nature*.  
<https://doi.org/10.1038/s41586-018-0102-6>.
- Barry, C., and N. Burgess. 2017. ‘To Be a Grid Cell: Shuffling Procedures for Determining “Gridness”’. Preprint. Neuroscience. <https://doi.org/10.1101/230250>.
- Barry, Caswell, Robin Hayman, Neil Burgess, and Kathryn J Jeffery. 2007. ‘Experience-Dependent Rescaling of Entorhinal Grids’. *Nature Neuroscience* 10 (6): 682–84. <https://doi.org/10.1038/nn1905>.
- Bates, Douglas, Martin Mächler, Ben Bolker, and Steve Walker. 2015. ‘Fitting Linear Mixed-Effects Models Using **Lme4**’. *Journal of Statistical Software* 67 (1).  
<https://doi.org/10.18637/jss.v067.i01>.

Behrens, Timothy E.J., Timothy H. Muller, James C.R. Whittington, Shirley Mark, Alon B. Baram, Kimberly L. Stachenfeld, and Zeb Kurth-Nelson. 2018. 'What Is a Cognitive Map? Organizing Knowledge for Flexible Behavior'. *Neuron*.  
<https://doi.org/10.1016/j.neuron.2018.10.002>.

Benjamini, Yoav, and Yosef Hochberg. 1995. 'Controlling the False Discovery Rate: A Practical and Powerful Approach to Multiple Testing'. *Journal of the Royal Statistical Society: Series B (Methodological)* 57 (1): 289–300.  
<https://doi.org/10.1111/j.2517-6161.1995.tb02031.x>.

Betts, Holly C., Mark N. Puttick, James W. Clark, Tom A. Williams, Philip C. J. Donoghue, and Davide Pisani. 2018. 'Integrated Genomic and Fossil Evidence Illuminates Life's Early Evolution and Eukaryote Origin'. *Nature Ecology & Evolution* 2 (10): 1556–62.  
<https://doi.org/10.1038/s41559-018-0644-x>.

Bjerknes, Tale L., Edvard I. Moser, and May Britt Moser. 2014. 'Representation of Geometric Borders in the Developing Rat'. *Neuron* 82 (1): 71–78.  
<https://doi.org/10.1016/j.neuron.2014.02.014>.

Blatchley, Willis Stanley. 1896. *Indiana Caves and Their Fauna*. 21st Annual Report. Indiana Department of Geology and Natural Resources.

Boccara, Charlotte N, Francesca Sargolini, Veslemøy Hult Thoresen, Trygve Solstad, Menno P Witter, Edvard I Moser, and May-Britt Moser. 2010. 'Grid Cells in Pre- and Parasubiculum'. *Nature Neuroscience* 13 (8): 987–94.  
<https://doi.org/10.1038/nn.2602>.

Bonnevie, Tora, Benjamin Dunn, Marianne Fyhn, Torkel Hafting, Dori Derdikman, John L Kubie, Yasser Roudi, Edvard I Moser, and May-Britt Moser. 2013. 'Grid Cells Require Excitatory Drive from the Hippocampus'. *Nature Neuroscience* 16 (3): 309–17.  
<https://doi.org/10.1038/nn.3311>.

Brody, C. D. 2003. 'Timing and Neural Encoding of Somatosensory Parametric Working Memory in Macaque Prefrontal Cortex'. *Cerebral Cortex* 13 (11): 1196–1207.  
<https://doi.org/10.1093/cercor/bhg100>.

Brun, Vegard Heimly, Stefan Leutgeb, Hui-Qiu Wu, Robert Schwarcz, Menno P. Witter, Edvard I. Moser, and May-Britt Moser. 2008. 'Impaired Spatial Representation in CA1 after Lesion of Direct Input from Entorhinal Cortex'. *Neuron* 57 (2): 290–302. <https://doi.org/10.1016/j.neuron.2007.11.034>.

Buchler, E.R., and S.B. Childs. 1981. 'Orientation to Distant Sounds by Foraging Big Brown Bats (*Eptesicus Fuscus*)'. *Animal Behaviour* 29 (2): 428–32. [https://doi.org/10.1016/S0003-3472\(81\)80102-9](https://doi.org/10.1016/S0003-3472(81)80102-9).

Burak, Yoram, and Ila R. Fiete. 2009. 'Accurate Path Integration in Continuous Attractor Network Models of Grid Cells'. *PLoS Computational Biology*. <https://doi.org/10.1371/journal.pcbi.1000291>.

Burgess, Neil, Caswell Barry, and John O'Keefe. 2007. 'An Oscillatory Interference Model of Grid Cell Firing'. *Hippocampus* 17 (9): 801–12. <https://doi.org/10.1002/hipo.20327>.

Bush, Daniel, Caswell Barry, Daniel Manson, and Neil Burgess. 2015. 'Using Grid Cells for Navigation'. *Neuron*. <https://doi.org/10.1016/j.neuron.2015.07.006>.

Butler, William N., Kiah Hardcastle, and Lisa M. Giocomo. 2019. 'Remembered Reward Locations Restructure Entorhinal Spatial Maps'. *Science* 363 (6434): 1447–52. <https://doi.org/10.1126/science.aav5297>.

Buzsáki, György, and Edvard I Moser. 2013. 'Memory, Navigation and Theta Rhythm in the Hippocampal-Entorhinal System'. *Nature Neuroscience* 16 (2): 130–38. <https://doi.org/10.1038/nn.3304>.

Campbell, Malcolm G., Alexander Attinger, Samuel A. Ocko, Surya Ganguli, and Lisa M. Giocomo. 2021. 'Distance-Tuned Neurons Drive Specialized Path Integration Calculations in Medial Entorhinal Cortex'. *Cell Reports* 36 (10): 109669. <https://doi.org/10.1016/j.celrep.2021.109669>.

Campbell, Malcolm G., Samuel A. Ocko, Caitlin S. Mallory, Isabel I.C. Low, Surya Ganguli, and Lisa M. Giocomo. 2018. 'Principles Governing the Integration of Landmark and Self-Motion Cues in Entorhinal Cortical Codes for Navigation'. *Nature Neuroscience* 21 (8): 1096–1106. <https://doi.org/10.1038/s41593-018-0189-y>.

Chen, Guifen, Daniel Manson, Francesca Cacucci, and Thomas Joseph Wills. 2016. ‘Absence of Visual Input Results in the Disruption of Grid Cell Firing in the Mouse’. *Current Biology* 26 (17): 2335–42. <https://doi.org/10.1016/j.cub.2016.06.043>.

Chrobak, J. J., and G. Buzsáki. 1998. ‘Gamma Oscillations in the Entorhinal Cortex of the Freely Behaving Rat’. *The Journal of Neuroscience* 18 (1): 388–98. <https://doi.org/10.1523/JNEUROSCI.18-01-00388.1998>.

Chung, Jason E., Jeremy F. Magland, Alex H. Barnett, Vanessa M. Tolosa, Angela C. Tooker, Kye Y. Lee, Kedar G. Shah, Sarah H. Felix, Loren M. Frank, and Leslie F. Greengard. 2017. ‘A Fully Automated Approach to Spike Sorting’. *Neuron* 95 (6): 1381–1394.e6. <https://doi.org/10.1016/j.neuron.2017.08.030>.

Colgin, Laura Lee, Tobias Denninger, Marianne Fyhn, Torkel Hafting, Tora Bonnevie, Ole Jensen, May-Britt Moser, and Edvard I. Moser. 2009. ‘Frequency of Gamma Oscillations Routes Flow of Information in the Hippocampus’. *Nature* 462 (7271): 353–57. <https://doi.org/10.1038/nature08573>.

Constantinescu, Alexandra O., Jill X. O'Reilly, and Timothy E. J. Behrens. 2016. ‘Organizing Conceptual Knowledge in Humans with a Gridlike Code’. *Science* 352 (6292): 1464–68. <https://doi.org/10.1126/science.aaf0941>.

Coughlan, Gillian, Jan Laczó, Jakub Hort, Anne-Marie Minihane, and Michael Hornberger. 2018. ‘Spatial Navigation Deficits — Overlooked Cognitive Marker for Preclinical Alzheimer Disease?’ *Nature Reviews Neurology*. <https://doi.org/10.1038/s41582-018-0031-x>.

Davis, A. E., A. M. Gimenez, and B. Therrien. 2001. ‘Effects of Entorhinal Cortex Lesions on Sensory Integration and Spatial Learning’. *Nursing Research* 50 (2): 77–85. <https://doi.org/10.1097/00006199-200103000-00003>.

Derdikman, Dori, Jonathan R Whitlock, Albert Tsao, Marianne Fyhn, Torkel Hafting, May-Britt Moser, and Edvard I Moser. 2009. ‘Fragmentation of Grid Cell Maps in a Multicompartment Environment’. *Nature Neuroscience* 12 (10): 1325–32. <https://doi.org/10.1038/nn.2396>.

- Diehl, Geoffrey W., Olivia J. Hon, Stefan Leutgeb, and Jill K. Leutgeb. 2017. 'Grid and Nongrid Cells in Medial Entorhinal Cortex Represent Spatial Location and Environmental Features with Complementary Coding Schemes'. *Neuron* 94 (1): 83-92.e6. <https://doi.org/10.1016/j.neuron.2017.03.004>.
- Doeller, Christian F., Caswell Barry, and Neil Burgess. 2010. 'Evidence for Grid Cells in a Human Memory Network'. *Nature* 463 (7281): 657–61. <https://doi.org/10.1038/nature08704>.
- Domnisoru, Cristina, Amina A. Kinkhabwala, and David W. Tank. 2013. 'Membrane Potential Dynamics of Grid Cells'. *Nature*. <https://doi.org/10.1038/nature11973>.
- Eichenbaum, H, M Kuperstein, A Fagan, and J Nagode. 1987. 'Cue-Sampling and Goal-Approach Correlates of Hippocampal Unit Activity in Rats Performing an Odor-Discrimination Task'. *The Journal of Neuroscience* 7 (3): 716–32. <https://doi.org/10.1523/JNEUROSCI.07-03-00716.1987>.
- Eichenbaum, H, C Stewart, and R Morris. 1990. 'Hippocampal Representation in Place Learning'. *The Journal of Neuroscience* 10 (11): 3531–42. <https://doi.org/10.1523/JNEUROSCI.10-11-03531.1990>.
- Erdem, Uğur M., and Michael Hasselmo. 2012. 'A Goal-Directed Spatial Navigation Model Using Forward Trajectory Planning Based on Grid Cells'. *The European Journal of Neuroscience* 35 (6): 916–31. <https://doi.org/10.1111/j.1460-9568.2012.08015.x>.
- Erdem, Uğur M., and Michael E. Hasselmo. 2014. 'A Biologically Inspired Hierarchical Goal Directed Navigation Model'. *Journal of Physiology, Paris* 108 (1): 28–37. <https://doi.org/10.1016/j.jphysparis.2013.07.002>.
- Etienne, Ariane S., and Kathryn J. Jeffery. 2004. 'Path Integration in Mammals'. *Hippocampus* 14 (2): 180–92. <https://doi.org/10.1002/hipo.10173>.
- Fiete, I. R., Y. Burak, and T. Brookings. 2008. 'What Grid Cells Convey about Rat Location'. *Journal of Neuroscience*. <https://doi.org/10.1523/JNEUROSCI.5684-07.2008>.

Fiorillo, Christopher D., Philippe N. Tobler, and Wolfram Schultz. 2003. 'Discrete Coding of Reward Probability and Uncertainty by Dopamine Neurons'. *Science* 299 (5614): 1898–1902. <https://doi.org/10.1126/science.1077349>.

Fox, John, and Sanford Weisberg. 2019. *An R Companion to Applied Regression*. 3rd ed. Thousand Oaks, California: Sage.  
<https://socialsciences.mcmaster.ca/jfox/Books/Companion/index.html>.

Fries, P., T. Womelsdorf, R. Oostenveld, and R. Desimone. 2008. 'The Effects of Visual Stimulation and Selective Visual Attention on Rhythmic Neuronal Synchronization in Macaque Area V4'. *Journal of Neuroscience* 28 (18): 4823–35.  
<https://doi.org/10.1523/JNEUROSCI.4499-07.2008>.

Fu, Hongjun, Gustavo A. Rodriguez, Mathieu Herman, Sheina Emrani, Eden Nahmani, Geoffrey Barrett, Helen Y. Figueiroa, Eliana Goldberg, S. Abid Hussaini, and Karen E. Duff. 2017. 'Tau Pathology Induces Excitatory Neuron Loss, Grid Cell Dysfunction, and Spatial Memory Deficits Reminiscent of Early Alzheimer's Disease'. *Neuron*.  
<https://doi.org/10.1016/j.neuron.2016.12.023>.

Fuhs, Mark C., and David S. Touretzky. 2006. 'A Spin Glass Model of Path Integration in Rat Medial Entorhinal Cortex'. *Journal of Neuroscience* 26 (16): 4266–76.  
<https://doi.org/10.1523/JNEUROSCI.4353-05.2006>.

Fyhn, Marianne, Sturla Molden, Menno P. Witter, Edvard I. Moser, and May-Britt Moser. 2004. 'Spatial Representation in the Entorhinal Cortex'. *Science* 305 (5688): 1258–64. <https://doi.org/10.1126/science.1099901>.

Gardner, Richard J., Erik Hermansen, Marius Pachitariu, Yoram Burak, Nils A. Baas, Benjamin A. Dunn, May-Britt Moser, and Edvard I. Moser. 2022. 'Toroidal Topology of Population Activity in Grid Cells'. *Nature* 602 (7895): 123–28.  
<https://doi.org/10.1038/s41586-021-04268-7>.

Gardner, Richard J., Li Lu, Tanja Wernle, May-Britt Moser, and Edvard I. Moser. 2019. 'Correlation Structure of Grid Cells Is Preserved during Sleep'. *Nature Neuroscience* 22 (4): 598–608. <https://doi.org/10.1038/s41593-019-0360-0>.

- Geisler, Caroline, David Robbe, Michaël Zugaro, Anton Sirota, and György Buzsáki. 2007. ‘Hippocampal Place Cell Assemblies Are Speed-Controlled Oscillators’. *Proceedings of the National Academy of Sciences* 104 (19): 8149–54.  
<https://doi.org/10.1073/pnas.0610121104>.
- Gerlei, Klara. 2019. ‘Anatomical and Functional Investigation of the Deep Medial Entorhinal Cortex’. University of Edinburgh.
- Geva-Sagiv, Maya, Liora Las, Yossi Yovel, and Nachum Ulanovsky. 2015. ‘Spatial Cognition in Bats and Rats: From Sensory Acquisition to Multiscale Maps and Navigation’. *Nature Reviews Neuroscience* 16 (2): 94–108. <https://doi.org/10.1038/nrn3888>.
- Gil, Mariana, Mihai Ancau, Magdalene I Schlesiger, Angela Neitz, Kevin Allen, Rodrigo J De Marco, and Hannah Monyer. 2018. ‘Impaired Path Integration in Mice with Disrupted Grid Cell Firing’. *Nature Neuroscience* 21: 81–91.  
<https://doi.org/10.1038/s41593-017-0039-3>.
- Góis, Zé Henrique T.D., and Adriano B.L. Tort. 2018. ‘Characterizing Speed Cells in the Rat Hippocampus’. *Cell Reports* 25 (7): 1872–1884.e4.  
<https://doi.org/10.1016/j.celrep.2018.10.054>.
- Griffin, Amy L., Howard Eichenbaum, and Michael E. Hasselmo. 2007. ‘Spatial Representations of Hippocampal CA1 Neurons Are Modulated by Behavioral Context in a Hippocampus-Dependent Memory Task’. *The Journal of Neuroscience* 27 (9): 2416–23. <https://doi.org/10.1523/JNEUROSCI.4083-06.2007>.
- Guanella, Alexis, Daniel Kiper, and Paul Verschure. 2007. ‘A Model of Grid Cells Based on a Twisted Torus Topology’. *International Journal of Neural Systems* 17 (04): 231–40.  
<https://doi.org/10.1142/S0129065707001093>.
- Hafting, Torkel, Marianne Fyhn, Tora Bonnevie, May-Britt Moser, and Edvard I. Moser. 2008. ‘Hippocampus-Independent Phase Precession in Entorhinal Grid Cells’. *Nature* 453 (7199): 1248–52. <https://doi.org/10.1038/nature06957>.
- Hafting, Torkel, Marianne Fyhn, Sturla Molden, May Britt Moser, and Edvard I. Moser. 2005. ‘Microstructure of a Spatial Map in the Entorhinal Cortex’. *Nature*.  
<https://doi.org/10.1038/nature03721>.

Hampson, Robert E., Charles J. Heyser, and Sam A. Deadwyler. 1993. 'Hippocampal Cell Firing Correlates of Delayed-Match-to-Sample Performance in the Rat.' *Behavioral Neuroscience* 107 (5): 715–39. <https://doi.org/10.1037/0735-7044.107.5.715>.

Hardcastle, Kiah, Surya Ganguli, and Lisa M. Giocomo. 2015. 'Environmental Boundaries as an Error Correction Mechanism for Grid Cells'. *Neuron* 86 (3): 827–39. <https://doi.org/10.1016/j.neuron.2015.03.039>.

Hardcastle, Kiah, Niru Maheswaranathan, Surya Ganguli, and Lisa M. Giocomo. 2017. 'A Multiplexed, Heterogeneous, and Adaptive Code for Navigation in Medial Entorhinal Cortex'. *Neuron* 94 (2): 375-387.e7. <https://doi.org/10.1016/j.neuron.2017.03.025>.

Hartley, T., N. Burgess, C. Lever, F. Cacucci, and J. O'Keefe. 2000. 'Modeling Place Fields in Terms of the Cortical Inputs to the Hippocampus'. *Hippocampus* 10 (4): 369–79. [https://doi.org/10.1002/1098-1063\(2000\)10:4<369::AID-HIPO3>3.0.CO;2-0](https://doi.org/10.1002/1098-1063(2000)10:4<369::AID-HIPO3>3.0.CO;2-0).

Hikosaka, K. 2000. 'Delay Activity of Orbital and Lateral Prefrontal Neurons of the Monkey Varying with Different Rewards'. *Cerebral Cortex* 10 (3): 263–71. <https://doi.org/10.1093/cercor/10.3.263>.

Horner, Aidan J., James A. Bisby, Ewa Zotow, Daniel Bush, and Neil Burgess. 2016. 'Grid-like Processing of Imagined Navigation'. *Current Biology* 26 (6): 842–47. <https://doi.org/10.1016/j.cub.2016.01.042>.

Howe, Mark W., Patrick L. Tierney, Stefan G. Sandberg, Paul E. M. Phillips, and Ann M. Graybiel. 2013. 'Prolonged Dopamine Signalling in Striatum Signals Proximity and Value of Distant Rewards'. *Nature* 500 (7464): 575–79. <https://doi.org/10.1038/nature12475>.

Howett, David, Andrea Castegnaro, Katarzyna Krzywicka, Johanna Hagman, Deepti Marchment, Richard Henson, Miguel Rio, John A King, Neil Burgess, and Dennis Chan. 2019. 'Differentiation of Mild Cognitive Impairment Using an Entorhinal Cortex-Based Test of Virtual Reality Navigation'. *Brain* 142 (6): 1751–66. <https://doi.org/10.1093/brain/awz116>.

Huhn, Zsofia, Zoltan Somogyvari, Tamas Kiss, and Peter Erdi. 2009. 'Extraction of Distance Information from the Activity of Entorhinal Grid Cells: A Model Study'. In *2009 International Joint Conference on Neural Networks*, 1298–1303.  
<https://doi.org/10.1109/IJCNN.2009.5178864>.

Jacob, Pierre Yves, Fabrizio Capitano, Bruno Poucet, Etienne Save, and Francesca Sargolini. 2019. 'Path Integration Maintains Spatial Periodicity of Grid Cell Firing in a 1D Circular Track'. *Nature Communications* 10 (1).  
<https://doi.org/10.1038/s41467-019-08795-w>.

Jayakumar, Ravikrishnan P., Manu S. Madhav, Francesco Savelli, Hugh T. Blair, Noah J. Cowan, and James J. Knierim. 2019. 'Recalibration of Path Integration in Hippocampal Place Cells'. *Nature* 566 (7745): 533–37.  
<https://doi.org/10.1038/s41586-019-0939-3>.

Jones, Gareth, and Marc W Holderied. 2007. 'Bat Echolocation Calls: Adaptation and Convergent Evolution'. *Proceedings of the Royal Society B: Biological Sciences* 274 (1612): 905–12. <https://doi.org/10.1098/rspb.2006.0200>.

Jun, Heechul, Allen Bramian, Shogo Soma, Takashi Saito, Takaomi C. Saido, and Kei M. Igarashi. 2020. 'Disrupted Place Cell Remapping and Impaired Grid Cells in a Knockin Model of Alzheimer's Disease'. *Neuron* 107 (6): 1095-1112.e6.  
<https://doi.org/10.1016/j.neuron.2020.06.023>.

Kobayashi, Shunsuke, Johan Lauwereyns, Masashi Koizumi, Masamichi Sakagami, and Okihide Hikosaka. 2002. 'Influence of Reward Expectation on Visuospatial Processing in Macaque Lateral Prefrontal Cortex'. *Journal of Neurophysiology* 87 (3): 1488–98. <https://doi.org/10.1152/jn.00472.2001>.

Kornienko, Olga, Patrick Latuske, Mathis Bassler, Laura Kohler, and Kevin Allen. 2018. 'Non-Rhythmic Head-Direction Cells in the Parahippocampal Region Are Not Constrained by Attractor Network Dynamics'. *eLife* 7: 1–25.  
<https://doi.org/10.7554/eLife.35949>.

Kropff, Emilio, James E. Carmichael, May Britt Moser, and Edvard I. Moser. 2015. 'Speed Cells in the Medial Entorhinal Cortex'. *Nature* 523 (7561): 419–24.  
<https://doi.org/10.1038/nature14622>.

Krupic, Julija, Marius Bauza, Stephen Burton, Caswell Barry, and John O’Keefe. 2015. ‘Grid Cell Symmetry Is Shaped by Environmental Geometry’. *Nature*.  
<https://doi.org/10.1038/nature14153>.

Kubie, John, and André Fenton. 2012. ‘Linear Look-Ahead in Conjunctive Cells: An Entorhinal Mechanism for Vector-Based Navigation’. *Frontiers in Neural Circuits* 6.  
<https://doi.org/10.3389/fncir.2012.00020>.

Kunz, Lukas, T.N. Schröder, H. Lee, C. Montag, B. Lachmann, R. Sariyska, M. Reuter, et al. 2015. ‘Reduced Grid-Cell– like Representations in Adults at Genetic Risk for Alzheimer’s Disease’. *Science*. <https://doi.org/10.1126/science.aac8128>.

LaChance, Patrick A., Travis P. Todd, and Jeffrey S. Taube. 2019. ‘A Sense of Space in Postrhinal Cortex’. *Science* 365 (6449): eaax4192.  
<https://doi.org/10.1126/science.aax4192>.

Langston, Rosamund F., James A. Ainge, Jonathan J. Couey, Cathrin B. Canto, Tale L. Bjerknes, Menno P. Witter, Edvard I. Moser, and May-Britt Moser. 2010. ‘Development of the Spatial Representation System in the Rat’. *Science* 328 (5985): 1576–80. <https://doi.org/10.1126/science.1188210>.

Lavoie, A.M., and S.J.Y. Mizumori. 1994. ‘Spatial, Movement- and Reward-Sensitive Discharge by Medial Ventral Striatum Neurons of Rats’. *Brain Research* 638 (1–2): 157–68. [https://doi.org/10.1016/0006-8993\(94\)90645-9](https://doi.org/10.1016/0006-8993(94)90645-9).

Leon, Matthew I., and Michael N. Shadlen. 1999. ‘Effect of Expected Reward Magnitude on the Response of Neurons in the Dorsolateral Prefrontal Cortex of the Macaque’. *Neuron* 24 (2): 415–25. [https://doi.org/10.1016/S0896-6273\(00\)80854-5](https://doi.org/10.1016/S0896-6273(00)80854-5).

Lever, C., S. Burton, A. Jeewajee, J. O’Keefe, and N. Burgess. 2009. ‘Boundary Vector Cells in the Subiculum of the Hippocampal Formation’. *Journal of Neuroscience* 29 (31): 9771–77. <https://doi.org/10.1523/JNEUROSCI.1319-09.2009>.

Light, Kenneth R., Brian Cotten, Talia Malekan, Sophie Dewil, Matthew R. Bailey, Charles R. Gallistel, and Peter D. Balsam. 2019. ‘Evidence for a Mixed Timing and Counting Strategy in Mice Performing a Mechner Counting Task’. *Frontiers in Behavioral Neuroscience* 13. <https://www.frontiersin.org/articles/10.3389/fnbeh.2019.00109>.

Lindsay, Grace W. 2020. ‘Attention in Psychology, Neuroscience, and Machine Learning’. *Frontiers in Computational Neuroscience* 14 (April): 29. <https://doi.org/10.3389/fncom.2020.00029>.

Lomb, N. R. 1976. ‘Least-Squares Frequency Analysis of Unequally Spaced Data’. *Astrophysics and Space Science* 39 (2): 447–62. <https://doi.org/10.1007/BF00648343>.

Lopes, Gonzalo, Niccola Bonacchi, Joao Frazao, Joana P. Neto, Bassam V. Atallah, Sofia Soares, Luas Moreira, et al. 2015. ‘Bonsai: An Event-Based Framework for Processing and Controlling Data Streams’. *Frontiers in Neuroinformatics* 9 (April). <https://doi.org/10.3389/fninf.2015.00007>.

Low, Isabel I.C., Alex H. Williams, Malcolm G. Campbell, Scott W. Linderman, and Lisa M. Giocomo. 2021. ‘Dynamic and Reversible Remapping of Network Representations in an Unchanging Environment’. *Neuron* 109 (18): 2967–2980.e11. <https://doi.org/10.1016/j.neuron.2021.07.005>.

Marr, David. 1982. *Vision: A Computational Investigation into the Human Representation and Processing of Visual Information*. San Francisco: W. H. Freeman and Company.

McNaughton, Bruce L., Francesco P. Battaglia, Ole Jensen, Edvard I Moser, and May-Britt Moser. 2006. ‘Path Integration and the Neural Basis of the “Cognitive Map”’. *Nature Reviews Neuroscience* 7 (8): 663–78. <https://doi.org/10.1038/nrn1932>.

Miao, Chenglin, Qichen Cao, Hiroshi T. Ito, Homare Yamahachi, Menno P. Witter, May-Britt Moser, and Edvard I. Moser. 2015. ‘Hippocampal Remapping after Partial Inactivation of the Medial Entorhinal Cortex’. *Neuron* 88 (3): 590–603. <https://doi.org/10.1016/j.neuron.2015.09.051>.

Mittelstaedt, M. -L., and H. Mittelstaedt. 1980. ‘Homing by Path Integration in a Mammal’. *Naturwissenschaften* 67 (11): 566–67. <https://doi.org/10.1007/BF00450672>.

Mokrisova, I, J Laczo, R Andel, I Gazova, M Vyhalek, Z Nedelska, D Levcik, J Cerman, K Vlcek, and J Hort. 2016. ‘Real-Space Path Integration Is Impaired in Alzheimer’s Disease and Mild Cognitive Impairment’. *Behavioural Brain Research* 307: 150–58. <https://doi.org/10.1016/j.bbr.2016.03.052>.

Morris, R. G. M., P. Garrud, J. N. P. Rawlins, and J. O'Keefe. 1982. 'Place Navigation Impaired in Rats with Hippocampal Lesions'. *Nature* 297 (5868): 681–83.  
<https://doi.org/10.1038/297681a0>.

Moser, Edvard I. 2014. 'Grid Cells and the Entorhinal Map of Space'. Presented at the Nobel Prize in Physiology or Medicine.  
<https://www.nobelprize.org/uploads/2018/06/edvard-moser-lecture-slides.pdf>.

Nagele, Johannes, Andreas V.M. Herz, and Martin B. Stemmler. 2020. 'Untethered Firing Fields and Intermittent Silences: Why Grid-Cell Discharge Is so Variable'. *Hippocampus* 30 (4): 367–83. <https://doi.org/10.1002/hipo.23191>.

O'Keefe, J., and J. Dostrovsky. 1971. 'The Hippocampus as a Spatial Map. Preliminary Evidence from Unit Activity in the Freely-Moving Rat'. *Brain Research* 34 (1): 171–75.  
[https://doi.org/10.1016/0006-8993\(71\)90358-1](https://doi.org/10.1016/0006-8993(71)90358-1).

O'Keefe, John, and Lynn Nadel. 1978. 'The Hippocampus as a Cognitive Map'.

O'Keefe, John, and Michael L. Recce. 1993. 'Phase Relationship between Hippocampal Place Units and the EEG Theta Rhythm'. *Hippocampus* 3 (3): 317–30.  
<https://doi.org/10.1002/hipo.450030307>.

Osborne, Jason E., and Joshua T. Dudman. 2014. 'RIVETS: A Mechanical System for In Vivo and In Vitro Electrophysiology and Imaging'. Edited by Benjamin Arenkiel. *PLoS ONE* 9 (2): e89007. <https://doi.org/10.1371/journal.pone.0089007>.

Pastoll, Hugh, Lukas Solanka, Mark C W Van Rossum, and Matthew F Nolan. 2013. 'Article Feedback Inhibition Enables Theta-Nested Gamma Oscillations and Grid Firing Fields'. *NEURON* 77: 141–54. <https://doi.org/10.1016/j.neuron.2012.11.032>.

Pérez-Escobar, José Antonio, Olga Kornienko, Patrick Latuske, Laura Kohler, and Kevin Allen. 2016. 'Visual Landmarks Sharpen Grid Cell Metric and Confer Context Specificity to Neurons of the Medial Entorhinal Cortex'. *eLife* 5 (July): e16937.  
<https://doi.org/10.7554/eLife.16937>.

Pettit, Noah L., Xintong C. Yuan, and Christopher D. Harvey. 2022. 'Hippocampal Place Codes Are Gated by Behavioral Engagement'. *Nature Neuroscience* 25 (5): 561–66. <https://doi.org/10.1038/s41593-022-01050-4>.

Porter, Steven L., George H. Wadhams, and Judith P. Armitage. 2011. 'Signal Processing in Complex Chemotaxis Pathways'. *Nature Reviews Microbiology* 9 (3): 153–65. <https://doi.org/10.1038/nrmicro2505>.

Press, William H., and George B. Rybicki. 1989. 'Fast Algorithm for Spectral Analysis of Unevenly Sampled Data'. *The Astrophysical Journal* 338 (March): 277. <https://doi.org/10.1086/167197>.

Russell, James C., David R. Towns, Sandra H. Anderson, and Mick N. Clout. 2005. 'Intercepting the First Rat Ashore'. *Nature* 437 (7062): 1107. <https://doi.org/10.1038/4371107a>.

Sarel, Ayelet, Arseny Finkelstein, Liora Las, and Nachum Ulanovsky. 2017. 'Vectorial Representation of Spatial Goals in the Hippocampus of Bats'. *Science* 355 (6321): 176–80. <https://doi.org/10.1126/science.aak9589>.

Sargolini, Francesca, Marianne Fyhn, Torkel Hafting, Bruce L. McNaughton, Menno P. Witter, May Britt Moser, and Edvard I. Moser. 2006. 'Conjunctive Representation of Position, Direction, and Velocity in Entorhinal Cortex'. *Science* 312 (5774): 758–62. <https://doi.org/10.1126/science.1125572>.

Savelli, Francesco, D. Yoganarasimha, and James J. Knierim. 2008. 'Influence of Boundary Removal on the Spatial Representations of the Medial Entorhinal Cortex'. *Hippocampus* 18 (12): 1270–82. <https://doi.org/10.1002/hipo.20511>.

Scargle, J. D. 1982. 'Studies in Astronomical Time Series Analysis. II - Statistical Aspects of Spectral Analysis of Unevenly Spaced Data'. *The Astrophysical Journal* 263 (December): 835. <https://doi.org/10.1086/160554>.

Schaeffer, Rylan, Mikail Khona, and Ila Rani Fiete. 2022. 'No Free Lunch from Deep Learning in Neuroscience: A Case Study through Models of the Entorhinal-Hippocampal Circuit'. Preprint. Neuroscience. <https://doi.org/10.1101/2022.08.07.503109>.

- Schiller, D., H. Eichenbaum, E. A. Buffalo, L. Davachi, D. J. Foster, S. Leutgeb, and C. Ranganath. 2015. 'Memory and Space: Towards an Understanding of the Cognitive Map'. *Journal of Neuroscience* 35 (41): 13904–11. <https://doi.org/10.1523/JNEUROSCI.2618-15.2015>.
- Shipston-Sharman, Oliver, Lukas Solanka, and Matthew F. Nolan. 2016. 'Continuous Attractor Network Models of Grid Cell Firing Based on Excitatory–Inhibitory Interactions'. *Journal of Physiology*. <https://doi.org/10.1113/JP270630>.
- Skagg, William, E, Bruce McNaughton L, Katalin Gothard M, and Etan Markus J. 1993. 'An Information-Theoretic Approach to Deciphering the Hippocampal Code'. *Proceedings of the IEEE*, no. 1990: 1030–1037.
- Solanka, Lukas, Mark C.W. Van Rossum, and Matthew F. Nolan. 2015. 'Noise Promotes Independent Control of Gamma Oscillations and Grid Firing within Recurrent Attractor Networks'. *eLife*. <https://doi.org/10.7554/eLife.06444>.
- Solstad, Trygve, Charlotte N. Boccara, Emilio Kropff, May-Britt Moser, and Edvard I. Moser. 2008. 'Representation of Geometric Borders in the Entorhinal Cortex'. *Science* 322 (5909): 1865–68. <https://doi.org/10.1126/science.1166466>.
- Solstad, Trygve, Edvard I. Moser, and Gaute T. Einevoll. 2006. 'From Grid Cells to Place Cells: A Mathematical Model'. *Hippocampus* 16 (12): 1026–31. <https://doi.org/10.1002/hipo.20244>.
- Sorscher, Ben, Gabriel C Mel, Samuel A Ocko, Lisa Giocomo, Surya Ganguli, and Applied Physics. 2020. 'A Unified Theory for the Computational and Mechanistic Origins of Grid Cells', 1–41.
- Squire, Larry R. 1992. 'Memory and the Hippocampus: A Synthesis from Findings with Rats, Monkeys, and Humans.' *Psychological Review* 99 (2): 195–231. <https://doi.org/10.1037/0033-295X.99.2.195>.
- Sreenivasan, Sameet, and Ila Fiete. 2011. 'Grid Cells Generate an Analog Error-Correcting Code for Singularly Precise Neural Computation'. *Nature Neuroscience* 14 (10): 1330–37. <https://doi.org/10.1038/nn.2901>.

Steinmetz, Nicholas A., Cagatay Aydin, Anna Lebedeva, Michael Okun, Marius Pachitariu, Marius Bauza, Maxime Beau, et al. 2021. 'Neuropixels 2.0: A Miniaturized High-Density Probe for Stable, Long-Term Brain Recordings'. *Science* 372 (6539): eabf4588. <https://doi.org/10.1126/science.abf4588>.

Stemmler, Martin, Alexander Mathis, and Andreas V.M. Herz. 2015. 'Neuroscience: Connecting Multiple Spatial Scales to Decode the Population Activity of Grid Cells'. *Science Advances* 1 (11): 1–12. <https://doi.org/10.1126/science.1500816>.

Stensola, Hanne, Tor Stensola, Trygve Solstad, Kristian FrØland, May Britt Moser, and Edvard I. Moser. 2012. 'The Entorhinal Grid Map Is Discretized'. *Nature* 492 (7427): 72–78. <https://doi.org/10.1038/nature11649>.

Stensola, Tor, Hanne Stensola, May-Britt Moser, and Edvard I Moser. 2014. 'Shearing-Induced Asymmetry in Entorhinal Grid Cells'. *Nature* 518. <https://doi.org/10.1038/nature14151>.

Sun, Hong, and Tian-Ren Yao. 1994. 'A Neural-like Network Approach to Residue-to-Decimal Conversion'. In *Proceedings of 1994 IEEE International Conference on Neural Networks (ICNN'94)*, 6:3883–87 vol.6. <https://doi.org/10.1109/ICNN.1994.374831>.

Taube, Jeffrey S. 2007. 'The Head Direction Signal: Origins and Sensory-Motor Integration'. *Annual Review of Neuroscience* 30 (1): 181–207. <https://doi.org/10.1146/annurev.neuro.29.051605.112854>.

Taube, Js, Ru Muller, and Jb Ranck. 1990. 'Head-Direction Cells Recorded from the Postsubiculum in Freely Moving Rats. I. Description and Quantitative Analysis'. *The Journal of Neuroscience* 10 (2): 420–35. <https://doi.org/10.1523/JNEUROSCI.10-02-00420.1990>.

Tennant, Sarah A. 2017. 'An Investigation of Circuit Mechanisms of Spatial Memory and Navigation in Virtual Reality'. University of Edinburgh.

Tennant, Sarah A., Harry Clark, Ian Hawes, Wing Kin Tam, Junji Hua, Wannan Yang, Klara Z. Gerlei, Emma R. Wood, and Matthew F. Nolan. 2022. 'Spatial Representation by Ramping Activity of Neurons in the Retrohippocampal Cortex'. *Current Biology* 32 (20): 4451-4464.e7. <https://doi.org/10.1016/j.cub.2022.08.050>.

Tennant, Sarah A., Lukas Fischer, Derek L.F. Garden, Klára Zsófia Gerlei, Cristina Martinez-Gonzalez, Christina McClure, Emma R. Wood, and Matthew F. Nolan. 2018. 'Stellate Cells in the Medial Entorhinal Cortex Are Required for Spatial Learning'. *Cell Reports*. <https://doi.org/10.1016/j.celrep.2018.01.005>.

Trettel, Sean G., John B. Trumper, Ernie Hwaun, Ila R. Fiete, and Laura Lee Colgin. 2019. 'Grid Cell Co-Activity Patterns during Sleep Reflect Spatial Overlap of Grid Fields during Active Behaviors'. *Nature Neuroscience* 22 (4): 609–17. <https://doi.org/10.1038/s41593-019-0359-6>.

Tu, Sicong, Stephanie Wong, John R. Hodges, Muireann Irish, Olivier Piguet, and Michael Hornberger. 2015. 'Lost in Spatial Translation - A Novel Tool to Objectively Assess Spatial Disorientation in Alzheimer's Disease and Frontotemporal Dementia'. *Cortex*. <https://doi.org/10.1016/j.cortex.2015.03.016>.

Waaga, Torgeir, Haggai Agmon, Valentin A. Normand, Anne Nagelhus, Richard J. Gardner, May-Britt Moser, Edvard I. Moser, and Yoram Burak. 2022. 'Grid-Cell Modules Remain Coordinated When Neural Activity Is Dissociated from External Sensory Cues'. *Neuron* 110 (11): 1843-1856.e6. <https://doi.org/10.1016/j.neuron.2022.03.011>.

Watanabe, Masataka. 1996. 'Reward Expectancy in Primate Prefrontal Neurons'. *Nature* 382 (6592): 629–32. <https://doi.org/10.1038/382629a0>.

Wehner, R, and S Wehner. 1986. 'Path Integration in Desert Ants — Approaching a Long-Standing Puzzle in Insect'. *Monitor Zoologico Italiano* 20 (3): 309–31.

Welday, A. C., I. G. Shlifer, M. L. Bloom, K. Zhang, and H. T. Blair. 2011. 'Cosine Directional Tuning of Theta Cell Burst Frequencies: Evidence for Spatial Coding by Oscillatory Interference'. *Journal of Neuroscience* 31 (45): 16157–76. <https://doi.org/10.1523/JNEUROSCI.0712-11.2011>.

Williams, Timothy C., Janet M. Williams, and Donald R. Griffin. 1966. 'The Homing Ability of the Neotropical Bat *Phyllostomus hastatus*, with Evidence for Visual Orientation'. *Animal Behaviour* 14 (4): 468–73. [https://doi.org/10.1016/S0003-3472\(66\)80047-7](https://doi.org/10.1016/S0003-3472(66)80047-7).

Wills, Tom J., Francesca Cacucci, Neil Burgess, and John O'Keefe. 2010. 'Development of the Hippocampal Cognitive Map in Preweanling Rats'. *Science* 328 (5985): 1573–76. <https://doi.org/10.1126/science.1188224>.

Wood, Emma R., Paul A. Dudchenko, R.Jonathan Robitsek, and Howard Eichenbaum. 2000. 'Hippocampal Neurons Encode Information about Different Types of Memory Episodes Occurring in the Same Location'. *Neuron* 27 (3): 623–33. [https://doi.org/10.1016/S0896-6273\(00\)00071-4](https://doi.org/10.1016/S0896-6273(00)00071-4).

Yoon, Ki Jung, Sam Lewallen, Amina A. Kinkhabwala, David W. Tank, and Ila R. Fiete. 2016. 'Grid Cell Responses in 1D Environments Assessed as Slices through a 2D Lattice'. *Neuron*. <https://doi.org/10.1016/j.neuron.2016.01.039>.

Yoon, Kijung, Michael A Buice, Caswell Barry, Robin Hayman, Neil Burgess, and Ila R Fiete. 2013. 'Specific Evidence of Low-Dimensional Continuous Attractor Dynamics in Grid Cells'. *Nature Neuroscience* 16 (8): 1077–84. <https://doi.org/10.1038/nn.3450>.